Faculty of Sciences

Department of Physics and Astronomy

PRODUCTION OF SELECTED RADIONUCLIDES WITH PRIMARY PROTONS AND SECONDARY NEUTRONS AT A 70 MEV H^- CYCLOTRON FACILITY

by

MOGAKOLODI ADOLF MOTETSHWANE

Student ID Number: 14100381

BSc (Physics) (University of Botswana)

NQF Level 8 (Medical Physics) (University of the Witwatersrand)

MSc (Physics) (Botswana International University of Science and Technology)

A Thesis Submitted to the Faculty of Sciences in Partial Fulfilment of the Requirements for the Award of the Doctor of Philosophy in Physics of BIUST

Supervisors:

Prof. Gregory Campbell Hillhouse
Department of Physics and Astronomy
Faculty of Sciences, BIUST
hillhouseg@biust.ac.bw

Dr. Gideon Francois Steyn
Department of Subatomic Physics
iThemba LABS
deon@tlabs.ac.bw

March, 2023

BOTSWANA INTERNATIONAL UNIVERSITY OF SCIENCE & TECHNOLOGY

POSTGRADUATE SCHOOL

Declaration Regarding the Work and Copyright

DECLARATION REGARDING THE WORK AND COPYRIGHT

Candidate (please write in caps or type) ADOLF MOTETSHWANE

Student ID: 14100381

Thesis Titled: PRODUCTION OF SELECTED RADIONUCLIDES WITH PRIMARY PROTONS AND SECONDARY NEUTRONS AT A 70 MEV H^- CYCLOTRON FACILITY

I, the **Candidate**, certify that the Thesis is all my own original work and that I have not obtained a degree in this University or elsewhere on the basis of any of this work.

(If the thesis is based on a group project, then the student must indicate the extent of her / his contribution, with reference to any other theses submitted or published by each collaborator in the project, and a declaration to this effect must be included in the thesis)

This dissertation/thesis is copyright material protected under the Berne Convention, the Copyright and Neighbouring Rights Act, Act. No. 8 of 2000 and other international and national enactments, in that behalf, on intellectual property. It must not be reproduced by any means, in full or in part, except for short extracts in fair dealing; for researcher private study, critical scholarly review or discourse with an acknowledgement, without the written permission of the office of the Postgraduate School, on behalf of both the author and the BIUST.

Signed: ---------- Date: 09/08/2023

Primary Supervisor: Prof Gregory Campbell Hillhouse

I, the Candidate's **Primary Supervisor**, hereby confirm that I have inspected the above titled thesis and, to the best of my knowledge, it is based on the original work of the candidate.

Signed: G. Hillhouse Date: 09/08/2023

Abstract

Production of Selected Radionuclides with Primary Protons and Secondary Neutrons at a 70 MeV H^- Cyclotron Facility

This study addresses five aspects in the field of radionuclide production, four of which are relevant to a new generation of high-current, 70 MeV H^- cyclotrons. A related aspect has also been investigated in the proton energy region 100–200 MeV. All the experimental work of this study was performed at the cyclotron facility of the iThemba Laboratory for Accelerator-Based Sciences (iThemba LABS) near Cape Town, South Africa, with external proton beams delivered by the k = 200 MeV separated-sector cyclotron (SSC) of the laboratory.

The feasibility to produce ^{225}Ac/^{213}Bi and ^{230}U/^{226}Th generators at a 70 MeV H^- facility by employing proton-induced reactions on thorium (Th+p) has been investigated. This is of relevance to iThemba LABS as a new commercial 70 MeV H^- cyclotron is currently being installed at the laboratory, expected to become operational in 2023, i.e. the near future. Since the SSC regularly produces 66 MeV proton beams for the routine radionuclide production programme, such beams were available to perform experimental work at an energy close to 70 MeV. New excitation-function measurements were performed for Th+p reactions by means of the stacked-foil technique, utilizing primary proton beams of 40 and 66 MeV. Both ^{213}Bi and ^{226}Th are alpha-particle emitters with importance in targeted alpha-particle therapy (TAT).

A separate study involving Th+p reactions focused on the potential production of ^{225}Ra/^{225}Ac generators, in the proton energy region 100-200 MeV, at iThemba LABS. New excitation-function measurements were performed utilizing a primary proton beam of 200 MeV. The alpha-emitter ^{225}Ac has been used directly in TAT in recent years. Interest in the ^{225}Ra/^{225}Ac generator stems from its ability to provide ^{225}Ac with a very high radionuclidic purity, which is not achievable with any of the direct production routes. A possible stacked-target concept for routine production purposes is presented and discussed.

The 70 MeV commercial cyclotron will enable the transfer of most of the routine radionuclide production programme, based on 66 MeV protons from the SSC, to the new machine. This will free the SSC to focus on other research objectives. A subtopic of this study was to investigate the targetry required for the new 70 MeV cyclotron, based on similar targetry used for many years on the SSC but upgraded to accommodate higher beam intensities. The inclusion of Th in various tandem target configurations was also explicitly considered. Also of importance for this study was the secondary neutron fluxes that would be generated by proton beams on these production targets, which was investigated using Monte Carlo simulations.

This work also presents data obtained from secondary-neutron activations of samples behind a radionuclide production target during routine bombardments with 66 MeV protons. Radioactive residues from 121 neutron-induced reactions were identified on activated samples covering a wide mass region (Be to Bi). Based on the measured yields and neutron spectra obtained from Monte Carlo simulations, average cross sections were calculated. These values are compared with corresponding predictions as published in the TENDL nuclear data libraries.

The last subtopic of this study focused on producing the therapeutic radionuclide ^{67}Cu in the secondary-neutron flux behind a primary tandem target under bombardment with a 70 MeV proton beam. Metallic Zn and ZnO were considered as targets. Yield estimates were made for enriched ^{67}Zn and ^{68}Zn targets as well as for ^{nat}Zn targets. It was necessary to identify which of ^{67}Zn or ^{68}Zn would be the best target nucleus for ^{67}Cu production in this case.

Acknowledgements

First and foremost, I would like to thank God, the Almighty, for bringing the right people to work with into my life.

I wish to extend my deepest gratitude to my supervisors, Prof Gregory C. Hillhouse and Dr Gideon F. Steyn for guiding me throughout this study and never giving up on me even when the going got tough, especially when COVID-19 took a toll on my progress.

I am especially indebted to the director of iThemba LABS, Dr Faïçal Azaiez, and his deputies, Dr Rudzani Nemutudi and Dr Rudolph Nchodu, for agreeing to the Memorandum of Understanding (MoU) between iThemba LABS and the Botswana International University of Science and Technology (BIUST). This collaboration is mutually beneficial in the region as both institutes are pursuing new accelerator projects. NRF iThemba LABS is establishing a dedicated 70 MeV cyclotron facility for radionuclide production. The Botswana Government, through BIUST, is planning to establish the Botswana Institute for Nuclear Science and Technology (BINST) with assistance from the International Atomic Energy Agency (IAEA). The MoU is important for both institutes in terms of training and capacity building.

Thanks to our expert friend, Dr Ferenc Szelecsényi from ATOMKI for his valuable pieces of advice. We would not have made it this far without you.

A very big thank you to the technical and support staff at iThemba LABS, Dr Lowry Conradie, Mr Dirk Fourie, Dr Muneer Sakildien and your dedicated staff. Without your contributions I would never have been able to conduct my experiments.

I am also deeply grateful to Dr Mathis Wiedeking and his impartial “right-hand men/women” for making our welfare as students their priority.

My special thanks go out to South Africa’s National Research Foundation (NRF), of which iThemba LABS is a business unit, for availing everything that I needed to work on my project, such as consumables, target materials, equipment (including personal protective equipment), transportation, and the on-site accommodation which made it possible for me to count my activated samples round the clock. Without support from iThemba LABS, this study would not have been feasible due to financial constraints.

To the BIUST and iThemba LABS staff, thank you for giving me the opportunity to work on this golden research project within the collaboration enabled by the MoU. I thank all those who assisted me, not only the ones mentioned.

I cannot express enough gratitude to my friend, Mr Otsile Tikologo, for spending countless sleepless nights with me to help resolve LaTeX software system issues that overwhelmed me.

Last but not least, I would like to give my most sincere thanks to my family for all the hope and support they gave me to persevere in my studies.

List of Tables

3.1 Comparison of proton energies and beam attenuation factors associated with the Th foils in the 66 MeV stack, obtained from the code STACK and the Monte Carlo code MCNP6. (See Section 2.7 for definition of the notation.) . . . 34

3.2 Decay data of investigated radionuclides[a]. . . . 35

3.3 Measured cross sections for formation of ^{225}Ac, ^{225}Ra, and ^{230}Pa in proton irradiation of ^{232}Th. . . . 41

3.4 Measured cross sections for formation of ^{22}Na and ^{24}Na in proton irradiation of ^{nat}Mg. 44

3.5 Yields of radionuclides considered for tandem targetry at a 70 MeV cyclotron facility. 49

3.6 ^{227}Ac impurity level in a Th target (as a percentage of the ^{225}Ac activity) at the end of a 24-hour bombardment, for selected energy windows. . . . 51

4.1 Measured cross sections for formation of ^{225}Ac and ^{225}Ra in proton irradiation of ^{232}Th. 58

4.2 Production yields of ^{227,225}Ac$^{!}$ and ^{225}Ac* for the triple-target system of Figure 4.7. . . 62

4.3 Production yields of ^{227,225}Ac$^{!}$ and ^{225}Ac* for the triple-target system of Figure 4.7, assuming a beam current of 250 μA. . . . 63

5.1 Material layers of the Rb/Ga tandem-target systems, located on the beam axis, for the VBTS (66 MeV protons) and the new 70 MeV target stations. . . . 66

5.2 Yields of ^{22}Na, ^{82}Sr, and ^{68}Ge from Mg/Ga and Rb/Ga tandem targets relevant to the VBTS (66 MeV proton beams) and the new 70 MeV cyclotron facility. . . . 67

5.3 Total neutron production from tandem targets during bombardment with a 70 MeV proton beam as well as the average forward neutron flux in the cavity behind the target. . . . 74

6.1 Targets/samples activated by neutrons behind a VBTS target during Run-1. . . . 80

6.2 Targets/samples activated by neutrons behind a VBTS target during Run-2. . . . 81

6.3 Zn sample/target materials employed and abundances* of their constituent stable isotopes. . . . 81

6.4 Targets/samples activated by neutrons behind a VBTS target during Run-3. . . . 81

6.5 The group cross section according to the closed-form Newton-Cotes formulae. . . . 94

6.6 Target nuclides, neutron-induced reactions and the decay data of observed residues used for their identification and quantification. . . . 99

6.6 Target nuclides, neutron-induced reactions and the decay data of observed residues used for their identification and quantification (continuing from previous page). . . . 100

6.6 Target nuclides, neutron-induced reactions and the decay data of observed residues used for their identification and quantification (continuing from previous page). . . . 101
6.7 Physical yields for a capture reaction and a threshold reaction, utilizing different interpolation strategies to determine group-averaged cross sections from the point-wise TENDL-2021 data. Upper and lower limits are also shown, determined from the minimum and maximum cross-section values in the individual groups. 102
6.8 Predicted average physical yields (TENDL-2019 + MCNP6) as well as corresponding measurements and associated cross sections. 104
6.8 Predicted average physical yields (TENDL-2019 + MCNP6) as well as corresponding measurements and associated cross sections (continuing from previous page). 105
6.8 Predicted average physical yields (TENDL-2019 + MCNP6) as well as corresponding measurements and associated cross sections (continuing from previous page). 106
6.9 Predicted average physical yields (TENDL-2021 + MCNP6) as well as corresponding measurements and associated cross sections. 107
6.9 Predicted average physical yields (TENDL-2021 + MCNP6) as well as corresponding measurements and associated cross sections (continuing from previous page). 108
6.9 Predicted average physical yields (TENDL-2021 + MCNP6) as well as corresponding measurements and associated cross sections (continuing from previous page). 109
6.10 Averages (of all 121 reactions) and associated standard deviations of Base-10 logarithms of the ratios between predicted and measured physical yields, for all MCNP6 physics selections, utilizing cross sections from the TENDL-2019 and TENDL-2021 libraries, respectively. 114
6.11 Number of reactions where ratios between predicted and measured physical yields is smaller than the factor indicated, for each MCNP6 physics selection, utilizing cross sections from the TENDL-2019 and TENDL-2021 libraries, respectively. The case for an averaged neutron spectrum is also included. 115
6.12 Experimental physical yields of ^{22,24}Na obtained from neutron activation experiment Run-2. 118

7.1 Experimentally determined average ^{67}Cu formation cross sections of neutron-induced reactions on highly enriched ^{67}Zn. 126
7.2 Experimentally determined physical yields compared to predictions based on MCNP + TENDL for ^{67}Cu produced by secondary neutron activation in the bombardment of a Rb/Ga tandem target with 66 MeV protons in the VBTS. 127
7.3 Predicted ^{67}Cu physical yields in the proton bombardment of enriched ^{68}Zn and ^{70}Zn targets. 133
7.4 Production yields of ^{67}Cu in the proton bombardment of enriched ^{68}Zn and ^{70}Zn targets. 134
7.5 Predicted ^{67}Cu physical yields from secondary-neutron activation of 100% enriched ^{68}Zn in a new 70 MeV target station, using TENDL-2019 cross sections. 135
7.6 Predicted ^{67}Cu physical yields from secondary-neutron activation of 100% enriched ^{68}Zn in a new 70 MeV target station, using TENDL-2021 cross sections. 135
7.7 Predicted ^{67}Cu production yields from secondary-neutron activation of 100% enriched ^{68}Zn in a new 70 MeV target station, using TENDL-2019 cross sections. 136

7.8 Predicted ^{67}Cu production yields from secondary-neutron activation of 100% enriched ^{68}Zn in a new 70 MeV target station, using TENDL-2021 cross sections. 136
7.9 Predicted ^{67}Cu production yields from secondary-neutron activation of 100% enriched ^{68}Zn in a new 70 MeV target station, using TENDL-2019 cross sections. Comparison of ^{68}ZnO and metallic ^{68}Zn secondary targets (see Fig. 7.7). 137
7.10 Predicted ^{67}Cu production yields from secondary-neutron activation of ZnO targets, having different Zn isotopic compositions, in a new 70 MeV target station. Cross sections were taken from the TENDL-2019 library. 138

A.1 Total neutron yield and forward neutron flux in coarse energy bins for a Rb/Ga tandem target under bombardment with a 70 MeV proton beam. 145
A.2 Total neutron and forward neutron flux ratios for selected tandem targets relative to the Rb/Ga target under bombardment with a 70 MeV proton beam. 146

B.1 Group boundaries (bins) of the Modified LaBauve neutron multigroup structure. . . . 147

C.1 Physical yields determined from TENDL-2019 cross sections and neutron spectra generated with MCNP 6.2. 148
C.1 Physical yields determined from TENDL-2019 cross sections and neutron spectra generated with MCNP 6.2 (continuing from previous page). 149
C.1 Physical yields determined from TENDL-2019 cross sections and neutron spectra generated with MCNP 6.2 (continuing from previous page). 150

D.1 Physical yields determined from TENDL-2021 cross sections and neutron spectra generated with MCNP 6.2. 151
D.1 Physical yields determined from TENDL-2021 cross sections and neutron spectra generated with MCNP 6.2 (continuing from previous page). 152
D.1 Physical yields determined from TENDL-2021 cross sections and neutron spectra generated with MCNP 6.2 (continuing from previous page). 153

List of Figures

1.1 A typical weekly beam schedule of the separated-sector cyclotron (SSC) of iThemba LABS prior to the termination of radiotherapy in 2017. 3

2.1 Target station 1, usually referred to as the Elephant, for irradiating batch targets during radionuclide production runs. Salient components indicated by numbers are as follows: (1) the electrified overhead rail; (2) an approaching target transporter; (3) a target holder; (4) transporter terminus; (5) robot arm; (6) beam diagnostic chamber; (7) beamline; (8) front radiation shield; (9) rear radiation shield; (10) rail on which the rear part of the radiation shield moves to open and close the station; (11) pusher arm to locate the target holder and connect cooling water. 9

2.2 Target station 3, usually referred to as the vertical-beam target station (VBTS), for the bombardment of larger-format batch targets. Salient components indicated by numbers are as follows: (1) the electrified rail; (2) target transporter terminus; (3) robot arm; (4) diagnostic chamber and vertical beamline; (5) radiation shield; (6) target transfer hatch; (7) the rail on which shield sectors move when opening or closing the station; (8) inlet and outlet lines for cooling water. Scale: the ceiling of the vault is 2 m above the floor. 11

2.3 LEFT: Schematic diagram illustrating the principle of tandem targets for the simultaneous production of two radionuclides with the same beam. Target A occupies the higher-energy slot and target B the lower-energy slot inside the target holder. The targets are surrounded by fast-flowing cooling water and the beam is incident on the target holder after passing through a double-foil, helium-cooled beamline exit window. RIGHT: Exploded schematic of a loaded target holder. Salient components indicated by numbers are as follows: (1) aluminium back-end plug with bayonet fitting; (2) twin encapsulated targets; (3) quadruple inlet ports for cooling water; (4) quadruple outlet ports for cooling water; (5) moulded rubber seals; (6) aluminium target-holder body. 12

2.4 LEFT: A VBTS target holder. RIGHT: Examples of encapsulated Rb targets used at iThemba LABS on (a) the Elephant, (b) the VBTS, for the production of the radionuclide ^{82}Sr. 13

2.5 Central region of the VBTS, showing (1) the pusher assembly, (2) target-holder mounting fork, (3) assembly containing the helium-cooled, double-foil Havar window, (4) cooling-water lines, (5) helium lines, and (6) vertical beamline. The photograph was taken with the VBTS is in its open state. 14

2.6 Loading of the neutron activation chamber into the spare VBTS pusher assembly. (a) Note the unoccupied cavity in the centre of the pusher assembly. (b) A sample chamber is brought to the pusher assembly by means of the 2 m rod and suction cup, ready to be placed inside the cavity. (c) Sample chamber correctly loaded. (d) The target holder locates snugly over the activation chamber. 14
2.7 Top view of the new 70 MeV cyclotron facility, showing the cyclotron in the centre vault (blue in colour) and two target stations each in the South and North vaults (silver in colour and located to the left side and the right side of the cyclotron). 15
2.8 Cross-sectional side view through the beam axis of the new 70 MeV target station, showing (1) horizontal beamline, (2) 4-sector collimator, (3) target mount, (4) inner iron shield, (5) middle borated paraffin-wax shield, (6) outer lead shield, (7) pusher arm, (8) head of pusher arm, and (9) support structure with rails. The station is shown in a closed, beam-ready state. 16
2.9 A zoomed-in view of the target region of Figure 2.8, showing (1) the target mount, (2) 4-sector collimator, (3) secondary-neutron cavity in the head of the pusher assembly, (4) cooling-water inlet line, (5) cooling-water return line, (6) helium-cooled double-foil Havar window, and (7) target holder. 16
2.10 The RERAME-II irradiation chamber in an opened state, showing (1) the incident beamline, (2) beamstop, (3) door, (4) adjustable vice, (5) collimator, and (6) O-ring seal. 17
2.11 Diagram showing a cross-sectional view of the RERAME-II irradiation chamber (TOP) and and enlarged view of the collimator assembly (BOTTOM). 18
2.12 Schematic diagram of the irradiation chamber used for the stacked-foil experiment with a 200 MeV proton beam. 20
2.13 Facility for measuring off-line gamma-ray spectra of activated foils or samples, showing (1) the high-purity germanium (HPGe) detector, (2) liquid nitrogen dewar, (3) composite copper/lead shield, (4) source frame located on source holder, and (5) source-holder rail. 21
2.14 LEFT: Schematic diagram of a stacked-foil experiment, showing a beam incident on (1) a collimator, (2) the collimated beam traversing through the foil stack, before (3) reaching the beam stop. The electric current is measured separately on the collimator (4) and experimental chamber (5). RIGHT: Beam penetration through a single target foil. 22

3.1 Relevant part of the Karlsruhe Chart of the Nuclides for ^{232}Th+p reactions leading to ^{225}Ac and ^{230}U. Black represents stable nuclides. Yellow represents α-decay. Blue represents β^-- decay. Red represents β^+-emission and electron capture decay modes. With permission © Nucleonica GmbH 2022. 31
3.2 Energy distributions of protons in selected Th foils of the 66 MeV stack, obtained with the Monte Carlo code MCNP6. The number of particle histories was 10×10^6 in each case and the number of energy bins 200 for each distribution. 34
3.3 abc 36
3.4 abcd 36
3.5 IAEA reference excitation function for the ^{27}Al(p,x)^{22}Na reaction (Hermanne *et al.* [HER2018]) and corresponding cross sections measured in this study for monitoring the 66 MeV stack. . 37
3.6 Cross-section ratio of ^{22}Na/^{7}Be in Al plotted versus proton energy, used as an additional monitor in the 66 MeV stack. Literature values are from Szelecsényi *et al.* [SZE2017]. 37

3.7 Reduced chi-squared statistic (χ^2_{red}) plotted versus the ^{225}Ra/^{225}Ac cross-section ratio for selected thorium foils of the 66 MeV stack. Each point represents the value of the goodness-of-fit criterion pertaining to a least-squares fit of a calculated decay curve on a set of ^{221}Fr daughter activities, measured repeatedly over a period of approximately 60 days (see text). The text in magenta indicates the associated proton energies of the foils obtained from the MCNP6 Monte Carlo simulation of the stack. 39

3.8 Cross sections for the formation of ^{225}Ac in the proton bombardment of ^{232}Th. Note that the TENDL-2021 values have been renormalized using a scale factor *SF* = 0.13. Literature values are from Gauvin [GAU1963], Ermolaev *et al.* [ERM2012], Weidner *et al.* [WEI2012b], and Duchemin *et al.* [DUC2015]. 40

3.9 Cross sections for the formation of ^{230}Pa in the proton bombardment of ^{232}Th. Note that the TENDL-2021 values have been renormalized using a scale factor *SF* = 0.95. Literature values are from Kudo *et al.* [KUD1982], Roshchin *et al.* [ROS1997], Morgenstern *et al.* [MOR2008], Jost *et al.* [JOS2013], and Radchenko *et al.* [RAD2016]. 43

3.10 Cross sections for the formation of ^{22}Na in the proton bombardment of ^{nat}Mg. Note that the TENDL-2019 values have been renormalized, using a scale factor *SF* = 0.66. Literature values are from Lagunas-Solar and Carvacho [LAG1990], Sisterson *et al.* [SIS1997], and Michel at al. [MIC1997]. 45

3.11 Cross sections for the formation of ^{24}Na in the proton bombardment of ^{nat}Mg. Note that the TENDL-2019 values have not been renormalized. Literature values are from Wilson *et al.* [WIL1976], Lagunas-Solar and Carvacho [LAG1990], and Michel at al. [MIC1997]. 45

3.12 Integral physical yields for the production of ^{225}Ac and ^{22}Na in the proton bombardment of ^{232}Th and ^{nat}Mg, respectively. 46

3.13 Integral physical yields for the production of ^{230}Pa in the proton bombardment of ^{232}Th. Note that the IAEA evaluated curve is shifted marginally towards higher energies for purposes of display as the two curves would otherwise largely overlap below 30 MeV. 47

3.14 Fitted and/or evaluated excitation functions for the reactions ^{nat}Mg(p,x)^{22}Na, ^{232}Th(p,x)^{225}Ac, ^{nat}Ga(p,x)^{68}Ge, ^{nat}Rb(p,x)^{82}Sr, and ^{232}Th(p,3n)^{230}Pa. A and B denote the higher and lower energy windows (also called energy slots), respectively. 48

3.15 Physical-yield ratio of ^{227}Ac to ^{225}Ac, expressed as a percentage, as a function of entrance proton energy for the case of an exit proton energy of 38 MeV. Note that the suggested energy window for ^{225}Ac production on a Th target is 62 → 38 MeV in this study. 50

4.1 IAEA reference excitation functions for the ^{27}Al(p,x)^{22}Na and ^{nat}Cu(p,x)^{58}Co reactions (Hermanne et al. [HER2018]) and corresponding cross sections measured in this study for monitoring the 200 MeV stack. 55

4.2 Activity of ^{211}Fr in foil Th-4 versus time since EOB. The decay curves were renormalized to join at a common point at the time of EOB (i.e. t = 0) for purposes of display. 56

4.3 Reduced chi-squared statistic (χ^2_{red}) plotted versus the ^{225}Ra/^{225}Ac cross-section ratio for thorium foil Th-4 of the 200 MeV stack. Each point represents the value of the goodness-of-fit criterion pertaining to a least-squares fit of a calculated decay curve on a set of ^{221}Fr daughter activities, measured repeatedly over a period of more than 80 days (also see Figure 4.2). . . . 57

4.4 Cross sections for the formation of ^{225}Ac in the proton bombardment of ^{232}Th. Note that the TENDL-2019 and TENDL-2021 values have been renormalized using scale factors of *SF* = 0.40 and *SF* = 0.35, respectively. The TENDL cross sections contain the minority contribution from ^{225}Th beta decay. Literature values are from Titarenko et al. [TIT2002], Zhuikov et al. [ZHU2011], Ermolaev et al. [ERM2012], Weidner et al. [WEI2012b], and Griswold et al. [GRI2016]. 58
4.5 Cross sections for the formation of ^{225}Ra in the proton bombardment of ^{232}Th. Note that the TENDL-2019 values have been renormalized using a scale factor of *SF* = 0.7. The IAEA evaluated curve is shown both unscaled as well as renormalized using a scale factor of *SF* = 1.35. Literature values are from Weidner et al. [WEI2012b]. 59
4.6 Integral physical yields for the production of ^{225}Ac (LEFT) and ^{225}Ra (RIGHT) in the proton bombardment of ^{232}Th. The data are from the IAEA-NDS Medical Portal. The scale factor introduced in the case of ^{225}Ra is 1.35. 60
4.7 Schematic diagram illustrating the principle of a triple-stacked Th target with similar thermal load per target, achieved by reducing the target thickness with decreasing proton energy. The Inconel-encapsulated Th targets are denoted T1, T2, and T3, with BS the elements of a water-cooled beamstop. 61
4.8 Decay curve of ^{225}Ra and growth-and-decay curve of ^{225}Ac formed via ^{225}Ra decay. Time t = 0 is the effective time of the end of the chemical separation of ^{225}Ra from the ^{232}Th target. All activities on the y-axis is relative to the activity of ^{225}Ra at time t = 0. 62

5.1 Simplified model of a 70 MeV Rb/Ga tandem target, as generated with the MCNP visual editor. 69
5.2 Neutron flux (i.e. neutrons/cm^2 produced with an integrated proton charge of 1 μAh) versus neutron energy in the forward cavity behind a Rb/Ga tandem target during irradiation with a 70 MeV proton beam. 71
5.3 Total number of neutrons produced in all space (i.e. a 4π sr geometry around the target) with an integrated proton charge of 1 μAh, during irradiation of a Rb/Ga tandem target with a 70 MeV proton beam. 71
5.4 Comparison of neutron flux ratios for various tandem targets relative to the Rb/Ga target, as indicated, in the forward cavity downstream of the target (see text). Above 1 MeV the scale on the x-axis is linear (black text) but below 1 MeV it is logarithmic (red text). The red dashed lines represent the case for the Rb/Ga target itself, while the black histograms represent the indicated targets. 72
5.5 Comparison of neutron flux ratios for the Zr/Y_2O_3 tandem target relative to the Rb/Ga target, as indicated. Above 1 MeV the scale on the x-axis is linear (black text) but below 1 MeV it is logarithmic (red text). The red dashed lines represent the case for the Rb/Ga target itself, while the black histograms represent the indicated target. 73
5.6 TOP: Comparison of neutron flux ratios for the 66 MeV Rb/Ga tandem target relative to the 70 MeV Rb/Ga target. BOTTOM: Comparison of neutron flux ratios for the 70 MeV Rb/Ga tandem target inside a new target station relative to the 70 MeV Rb/Ga target inside vacuum. Above 1 MeV the scale on the x-axis is linear (black text) but below 1 MeV it is logarithmic (red text). The red dashed lines represent the case for the 70 MeV Rb/Ga target in vacuum, while the black histograms represent the compared situation as indicated. 74

6.1 Schematic top view of the neutron irradiation chamber, showing the locations of the magnesium samples during Run-2. 82

6.2 The geometry of the VBTS model and vertical beamline as generated with the MCNP6 code system. Note that subsequent figures zoom into the target region to show more detail. The image is coloured by materials selection. 87

6.3 The target region of the VBTS model as generated with the MCNP6 code system. Note that Figure 6.4 zooms in further to show the region of the neutron activation chamber. 88

6.4 Zoomed-in view showing the target holder, tandem Rb/Ga targets, and the neutron activation chamber located in the target pusher assembly of the VBTS model, as generated with the MCNP6 code system. See also Figures 6.2 and 6.3. 88

6.5 Photograph of the target-holder back plate and inserts, showing the protrusion/shoulder introduced onto the beam axis once an assembled target would be loaded into the irradiation position. 89

6.6 Schematic diagram illustrating the modelling of a circularly swept (rastered) beam (see text). . 91

6.7 Illustration of a neutron energy group defined for an arbitrary excitation function (cross section $\sigma(E)$ versus neutron energy E) to discretize the cross section in that group (or bin). The nomenclature introduced in this figure are also used in the Newton-Cotes expressions listed in Table 6.5. 94

6.8 Excitation functions of the ^{23}Na(n,2n)^{22}Na and ^{23}Na(n,γ)^{24}Na reactions. The curves are cubic spline fits through the relevant pointwise data from the TENDL-2021 library. LEFT: Logarithmic scale on x-axis. RIGHT: Linear scale on x-axis. 103

6.9 Base-10 logarithm of the ratio between predicted and measured physical yields, plotted versus the reaction ID number, for different MCNP6 physics selections used in calculating the the neutron flux. The cross sections used in the predictions were taken from the TENDL-2019 library. 110

6.10 Base-10 logarithm of the ratio between predicted and measured physical yields, plotted versus the reaction ID number, for different MCNP6 physics selections used in calculating the the neutron flux. The cross sections used in the predictions were taken from the TENDL-2021 library. 111

6.11 Number of reactions versus the base-10 logarithm of the ratio between predicted and measured physical yields, plotted as a histogram. The cross sections used in the predictions were taken from the TENDL-2019 library. 112

6.12 Number of reactions versus the base-10 logarithm of the ratio between predicted and measured physical yields, plotted as a histogram. The cross sections used in the predictions were taken from the TENDL-2021 library. 113

6.13 Base-10 logarithm of the ratio between predicted physical yields based on TENDL-2019 and TENDL-2021 cross sections, plotted versus the reaction ID number, for the case where an average neutron spectrum has been adopted for the neutron flux (see text for more detail). . . 116

6.14 Base-10 logarithm of the ratio between predicted and measured physical yields, plotted versus the reaction ID number. The arithmetic average neutron flux spectrum from all six MCNP6 physics selections was used in the predictions and the error bars are based on the associated standard deviations. The cross sections used in the predictions were taken from the TENDL-2019 library. 117
6.15 Base-10 logarithm of the ratio between predicted and measured physical yields, plotted versus the reaction ID number. The arithmetic average neutron flux spectrum from all six MCNP6 physics selections was used in the predictions and the error bars are based on the associated standard deviations. The cross sections used in the predictions were taken from the TENDL-2021 library. 118

7.1 Evaluated excitation functions for the formation of ^{64}Cu (broken curves) and ^{67}Cu (solid red curves) in the proton bombardment of enriched ^{70}Zn and ^{68}Zn, respectively. 122
7.2 Integral physical yields for the production of ^{64}Cu (broken curves) and ^{67}Cu (solid red curves) in the proton bombardment of enriched ^{70}Zn and ^{68}Zn, respectively. 123
7.3 Schematic diagram of the tandem targets considered for bombardment with a 70 MeV primary proton beam, followed by another target for activation with secondary neutrons. The relevant target materials and radioisotopes of main interest are as indicated. 128
7.4 The model geometry of the new 70 MeV target station with its horizontal beamline as generated with the MCNP6 code system. Note that subsequent figures zoom into the target region to show more detail. The image is coloured by materials selection. 129
7.5 Zoomed-in view showing the standard target holder, tandem Rb/Ga targets, and the neutron activation chamber located in the head of the pusher arm, as generated with the MCNP6 code system. See also Figure 7.4. 130
7.6 Zoomed-in view showing the modified target holder, tandem Rb/Ga targets, and the neutron activation chamber located in the head of the pusher arm, as generated with the MCNP6 code system. See also Figures 7.4 and 7.5. 130
7.7 LEFT: Schematic top view of the ZnO secondary target concept. RIGHT: Schematic top view of the metallic Zn secondary target concept. 132

A.1 Comparison of neutron flux ratios for various tandem targets relative to the Rb/Ga target, as indicated, for the case of total neutrons emitted in 4π space. Above 1 MeV the scale on the x-axis is linear (black text) but below 1 MeV it is logarithmic (red text). The red dashed line represents the case for the Rb/Ga target itself, while the black histogram represents the indicated target. 144

Table of Contents

Abstract . . . 1
Acknowledgements . . . 3

List of Tables **4**

List of Figures **7**

1 Motivation and Outline **1**
1.1 BACKGROUND . . . 1
1.2 TARGETED RADIONUCLIDE THERAPY . . . 4
1.3 SECONDARY NEUTRON ACTIVATIONS . . . 5
1.4 TANDEM TARGETS AND PRODUCTION YIELDS . . . 6
1.5 OBJECTIVES . . . 6
1.6 OUTLINE OF THESIS . . . 7

2 Facilities and Experimental Techniques **8**
2.1 INTRODUCTION . . . 8
2.2 EXISTING TARGET STATIONS ON THE SSC . . . 8
2.2.1 Target station 1 – Elephant . . . 8
2.2.2 Target station 2 – Babe . . . 10
2.2.3 Target station 3 – VBTS . . . 11
2.3 NEUTRON ACTIVATION CHAMBER . . . 13
2.4 NEW 70 MeV TARGET STATIONS . . . 15
2.5 FACILITIES FOR STACKED-FOIL EXPERIMENTS . . . 17
2.6 RADIONUCLIDE ASSAYS . . . 20
2.7 ACTIVATION CROSS SECTIONS AND EXCITATION FUNCTIONS . . . 21
2.7.1 Penetration depth and beam energy . . . 21
2.7.2 The activation equation . . . 23
2.7.3 Spectrometric activity determination . . . 24
2.7.4 Activation cross sections . . . 25
2.7.5 Concluding remarks . . . 25
2.8 INTEGRAL YIELDS . . . 26
2.8.1 The physical yield . . . 26
2.8.2 The production yield at the end of bombardment . . . 27

3 Selected excitation functions of ^{232}Th+p and ^{nat}Mg+p reactions up to 70 MeV **29**

3.1 INTRODUCTION . . . 29
3.2 EXPERIMENTAL ASPECTS AND CONSIDERATIONS . . . 31
3.2.1 Irradiations . . . 31
3.2.2 Radionuclide assays . . . 32
3.2.3 Data analysis . . . 33
3.3 RESULTS AND DISCUSSION . . . 40
3.3.1 Excitation functions . . . 40
3.3.2 Integral yields . . . 44
3.4 TARGETRY . . . 47
3.5 COMMENTS ON ACTINIUM-227 CONTAMINATION . . . 50
3.6 CONCLUSIONS . . . 51

4 Selected excitation functions of ^{232}Th+p reactions between 100 and 200 MeV **53**
4.1 INTRODUCTION AND BACKGROUND . . . 53
4.2 EXPERIMENTAL ASPECTS AND CONSIDERATIONS . . . 54
4.2.1 Irradiations . . . 54
4.2.2 Radionuclide assays . . . 54
4.2.3 Data analysis . . . 55
4.3 RESULTS AND DISCUSSION . . . 58
4.3.1 Excitation functions . . . 58
4.3.2 Integral yields . . . 60
4.4 TARGETRY . . . 60
4.5 CONCLUSIONS . . . 64

5 Radionuclides and neutron production from tandem targetry with 70 MeV protons **65**
5.1 INTRODUCTION . . . 65
5.2 RADIONUCLIDE PRODUCTION – ADDITIONAL ASPECTS . . . 66
5.2.1 Rb/Ga tandem targets for ^{82}Sr/^{68}Ga production . . . 66
5.2.2 Mg/Ga tandem targets for ^{22}Na/^{68}Ga production . . . 67
5.2.3 Zr/Y_2O_3 tandem targets for ^{88}Y production . . . 68
5.2.4 Be/Ga tandem targets for fast neutron production . . . 68
5.2.5 Tandem targets containing Th . . . 69
5.3 NEUTRON PRODUCTION . . . 69
5.3.1 Spectra and flux ratios . . . 69
5.3.2 Total neutron production . . . 74
5.4 CONCLUSIONS . . . 75

6 Activation of samples in the secondary neutron flux behind a VBTS target **76**
6.1 BACKGROUND AND OBJECTIVES . . . 76
6.1.1 Expanding an existing investigation . . . 76
6.1.2 Previous studies from the literature . . . 76
6.1.3 Objectives . . . 78
6.2 EXPERIMENTAL ASPECTS AND CONSIDERATIONS . . . 79

6.2.1 Primary target composition . . . 79
6.2.2 Neutron-activated samples . . . 79
6.2.3 Bombardments . . . 82
6.2.4 Radionuclide assays . . . 82
6.3 MONTE CARLO SIMULATIONS . . . 83
6.3.1 Overview and history . . . 83
6.3.2 Nuclear models and physics selections . . . 85
6.3.3 Geometry specification . . . 87
6.3.4 The effect of the error in geometry on previous results . . . 89
6.3.5 Proton-beam simulations and particle histories . . . 90
6.4 DATA ANALYSIS . . . 91
6.4.1 Energy-group structure . . . 91
6.4.2 Pointwise and group-averaged cross sections . . . 91
6.4.3 The mean formation cross section . . . 94
6.4.4 Accumulated charge . . . 95
6.4.5 Predicted physical yields . . . 95
6.4.6 Experimental physical yields . . . 95
6.4.7 Comparison between predicted and experimental yields . . . 95
6.4.8 Effective cross sections and uncertainties . . . 97
6.5 RESULTS AND DISCUSSION . . . 98
6.5.1 Neutron-induced activation products . . . 98
6.5.2 Sensitivity to multigroup structure . . . 102
6.5.3 Physical yields and yield ratios . . . 103
6.5.4 Averaged neutron spectrum and yield outliers . . . 115
6.5.5 Testing for asymmetry in the neutron flux . . . 118
6.5.6 Comments in conclusion . . . 119

7 Production of ^{67}Cu **120**
7.1 BACKGROUND AND OBJECTIVES . . . 120
7.1.1 The supply and demand mismatch . . . 120
7.1.2 Copper radioisotopes in medicine . . . 121
7.1.3 Production of ^{67}Cu with medium-energy protons . . . 122
7.1.4 Production of ^{67}Cu with composite light projectiles . . . 124
7.1.5 Production of ^{67}Cu with heavy ions . . . 125
7.1.6 Production of ^{67}Cu with photonuclear reactions . . . 125
7.1.7 Production of ^{67}Cu with neutron-induced reactions . . . 126
7.2 MONTE CARLO SIMULATIONS . . . 128
7.3 ACTIVATION CAVITY AND SECONDARY TARGETS . . . 131
7.3.1 A candidate ZnO secondary target . . . 132
7.3.2 A candidate metallic Zn secondary target . . . 133
7.4 RESULTS AND DISCUSSION . . . 133
7.4.1 Proton-induced reactions on ^{68}Zn and ^{70}Zn . . . 133
7.4.2 Neutron-induced reactions on ^{68}Zn . . . 134

7.5 COMMENTS IN CONCLUSION 139
7.5.1 Comments on enrichment – economies of scale 139

8 Summary and Conclusion **141**

A Neutron source terms in coarse energy intervals – additional information **144**

B Modified LaBauve energy-group structure **147**

C Calculated physical yields: TENDL-2019 **148**

D Calculated physical yields: TENDL-2021 **151**

Bibliography **154**

Chapter 1

Motivation and Outline

Section 1.1 of this chapter gives a background of the accelerator facilities of relevance to the radionuclide production programme at the iThemba Laboratory for Accelerator-Based Sciences (iThemba LABS) near Cape Town, South Africa. This programme experienced an evolution over several decades, mainly driven by projects to increase the production capacity. iThemba LABS is again at a milestone in terms of this evolution due to the purchase of a commercial 70 MeV H^- cyclotron dedicated to radionuclide production. The main focus areas of this thesis are subsequently introduced in Sections 1.2 through 1.4, i.e. targeted radionuclide therapy, secondary neutron activations, and production yields from tandem targets of relevance to a 70 MeV proton cyclotron, respectively. The therapeutic radionuclides ^{67}Cu and ^{225}Ac are prominent sub-topics of this thesis although several other radionuclides (e.g. ^{22}Na, ^{68}Ge, ^{82}Sr, ^{88}Y, ^{230}U, etc.) are also important from the perspectives of this project. A list of objectives are presented in Section 1.5 and the thesis outline is discussed in Section 1.6.

1.1 BACKGROUND

The separated-sector cyclotron (SSC) facility of iThemba LABS was designed to accommodate a radionuclide production programme from its inception. The facility was conceived to be multi-disciplinary, serving the diverse needs of notably different communities. In addition to producing radionuclides, the available beam time was to be shared more-or-less proportionally with two other main programmes, namely experimental nuclear physics and radiotherapy with both protons and neutrons. This shared mode of operation had pros and cons. One of the pros was that a scarce and expensive resource could be optimally exploited to benefit a larger number of users. A notable con was that the individual programmes had to contend with unavoidable constraints on the available beam time as well as a weekly operating schedule that tended to become rather complex. The needs of the different programmes also evolved over time and beam-time requests eventually became significantly over-subscribed. Various initiatives helped to improve the delivery of beam to diverse users, leading to a few innovative upgrades to the SSC and ancillary infrastructure. This makes the history of the SSC rather interesting, some aspects of which will be expounded on at appropriate places in the thesis.

The SSC is a $k = 200$ MeV variable-energy cyclotron equipped with two $k = 8$ MeV solid-pole injector cyclotrons. The injector named Solid-Pole Cyclotron 1 (SPC1) is dedicated to high-

intensity proton beams for applications such as radionuclide production and radiotherapy, while Solid-Pole Cyclotron 2 (SPC2) is mainly used to provide beams of heavy ions and polarized protons for nuclear physics experiments.

Because of historical reasons, routine radionuclide production on the SSC is exclusively performed with 66 MeV proton beams. This decision was made even before first beam was extracted from the machine, largely dictated by the neutron therapy programme that required this particular beam energy. Energy changes on the SSC are time consuming, often taking a full 8-hour shift or even longer to complete, mainly because the large magnets take time to stabilize when their field strengths are changed. A scheme where both neutron therapy and radionuclide production would use the same proton-beam energy would reduce the number of energy changes per week and was consequently adopted.

The first test beam delivered by the SSC to a radionuclide production vault took place in October 1986. Development of bombardment infrastructure and targetry continued throughout 1987 and routine production commenced in 1988. At that time provision was made for a maximum beam current of 100 μA. This remained the *de facto* upper limit for nearly 20 years. Initial efforts focused on optimizing the available beam time and not increasing the beam intensity. A system enabling rapid beam switching (about 1–2 minutes) between the neutron therapy vault and the first radionuclide production vault was developed to utilize the set-up time between patient irradiations for radionuclide production. Since patient treatments were only performed during daylight working hours on certain weekdays, uninterrupted beam could be utilized for radionuclide production during the nights. This system worked very well for many years. However, as the programme continued through its second decade, it became clear that the laboratory would not be able to meet its future requirements in terms of the delivery of radionuclides to a growing client base (see e.g. [STE2013]). In addition, iThemba LABS became increasingly dependent on income generated from radionuclide sales.

Shortly after the start of the new millennium, a large development effort commenced to increase the intensity of 66 MeV proton beams delivered by the SSC and to establish a new target station as well as targetry that could accommodate these more intense beams. A second target station for batch targetry was designed and built in-house and installed in a second irradiation vault dedicated for radionuclide production. In addition, a beam splitter was built that made it possible to provide beams to both production vaults simultaneously. The SSC was equipped with so-called flat-top resonators, amongst other developments, to enable the extraction of more intense beams [CON2005]. These developments were brought into routine use towards the end of 2006 and provided about a three-fold increase in production capacity.

The three-fold increase described above proved to be very significant for iThemba LABS, particularly in the case of relatively long-lived, high-value radionuclides for the export market, such as ^{22}Na, ^{68}Ga and ^{82}Sr. Nevertheless, the laboratory still had to operate with its major constraint, i.e. too many diverse programmes depending on beam from its largest accelerator. In particular, the nuclear physics programme of the SSC had to be accommodated mainly on weekends. Figure 1.1 shows a typical beam schedule prior to significant changes in recent times, in particular the phasing out of proton and neutron therapy. This latter aspect will be addressed in more detail in the next paragraph. Users expressed a need for change as certain



Figure 1.1: A typical weekly beam schedule of the separated-sector cyclotron (SSC) of iThemba LABS prior to the termination of radiotherapy in 2017.

kinds of physics experiments could not be performed on such a fragmented, weekend-only basis. A need was also expressed to introduce radioactive ion beams (RIBs) at iThemba LABS, which would be incompatible with the beam schedule of Figure 1.1. The time had come for a major re-positioning of the role of the SSC.

Proton and neutron therapy at iThemba LABS were phased out in 2017. This decision was based mainly on the significant progress in recent years on dedicated proton therapy centres as well as the reduced cost of these facilities. It was argued that a dedicated proton therapy facility with a smaller footprint, located at one of the large academic hospitals in South Africa, would better serve the country and the medical community. Such an initiative should be pursued and supported by iThemba LABS, perhaps as a private/public partnership functioning as an independent entity. Furthermore, the operational models of some of the smaller accelerators operated by iThemba LABS also seemed particularly attractive for the radionuclide production programme. This refers to three smaller accelerators, namely an 11 MeV Siemens Eclipse positron emission tomography (PET) cyclotron, a 3 MV Tandetron used mainly for ion beam analysis (IBA), and a 6 MV tandem accelerator that performs IBA but also hosts the only accelerator mass spectrometry (AMS) facility on the African continent. Similar to these smaller, dedicated accelerator facilities, radionuclide production as a programme would also benefit greatly if it could have its own dedicated accelerator. Separated from the SSC, the radionuclide production capacity could again be significantly expanded at iThemba LABS. This would also free the SSC to pursue more research, henceforth predominantly dedicated to nuclear physics and radiobiology experiments. Such a partitioning of dedicated accelerators for different fields of application would greatly benefit iThemba LABS and the communities that it serves.

In 2018 the South African government approved the acquisition by iThemba LABS of a commercial 70 MeV H^- cyclotron for radionuclide production. This would constitute the first phase of an initiative called the South African Isotope Facility (SAIF) and the project at large is referred to as the SAIF Project [STE2018a, AZA2020]. Following a tender process, the bid for

a Cyclone 70 cyclotron from Ion Beam Applications S.A. (IBA) in Belgium was approved. This machine was shipped to South Africa towards the end of 2021. It will be installed during the course of 2022 and first beam is expected in 2023. The radiotherapy vaults previously used for proton and neutron therapy are being re-purposed to accommodate the new cyclotron and target stations. The required building alterations and other construction work are in progress. The cyclotron will supply dual proton beams to two irradiation vaults simultaneously. The maximum specified current of each beam is 375 μA and the energy will be variable between 35 and 70 MeV. While IBA will supply the cyclotron and some components of the external beamlines, the target stations and targetry will be according to in-house designs by iThemba LABS. At the time of writing, the construction of the first two target stations (of four) has commenced at TF Design (Pty) Ltd, an engineering firm in Stellenbosch, South Africa. Since the maximum beam energy of 70 MeV is not significantly higher than the 66 MeV that has been utilized for more than three decades, the same kind of technology in terms of targetry will be retained, except for small adjustments to production energy windows where required.

The bulk of the current radionuclide production based on 66 MeV protons will be transferred to the new 70 MeV cyclotron facility. This will largely free the SSC from this duty except to provide a back-up capability. It is possible that some radionuclides may in future still be produced on the SSC on a much smaller scale, e.g. some alpha emitters like ^{211}At and/or radionuclides requiring projectiles different from protons. Such productions will mainly be to support research activities and will not be of a commercial (or semi-commercial) nature.

The advent of the new 70 MeV H^- cyclotron at iThemba LABS, in addition to the existing SSC, will introduce an exciting period that will open opportunities for new investigations as well as the possibility to expand on the collection of radionuclides that the laboratory currently delivers. Not only should the focus be on the bulk supply of those radionuclides that generate income but also on support to research and new technologies. There are various radionuclides that do not currently have a high demand in the world but with manifest potential to become important in future.

As a general rule, accelerators are developed to best suit particular fields of application. There are always constraints, determining what a particular accelerator can do. The new generation of commercial 70 MeV H^- cyclotrons was developed to satisfy a particular niche. Those strengths are well known and would have informed the decision to purchase such a machine in the first place. Once established, however, such a facility may also be able to fulfil secondary roles in addition to its primary role. It may support something that is useful, even if not specifically optimized and/or intended for that purpose. The question may be asked “what else can it do?” Some of the topics of this thesis project may be viewed to fall into that category.

1.2 TARGETED RADIONUCLIDE THERAPY

Most of the radionuclides produced at iThemba LABS over the last three decades were required for diagnostic medical purposes. A decision was made circa 2018 to also investigate the possibility to provide certain high-value (and scarce) therapeutic radionuclides that have not hitherto been produced in South Africa.

One of the pertinent questions that this study endeavours to answer is whether commercial 70 MeV H^- cyclotrons can play a role in (or contribute to) the supply of the alpha emitter ^{225}Ac. Worldwide, this radionuclide is in short supply and, for reasons that will be discussed later, this supply problem is very difficult to solve. The published literature reveals differences of opinion on the viability of this particular energy region for this purpose. Since the available cross-section data for the ^{232}Th+p production route, in the energy region up to 70 MeV, were found to be rather sparse and also showed notable discrepancies, an excitation-function experiment was performed as part of this investigation to improve the relevant data base. For this purpose the stacked-foil technique was used, which will be explained in due course. Not only is ^{225}Ac important as a therapeutic radionuclide in its own right, it is also a precursor of ^{213}Bi, which is another alpha emitter that is becoming increasingly important in targeted alpha therapy (TAT). Therefore there exists a significant potential demand for ^{225}Ac/^{213}Bi generators in future. As a by-product of this study, data relevant to the ^{230}U/^{226}Th generator were also obtained. In this latter case, the daughter isotope ^{226}Th has been suggested as a potential candidate for the application of TAT to the treatment of certain types of blood cancer [MOR2008].

A separate experiment was performed as part of the present investigation on the production of ultra-pure ^{225}Ac via the decay of its precursor, ^{225}Ra. In this case the focus was on ^{232}Th+p reactions in the energy region 100–200 MeV, i.e. within the upper energy domain of the SSC. Currently the SSC does not have the capability to produce proton beams of high intensity (i.e. beam currents above several tens of microampere) at proton energies other than 66 MeV, however, in principle the machine can be upgraded to have such functionality. Alternatively, this part of the study may point out what the requirements are in terms of minimum accelerator functionality to exploit this production route. It has to be pointed out that various aspects of these ideas are not new. Nevertheless, this part of the study endeavours to add something new to an existing but limited body of information, again utilizing the stacked-foil technique to improve a very sparse data base.

The radionuclide ^{67}Cu has become very important in targeted radiotherapy in recent years; the two radioisotopes, ^{64}Cu and ^{67}Cu, form a so-called theranostic pair. The focus in this project was on ^{67}Cu production via neutron-induced reactions directly behind a primary radionuclide production target, utilizing the secondary neutron flux. The new target stations for the 70 MeV cyclotron facility were designed to exploit the secondary neutron flux for the production of certain neutron-rich β^--emitting radionuclides close to the line of stability. The objective is not bulk production but to support research, based on an argument that secondary neutrons may be a valuable resource, historically neglected until recent times.

1.3 SECONDARY NEUTRON ACTIVATIONS

Another aspect of the present study was to expand the secondary-neutron activation data set of a previous investigation and to re-analyze the larger data set. The original data were measured on a relatively large collection of samples activated with secondary neutrons behind a production target during a routine bombardment with 66 MeV protons. This formed the basis of the MSc project of the author [MOT2019]. It became evident, during completion of the MSc project, that additional activations and measurements would have to be performed and that

the results presented in the MSc thesis should only be considered as preliminary. Based on the now-completed study at 66 MeV and additional Monte Carlo simulations, yield estimates were made of certain radionuclides of relevance to the future 70 MeV cyclotron programme, including ^{67}Cu and co-produced Cu contaminants on both natural and enriched Zn targets.

1.4 TANDEM TARGETS AND PRODUCTION YIELDS

The main export products of iThemba LABS are the three relatively long-lived radionuclides ^{22}Na, ^{68}Ge and ^{82}Sr. They are routinely produced using tandem targetry in two configurations: Rb/Ga (^{82}Sr/^{68}Ge) and Mg/Ga (^{22}Na/^{68}Ge). The transition from a primary proton-beam energy of 66 MeV to 70 MeV is not large but does have a notable effect on the choices of production energy windows and corresponding thicknesses of the individual targets. This will be briefly discussed in the thesis in addition to the expected thick-target yields based on available nuclear data. The inclusion of thorium as a target material in this production regimen increases the number of useful permutations of tandem targets that can be employed. From the perspective of this thesis project, the secondary neutron production from these tandem configurations is a main area of investigation, in particular how different configurations and other geometrical factors will affect the ^{67}Cu yield and purity. This was investigated based on available nuclear data and appropriate Monte Carlo simulations.

1.5 OBJECTIVES

From the information captured in Sections 1.1 through 1.4 a number of objectives could be formulated, which are summarized below:

- Perform new excitation-function measurements for Th+p reactions relevant to ^{225}Ac/^{213}Bi and ^{230}U/^{226}Th generators in the energy region below and up to 70 MeV to improve the existing database, and investigate the prospects for their production with a dedicated 70 MeV H^- cyclotron. As a secondary investigation, include Mg foils in the stacked-foil experiments to check against existing data for ^{22}Na and ^{24}Na formation, which also currently present some discrepancies.

- Perform new excitation-function measurements for Th+p reactions relevant to ^{225}Ra/^{225}Ac generators in the energy region 100–200 MeV to investigate the feasibility of securing an ultra-pure ^{225}Ac supply, possibly utilizing the $k = 200$ MeV SSC for this purpose.

- Make yield estimates of radionuclides of importance (or potential future importance) to iThemba LABS from concept tandem-target configurations that are likely to be exploited in future beam operations with the new 70 MeV cyclotron.

- Perform activation studies with secondary neutrons emitted by current routine radionuclide production targets under bombardment with 66 MeV proton beams from the SSC over a broad mass region. Compare the measured yields with predictions based on Monte Carlo simulations in conjunction with the latest cross-section compilations available from the International Atomic Energy Agency (IAEA) or other appropriate nuclear data centres.

- Survey the ^{67}Cu production methods and investigate the secondary neutron activation potential for this purpose.

1.6 OUTLINE OF THESIS

Chapter 1 is Motivation and Outline. Chapter 2 describes the various existing facilities used for the experimental work of this project as well as some of the new facilities that will become available on completion of the 70 MeV cyclotron complex. Some of the experimental techniques used are also introduced in this chapter.

Chapter 3 presents the results of the ^{232}Th+p stacked-foil experiments performed with proton beams of 40 and 66 MeV. In conjunction with existing data from the literature, yield estimates are made up to 70 MeV. Of particular interest is the pairing of thorium with other target materials of importance to iThemba LABS, exploring the possibility of co-production of ^{225}Ac/^{213}Bi and ^{230}U/^{226}Th generators with the new 70 MeV cyclotron facility. These foil stacks also contained Mg foils in order to verify the quality of existing data for the reaction ^{nat}Mg(p,x)^{22}Na, which is also important for iThemba LABS. Activation experiments often produce data for additional radionuclides of lesser importance. A few such cases are also presented in this thesis.

Chapter 4 presents the results of the ^{232}Th+p stacked-foil experiment performed with a 200 MeV proton beam. The production possibility of ^{225}Ra/^{225}Ac generators in the energy region 100–200 MeV was explored. A concept stacked-target configuration is suggested.

Chapter 5 presents yield estimates for various tandem-target configurations that can be employed at the new 70 MeV cyclotron facility.

Chapter 6 describes the secondary-neutron activations performed behind a radionuclide production target during routine bombardments with 66 MeV protons. Yields are presented of radioactive residues from 121 different neutron-induced reactions. Average cross sections were derived based on the measured yields in conjunction with neutron spectra obtained from Monte Carlo simulations. These values are compared with corresponding predictions included in the well-known nuclear data library TENDL [KON2019].

Chapter 7 is dedicated to the production of ^{67}Cu in the secondary neutron flux behind a primary tandem target under bombardment with a 70 MeV proton beam. Eight tandem-target configurations were included in the study, namely Rb/Ga (^{82}Sr/^{68}Ge), Mg/Ga (^{22}Na/^{68}Ge), Th/Ga (^{225}Ac/^{68}Ge), Mg/Th (^{22}Na/^{230}U), Rb/Th (^{82}Sr/^{230}U), Th/Th (^{225}Ac/^{230}U), Zr/Y_2O_3 (^{88}Y/^{88}Y), and Be/Ga (n + ^{68}Ge). Both metallic Zn and ZnO were considered as target materials. Yield estimates were made for natural Zn as well as enriched ^{67}Zn and ^{68}Zn target materials. Indeed, it was necessary to find out which of ^{67}Zn or ^{68}Zn would be most suitable, both from a ^{67}Cu yield and radionuclidic purity perspective.

A summary and conclusions are presented in Chapter 8. This chapter also mentions some possible areas for further investigation.

Chapter 2

Facilities and Experimental Techniques

2.1 INTRODUCTION

iThemba LABS currently operates two dedicated target stations for radionuclide production with batch targets, utilizing 66 MeV proton beams delivered by the SSC. A third target station for semi-permanent targets existed for many years but has recently been removed from service and disassembled. In addition, two different activation chambers are available and both were used for the stacked-foil experiments of this study. A total of four beamlines are dedicated for radionuclide production with the SSC, three with a horizontal orientation in one irradiation vault and a single vertical beamline in a second irradiation vault. One existing target station is equipped with the capability to exploit the secondary neutron flux for activating secondary target materials. All the new 70 MeV stations are likewise being equipped with this capability. The design of the new 70 MeV target stations was heavily influenced by the experience gained on the SSC over more than three decades. The main features of both the old and new facilities are described in Section 2.2.

2.2 EXISTING TARGET STATIONS ON THE SSC

2.2.1 Target station 1 – Elephant

This is the first horizontal-beam target station brought into operation at iThemba LABS, usually referred to as the Elephant. It has been fully operational since 1987 and is still extensively utilized today. While this facility played no direct role in this thesis project, it is nevertheless a good starting point for a general discussion on the target stations at iThemba LABS as all the subsequent stations share common features with this facility, in particular the new 70 MeV target stations (which are sometimes referred to as the "new Elephants"). The main components of the Elephant are shown in Figure 2.1 and described below:

- At the top of Figure 2.1 (labelled as 1) is an overhead electrified rail. This rail system connects the Elephant to a processing hot-cell complex, target store, and target loading station. Activated targets become too radioactive to safely handle manually, therefore, remote-controlled handling and transport of target holders are required to limit the radiation dose received by staff. A target transporter (labelled as 2) is shown as it approaches

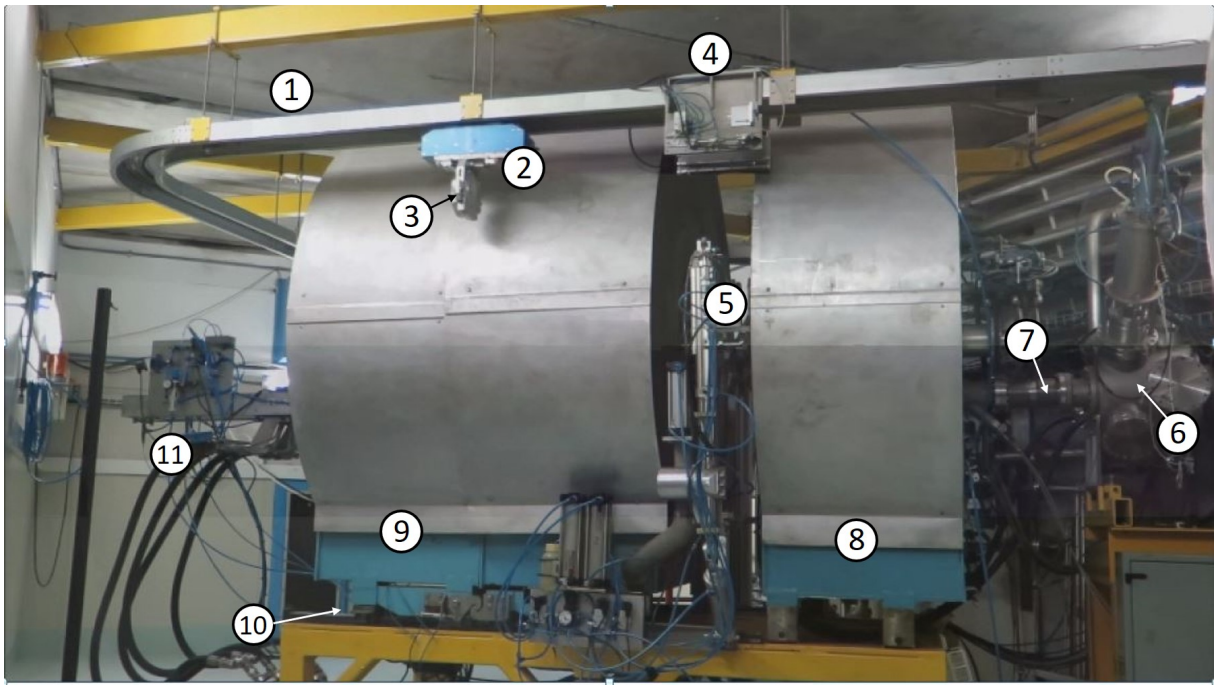


Figure 2.1: Target station 1, usually referred to as the Elephant, for irradiating batch targets during radionuclide production runs. Salient components indicated by numbers are as follows: (1) the electrified overhead rail; (2) an approaching target transporter; (3) a target holder; (4) transporter terminus; (5) robot arm; (6) beam diagnostic chamber; (7) beamline; (8) front radiation shield; (9) rear radiation shield; (10) rail on which the rear part of the radiation shield moves to open and close the station; (11) pusher arm to locate the target holder and connect cooling water.

the rail terminus (labelled as 4), from where the target holder (labelled as 3) can be transferred to or from a target magazine inside the station by means of an electro-pneumatic robot arm (labelled as 5).

- A diagnostic chamber (labelled as 6) located on the beamline (labelled as 7), in close proximity to the station, contains a Faraday cup and a harp for the initial alignment of the beam at a low intensity, prior to increasing the beam intensity for the routine production run. The beam spot is swept on a circular trajectory around the beam axis in order to spread the thermal load on target during bombardment and to prevent so-called hot spots. The sweep frequency used on the Elephant is 450 Hz.

- A four-sector collimator, located inside the front radiation shield around the beam axis (labelled as 8), is used to monitor the beam alignment throughout a bombardment. The collimator also assists in the initial beam focusing and alignment during the stage when beam intensity is gradually being increased. The current on each individual graphite sector is measured separately, providing the main interlock to prevent accidental damage to the station should the beam drift out of alignment. An overcurrent on any sector will immediately trigger the radio frequency (RF) system to be switched off, removing the beam within a response time of about 30 milliseconds.

- Targets are irradiated in a normal air atmosphere, outside the vacuum of the cyclotron and beamline. A helium-cooled, double-foil Havar window isolates the beamline vacuum from the target station. This window is located between the four-sector collimator and the

target holder, in close proximity to these components. The Havar foils are thin (nominally 25 μm) therefore causing negligible degradation to the incident beam energy.

- Most of the material budget of the target station resides in the various components of the local radiation shield. The heavy, multi-layered shield completely surrounds a target during bombardment, reducing the neutron flux into the vault by approximately three orders of magnitude, preventing excessive activation inside the vault and also reduces radiation damage to sensitive materials, e.g. polymers such as cable insulation, lubricants, etc. [MIL1989, STE1992]. A description of the shielding materials and their functions will be given in Section 2.4, where the new 70 MeV target stations are described.

- The target station can be in an open state (required for target transfers with the robot arm) or in a closed state (when preparing the station to receive beam). One section of the radiation shield (labelled as 9) can move on rails (labelled as 10) to facilitate this change of state.

- An electro-pneumatically controlled pusher arm locates the target holder in the irradiation position and also connects the cooling water required to remove the heat generated by the beam in the targets during a bombardment.

- The entire station is electrically isolated from earth, acting as a giant Faraday cup. This enables the direct measurement of all electric charge accumulated on the station during a bombardment. The beam current is measured continuously and logged in 1-second intervals, providing a full beam history for each production run.

Presently, the Elephant is mainly used for the production of relatively short-lived medical radionuclides, such as ^{67}Ga and ^{123}I.

2.2.2 Target station 2 – Babe

The second target station for radionuclide production commissioned by iThemba LABS was intended to accommodate semi-permanent targets. Unlike batch targets, the semi-permanent targets are not exchanged in their totality at the end of bombardment (EOB). The bombarded target material is usually either a liquid or a gas, which can be removed while the bulk of the actual target system remains undisturbed in the station. Target Station 2, usually referred to as Babe, looked like a smaller version of the Elephant. Since no target holders had to be transported, there were no overhead rail to the station and robot arm for target exchanges. For several years this station was used for the production of the positron emitter ^{18}F, utilizing the ^{18}O(p,n)^{18}F nuclear reaction. The bombarded target material was ^{18}O-enriched water. The target water was loaded to, or unloaded from, the target system via thin circular tubes through which the liquid could be transported as a bolus by means of a compressed gas.

After several years of operation, however, a dedicated 11 MeV PET cyclotron facility was established at iThemba LABS and the Babe station became dormant. It has recently been decommissioned and removed from the vault to make space for a new target station, dedicated to the production of the alpha-emitter ^{211}At. Astatine-211 is produced by means of the reaction ^{209}Bi(α,2n)^{211}At. The Babe station was found to be incompatible with the requirements for

low-energy α-particle beams, requiring a redesign of the infrastructure to be used on that beamline. Since the particular version of the 70 MeV cyclotron purchased by iThemba LABS cannot accelerate positive ions, that machine will have no α-particle beam capability. Instead, the SSC will provide the 28 MeV α-particle beams required. It is foreseen that ^{211}At will be the only remaining radionuclide to be produced on a regular basis with the SSC once the switchover to the new 70 MeV facility has been completed.

2.2.3 Target station 3 – VBTS

The vertical-beam target station (VBTS) was designed to operate at higher beam intensities than the Elephant, specifically to increase the production rate of longer-lived radionuclides. It is extensively used for the production of ^{22}Na ^{68}Ge, and ^{82}Sr. While the beam current on a typical Elephant target is interlocked to not exceed an upper limit of 100 μA, on the VBTS beam currents are usually in the region of 200–250 μA.

A photograph of the VBTS is shown in Figure 2.2. The design philosophy is the same as for the Elephant, the main difference being the vertical orientation of the beam. Target transport to and from the VBTS vault is similar to the Elephant vault and target transfers between the transporter and the station are also done with a robot arm (labelled as 2). The radiation shield consists of two near-identical semi-cylinders that move on rails, however, it is not necessary for the station to be brought to be fully opened when a target holder has to be exchanged.

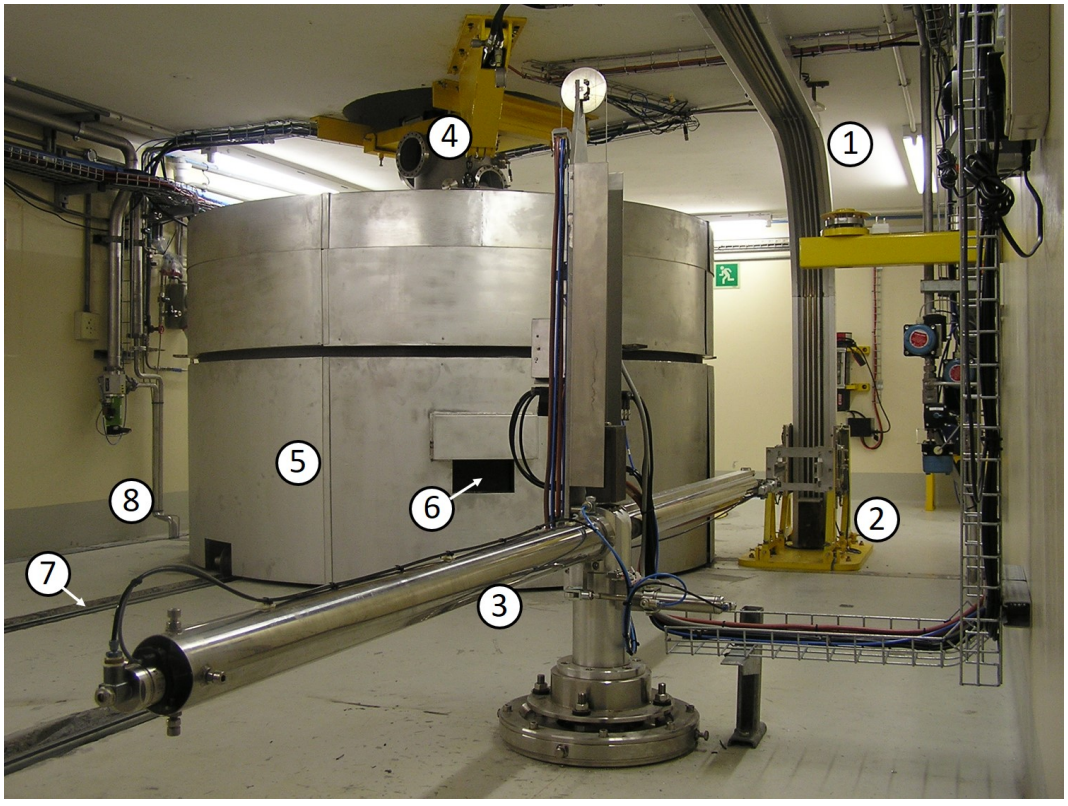


Figure 2.2: Target station 3, usually referred to as the vertical-beam target station (VBTS), for the bombardment of larger-format batch targets. Salient components indicated by numbers are as follows: (1) the electrified rail; (2) target transporter terminus; (3) robot arm; (4) diagnostic chamber and vertical beamline; (5) radiation shield; (6) target transfer hatch; (7) the rail on which shield sectors move when opening or closing the station; (8) inlet and outlet lines for cooling water. Scale: the ceiling of the vault is 2 m above the floor.

Instead, a small hatch (labelled as 6) is provided in one of the half-shields (see Figure 2.2) which can be opened and closed by lifting or lowering a small section (or wedge) of the shield with a hydraulic hoist. This change was necessary because of space limitations inside the vault, which also introduced a number of other unavoidable differences. The VBTS is not electrically isolated from earth as there was no space for a support frame with insulators. The station can therefore not act as a Faraday cup. Instead, beam current and accumulated charge are measured with a capacitive probe located in a diagnostic chamber upstream of the station (see e.g. [STE2013]). Another difference is that the 9-position target magazine, employed on the Elephant, had to be omitted. The VBTS can only accommodate one target holder at a time. In practice, however, operation of the VBTS is very similar to that of the Elephant. The magazine is not strictly necessary for a facility focused on the production of relatively long-lived radionuclides as target exchanges happen less frequently (not more than once a week).

The principle of tandem targets is shown schematically in Figure 2.3. This is by far the most-utilized configuration at iThemba LABS for routine radionuclide productions. During bombardment, the targets are completely surrounded by fast-flowing cooling water (i.e. a 4π cooling geometry). In cases where sensitive target materials cannot come directly into contact with the cooling water, those materials are encapsulated (or clad) with a metal that has a sufficiently high melting point. Depending on the target material, aluminium, niobium and stainless steel are mainly chosen as capsule material.

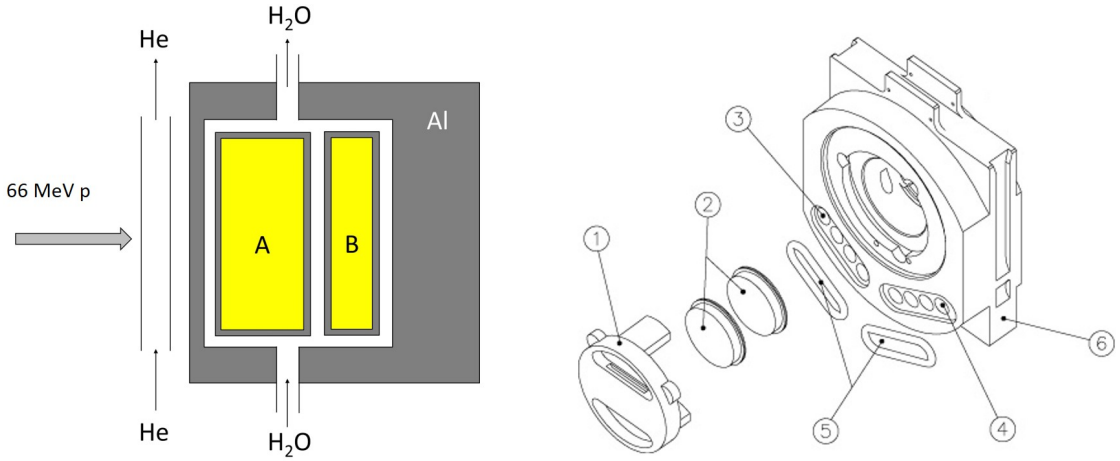


Figure 2.3: LEFT: Schematic diagram illustrating the principle of tandem targets for the simultaneous production of two radionuclides with the same beam. Target A occupies the higher-energy slot and target B the lower-energy slot inside the target holder. The targets are surrounded by fast-flowing cooling water and the beam is incident on the target holder after passing through a double-foil, helium-cooled beamline exit window. RIGHT: Exploded schematic of a loaded target holder. Salient components indicated by numbers are as follows: (1) aluminium back-end plug with bayonet fitting; (2) twin encapsulated targets; (3) quadruple inlet ports for cooling water; (4) quadruple outlet ports for cooling water; (5) moulded rubber seals; (6) aluminium target-holder body.

Figure 2.4 shows a photograph of a typical VBTS target holder as well as encapsulated rubidium targets for the production of ^{82}Sr. The targets indicated as (a) and (b) in the figure have similar thicknesses but significantly different diameters (outer diameters of 22 and 40 mm, respectively). The smaller one (a) is an Elephant target while the larger one (b) is a VBTS target. The similar target thicknesses ensure similar energy windows, however, the larger diameter of

the VBTS target provides a larger surface area in contact with the cooling water, thus a larger surface from which to remove heat. This is the main provision that allows the VBTS to be operated with higher beam intensities. Similar to the Elephant, the beam is also swept in a circular fashion on VBTS targets but with a larger sweep radius and also with a higher sweep frequency of 3 kHz. More detail on tandem targets will be presented in Chapter 5.

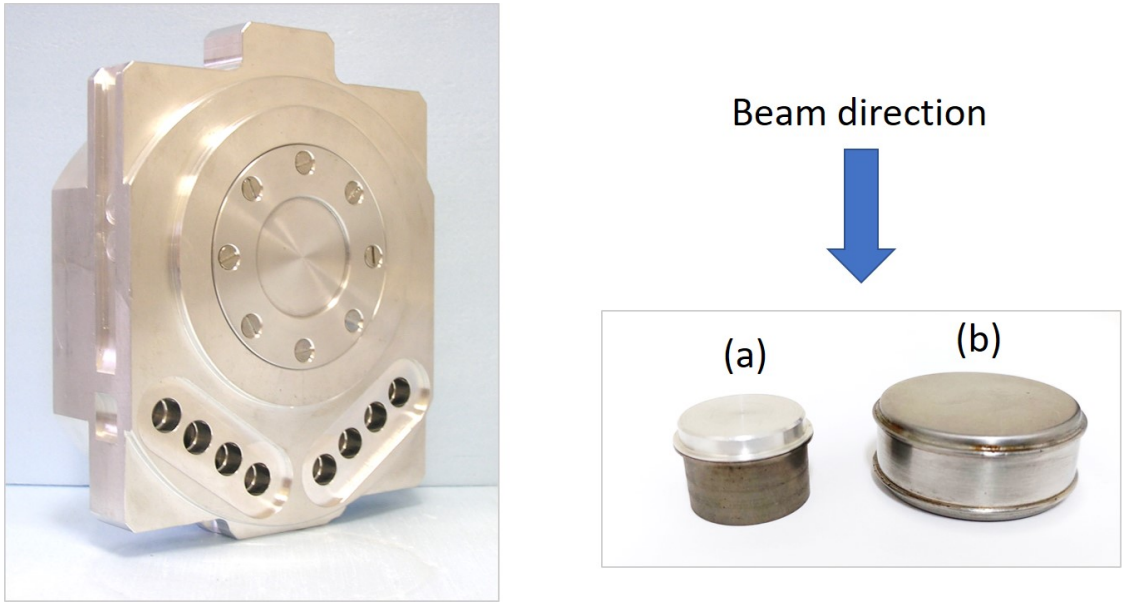


Figure 2.4: LEFT: A VBTS target holder. RIGHT: Examples of encapsulated Rb targets used at iThemba LABS on (a) the Elephant, (b) the VBTS, for the production of the radionuclide ^{82}Sr.

2.3 NEUTRON ACTIVATION CHAMBER

The decision to start activating samples in the secondary-neutron flux directly behind a VBTS target was made at the time when the MSc project of this author commenced [MOT2019]. Fortunately, the pusher assembly of the station afforded this possibility with relative ease. The pusher assembly (see Figures 2.5 and 2.6) is very simple in design and consists of four main parts. It has a circular base plate onto which two cylindrical stainless steel bellows (vacuum type) with different diameters are welded. At the top of the assembly is a movable platform, also welded onto the bellows. The platform can be raised by filling the chamber between the inner and outer bellows with compressed air. Likewise, it can be lowered by removing air. The existing platform already had a cavity in its centre, inside the inner bellows. The top of this cavity proved to be a very convenient place to locate a small chamber into which samples for neutron activation could be sealed. Two such chambers were constructed, each with an inner diameter of 70 mm and a depth of 10 mm.

It had to be demonstrated that such a chamber could be loaded into the VBTS and removed after a production run in a safe way. A non-radioactive, spare pusher assembly was used to practice this, utilizing a 2 m long rod that had a suction cup at one end. The operator would hold the other end of the rod in his hands, ensuring a safe distance to the suction cup. The suction cup was connected to a vacuum pump. It was demonstrated that, with the aid of this tool, one could easily place an activation chamber in the VBTS pusher assembly through the

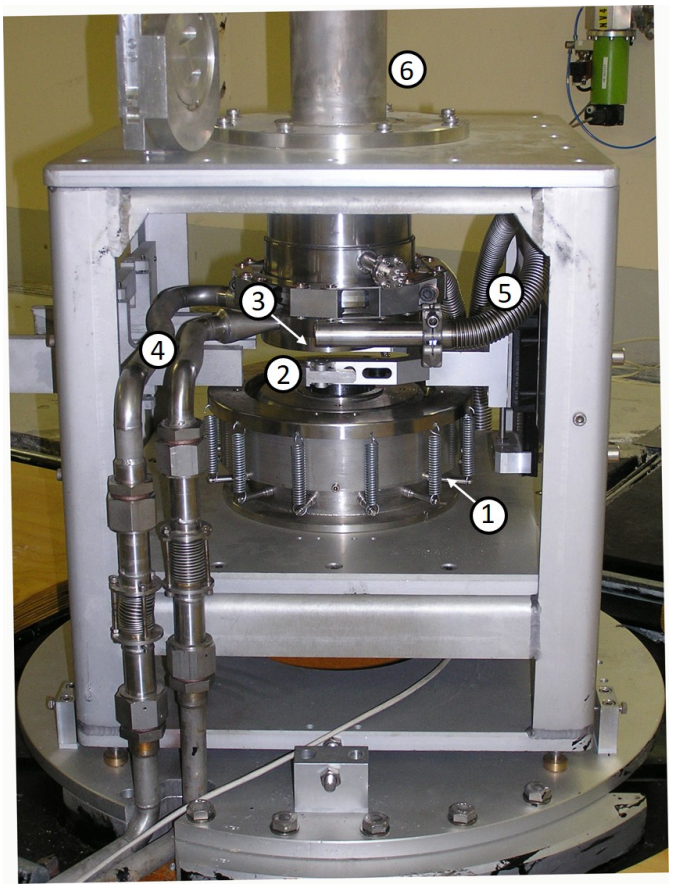


Figure 2.5: Central region of the VBTS, showing (1) the pusher assembly, (2) target-holder mounting fork, (3) assembly containing the helium-cooled, double-foil Havar window, (4) cooling-water lines, (5) helium lines, and (6) vertical beamline. The photograph was taken with the VBTS is in its open state.

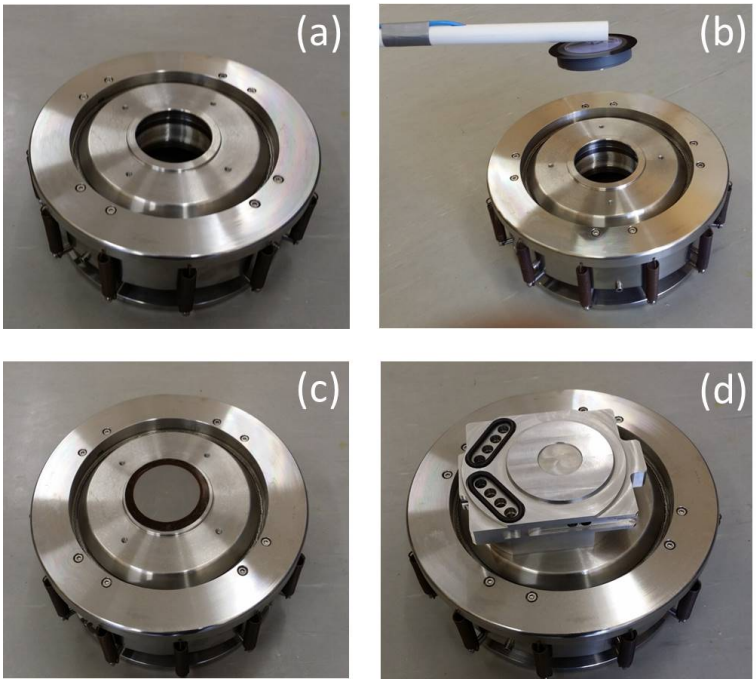


Figure 2.6: Loading of the neutron activation chamber into the spare VBTS pusher assembly. (a) Note the unoccupied cavity in the centre of the pusher assembly. (b) A sample chamber is brought to the pusher assembly by means of the 2 m rod and suction cup, ready to be placed inside the cavity. (c) Sample chamber correctly loaded. (d) The target holder locates snugly over the activation chamber.

hatch of the VBTS shield (see Figure 2.2) and rapidly remove it afterwards. The procedure is shown in Figure 2.6. After removal from the VBTS, a sample chamber would be wheeled out of the vault inside a lead container (also called a lead pig).

2.4 NEW 70 MeV TARGET STATIONS

The lay-out drawing of Figure 2.7 shows the cyclotron and four target stations from above when all roof structures are removed. It is evident that the design of the new target stations is based on the existing Elephant but there are a number of differences. Provision is made for only one target holder in the station at a time (i.e. the magazine was discarded to simplify the design). The pusher arm was redesigned to supply four times more cooling water to the targets. The new target holders reflect those of the current VBTS but the actual target outside diameter has been increased to nominally 52 mm, compared to the corresponding VBTS dimension of 40 mm and Elephant dimension of 22 mm (see also Figure 2.4). This increase in size will allow more surface area in contact with the cooling water, thus higher beam currents will be tolerated than on the older stations. It should be noted that any increase in target size comes with a trade-off, however, in that more target material has to be chemically processed after bombardment and consequently more liquid radioactive waste is produced. From an operational perspective, the new target stations will be very similar to the existing Elephant and VBTS.

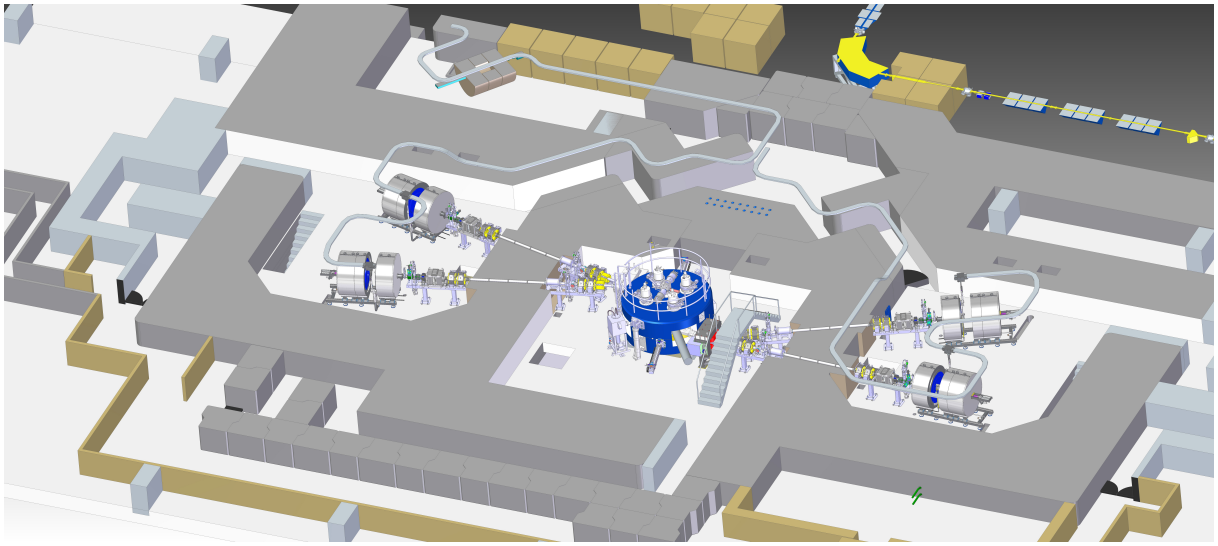


Figure 2.7: Top view of the new 70 MeV cyclotron facility, showing the cyclotron in the centre vault (blue in colour) and two target stations each in the South and North vaults (silver in colour and located to the left side and the right side of the cyclotron).

Figure 2.8 shows a cross-sectional side view (or cut) through the centre of a new target station. It is noticeable how small the actual target is compared to the size of the station, which is dominated by the three layers of the radiation shield. This multi-layer shield consists of a 500 mm thick inner iron layer, a 200 mm thick paraffin wax middle layer, and a 40 mm thick lead outer layer. The paraffin wax is impregnated with fine boron carbide powder (2.5% by weight). The iron inner shield effectively slows down high-energy neutrons (those above about 4 MeV) to intermediate energies via non-elastic nuclear interactions. Neutrons below

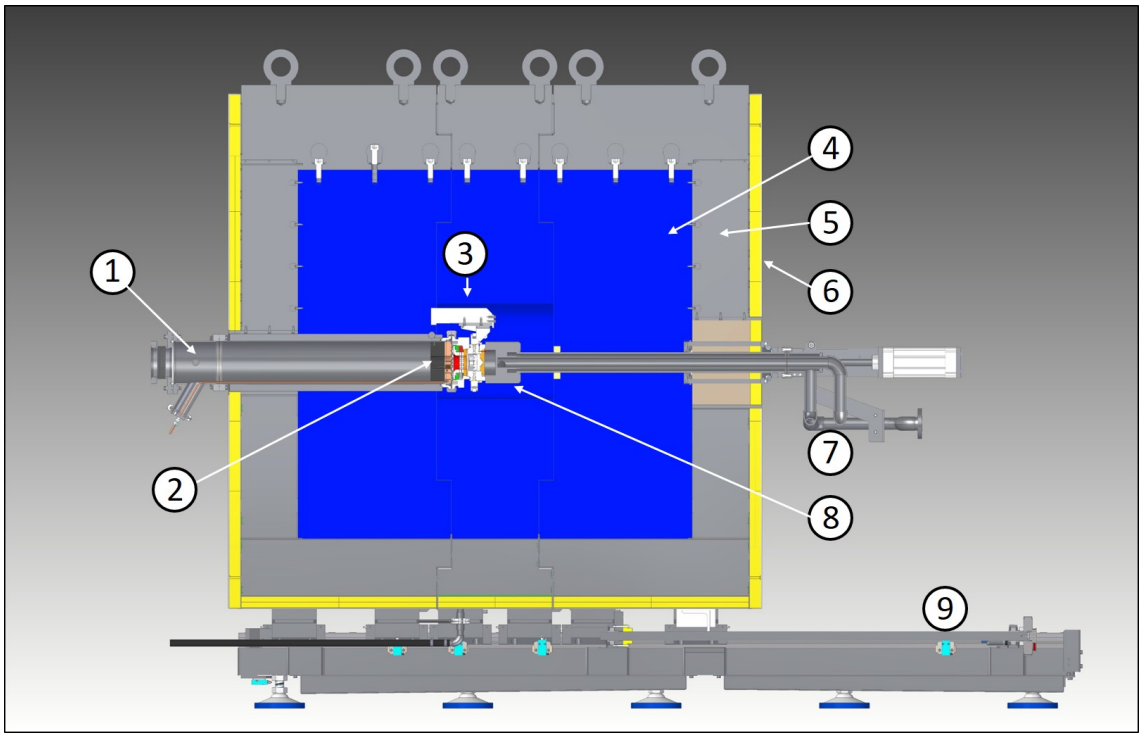


Figure 2.8: Cross-sectional side view through the beam axis of the new 70 MeV target station, showing (1) horizontal beamline, (2) 4-sector collimator, (3) target mount, (4) inner iron shield, (5) middle borated paraffin-wax shield, (6) outer lead shield, (7) pusher arm, (8) head of pusher arm, and (9) support structure with rails. The station is shown in a closed, beam-ready state.

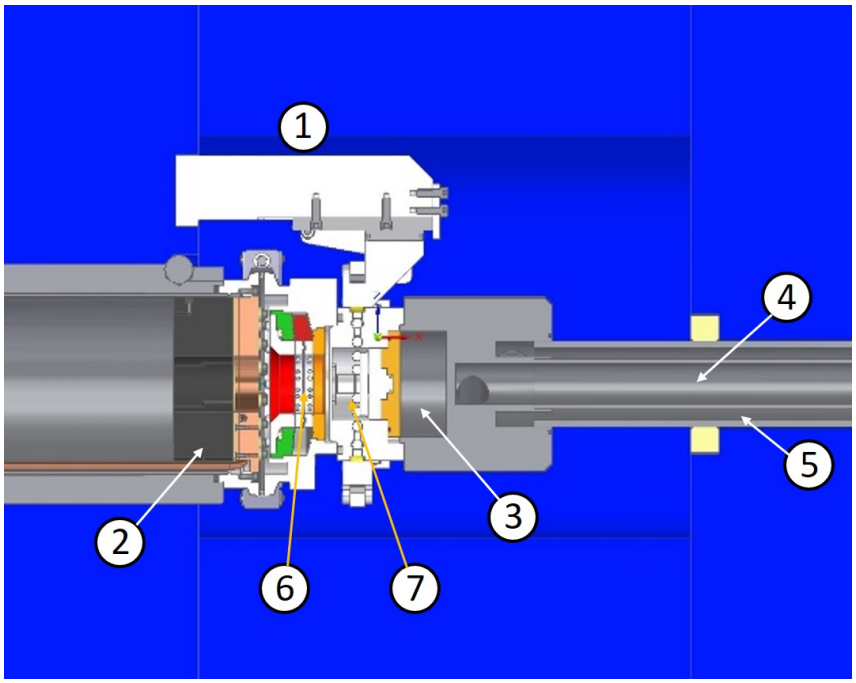


Figure 2.9: A zoomed-in view of the target region of Figure 2.8, showing (1) the target mount, (2) 4-sector collimator, (3) secondary-neutron cavity in the head of the pusher assembly, (4) cooling-water inlet line, (5) cooling-water return line, (6) helium-cooled double-foil Havar window, and (7) target holder.

4 MeV are moderated to thermal energies in the middle hydrogenous layer by elastic scattering with the hydrogen nuclei in the paraffin wax. The boron serves to absorb a large fraction of the thermal neutrons by means of thermal neutron capture reactions. The outer lead shield mainly serves to attenuate gamma-rays emitted from the hydrogenous material, especially the

copious high-energy 2.2 MeV photons emitted in the capture of thermal neutrons by hydrogen. At iThemba LABS, the optimization of such three-layer shields had been investigated previously by means of Monte Carlo simulations (see e.g. Vermeulen [VER2014]).

An enlargement of the target region of Figure 2.8 is shown in Figure 2.9. The close proximity of the collimator, double-foil Havar beam-window assembly, target holder, and cavity to activate materials with secondary neutrons, is evident. To utilize secondary neutrons on these new stations, a cavity has been provided in the head of the pusher assembly. The cavity has a depth of 40 mm and a volume of 250 cm^3. One of the engineering challenges was to provide a cooling-water flow with sufficient linear velocity for the effective removal of heat during bombardment. This was investigated by means of computational fluid dynamics (CFD) modeling of the pusher assembly and target holder (as a case study in a CFD Workshop also attended by the author of this thesis but which falls outside the scope of this thesis project). A maximum flow rate of 250 L/min with a differential pressure below 10 bar was achieved.

2.5 FACILITIES FOR STACKED-FOIL EXPERIMENTS

One of the three beamlines in the horizontal-beam vault (or Elephant vault) is dedicated to experimental activation studies. It currently accommodates an irradiation chamber called RERAME-II [SZE2005]. The original RERAME (REcoil RAnge MEasurements) facility was designed and built at the Laboratorio Nazionale del Sud (LNS) in Catania, Italy, and was intended for the activation of very thin, fragile foils [FRE1994]. A similar set-up was established at iThemba LABS and used for several years on a nuclear physics beamline, before being relocated to a radionuclide production vault. It is ideally suited for the measurement of excitation functions. A photograph of the RERAME-II facility is shown in Figure 2.10.

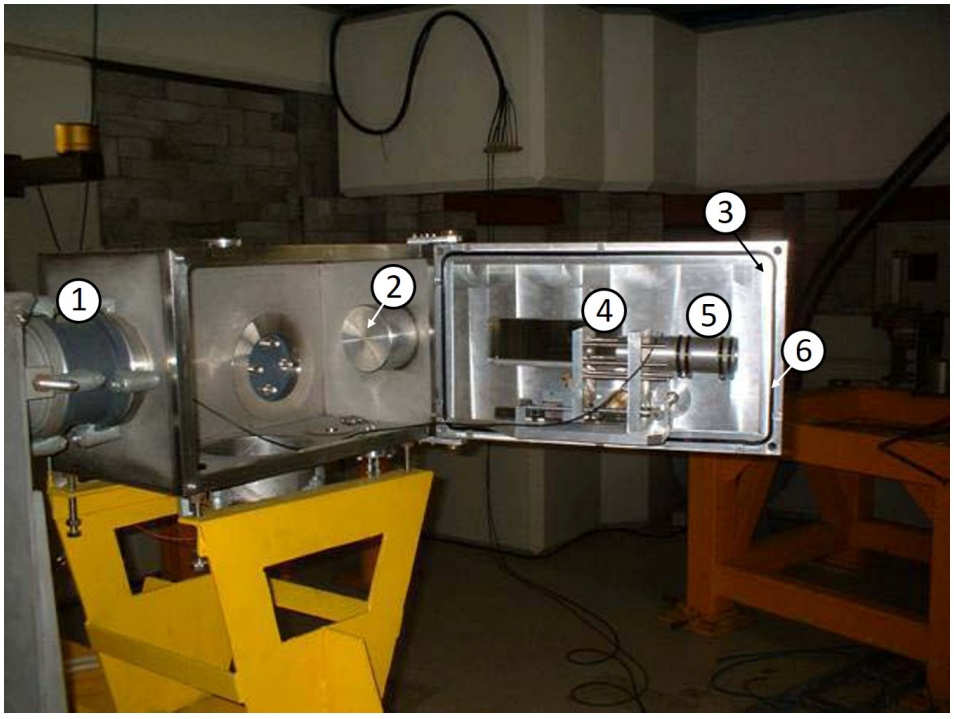


Figure 2.10: The RERAME-II irradiation chamber in an opened state, showing (1) the incident beamline, (2) beamstop, (3) door, (4) adjustable vice, (5) collimator, and (6) O-ring seal.

The target foils are held in position in a vice mechanism which, together with a collimator assembly, are conveniently mounted on the door of the chamber. When the door is opened wide (up to 180° is possible) parts that are normally inside the chamber are brought to the outside. This simplifies the rapid loading and unloading of target foils. A rotatable handle on the door controls the opening and closing of the jaws of the vice, allowing foil stacks of different total lengths to be accommodated. A beryllium oxide (BeO_2) viewer is used to focus the beam, a process that can be observed with a TV camera through a plexiglass window on the door. The chamber is electrically isolated and provided with electron suppression near the beamline entrance port. The chamber therefore acts as a true Faraday cup for the accurate measurement of the beam current and accumulated charge. The door has a vacuum seal along its outer edge, allowing the closed chamber to be pumped down to a vacuum better than 1×10^{-5} mbar. If necessary, water cooling of a foil holder can be employed. The chamber has also been equipped with several electrical feeds-through, one of which is normally used to provide for an independent measurement of the beam current on the collimator assembly.

A schematic diagram of the RERAME-II chamber is shown in Figure 2.11. Secondary electrons are prevented from scattering back and escaping upstream into the beamline. This is

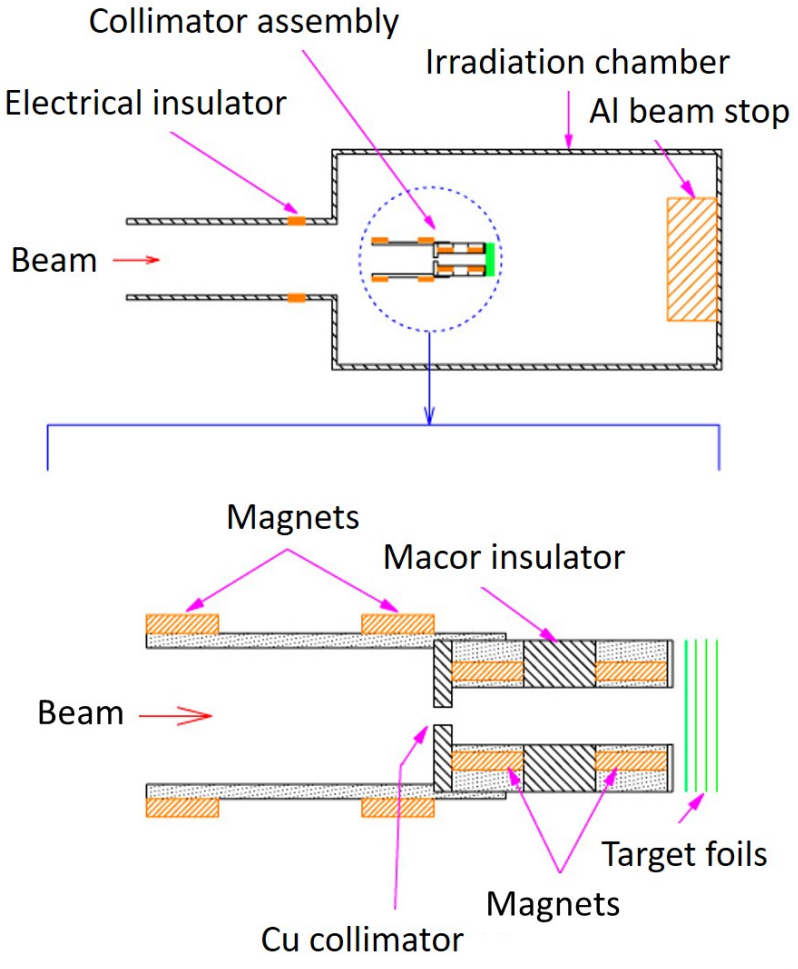


Figure 2.11: Diagram showing a cross-sectional view of the RERAME-II irradiation chamber (TOP) and and enlarged view of the collimator assembly (BOTTOM).

done via an appropriate placement of Macor insulators and strong permanent magnets of the samarium-cobalt type, as shown in the figure. A set of different size collimators are available and a collimator exchange can be performed rapidly. The current of the entire chamber is normally measured with a Brookhaven Instruments model 1000C current integrator while the current intercepted by the collimator is measured with a Keithly electrometer. Current values from both instruments are logged at 1-second intervals with a PC-based system running the well-known LabVIEW software [JEN2019].

In this study the RERAME-II facility was used for the measurement of excitation functions, by means of the stacked-foil technique, at two proton-beam energies, namely 40 and 66 MeV. One experimental run was performed at 40 MeV and two runs at 66 MeV, details of which will be given in subsequent chapters. The beams were focused such that about two-thirds of the current penetrated the foil stacks while one-third was intercepted by the collimator. This is normally done to prevent the beam from being too sharply focused but still being well-defined on target in a predictable manner. The collimator selected for these stacked-foil activations is thick enough to stop 66 MeV protons and has an aperture of 4 mm.

One stacked-foil experiment was also performed with a primary proton beam of 200 MeV. Normally the RERAME-II chamber would also be the facility of choice at this beam energy, however, its current location is in a vault where the maximum proton energy is only 100 MeV. The radionuclide production vaults are serviced with a beam switchyard that contains some dipole bending magnets designed for a maximum proton energy of 100 MeV, as it was never foreseen that this activity would require beams of higher energy. As the RERAME-II chamber was being used for several other experiments also during this period, we did not want to disturb the programme by moving it to another high-energy beamline. Instead, a different set-up was used for the 200 MeV run, utilizing a chamber that was last used more than two decades ago but was still available in a good condition. A schematic diagram of this temporary set-up is shown in Figure 2.12.

From a practical perspective, the small chamber of Figure 2.12 works in the same way as the RERAME-II chamber except that there is no collimator and also no electron suppression. It is therefore possible for some charge to escape back along the beamline. The lack of a collimator has both pros and cons. The beam focus has to be near-perfect, requiring more time for tuning. However, secondary-neutron production upstream of the foil stack is also reduced, limiting possible unwanted neutron-induced reactions from disturbing the measurements of primary interest. Also, this experiment relies more heavily on monitor reactions as the chamber cannot be assumed to have the properties of a true Faraday chamber.

The procedure followed to activate the foil stack was as follows. The beam viewer, shown as an insert in Figure 2.12, was initially placed in the position where the stack holder is located during bombardment. Both the viewer and the stack holder locates onto a quick-release, water-cooled mounting assembly with an accurate position inside the chamber. The chamber was then pumped down to vacuum. Once the vacuum reached the same level as that of the beamline, a vacuum isolation valve between the beamline and chamber was opened. The beam was then focused to a spot approximately 4 mm in diameter on the viewer. Afterwards the chamber was isolated from the beamline and vented, before replacing the viewer with the loaded

stack holder. Once the vacuum was restored and the isolation valve opened, the bombardment was performed. More detail on these activations will be given in Chapter 4.

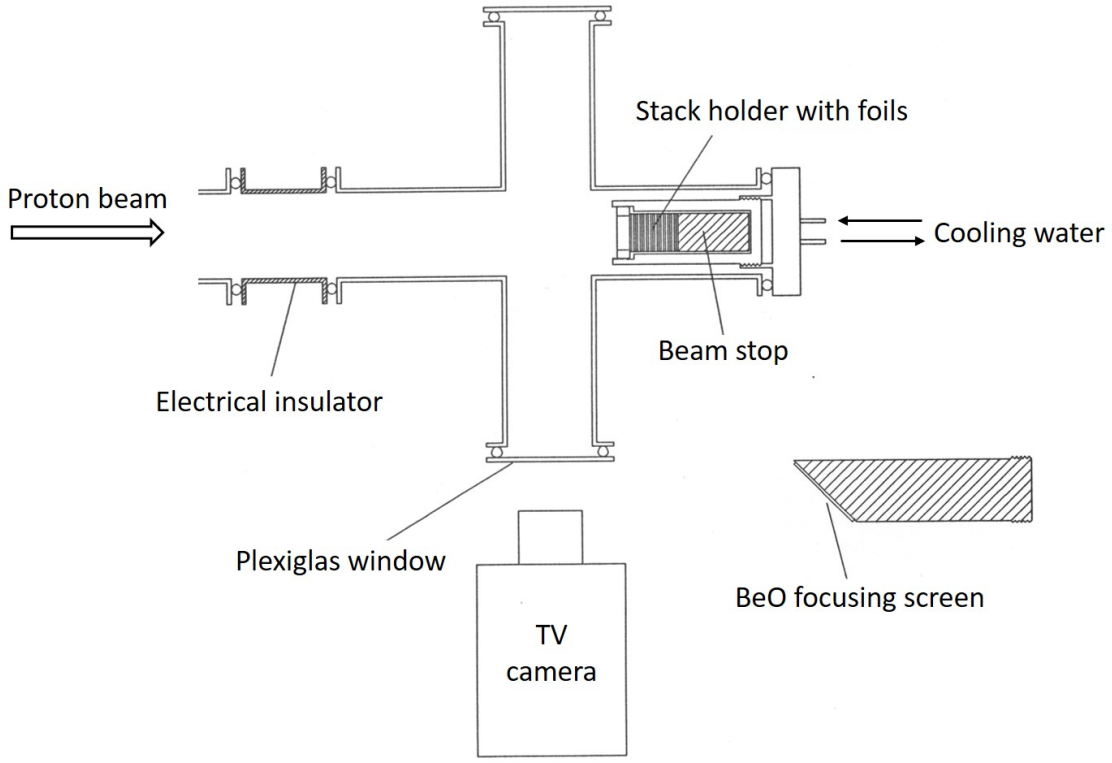


Figure 2.12: Schematic diagram of the irradiation chamber used for the stacked-foil experiment with a 200 MeV proton beam.

2.6 RADIONUCLIDE ASSAYS

Gamma-ray spectra of all activated foils and/or samples of interest were measured off-line, using high-purity germanium (HPGe) detectors. Measurements were performed in two counting rooms. The detector set-up in one of the counting rooms is shown in Figure 2.13. The HPGe detector has a horizontal configuration and is surrounded by a composite Cu/Pb shield to reduce background events. A standardized source holder can be moved on rails to adjust the source position to any source-detector distance between 0 and 2 m. The foils and/or other samples to be counted are normally mounted on standardized source frames that accurately locate onto the source holder. The set-up in the second counting room is very similar except that it has a 6 m long rail, suitable for counting stronger sources.

Most of the sources were counted multiple times. Earlier counting sessions were useful for identifying and quantifying shorter-lived radionuclides (e.g. half-lives of several hours to a few days), while later counting sessions with longer counting times typically provided this information more accurately for longer-lived radionuclides (e.g. half-lives of several days to many months or years). An added advantage of multiple counting sessions is to obtain yield data of individual radionuclides as a function of time, which can demonstrate decay according to the expected half-life. The so called decay-curve analysis, which will be discussed in Chapter 3, played a major role in Chapters 3 and 4 of this study.

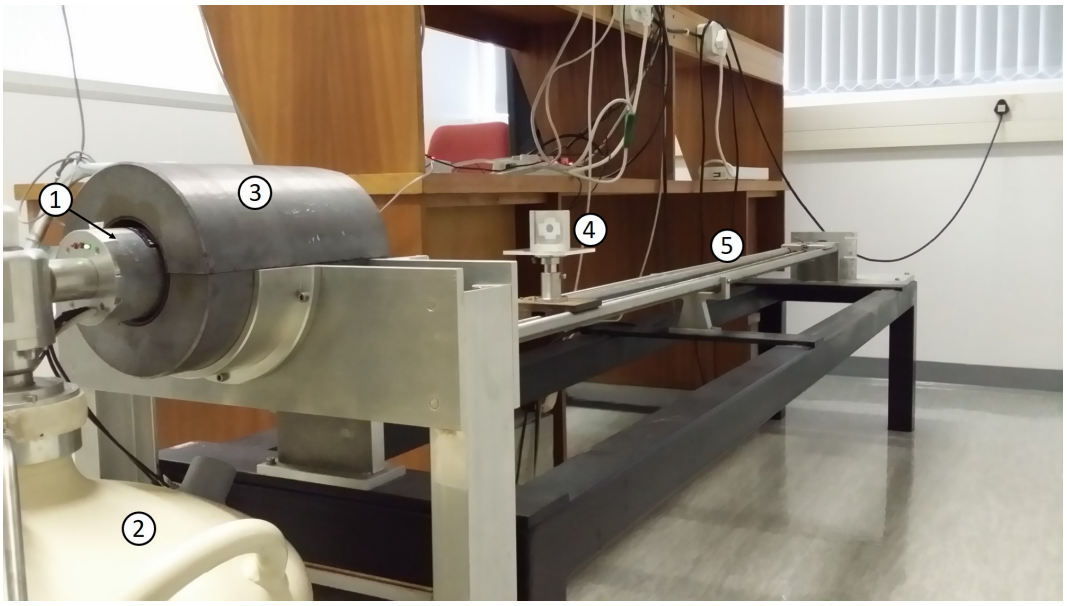


Figure 2.13: Facility for measuring off-line gamma-ray spectra of activated foils or samples, showing (1) the high-purity germanium (HPGe) detector, (2) liquid nitrogen dewar, (3) composite copper/lead shield, (4) source frame located on source holder, and (5) source-holder rail.

2.7 ACTIVATION CROSS SECTIONS AND EXCITATION FUNCTIONS

2.7.1 Penetration depth and beam energy

An excitation function of a radionuclide is its activation cross section expressed as a function of projectile energy. The activation cross section is, in general, energy dependent. Consider a beam of monoenergetic charged particles incident upon a solid target material. Once inside the material, a charged particle is surrounded by the Coulomb field created by the electrons and nuclei of the target atoms, interacting with it. In the case of a proton beam and at energies relevant to this study, the majority of interactions will be with the atomic electrons, slowing the protons down. In each interaction between a proton and an electron only a small amount of the proton's kinetic energy will be lost in a small-angle scattering event, therefore a large number of such interactions are likely to occur [AND1977, ZIE1980]. Consequently, the proton's kinetic energy decreases with increasing penetration depth. In the continuous slowing-down approximation (CSDA) the fluctuations associated with individual interactions are neglected, leading to a unique energy of the charged particle as a function of penetration depth. The particle's CSDA range is also unique. In the following paragraphs a stacked-foil experiment will first be described in the context of the CSDA, before describing important processes beyond this approximation and how they have been taken into consideration.

A schematic diagram of a typical stacked-foil experiment is shown in Figure 2.14. As the collimated beam traverses the foil stack it loses energy. Let the foils be numbered from 1 to J along the beam axis. Consider an arbitrary selected foil with number j, located somewhere inside the stack. In the CSDA, and provided the incident beam is monoenergetic, the beam energy will have a unique value at the foil entrance surface, E_j, as well as a unique energy at the exit surface, $E_j - \Delta E_j$, where ΔE_j is the energy loss in the foil. It is assumed that the foil is thin, therefore $\Delta E_j \ll E_j$ (also called the thin-target approximation). The energy loss in the foil can then be expressed in terms of the stopping power at the average energy associated with the

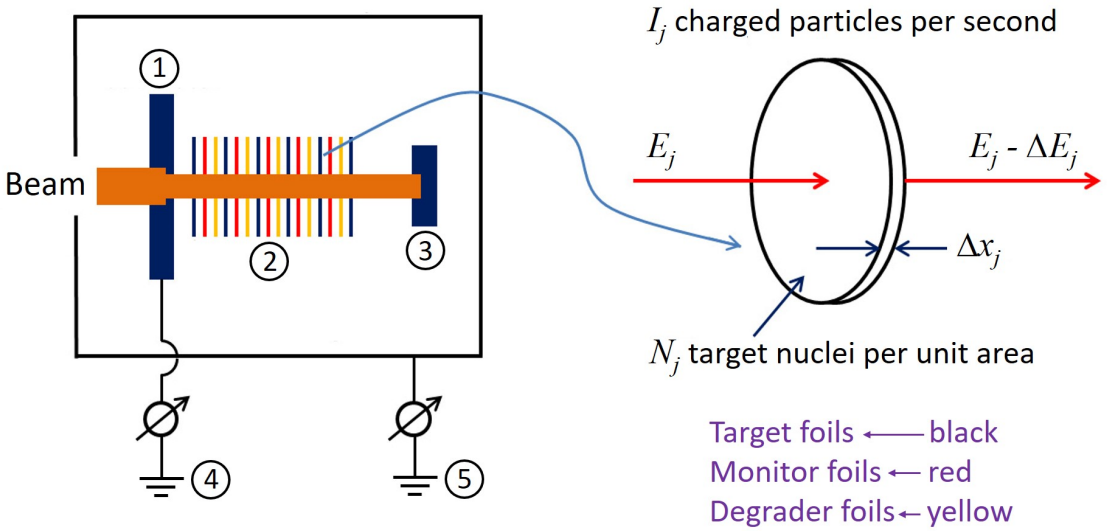


Figure 2.14: LEFT: Schematic diagram of a stacked-foil experiment, showing a beam incident on (1) a collimator, (2) the collimated beam traversing through the foil stack, before (3) reaching the beam stop. The electric current is measured separately on the collimator (4) and experimental chamber (5). RIGHT: Beam penetration through a single target foil.

foil, taking into consideration that stopping power is a unique function of energy in any given material:

$$\Delta E_j = S\left(\frac{E_j + E_{j+1}}{2}\right)\Delta x_j, \tag{2.1}$$

where Δx_j is the foil thickness and $E_{j+1} = E_j - \Delta E_j$. A number of Fortran codes that implement this approach have been developed at iThemba LABS (see e.g. Nortier [NOR1990]), utilizing the stopping-power expressions and parameter data of Andersen and Ziegler [AND1977]. The code ELOSS as well as a version of it modified for stacked-foil calculations, STACK, are still extensively used at iThemba LABS during the design stages of activation experiments. These codes are fast and one can quickly find the desired thicknesses of target foils, catcher foils, degrader foils and monitor foils required for a particular experiment. These codes were also employed for this purpose in the present project.

The numerous small-angle Coulomb scatterings are, however, not the only interactions that occur. Non-elastic nuclear interactions of the beam particles with atomic nuclei give rise to the formation of many radionuclides, both the desired ones and also undesired radio-contaminants. Stacked-foil investigations usually focus on maximizing the yield of desired radionuclides while minimizing the yields of co-produced contaminants. Non-elastic interactions also remove particles from the beam, reducing the beam intensity with increasing penetration depth. Large-angle scattering of beam particles can likewise remove these particles from the foil stack. Due to the discrete nature of all the energy-loss mechanisms, a statistical spread in beam energy builds up gradually as a function of penetration depth, a process referred to as energy straggling. Also, a real particle beam delivered by an accelerator is not normally monoenergetic but has a narrow spread in energies to begin with. These effects can all be included in the analysis of a stacked-foil experiment by means of Monte Carlo simulations. Such simulations can provide a realistic energy distribution for each foil in the stack. These distributions are Gaussian in character, from which a mean energy and standard deviation

can be derived for each and every foil. Such simulations implicitly provide energy uncertainties associated with individual foils as well as quantitative information on the attenuation of the beam intensity with increasing penetration depth. In this work the well-known Monte Carlo code MCNP6 [GOO2012] was used to model the activation experiments. It has to be mentioned that an older method exists to estimate beam intensity losses in materials, i.e. from published tables of non-elastic nuclear interaction probabilities (see e.g. Janni [JAN1982]). It is normally found that the results from Monte Carlo simulations are in good agreement with the older methods based on CSDA and the Janni tables.

2.7.2 The activation equation

The following derivation refers to Figure 2.14. The arbitrary selected foil identified with index j is again considered, where $1 \leq j \leq J$. Let N_j be the number of target nuclei per unit area of the foil and I_j the number of incident beam particles per second traversing the foil. The beam intensity may vary with time, therefore I_j is considered to be a function of time; $I_j = I_j(t)$. The number of residual nuclei (of a particular type) formed per second is related, by definition, to the relevant activation cross section (for that type) as follows:

$$R_j = \sigma_j N_j I_j, \tag{2.2}$$

where σ_j is the activation cross section (also called production cross section or formation cross section). The quantity R_j is sometimes referred to as the production rate. In general, the cross section is a function of energy [$\sigma_j = \sigma_j(E)$] and the production rate is a function of time [$R_j = R_j(t)$]. For a thin foil the following should be a good approximation:

$$\sigma_j = \sigma\left(\frac{E_j + E_{j+1}}{2}\right). \tag{2.3}$$

The number of target nuclei per unit area in the foil is given by

$$N_j = \frac{\rho \Delta x_j N_A}{A}, \tag{2.4}$$

where ρ is the density of the target material (or partial density of the target element in the case of mixtures or compounds), N_A is Avogadro's number, A is the atomic mass in units of AMU, and Δx_j is the thickness of foil number j in the stack. This description assumes that foil number 1 will be the first foil of a particular type at the front of the stack and foil number J the last foil of that same type at the back of the stack.

Let T denote the duration of the bombardment period, starting at time $t = 0$. The following times and quantities can then be defined:

$t = 0$:	Beginning of bombardment (BOB),
ΔT :	Time increment of current integrator log (1 second in this study),
n :	Total number of time increments in bombardment period,
$t = T = n\Delta T$:	End of bombardment (EOB).

The end of each time interval is given by

$$t_i = i\Delta T \quad \text{for all} \quad 1 \leq i \leq n. \tag{2.5}$$

The number of residual nuclei (of a given type) produced in time increment i in foil number j is given by

$$\Delta N_j(t_i) = R_j(t_i)\Delta T \qquad \text{for all} \quad 1 \leq i \leq n. \tag{2.6}$$

Let time $t = t_{ref}$ be a reference time after EOB (i.e. $t_{ref} \geq T$) and let the nuclide formed be associated with a radionuclide that has a half-life $T_{1/2}$. The contribution of the radioactivity formed in time increment i to the radioactivity at reference time $t = t_{ref}$ is given by

$$\Delta A_j(t_{ref}, t_i) = \lambda \Delta N_j(t_i) \exp[-\lambda(t_{ref} - t_i)], \tag{2.7}$$

where $\lambda = \ln(2)/T_{1/2}$ is the decay constant. Substitution of Equations 2.2 and 2.6 into 2.7 gives

$$\Delta A_j(t_{ref}, t_i) = \lambda N_j \sigma_j I_j(t_i) \Delta T \exp[-\lambda(t_{ref} - t_i)]. \tag{2.8}$$

The total activity of foil no. j at reference time $t = t_{ref}$ is obtained by summing over all time increments:

$$A_j(t_{ref}) = \sum_{i=1}^{n} \Delta A_j(t_{ref}, t_i) = \lambda N_j \sigma_j \Delta T \sum_{i=1}^{n} I_j(t_i) \exp[-\lambda(t_{ref} - t_i)]. \tag{2.9}$$

The beam intensity associated with foil no. j, $I_j(t_i)$, can be written as follows:

$$I_j(t_i) = I_{beam}(t_i) \times F_j, \tag{2.10}$$

where F_j is the beam attenuation factor (in this work these attenuation factors for final results were determined from Monte Carlo simulations) and $I_{beam}(t_i)$ is the measured intensity of the incident beam at time t_i. Substitution of Equation 2.10 into Equation 2.9 finally gives

$$A_j(t_{ref}) = \lambda N_j \sigma_j F_j \Delta T \sum_{i=1}^{n} I_{beam}(t_i) \exp[-\lambda(t_{ref} - t_i)]. \tag{2.11}$$

Equation 2.11 is a convenient form of the so-called activation equation and the one used in this study. Other forms exist in the literature, e.g. for a constant beam intensity (see e.g. Bonardi *et al.* [BON2003]), in which case the equation can be further simplified by eliminating the summation.

2.7.3 Spectrometric activity determination

The measured activity of foil no. j is determined from its full-energy photo-peak area. Since these measurements take place over finite time intervals, every measured activity can be associated with a unique time within its counting interval. Let the counting times of foil no. j be defined as follows:

$t = t_{start}$: Beginning of counting period,
$t = t_{stop}$: End of counting period.

The real time of the measurement is given by

$$\tau_{real} = t_{stop} - t_{start}, \tag{2.12}$$

and the live time by

$$\tau_{live} = \tau_{real} - \Delta\tau, \tag{2.13}$$

where $\Delta\tau$ is the dead time of the spectrometry system, a quantity that is generally count-rate dependent. The measured activity (of a given type) is given by

$$A_j(t_m) = \frac{A_p}{\tau_{live}\epsilon_\gamma\epsilon_d}, \tag{2.14}$$

where A_p is the area of the full-energy photo-peak of a characteristic γ-line, ϵ_γ is the branching ratio of that γ-line, ϵ_d is the detector efficiency for that particular γ-energy, and t_m is the mean value within the time interval (t_{start}, t_{stop}) where the actual activity equals the average activity over that counting period. Thus

$$A_j(t_m) = \frac{1}{(t_{stop} - t_{start})} \int_{t_{start}}^{t_{stop}} A_j(t)dt. \tag{2.15}$$

Referring all activities in terms of the starting activity at $t = t_{start}$ gives

$$A_j(t_{start})\exp(-\lambda t_m) = \frac{A_j(t_{start})}{(t_{stop} - t_{start})} \int_{t_{start}}^{t_{stop}} \exp(-\lambda t)dt. \tag{2.16}$$

After integration and rearranging terms t_m is found to be

$$t_m = -\frac{1}{\lambda}\ln\left[\frac{\exp(-\lambda t_{start}) - \exp(-\lambda t_{stop})}{-\lambda(t_{start} - t_{stop})}\right]. \tag{2.17}$$

2.7.4 Activation cross sections

An expression for the cross section derived from spectrometric measurements is finally obtained from Equations 2.11 and 2.14 by equating the reference and measurement times:

$$A_j(t_m) = \lambda N_j\sigma_j F_j\Delta T\sum_{i=1}^{n} I_{beam}(t_i)\exp[-\lambda(t_m - t_i)] = \frac{A_p}{\tau_{Live}\epsilon_\gamma\epsilon_d}. \tag{2.18}$$

One finds a general expression for the cross section by rearranging terms:

$$\sigma_j = \frac{A_p}{\lambda N_j\tau_{Live}\epsilon_\gamma\epsilon_d F_j\Delta T\sum_{i=1}^{n} I_{beam}(t_i)\exp[-\lambda(t_m - t_i)]}. \tag{2.19}$$

The set of values $I_{beam}(t_i)$, for all $1 \leq i \leq n$, generally is referred to as the "beam history". Equation 2.19 was extensively utilized in this study to extract cross-section values from measured gamma-ray spectra. A formal definition of an excitation function is the set of values σ_j, for all $1 \leq j \leq J$, which is generally shown as a plot of cross section versus projectile energy.

2.7.5 Concluding remarks

The designation of foils in a stacked-foil experiment is often not strict. For example, all foils degrade the beam energy, not only the so-called "degrader foils". In addition to the target foils and monitor foils, some foils also act as "catcher foils". Recoiling nuclei and/or fission fragments formed in close proximity to a foil surface may escape and be collected in an adjacent foil. It is sometimes useful to ensure that adjacent foils are of a sufficiently different material

to be able to determine the escaped fraction experimentally during the counting. Sometimes it is useful to permanently sandwich a target foil between two catcher foils and to count these activated sandwiches as a whole. There are various ways to design a good experiment – each must be judged on its own merits and none are perfect. Sisterson [SIS2008] showed that recoil losses are usually quite small (well below the 1% level) and can often be neglected, becoming significant only for very thin foils. Dedicated catcher foils may nevertheless be useful in certain cases to avoid contamination of adjacent foils, especially in the cases where fission fragments (covering a wide mass range) are copiously produced.

Many of the techniques described above can also be utilized for thicker targets, as any such target can be modelled as an assembly of thinner targets by subdivision. In the code STACK, for example, a parameter can be specified allowing each foil to be subdivided into a number of thinner layers, ensuring the thin-target approximation (see Subsection 2.7.1) remains valid.

2.8 INTEGRAL YIELDS

2.8.1 The physical yield

Once an excitation function for the production of a radionuclide via a particular production route has been determined, it is useful to compute the integral physical yield (also sometimes called thick-target yield) as this provides a quick way to find yields of targets in specific energy windows within the available energy region investigated. The integral physical yield curve is a monotonically increasing function of projectile energy, starting at the threshold energy of the relevant nuclear reaction. Let $\sigma(E)$ be a known excitation function with units in mb. Let $S(E)$ be the stopping power function of a target material in units of MeV·(g/cm^2)$^{-1}$. In order to be more general, the target material is a compound consisting of well-defined molecules. The integral physical yield (in units of Bq/μAh) is given by

$$Y_P(E') = K_{norm} \int_{E_{thres}}^{E'} \frac{\sigma(E)}{S(E)} dE, \tag{2.20}$$

where E_{thres} is the threshold energy of the relevant reaction and $E' > E_{thres}$. The normalization factor K_{norm} is given by

$$K_{norm} = \lambda \left(\frac{N_A \eta}{A} \right) \left(\frac{3.6 \times 10^{-3}}{e} \right) \left(1 \times 10^{-27} \right), \tag{2.21}$$

where A is the molar mass of the target material in atomic mass units (AMU), η is the number of target atoms of the desired species per molecule of the target material, N_A is Avogadro's number, and e is the charge of the projectile (the value for protons is 1.602×10^{-19} C). Note that the number of protons corresponding to 1 μAh of accumulated charge is $3.6 \times 10^{-3}/e$. The conversion factor from mb to cm^2 is 1×10^{-27}.

If the target is a pure element, A in Equation 2.21 becomes the atomic mass (in AMU) and $\eta = 1$. The integral physical yield always represents an upper limit as it neglects losses, e.g. decay losses, beam attenuation losses, etc. In this work the functions $\sigma(E)$ and $S(E)$ were first evaluated by fitting of appropriate curves through selected data sets, either cubic splines or polynomials. The fitted functions were used in the evaluation of the integral in Equation 2.20.

2.8.2 The production yield at the end of bombardment

The relationship between the physical yield and the production yield at the end of bombardment (EOB) is derived below. It is useful to first subdivide the bombardment period, T, into a large number, n, of infinitesimal time intervals of duration Δt. The bombardment period is then given by

$$T = n\Delta t. \tag{2.22}$$

Let the bombardment produce R radioactive nuclei per second of the type described by the excitation function. The total number of radioactive nuclei formed during the bombardment is then given by

$$N_{total} = RT = Rn\Delta t. \tag{2.23}$$

This number is larger than the number of such radioactive nuclei left at EOB as some would have decayed during the bombardment period. The relationship between N_{EOB} and N_{total} is found by including radioactive decay and summing over all the time intervals of the bombardment period. The summation can be converted to an integral by taking the limit where $\Delta t \to 0$:

$$\begin{aligned}
N_{EOB} &= \sum_{i=1}^{n} R\Delta t \, \exp[-\lambda(T - i\Delta t)], \\
&= R\sum_{i=1}^{n} \exp[-\lambda(T - i\Delta t)]\Delta t, \\
&= R\int_{0}^{T} \exp[-\lambda(T - i\Delta t)]dt, \\
&= R\left[\frac{\exp(-\lambda T)}{\lambda}[\exp(\lambda T) - 1]\right], \\
&= R\left[\frac{1 - \exp(-\lambda T)}{\lambda}\right].
\end{aligned} \tag{2.24}$$

Multiplying both the numerator and denominator in Equation 2.24 with T leads to

$$\begin{aligned}
N_{EOB} &= RT\left[\frac{1 - \exp(-\lambda T)}{\lambda T}\right], \\
&= N_{total}\left[\frac{1 - \exp(-\lambda T)}{\lambda T}\right].
\end{aligned} \tag{2.25}$$

The factor in square brackets of Equation 2.25 is a survival probability, i.e. the fraction of radioactive nuclei formed during the entire bombardment still left at EOB. The relevant activities are found by multiplying both sides of the equal sign with λ, while the yields can be obtained by dividing both sides of the equal sign by the accumulated charge, Q:

$$\begin{aligned}
\left(\frac{\lambda N_{EOB}}{Q}\right) &= \left(\frac{\lambda N_{total}}{Q}\right)\left[\frac{1 - \exp(-\lambda T)}{\lambda T}\right], \\
\therefore Y_{EOB}(E') &= Y_P(E')\left[\frac{1 - \exp(-\lambda T)}{\lambda T}\right].
\end{aligned} \tag{2.26}$$

Equation 2.26 does not correct for beam attenuation losses. Normally it is sufficient to make an estimate as follows [JAN1982]:

$$Y_{EOB}(E') = Y_P(E')\left[\frac{1 - \exp(-\lambda T)}{\lambda T}\right]\left[1 - \bar{P}\right], \tag{2.27}$$

where $\bar{P}$ is a mean nonelastic nuclear interaction probability for the energy window of the target. The beam attenuation factor, $[1 - \bar{P}]$, can also be determined by performing a Monte Carlo simulation of the target and beam. For a production energy window (E_{in}, E_{out}), where both E_{in} and E_{out} are larger than the threshold energy and $E_{in} > E_{out}$, the following rule applies:

$$Y_P(E_{in}, E_{out}) = Y_P(E_{in}) - Y_P(E_{out}). \tag{2.28}$$

Chapter 3

Selected excitation functions of ^{232}Th+p and ^{nat}Mg+p reactions up to 70 MeV

3.1 INTRODUCTION

The ability to target malignant cells while sparing healthy cells is a highly desirable goal in cancer therapy. Targeted alpha therapy (TAT) is a specialized field of targeted radionuclide therapy (TRT) with the aim of exploiting the short path length of the α-particle in tissue to increase the selectivity of radiation treatment to malignant cells while decreasing the risk of damage to surrounding healthy cells [DUA2013]. Compared to other emissions from decaying radionuclides (e.g. β^--particles, neutrons and protons) the heavier α-particles with +2 electric charge typically deposit their energy over a much shorter range in tissue (typically 50–100 μm). An emitted α-particle deposits between 500 and 1500 times more energy per unit path length than a β^--particle. This high linear energy transfer (LET) of the order of 100 keV/μm provides excellent cytotoxicity that manifests itself within the range of typical cell dimensions. The main approach is for radiolabelled biomolecules (functioning as disease-targeting vectors) with selectivity for malignant cells to carry the α-emitting radionuclide as a toxic payload to those targeted cells, with each subsequent α-decay delivering a lethal dose preferentially to a malignant cell. In particular, the short path length of the α-particle makes it attractive as a modality for the treatment of so-called "minimal disease", i.e. micro metastases and/or residual remnants after surgical removal of a primary tumour, hematological cancers, and various types of small-cell carcinomas. In addition, unlike other forms of radiation, α-particles have the ability to cause significant double-stranded breaks in Deoxyribonucleic Acid (DNA) which are more resistant to DNA repair mechanisms, leading to apoptotic cell death (see e.g. [POU2021, NEL2021, ROB2020, FRI2020, ROB2018, DUA2013], and references therein).

Alpha-emitting radionuclides with potential for TAT are few. The most commonly reported α-emitters for this purpose in the literature include ^{225}Ac, ^{213}Bi, ^{223,224}Ra, ^{212}Pb, ^{226,227}Th, ^{211}At, and ^{149}Tb (see e.g. [NEL2021, RAD2021, EYC2021, DUA2013]). Some α-emitters are provided by generators, e.g. ^{225}Ac/^{213}Bi and ^{230}U/^{226}Th generators, both of which can be produced by the proton bombardment of thorium (^{232}Th has a 100% natural abundance).

Alluded to in Chapter 1, a new generation of high-current, 70 MeV H^- cyclotrons is well suited to provide certain high-value, relatively long-lived radionuclides in bulk, such as ^{22}Na,

^{68}Ge, and ^{82}Sr. A question that has yet to receive a definitive answer is whether proton-activated thorium can efficaciously be included in the production programme at such a facility, mainly for supplying the ^{225}Ac/^{213}Bi generator, but possibly also the ^{230}U/^{226}Th generator. The current situation seems to be one where a large ^{225}Ac supply-and-demand mismatch is likely to continue well into the foreseeable future (see e.g. the review article by Engle [ENG2018]). Efforts by larger proton accelerators, in particular by a number of linear accelerators (linacs) with significant radionuclide production programmes, will likely reduce this mismatch but not completely satisfy the growing demand. Therefore, some scope may exist for certain smaller accelerators to also contribute to ^{225}Ac supply.

The main objective of the present study was to investigate the feasibility of including natural thorium targets in the production regimen of a 70 MeV H^- cyclotron facility that supports a dedicated radionuclide production programme. While this topic is already quite mature at higher proton energies, especially above 100 MeV, various aspects still require scrutiny at energies of 70 MeV and below. The quality of existing data was also deemed problematic at these lower energies due to sparseness and discrepancies. Therefore, new excitation functions were measured for Th+p reactions to augment rather sparse data and resolve existing discrepancies. The radionuclides of main interest from the perspective of this study are ^{225}Ac and ^{230}U, in particular for their respective roles in ^{225}Ac/^{213}Bi and ^{230}U/^{226}Th generators. Targeted alpha therapy (TAT) is an active area of research and radiopharmaceutical development, with the demand for ^{225}Ac, in particular, reported to far exceed its supply, thus hampering clinical trials (see e.g. [ROB2020, ROB2018, OSS2018, ENG2018]).

It has to be stressed that our main interest was to determine the feasibility of making ^{225}Ac/^{213}Bi generators for supporting a ^{213}Bi-based radiopharmaceutical programme, and not ^{225}Ac for direct application in an ^{225}Ac-based radiopharmaceutical programme. With thorium targetry, the latter is affected by a low level of the long-lived radio-contaminant ^{227}Ac ($T_{1/2}$ = 21.772 y). According to Robertson *et al.* [ROB2020], an acceptable limit for ^{227}Ac in ^{225}Ac-based TAT has yet to be established. While an ^{225}Ac product with a significantly reduced ^{227}Ac contamination level (by more than three orders of magnitude) can be obtained from a ^{225}Ra/^{225}Ac generator, this comes at the cost of a much lower yield, clearly well outside the scope of a 70 MeV cyclotron. This very important ^{227}Ac contamination issue, which is less important from the perspective of ^{225}Ac/^{213}Bi generators, will be discussed in more detail in Section 3.5. It is convenient, however, to introduce here a different notation for directly-produced ^{225}Ac and ^{225}Ac provided via a ^{225}Ra/^{225}Ac generator, as first introduced by Robertson *et al.* [ROB2020] at TRIUMF in Canada. According to this scheme, a thorium target is bombarded with protons, followed by a "first pass" radiochemical separation to isolate ^{225}Ac, which will also contain some unavoidable co-produced ^{227}Ac contaminant. This "first-pass" or "directly-produced" ^{225}Ac is denoted as ^{227,225}Ac†. After the separation of ^{227,225}Ac†, isotopes of Ra are separated in a "second pass" radiochemical separation, including ^{225}Ra, which feeds ^{225}Ac via beta decay. This "second-pass" or "generator-produced" ^{225}Ac is denoted as ^{225}Ac*.

We want to emphasize again that the ultra-pure ^{225}Ac* product cannot be obtained by means of a 70 MeV H^- cyclotron as the proton energy is too low. In fact, ^{225}Ac* is a topic for the next chapter (Chapter 4) of this thesis. While "standard purity" ^{227,225}Ac† produced by means of a

70 MeV H^- cyclotron may perhaps be suitable for direct application in humans, here we are more interested in its use in ^{225}Ac/^{213}Bi generators. This can be better explained by referring to the relevant part of the Chart of the Nuclides, reproduced with permission in Figure 3.1. As can be seen from the figure, the dominant mode of decay of ^{225}Ac is α-emission (near 100%). In contrast, the dominant mode of decay of ^{227}Ac is β^--emission (98.26%) with α-emission contributing only 1.38% of disintegrations. The dominant decay chain of ^{225}Ac proceeds via strong α-emitters: ^{225}Ac(100% α)$\rightarrow$^{221}Fr(100% α)$\rightarrow$^{217}At(99.99% α)$\rightarrow$^{213}Bi. In contrast, the strongest ^{227}Ac decay chain leading to Bi is weak: ^{227}Ac(1.38% α)$\rightarrow$^{223}Fr(0.006% α)$\rightarrow$^{219}At(100% α)$\rightarrow$^{215}Bi. Thus, feeding of Bi via ^{227}Ac decay is negligible, therefore any ^{227}Ac present on an ^{225}Ac/^{213}Bi generator is quite unimportant and can readily be tolerated.

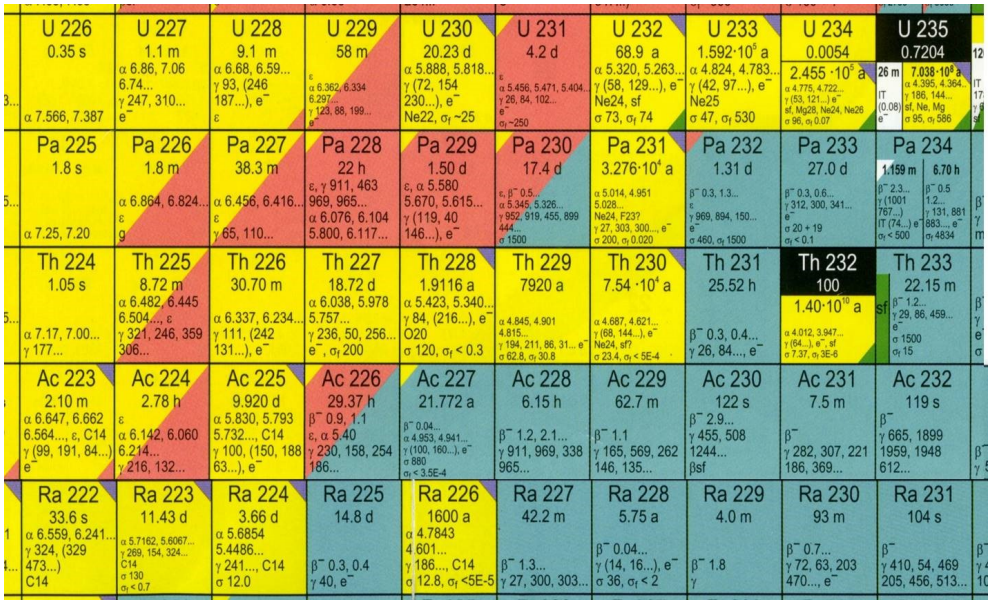


Figure 3.1: Relevant part of the Karlsruhe Chart of the Nuclides for ^{232}Th+p reactions leading to ^{225}Ac and ^{230}U. Black represents stable nuclides. Yellow represents α-decay. Blue represents β^-- decay. Red represents β^+-emission and electron capture decay modes. With permission © Nucleonica GmbH 2022.

A secondary objective of this series of stacked-foil experiments was to revisit the production of ^{22}Na by means of proton-induced reactions on natural magnesium. In this case, similarly, the existing excitation-function data for ^{nat}Mg+p exhibited some rather long-standing and quite large discrepancies. The main application of ^{22}Na is in positron sources for positron beam systems (see e.g. Krause-Rehberg *et al.* [KRA2004]). As already mentioned, ^{22}Na is an important radionuclide for iThemba LABS, regularly produced and exported. In this case ^{nat}Mg foils could easily be included in the relevant foil stacks without disturbing the main objectives of the study.

3.2 EXPERIMENTAL ASPECTS AND CONSIDERATIONS

3.2.1 Irradiations

Two foil stacks were irradiated with primary proton beams of nominally 40 and 66 MeV, delivered by the SSC. Each irradiation lasted 5 hours at a beam current of 50 nA. The stacks were activated six months apart to allow sufficient time for repeated counting of the relatively long-lived activation products of main interest. Both irradiations were performed in the RERAME

chamber (see Section 2.5). In addition to values derived from monitor reactions, the beam energies were also measured independently by means of a calibrated 90° analysis magnet. The requested beams from the cyclotron were for 40 and 66 MeV protons. The cyclotron staff performed the measurements with the analysis magnet and reported values of 40.0 ± 0.3 and 66.6 ± 0.5 MeV, henceforth referred to as the 40 and 66 MeV beams. Ideally we would have liked a 70 MeV beam instead of 66 MeV but the reality is that 66 MeV protons are routinely available for radionuclide production at iThemba LABS. This made it difficult to motivate for only a minor energy change to 70 MeV. Extrapolation of results to 70 MeV thus depended on trends exhibited by existing data as well as model calculations.

Each stack contained thirteen natural Th foils of 25 μm nominal thickness, 99.7% purity, supplied by Goodfellow, UK. All Th foils were sandwiched between 25 μm thick Kapton foils, which served as catchers for volatile reaction products, fission fragments, and recoil ions. This approach is similar to the approach by Weidner *et al.* [WEI2012a, WEI2012b] except that the Los Alamos team used Kapton tape, whereas in this work dry Kapton foils were used instead, joined only at the foil edges with small spots of adhesive. The method ensured that no adhesive was present in the path of the beam, which otherwise might have introduced layers of unknown thickness. We adopted this method as a precaution, taking into account that the present work entailed measurements at lower proton energies than the Weidner investigations, which would have resulted in larger energy losses in such layers and larger associated uncertainties. Behind each Th sandwich was placed a ^{nat}Mg foil of 50 μm nominal thickness (99.9% purity, Goodfellow, UK) and a series of monitor and degrader foils, which differed in the two stacks. In the 40 MeV stack, natural Cu and Ti foils served as monitors, interspersed with Al degrader foils of varying thicknesses to provide a data-point separation of approximately 2.5 MeV. The Cu foils of 50 μm nominal thickness, Ti foils of 25 μm nominal thickness, and Al foils with a range of thicknesses varying from 25 to 500 μm all had a specified purity of 99.9% or better, supplied by Goodfellow, UK. In the 66 MeV stack, some of the Al foils served as both degrader and monitor foils, again interspersed to provide a data-point separation of about 2.5 MeV. The areal thicknesses of individual foils were accurately determined by weighing.

3.2.2 Radionuclide assays

Starting a couple of days after EOB and continuing for several months after the activation of a stack, γ-ray spectra were measured off-line with a calibrated HPGe detector (from DSG Detector Systems, Germany) with a relative efficiency of 15% and a resolution of 1.8 keV FWHM at 1.33 MeV. The counting system consisted of a Canberra DSA 1000 multi-channel analyzer connected to a PC running the Canberra Genie 2000 analysis software. The foils were mounted on standard Al frames that fit accurately onto a custom-made source holder (see Section 2.6 for more detail). The same was done for standard calibration point sources of ^{60}Co, ^{133}Ba and ^{152}Eu, traceable to the National Institute of Standards and Technology (NIST) in the US. The Th and Kapton foils were not separated but counted as single Kapton-Th-Kapton source sandwiches. Not all the degrader Al foils were counted but only a selection that also served as monitors, in order to reproduce the relevant monitor excitation functions. All radionuclides of main interest formed in the Mg, Al, Cu and Ti foils could be identified and quantified from their

respective γ-ray emissions. For the Th foils, however, identification and quantification had to be performed based on the γ-ray emissions of daughter radionuclides in several cases.

Quantitative spectrometry of ^{225}Ac and ^{225}Ra was not possible via their respective characteristic γ-rays as these are quite weak, dominated by other strong γ-lines and the cumulative Compton background in the measured spectra. The 218.0 keV (11.44%) γ-line of the daughter nuclide ^{221}Fr could, however, be observed cleanly. Since ^{225}Ra feeds ^{225}Ac via 100% β^- decay and ^{225}Ac feeds ^{221}Fr via 100% α-decay, a decay-curve analysis of the ^{221}Fr activity could be performed to determine the $A = 225$ precursor yields. This required secular equilibrium of ^{221}Fr, which was assured as it has a relatively short half-life of 4.801 minutes.

The radionuclide ^{230}U is formed via the β^--decay of its precursor, ^{230}Pa, the latter of which is formed directly by the ^{232}Th(p,3n)^{230}Pa reaction. Thus, the relevant excitation function in this case is for the formation of ^{230}Pa.

3.2.3 Data analysis

The irradiations of both foil stacks were simulated with the Monte Carlo radiation transport code MCNP6 [GOO2012]. The geometry of each stack was modelled completely and an individual flux tally (so-called F4 tally) was defined on the volume suspended by each foil of interest, allowing the calculation of the proton energy distribution within a foil. The upper and lower energy limits as well as the discrete energy increment for each foil tally were individually tailored to capture the beam in an energy spectrum with sufficient detail. From the resulting energy distribution, the average energy, FWHM energy spread (caused by straggling) and correction factor for loss of protons via non-elastic nuclear interactions could be determined. Once this task was completed in a series of short test runs, a long run was performed with a particle history of 10×10^6 protons for each stack. This was sufficient to obtain good Monte Carlo event statistics. In these particular Monte Carlo runs the selected physics model was the Cascade-Exciton Model (CEM), which is the default of the MCNP6 code. All foils were modelled as squares with 25 mm widths and experimentally determined thicknesses, closely spaced in a stack. The beam was cylindrical with a 3 mm diameter, incident on the centre of the stack.

The simulation of an entire stacked-foil experiment in a single Monte Carlo run was not done before at iThemba LABS. A comparison was therefore made of the proton energies and beam attenuation factors associated with individual foils obtained by means of older deterministic calculations (i.e. with the in-house code STACK) with corresponding Monte Carlo results. As an example, the numerical values for Th foils in the 66 MeV stack are presented in Table 3.1. It is clear that the energy values are in good agreement within experimental uncertainties, including an incident beam-energy uncertainty of 0.5 MeV as supplied by the cyclotron staff. The attenuation of the beam at the depth of the last thorium foil (Th-13) is still less than 4%, thus the beam attenuation corrections are relatively small.

The effect of energy straggling is best illustrated by considering a monoenergetic incident beam, shown for selected thorium foils of the 66 MeV stack in Figure 3.2. For each foil the energy-bin size was adjusted in MCNP6 to capture the distribution in 200 bins. The widths of the distributions increase with penetration depth. It was found that even deep inside the stack (Th-13) the energy distribution was still very much Gaussian.

Table 3.1: Comparison of proton energies and beam attenuation factors associated with the Th foils in the 66 MeV stack, obtained from the code STACK and the Monte Carlo code MCNP6. (See Section 2.7 for definition of the notation.)

Foil	Code			
	STACK		MCNP6	
	E_j (MeV)	F_j	$E_j \pm \Delta E_j$ (MeV)	F_j
Th-1	66.88	0.9999	66.87 ± 0.50	0.9998
Th-2	64.50	0.9963	64.65 ± 0.52	0.9966
Th-3	62.05	0.9927	62.20 ± 0.55	0.9936
Th-4	59.82	0.9894	60.00 ± 0.57	0.9910
Th-5	57.53	0.9862	57.73 ± 0.60	0.9882
Th-6	55.18	0.9830	55.40 ± 0.62	0.9853
Th-7	52.74	0.9797	53.02 ± 0.65	0.9823
Th-8	50.52	0.9768	50.80 ± 0.67	0.9805
Th-9	48.22	0.9739	48.53 ± 0.71	0.9777
Th-10	45.85	0.9709	46.17 ± 0.72	0.9748
Th-11	43.76	0.9684	44.08 ± 0.75	0.9724
Th-12	41.61	0.9659	41.96 ± 0.76	0.9696
Th-13	39.35	0.9633	39.72 ± 0.81	0.9671

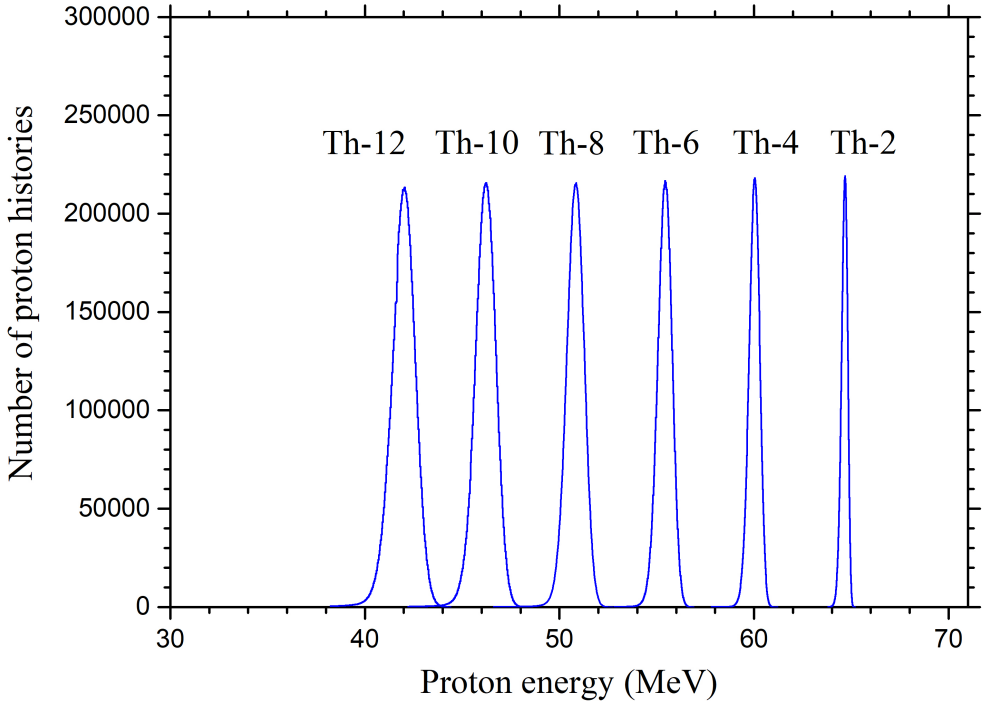


Figure 3.2: Energy distributions of protons in selected Th foils of the 66 MeV stack, obtained with the Monte Carlo code MCNP6. The number of particle histories was 10×10^6 in each case and the number of energy bins 200 for each distribution.

Cross sections were determined from the measured full-energy photopeak areas using the well-known activation equation, including corrections for decay during and after bombardment and during counting (see Section 2.7). The nuclear decay data used are presented in Table 3.2, taken from the NuDat 3.0 online library [SON2005].

Table 3.2: Decay data of investigated radionuclides[a].

Nuclide	Half-life	Decay mode	γ-rays (keV)	Intensity (%)
^{7}Be	53.22 d	ϵ: 100%	477.6035	10.44
^{22}Na	2.6018 y	EC + β^+: 100%	1274.537	99.94
^{24}Na	14.997 h	β^-: 100%	1368.626	99.9936
^{48}V	15.9735 d	EC + β^+: 100%	983.525	99.98
^{58}Co	70.86 d	EC + β^+: 100%	810.9593	99.45
^{62}Zn	9.186 h	EC + β^+: 100%	596.56	26.0
^{221}Fr	286.1 s	α: $\sim$100%; $\beta^- < 0.1\%$	218.0	11.44
^{225}Ac	9.920 d	α: 100%	–	–
^{225}Ra	14.9 d	β^-: 100%	–	–
^{230}Pa	17.4 d	ϵ: 92.2%; β^-: 7.8%; α: 0.0032%	951.88	29.6

[a]Taken from NuDaT 3.0 (http://www.nndc.bnl.gov/nudat2/). Checked for updates in August 2022.

The total uncertainties in the measured cross sections were obtained by summing all contributing uncertainties in quadrature. These values are expressed with a 1σ (68%) confidence level. In the majority of cases statistical uncertainties are negligible compared to systematic uncertainties except where the cross sections become very small, e.g. near reaction thresholds. The systematic uncertainties include an uncertainty in beam-current integration (3%), detector efficiency (5%), counting geometry (1%), and decay corrections (2%). An uncertainty of 3% was estimated for foil thickness except in the case of Mg, where the value was doubled to 6%. Whereas most of the foils appeared to have smooth, even surfaces, the Mg foils appeared more uneven due to surface imperfections. Results from the Mg foils also exhibited larger scatter compared to results from the other foils in the stacks.

For the 40 MeV stack the reactions ^{nat}Ti(p,x)^{48}V and ^{nat}Cu(p,x)^{62}Zn were chosen for monitoring purposes. The relevant cross sections extracted from the Ti and Cu monitor foils were compared with the IAEA-recommended reference cross sections (Hermanne *et al.* [HER2018]), downloaded from the IAEA-NDS Medical Portal (accessible via www-nds.iaea.org). The initial proton energies associated with the new measurements were adopted from the Monte Carlo simulation performed with a beam energy of 40.0 MeV. While the overall agreement was acceptable, there nevertheless appeared to be a small energy shift between the measured and reference data sets. A series of Monte Carlo simulations were subsequently performed with adjusted beam energies, by increments of 0.1 MeV or multiples of 0.1 MeV. The best overall agreement was obtained with a beam energy of 40.3 MeV, shown in Figures 3.3 and 3.4 for the two monitor reactions, respectively. A beam energy of 40.3 $\pm$ 0.3 MeV was therefore adopted for this experiment, which is marginally higher than the value of 40.0 $\pm$ 0.3 MeV obtained from the analysis magnet but still within the experimental uncertainty. Thus, the measured excitation functions of this study are presented with a true reference to the monitor excitation functions rather than the analysis-magnet values. As is evident from Figures 3.3 and 3.4, the general agreement between the IAEA reference values and our measured values is acceptable within experimental uncertainties.

In the case of the 66 MeV stack, the reaction ^{27}Al(p,x)^{22}Na (Hermanne *et al.* [HER2018]) was chosen for monitoring purposes as well as the ^{22}Na/^{7}Be cross-section ratio, the latter of which

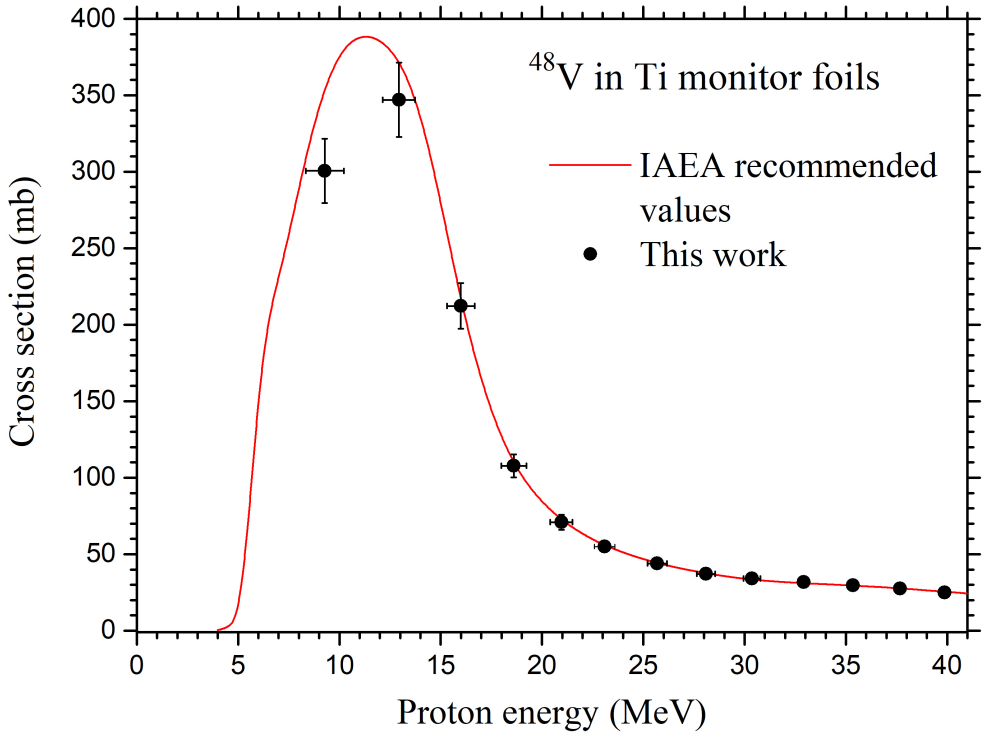


Figure 3.3: IAEA reference excitation function for the ^{nat}Ti(p,x)^{48}V reaction (Hermanne *et al.* [HER2018]) and corresponding cross sections measured in this study for monitoring the 40 MeV stack.

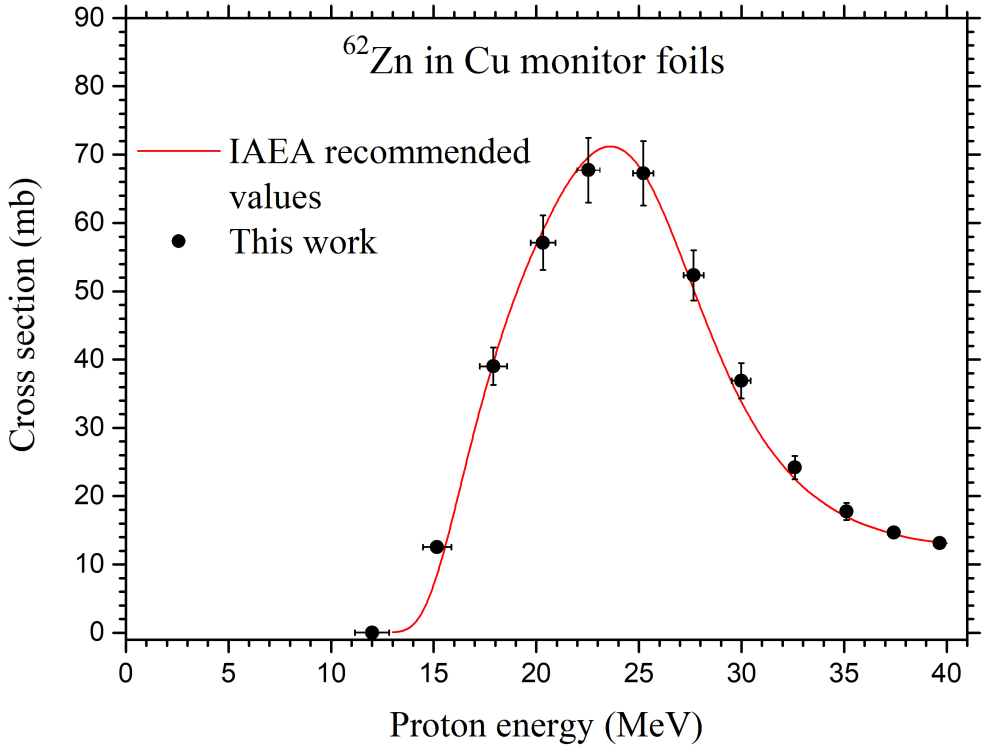


Figure 3.4: IAEA reference excitation function for the ^{nat}Cu(p,x)^{62}Zn reaction (Hermanne *et al.* [HER2018]) and corresponding cross sections measured in this study for monitoring the 40 MeV stack.

was shown in previous work to have particularly useful sensitivity in the proton-energy region 45–200 MeV (Szelecsényi *et al.* [SZE2017]). Similar to the 40 MeV stack, a series of Monte Carlo simulations were performed to determine the incident beam energy that best reproduces the reference excitation function, independent of the measurement with the analysis-magnet. The

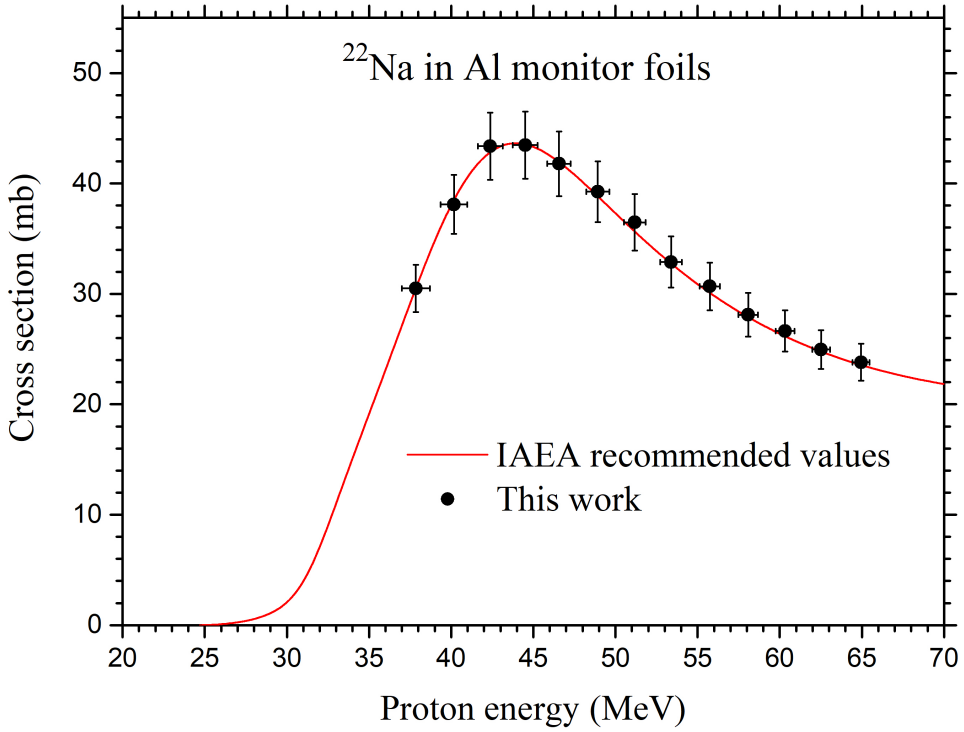


Figure 3.5: IAEA reference excitation function for the ^{27}Al(p,x)^{22}Na reaction (Hermanne *et al.* [HER2018]) and corresponding cross sections measured in this study for monitoring the 66 MeV stack.

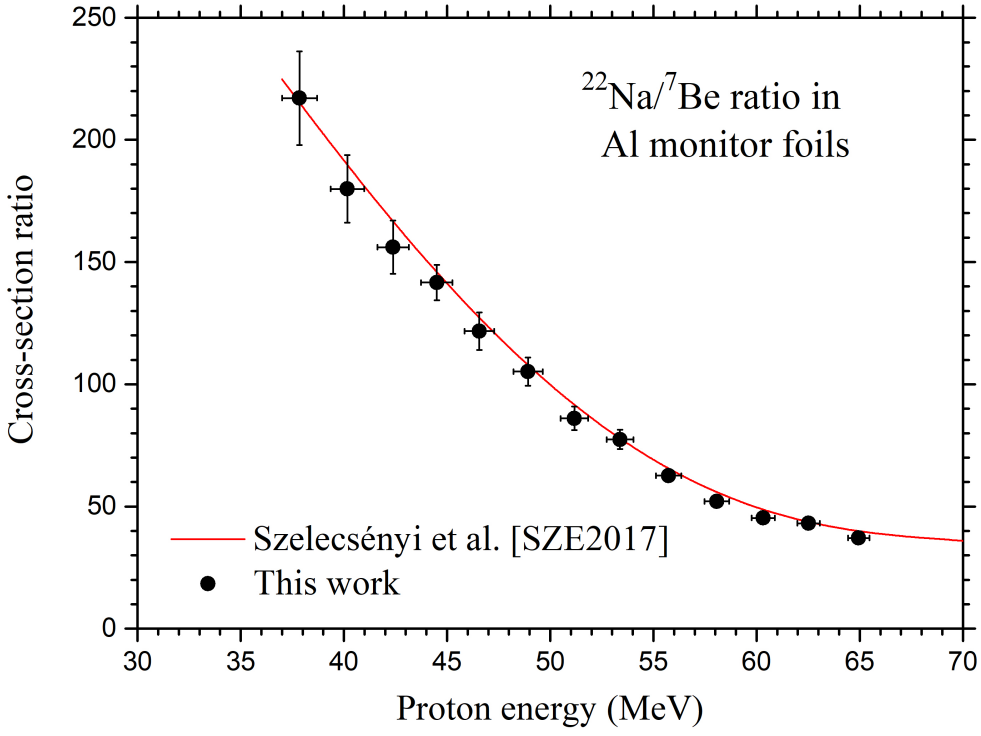


Figure 3.6: Cross-section ratio of ^{22}Na/^{7}Be in Al plotted versus proton energy, used as an additional monitor in the 66 MeV stack. Literature values are from Szelecsényi *et al.* [SZE2017].

best overall agreement was obtained with a beam energy of 67.0 MeV, shown in Figures 3.5 and 3.6 for ^{22}Na and the ^{22}Na/^{7}Be cross-section ratio in Al+p, respectively. A beam energy of 67.0 $\pm$ 0.5 MeV was therefore adopted, i.e. marginally higher than the value of 66.6 $\pm$ 0.5 MeV obtained from the analysis magnet. This situation is similar to the 40 MeV stack, i.e. for

both stacks the analysis-magnet values are marginally lower than values obtained from the monitor-foil analysis but by less than 1%, well within experimental uncertainties.

As already mentioned, cross sections and yields for the formation of ^{225}Ac and ^{225}Ra were determined from a decay-curve analysis of the measured activity of the daughter ^{221}Fr. This is the same approach as that of Weidner *et al.* [WEI2012a, WEI2012b] except that whereas those authors used a Markov chain Monte Carlo (MCMC) analysis with software that is not generally available, in this work a different strategy was pursued using commercially available software. Firstly, from existing data it was known that the formation cross sections of ^{225}Ra was unlikely to exceed 15% of that of ^{225}Ac in this energy region. Secondly, one could exploit the fact that for any given ^{225}Ra/^{225}Ac cross-section ratio the shape of the decay curve would be fixed. This means that for any given ^{225}Ra/^{225}Ac ratio, the corresponding ^{221}Fr decay curve can be represented by a shape function that contains no free parameters, multiplied by a single normalization factor that represents its source strength. For the purposes of this analysis, 31 such shape functions were established, for ^{225}Ra/^{225}Ac cross-section ratios ranging from 0 to 0.15 (or 0% to 15% ^{225}Ra relative to ^{225}Ac) in steps of 0.005 (i.e. 0.5% increments of ^{225}Ra relative to ^{225}Ac). These shape functions, together with a normalization factor as the only free parameter, were then incorporated as a set of user-defined functions in the automated curve fitting and equation discovery software TableCurve [SYS2020]. This entire set of functions could be fitted simultaneously, by means of the damped least-squares Levenberg-Marquardt algorithm of TableCurve, on a measured set of ^{221}Fr activities from the same source foil measured repeatedly over a period of approximately 60 days (i.e. ^{221}Fr activity as a function of time). The software would also automatically rank these 31 equations according to a selected goodness-of-fit criterion (e.g. the reduced chi-squared statistic amongst several others that are available). The premise was that the curve that fitted the measured decay-data best would provide a reasonable quantification of both the ^{225}Ra and ^{225}Ac content in that foil.

Growth-and-decay curves of ^{221}Fr from ^{225}Ra and ^{225}Ac decay were calculated numerically, including the bombardment period, using the actual bombardment conditions. This was done using a discrete time sequence, covering a period of 60 days in 5 sec intervals. Each of the 31 curves obtained in this way was normalized to unity at its maximum value, in order to represent a shape function. As a check, the decay part was also calculated analytically by solving the Bateman equation for the simple case of a chain of three isotopes, which agreed very well with the numerical approach. It was found that these curves could be well reproduced in TableCurve with 8-parameter Padé approximants. Finally, the set of user-defined functions contained 31 equations with the following form:

$$f(x) = A\left[\frac{a + cx + ex^2 + gx^3}{1 + bx + dx^2 + fx^3 + hx^4}\right], \tag{3.1}$$

where the independent variable x would be time, A is the only free parameter, while the coefficients a through h are constants determined by prior fitting of the numerically-derived shape functions in TableCurve. Figure 3.7 shows the reduced chi-squared statistic (χ^2_{red}) of the individual fits, plotted versus the ^{225}Ra/^{225}Ac ratio, for six of the Th foils. The minimum in each case represents the best fit. It is evident that the ^{225}Ra content is highest in the foil labelled Th-1, located at the high-energy side of the stack. The ^{225}Ra content systematically decreases

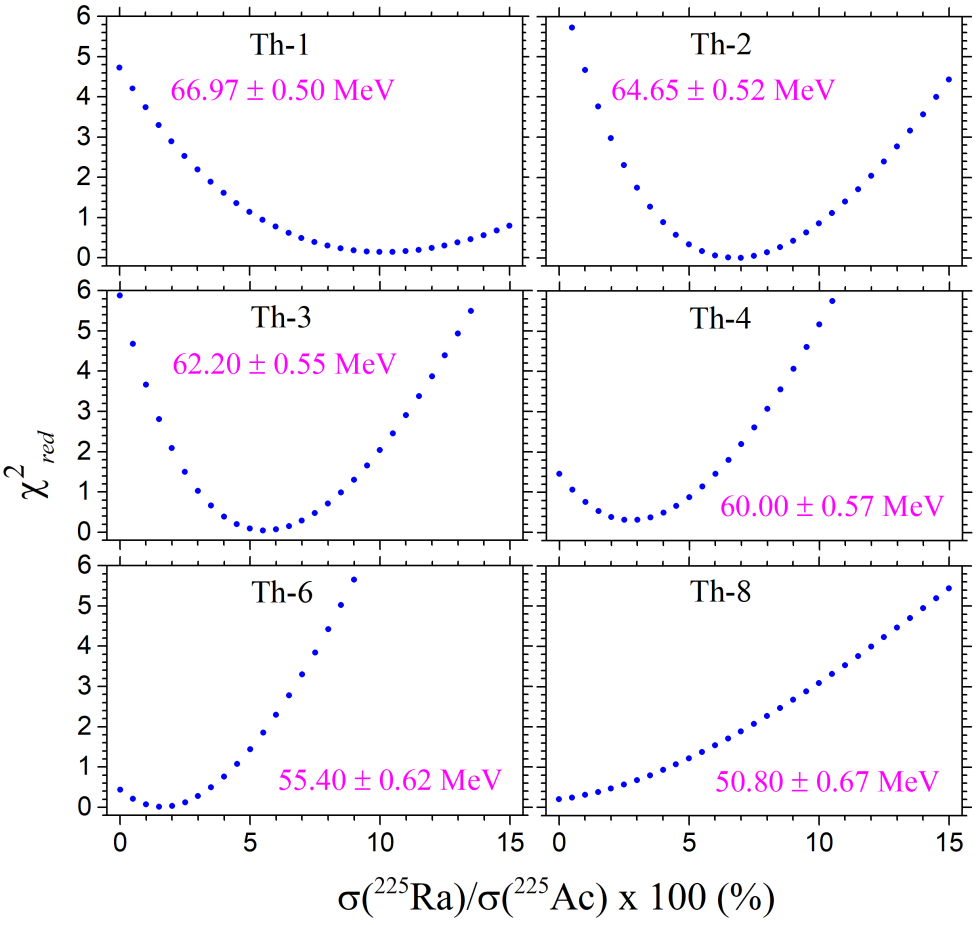


Figure 3.7: Reduced chi-squared statistic (χ^2_{red}) plotted versus the ^{225}Ra/^{225}Ac cross-section ratio for selected thorium foils of the 66 MeV stack. Each point represents the value of the goodness-of-fit criterion pertaining to a least-squares fit of a calculated decay curve on a set of ^{221}Fr daughter activities, measured repeatedly over a period of approximately 60 days (see text). The text in magenta indicates the associated proton energies of the foils obtained from the MCNP6 Monte Carlo simulation of the stack.

towards lower proton energies and is no longer observable in the foil labelled Th-8, thus only the seven foils at highest proton energies contained observable amounts of ^{225}Ra.

Two more points need to be mentioned concerning the least-squares fitting of Equation 3.1 on measured decay-curve data. Firstly, in order to assign equal significance to all measured values of a decay curve, inverse weighting was implemented. This was necessary because the values of measured yields spanned between one and two orders of magnitude. The default implementation in TableCurve is to make all weighting factors equal to 1, which in this case would have resulted in assigning more significance to data measured at earlier times. One is warned about this potential issue in the TableCurve manual [SYS2020] and suggested ways to address this. Secondly, the calculated decay curves (from which Equation 3.1 was obtained) can potentially be affected by precursors of ^{225}Ra, such as ^{225}Fr, which are also produced in ^{232}Th+p reactions. In fact, the ^{232}Th(p,2α)^{225}Fr reaction has a positive Q-value – that channel is open at all relevant energies. In practice, however, this is not an issue because ^{225}Fr has a much shorter half-life of only 4.77 minutes. It would have completely decayed to ^{225}Ra ($T_{1/2}$ = 14.6 d) by the time the spectra measurements commenced. Extracted cross sections for ^{225}Ra will therefore be cumulative. There is also evidence that ^{225}Fr yields would be small compared to ^{225}Ra yields at the relevant proton energies, to be discussed next.

3.3 RESULTS AND DISCUSSION

3.3.1 Excitation functions

The measured cross sections for ^{225}Ac, ^{225}Ra, and ^{230}Pa from ^{232}Th+p are presented in Table 3.3. The ^{225}Ac cross sections are compared with selected literature data sets in Figure 3.8. Our new data exhibit a well-delineated peak with a maximum at about 55 MeV and an effective threshold near 40 MeV. The values of Gauvin *et al.* [GAU1963] are consistently lower, in the region of the peak by more than a factor of 2. The most recent literature values are by Duchemin *et al.* [DUC2015] from a study that also investigated up to 70 MeV. These authors presented only four data points, with the two at lower energies in excellent agreement with the present results. Their data point closest to the peak region is higher than the trend of our data but still within their experimental uncertainty, while the value at highest energy seems to be higher and just outside the experimental uncertainty. The studies of Ermolaev *et al.* [ERM2012] and Weidner *et al.* [WEI2012b] were conducted at higher beam energies and the data shown constitute only the subsets of lowest values. The study by Weidner *et al.* [WEI2012b] presented eleven cross-section values below 200 MeV with only two values below 70 MeV. A point at 72.8 MeV has also been included in the figure as it is close enough to the present energy region of interest. Weidner's values at 72.8 and 64.9 MeV are in very good agreement with the trend of the present study. However, the value at their lowest energy, at 56.3 MeV, is well below the general trend for the peak region. At this energy the present study shows a still rising trend towards lower energies while Weidner's value seems to be dropping already towards the effective threshold,

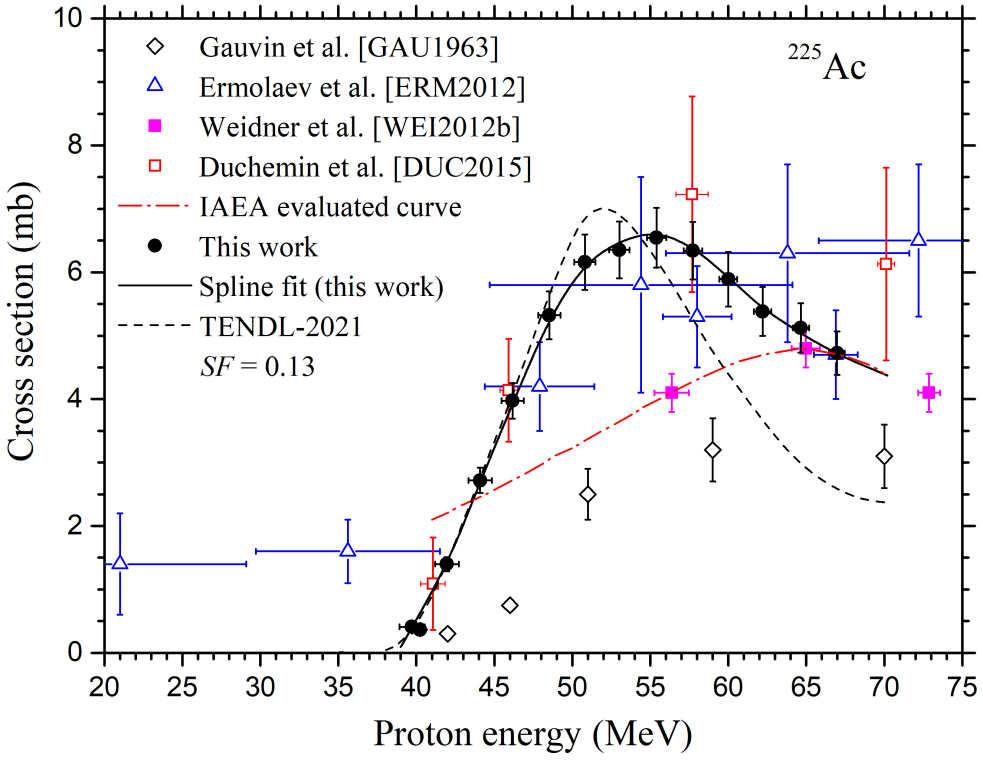


Figure 3.8: Cross sections for the formation of ^{225}Ac in the proton bombardment of ^{232}Th. Note that the TENDL-2021 values have been renormalized using a scale factor *SF* = 0.13. Literature values are from Gauvin [GAU1963], Ermolaev *et al.* [ERM2012], Weidner *et al.* [WEI2012b], and Duchemin *et al.* [DUC2015].

Table 3.3: Measured cross sections for formation of ^{225}Ac, ^{225}Ra, and ^{230}Pa in proton irradiation of ^{232}Th.

Proton energy (MeV)	Cross section (mb)		
	^{225}Ac	^{225}Ra	^{230}Pa
66.97 ± 0.50	$(4.73 \pm 0.34) \times 10^{+0}$	$(4.86 \pm 1.23) \times 10^{-1}$	$(1.78 \pm 0.12) \times 10^{+1}$
64.65 ± 0.52	$(5.12 \pm 0.39) \times 10^{+0}$	$(3.82 \pm 1.16) \times 10^{-1}$	$(1.87 \pm 0.13) \times 10^{+1}$
62.20 ± 0.55	$(5.38 \pm 0.39) \times 10^{+0}$	$(3.01 \pm 1.08) \times 10^{-1}$	$(2.00 \pm 0.14) \times 10^{+1}$
60.00 ± 0.57	$(5.89 \pm 0.43) \times 10^{+0}$	$(1.81 \pm 0.73) \times 10^{-1}$	$(2.16 \pm 0.15) \times 10^{+1}$
57.73 ± 0.60	$(6.34 \pm 0.45) \times 10^{+0}$	$(1.29 \pm 0.58) \times 10^{-1}$	$(2.05 \pm 0.14) \times 10^{+1}$
55.40 ± 0.62	$(6.55 \pm 0.47) \times 10^{+0}$	$(9.94 \pm 4.97) \times 10^{-2}$	$(2.26 \pm 0.16) \times 10^{+1}$
53.02 ± 0.65	$(6.35 \pm 0.45) \times 10^{+0}$	$(3.18 \pm 1.74) \times 10^{-2}$	$(2.33 \pm 0.16) \times 10^{+1}$
50.80 ± 0.67	$(6.16 \pm 0.44) \times 10^{+0}$	–	$(2.48 \pm 0.17) \times 10^{+1}$
48.53 ± 0.71	$(5.32 \pm 0.38) \times 10^{+0}$	–	$(2.62 \pm 0.18) \times 10^{+1}$
46.17 ± 0.72	$(3.97 \pm 0.28) \times 10^{+0}$	–	$(2.64 \pm 0.19) \times 10^{+1}$
44.08 ± 0.75	$(2.72 \pm 0.20) \times 10^{+0}$	–	$(2.81 \pm 0.20) \times 10^{+1}$
41.96 ± 0.76	$(1.40 \pm 0.11) \times 10^{+0}$	–	$(3.08 \pm 0.22) \times 10^{+1}$
40.25 ± 0.30	$(3.65 \pm 0.50) \times 10^{-1}$	–	$(3.23 \pm 0.23) \times 10^{+1}$
39.72 ± 0.81	$(4.11 \pm 0.63) \times 10^{-1}$	–	$(3.39 \pm 0.24) \times 10^{+1}$
38.06 ± 0.33	–	–	$(3.54 \pm 0.25) \times 10^{+1}$
35.74 ± 0.35	–	–	$(3.80 \pm 0.27) \times 10^{+1}$
33.30 ± 0.39	–	–	$(4.32 \pm 0.30) \times 10^{+1}$
30.74 ± 0.42	–	–	$(6.12 \pm 0.43) \times 10^{+1}$
28.50 ± 0.45	–	–	$(6.69 \pm 0.47) \times 10^{+1}$
26.11 ± 0.49	–	–	$(1.17 \pm 0.08) \times 10^{+2}$
23.54 ± 0.52	–	–	$(2.42 \pm 0.17) \times 10^{+2}$
21.41 ± 0.55	–	–	$(3.52 \pm 0.25) \times 10^{+2}$
19.12 ± 0.60	–	–	$(2.26 \pm 0.16) \times 10^{+2}$
16.54 ± 0.66	–	–	$(7.87 \pm 0.55) \times 10^{+1}$
13.63 ± 0.76	–	–	$(7.51 \pm 0.57) \times 10^{-1}$

also in contrast with Ermolaev's and Duchemin's data in this region. Several studies favour an effective threshold near 40 MeV except that of Ermolaev *et al.*, the latter of which found significant non-zero values as low down in energy as 21 MeV. Near 70 MeV, the present results are in agreement with Weidner while both Ermolaev and Duchemin found higher values, in good agreement with each other.

The discrepancies between the different data sets shown in Figure 3.8 are significant but not easy to explain. It is likely that the two data points of Ermolaev below the effective threshold near 40 MeV resulted from neutron activation of those foils as their primary beam energy was quite high (nominally 158 MeV), producing a significant forward flux of relatively high-energy neutrons from nuclear reactions upstream in the stack. Several neutron-induced reaction channels are open, e.g. ^{232}Th(n,5nt)^{225}Ac (Q = -33.426 MeV; E_{thres} = 33.571 MeV) according to the QCalc online Q-value calculator of Brookhaven National Laboratory (BNL) [PRI2016]. It is perhaps not a good idea to degrade a primary beam of that energy down to such low energies in one stack. It is important, however, to note that the concept of an "effective threshold" is quite arbitrary and purely based on observation. Various reaction channels leading to ^{225}Ra and ^{225}Ac are open at relatively low energies and the actual thresholds are much lower. Using the

QCalc online Q-value calculator, the following reaction channels were found to have the lowest thresholds for their formation: ^{232}Th(p,2ndα)^{225}Ra (Q = -10.961 MeV; E_{thres} = 11.008 MeV) and ^{232}Th(p,4nα)^{225}Ac (Q = -13.612 MeV; E_{thres} = 13.671 MeV). However, it appears that some reaction channels characterized by significant cluster emissions contribute minimally to the formation of those radioisotopes. Consistent with the results in the TENDL library, the production cross sections become significant at energies above the thresholds where more individual nucleons can emerge, e.g. ^{232}Th(p,6n2p)^{225}Ac (Q = -41.907 MeV; E_{thres} = 42.089 MeV).

Recently a Coordinated Research Project (CRP) of the IAEA published the results of cross-section evaluations for selected therapeutic radionuclides (Engle *et al.* [ENG2019]), the numerical values of which can be downloaded from the Medical Portal of the Nuclear Data Section (IAEA-NDS) website. The data for the ^{232}Th(p,x)^{225}Ac reaction from that evaluation are shown as a curve in Figure 3.8. The evaluators seem to have assigned considerably more weight to the values of Weidner *et al.* than any of the other data sets, especially in the energy region below 70 MeV. This is understandable, taking into consideration the large scatter in the data available to them. In this study, new integral yields were calculated based on a spline fit of the present results, also shown in the figure. Finally, the prediction from the TENDL-2021 library is shown for purposes of comparison after performing a renormalization (scale factor *SF* = 0.13) as these values are considerably higher than any measured values. A well-delineated peak is predicted with an effective threshold similar to our measurements, which is reassuring, although it is somewhat narrower. Note that these TENDL cross sections represent direct production pathways as well as a relatively small beta-decay contribution from ^{225}Th decay, the latter of which predominantly decays by alpha emission (90%). In the context of ^{225}Ac production, the focus of the majority of previous studies was more towards the higher energies, in particular the energy region 70–200 MeV, a discussion of which will be returned to later.

As can be seen from Table 3.3, the cross sections for formation of ^{225}Ra ($T_{1/2}$ = 14.9 d) are about an order of magnitude smaller than for ^{225}Ac ($T_{1/2}$ = 9.92 d) at the same energy. Thus, ^{225}Ra can at most contribute only a few percent to ^{225}Ac formation via its decay, also taking into account that the former has a larger half-life than the latter. The small ($<$ 1 mb) ^{225}Ra cross sections preclude production of ^{225}Ra/^{225}Ac generators, which has been alluded to earlier. It should also be noted that the data presented in Table 3.3 for ^{225}Ac do not contain contributions from ^{225}Ra decay due to the way the decay-curve analysis was performed.

The cross sections for the ^{232}Th(p,3n)^{230}Pa reaction of the present study are compared with selected literature values in Figure 3.9. The agreement between the different data sets is generally good, much improved compared to the ^{225}Ac case. The IAEA evaluated cross sections were adopted from threshold up to 30 MeV but between 30 and 70 MeV a new spline fit was performed. The IAEA evaluated data (Engle *et al.* [ENG2019]) only extend up to 40 MeV. It was found that the Padé fit by the evaluators do not reproduce their own selected data between 30 and 40 MeV very well, exhibiting a consistent underprediction that gets worse towards higher energies. The high-energy tail region of the excitation function is, admittedly, of less importance than the peak region when making yield estimates. By and large, for the majority of other radionuclides, the evaluated cross sections of Engle *et al.* are found to be based on excellent fits of the selected experimental cross-section data and this particular, somewhat

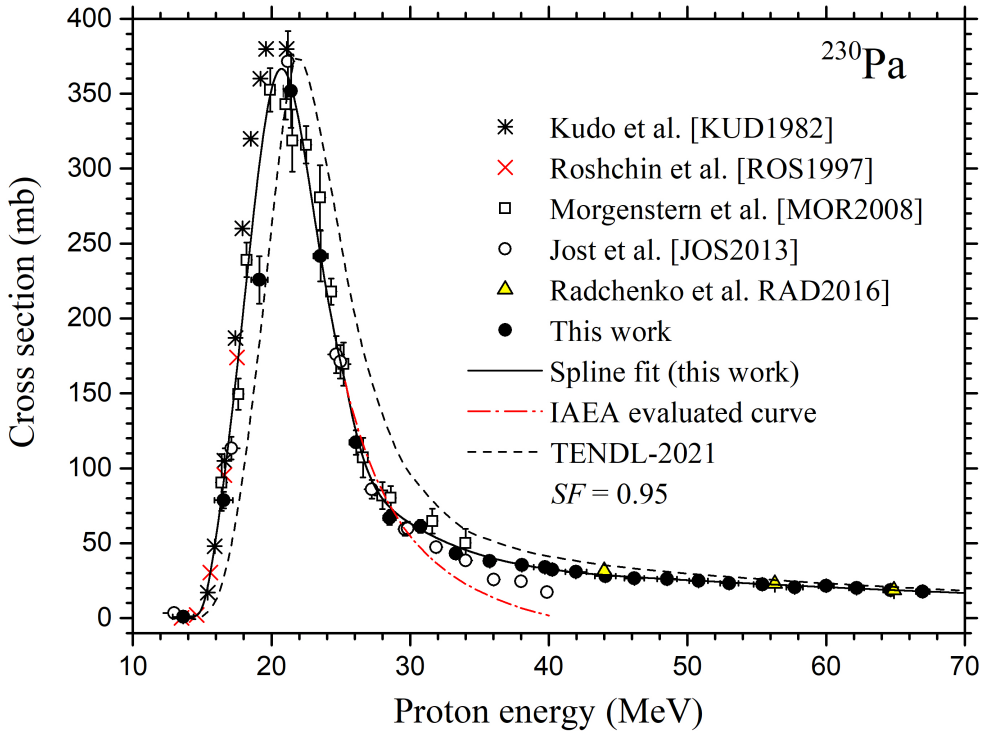


Figure 3.9: Cross sections for the formation of ^{230}Pa in the proton bombardment of ^{232}Th. Note that the TENDL-2021 values have been renormalized using a scale factor *SF* = 0.95. Literature values are from Kudo *et al.* [KUD1982], Roshchin *et al.* [ROS1997], Morgenstern *et al.* [MOR2008], Jost *et al.* [JOS2013], and Radchenko *et al.* [RAD2016].

poorer fit seems to be an isolated case. The TENDL-2021 prediction reproduces the shape of the experimental excitation function very well, in particular the effective threshold but the peak is somewhat shifted towards higher energies by about 2 MeV. For purposes of comparison, the TENDL values were renormalized (scale factor *SF* = 0.95) as these predictions are systematically higher than the experimental results by a small amount.

The measured cross sections of this work for ^{22}Na and ^{24}Na from ^{nat}Mg+p are presented in Table 3.4. Figure 3.10 shows the cross sections for the ^{nat}Mg(p,x)^{22}Na nuclear process. Magnesium has three stable isotopes, namely ^{24}Mg (78.99%), ^{25}Mg (10.00%), and ^{26}Mg (11.01%), according to which the TENDL-2021 cross sections for the individual target isotopes were weighed and summed incoherently. All experimental data sets show some scatter. The data set of Lagunas Solar *et al.* [LAG1990] has too much scatter to delineate the shape of the excitation function. The present measurements agree reasonably well with the values of Sisterson *et al.* [SIS1997] and Michel *et al.* [MIC1997]. The data of Lagunas Solar was disregarded for purposes of the spline fit but all other data were included. As before, this spline fit was used for calculating an integral-yield curve. The TENDL-2021 prediction reproduces the shape of the excitation function quite well but, once again, the absolute values are overpredicted. A renormalization was therefore performed for purposes of comparison (scale factor *SF* = 0.66).

Cross sections for ^{24}Na formation were also extracted from the measured Mg spectra, presented in Figure 3.11 as a side result. Similar to the ^{22}Na case, the data of Lagunas Solar *et al.* have too much scatter to delineate the shape of the excitation function. The other data exhibit good agreement. Without the need for any renormalization, the TENDL-2021 prediction reproduces both the shape and absolute magnitude of the excitation function quite well.

Table 3.4: Measured cross sections for formation of ^{22}Na and ^{24}Na in proton irradiation of ^{nat}Mg.

Isotope (MeV)	Cross section (mb)	
	^{22}Na	^{24}Na
66.78 ± 0.50	$(5.81 \pm 0.50) \times 10^{+1}$	$(6.27 \pm 0.54) \times 10^{+0}$
64.46 ± 0.53	$(5.95 \pm 0.51) \times 10^{+1}$	$(6.61 \pm 0.57) \times 10^{+0}$
62.00 ± 0.55	$(6.57 \pm 0.56) \times 10^{+1}$	$(7.23 \pm 0.62) \times 10^{+0}$
59.81 ± 0.57	$(6.47 \pm 0.56) \times 10^{+1}$	$(7.02 \pm 0.61) \times 10^{+0}$
57.54 ± 0.60	$(6.85 \pm 0.59) \times 10^{+1}$	$(7.36 \pm 0.63) \times 10^{+0}$
55.21 ± 0.62	$(6.85 \pm 0.59) \times 10^{+1}$	$(7.53 \pm 0.65) \times 10^{+0}$
52.77 ± 0.65	$(7.10 \pm 0.61) \times 10^{+1}$	$(8.07 \pm 0.70) \times 10^{+0}$
50.56 ± 0.67	$(7.42 \pm 0.64) \times 10^{+1}$	$(8.34 \pm 0.72) \times 10^{+0}$
48.28 ± 0.71	$(7.60 \pm 0.65) \times 10^{+1}$	$(8.10 \pm 0.70) \times 10^{+0}$
45.93 ± 0.71	$(7.82 \pm 0.67) \times 10^{+1}$	$(8.44 \pm 0.73) \times 10^{+0}$
43.84 ± 0.75	$(7.82 \pm 0.67) \times 10^{+1}$	$(8.32 \pm 0.72) \times 10^{+0}$
41.73 ± 0.76	$(7.67 \pm 0.66) \times 10^{+1}$	$(8.25 \pm 0.71) \times 10^{+0}$
39.87 ± 0.30	$(6.98 \pm 0.60) \times 10^{+1}$	$(7.33 \pm 0.63) \times 10^{+0}$
39.44 ± 0.81	$(6.95 \pm 0.60) \times 10^{+1}$	$(7.86 \pm 0.68) \times 10^{+0}$
37.67 ± 0.33	$(6.49 \pm 0.56) \times 10^{+1}$	$(7.20 \pm 0.62) \times 10^{+0}$
35.35 ± 0.36	$(5.11 \pm 0.44) \times 10^{+1}$	$(6.52 \pm 0.56) \times 10^{+0}$
32.92 ± 0.39	$(3.53 \pm 0.30) \times 10^{+1}$	$(5.80 \pm 0.50) \times 10^{+0}$
30.36 ± 0.42	$(2.42 \pm 0.21) \times 10^{+1}$	$(5.48 \pm 0.47) \times 10^{+0}$
28.09 ± 0.45	$(1.53 \pm 0.13) \times 10^{+1}$	$(5.55 \pm 0.48) \times 10^{+0}$
25.68 ± 0.48	$(9.92 \pm 0.87) \times 10^{+0}$	$(5.36 \pm 0.46) \times 10^{+0}$
23.09 ± 0.51	$(7.39 \pm 0.64) \times 10^{+0}$	$(4.61 \pm 0.40) \times 10^{+0}$
20.96 ± 0.55	$(5.45 \pm 0.49) \times 10^{+0}$	$(3.29 \pm 0.28) \times 10^{+0}$
18.61 ± 0.62	$(5.38 \pm 0.49) \times 10^{+0}$	$(1.59 \pm 0.14) \times 10^{+0}$
15.99 ± 0.68	$(9.61 \pm 0.84) \times 10^{+0}$	$(2.39 \pm 0.21) \times 10^{-1}$
12.94 ± 0.80	$(1.09 \pm 0.10) \times 10^{+1}$	$(4.87 \pm 0.43) \times 10^{-2}$
9.28 ± 0.93	$(6.58 \pm 0.60) \times 10^{+0}$	–
5.87 ± 1.35	$(6.23 \pm 0.56) \times 10^{-1}$	–

In Figures 3.9 and 3.10 we compared our new measurements with cross sections by authors who published not earlier than 1990. There are limited older data from the Fifties to the Seventies that were not included, mainly as the larger comparison is a bit messy and not very helpful. The decision was therefore made to do the comparison with results of measurements from the later era only, when high-resolution HPGe detectors became commercially available.

3.3.2 Integral yields

Thick-target yields for ^{225}Ac and ^{22}Na production have been calculated based on the spline fits on the experimental data shown in Figures 3.8 and 3.10, respectively. These are deliberately plotted on the same graph in Figure 3.12 to illustrate that a very similar value of just above 1.3 MBq/μAh is obtained for both radionuclides at 70 MeV, albeit the curves have different trends due to different effective thresholds. In our opinion, this result requires some pause for

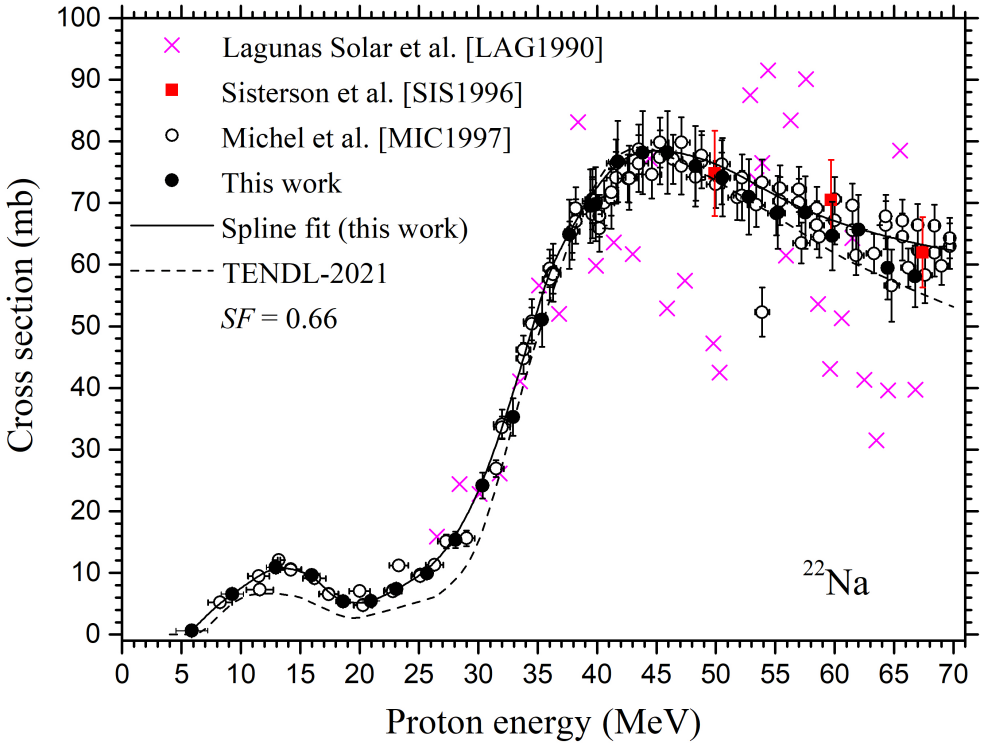


Figure 3.10: Cross sections for the formation of ^{22}Na in the proton bombardment of ^{nat}Mg. Note that the TENDL-2019 values have been renormalized, using a scale factor *SF* = 0.66. Literature values are from Lagunas-Solar and Carvacho [LAG1990], Sisterson *et al.* [SIS1997], and Michel at al. [MIC1997].

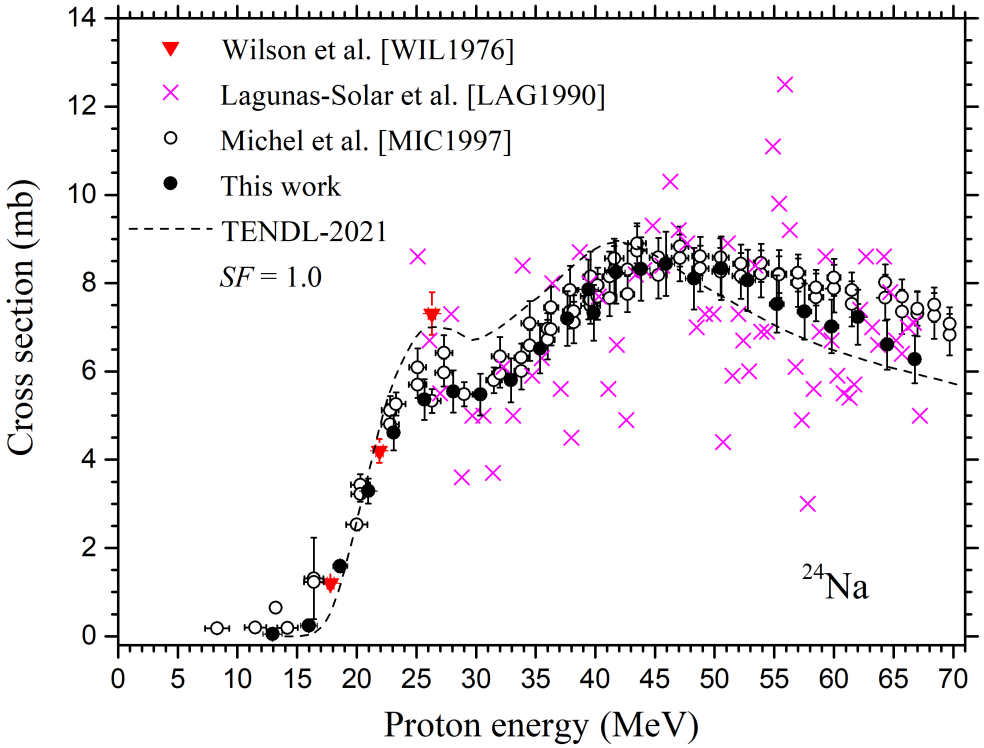


Figure 3.11: Cross sections for the formation of ^{24}Na in the proton bombardment of ^{nat}Mg. Note that the TENDL-2019 values have not been renormalized. Literature values are from Wilson *et al.* [WIL1976], Lagunas-Solar and Carvacho [LAG1990], and Michel at al. [MIC1997].

consideration. Both Ermolaev *et al.* [ERM2012] and Duchemin *et al.* [DUC2015] commented on the low yield at an energy of 70 MeV and below. Duchemin at al. expressed the view that

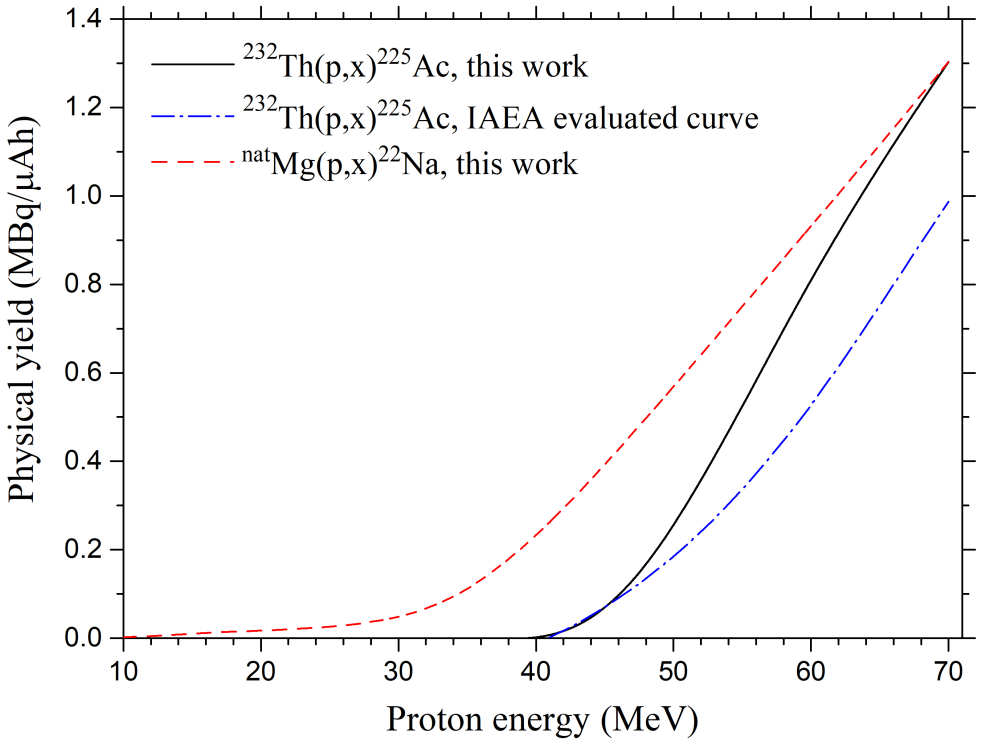


Figure 3.12: Integral physical yields for the production of ^{225}Ac and ^{22}Na in the proton bombardment of ^{232}Th and ^{nat}Mg, respectively.

^{225}Ac production "will be interesting only with accelerators able to deliver protons with an energy higher than 100 MeV". This latter view was expressed based on their own investigation at 70 MeV. The opinion that we came to is that, while the ^{225}Ac yield with 70 MeV protons is admittedly quite low, it is not too low for production purposes. In support of this view, it should be noted that iThemba LABS has been producing Ci quantities of ^{22}Na per annum via the bombardment of ^{nat}Mg targets with 66 MeV protons over the last two decades, despite the low yield. Similar Ci quantities can be obtained for ^{225}Ac, as clearly depicted by Figure 3.12. Small cross sections can be overcome by the bombardment of high-performance targets with high-intensity beams, which modern cyclotrons can ably deliver (e.g. targets that can withstand extended bombardments with beam powers of 15 kW or more).

Any counter arguments on ^{225}Ac production at a 70 MeV cyclotron facility should be made based on its final use, scale of production, and perceived importance. Robertson [ROB2018] reported a world-wide supply of ^{225}Ac of less than 2 Ci per annum in 2018, a situation which has probably not changed significantly to date. A review on viable methods of production by Engle [ENG2018] reported a similar annual yield, describing a difficult landscape from a production point of view, concluding that global supply of ^{225}Ac will likely continue to be sourced from a patchwork of production methods and laboratories. While difficult to predict future demand, Robertson *et al.* estimate a quantity of 5–10 Ci per annum for each ^{225}Ac-based therapy that is approved for clinical use, and should the development of ^{213}Bi-radiopharmaceuticals also increase, the demand can be considerably higher. Clearly, 70 MeV cyclotrons cannot contribute on a large scale to alleviate the overall ^{225}Ac demand shortage but can make a contribution, especially to the ^{213}Bi supply. There are caveats, however, such as the sourcing of the Th target material and availability of sufficient processing hot-cell facilities. Thorium supply should

not, in principle, be a major problem as it has a geochemical concentration of between 3 and 4 times higher than uranium in the Earth's crust, roughly 60% the abundance of lead (see e.g. IAEA-TECDOC-1877 [IAEA2019]). According to this IAEA report, South Africa has total thorium stockpiled reserves of about 15 000 tons.

Figure 3.12 also shows the IAEA evaluated thick-target yield curve (Engle *et al.* [ENG2019]) which is expected to have a smaller slope, reaching a value of about 1 MBq/μAh at 70 MeV. Duchemin *et al.* [DUC2015] reported a value of 1.6 MBq/μAh at 70 MeV, thus the 1.3 MBq/μAh found in the present study lies in-between.

Thick-target yields for the ^{232}Th(p,3n)^{230}Pa reaction are shown in Figure 3.13. The curve of this study is the same as the IAEA evaluated curve from threshold to 30 MeV, then deviating with a higher trend towards higher energies. The IAEA evaluation only extends to 40 MeV.

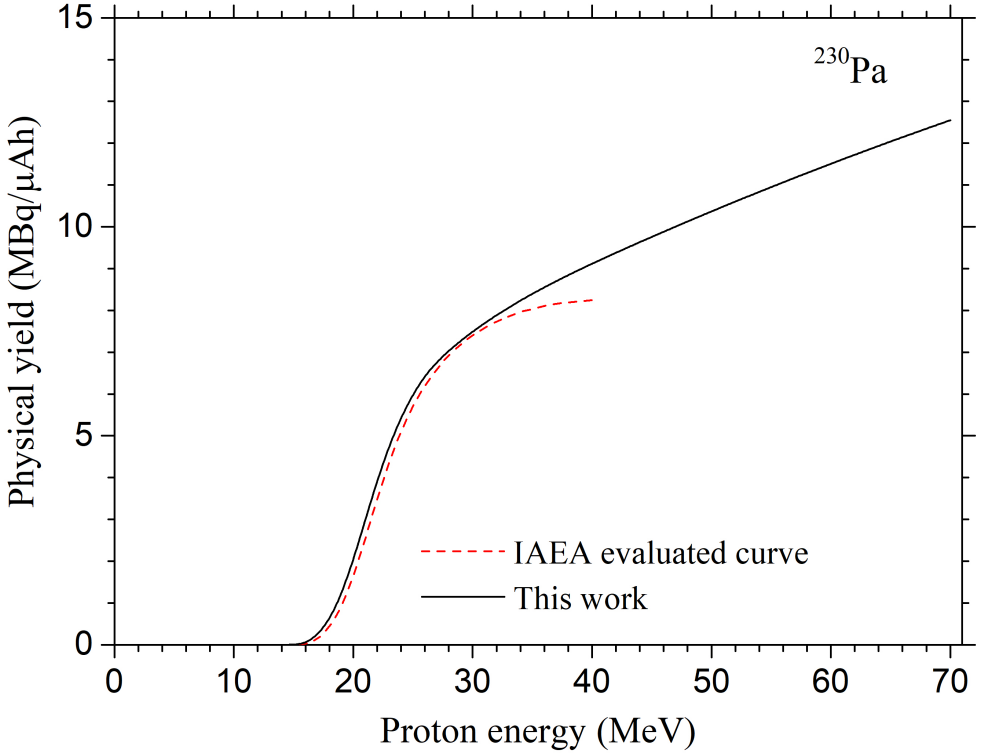


Figure 3.13: Integral physical yields for the production of ^{230}Pa in the proton bombardment of ^{232}Th. Note that the IAEA evaluated curve is shifted marginally towards higher energies for purposes of display as the two curves would otherwise largely overlap below 30 MeV.

3.4 TARGETRY

Two tandem-target configurations that are routinely utilized at iThemba LABS for large-scale productions are ^{nat}Mg/^{nat}Ga (for ^{22}Na/^{68}Ge) and ^{nat}Rb/^{nat}Ga (for ^{82}Sr/^{68}Ge). Currently these targets are bombarded with 66 MeV protons and beam currents typically in the range 200–250 μA. Similar targetry is envisaged for the new 70 MeV cyclotron facility, albeit scaled up for the modest increase in beam energy but also to accommodate higher beam intensities. Routine bombardments with 70 MeV proton beams of 300 μA (or even higher) seem feasible. The tandem-target concept has already been described in Section 2.2 and a schematic diagram presented in Figure 2.3. The feasibility of introducing Th targets into such a production scheme

at a 70 MeV cyclotron facility remains to be answered. In this investigation we were primarily interested in six combinations of tandem targets, namely those with ^{nat}Mg, ^{nat}Rb or ^{232}Th in the higher-energy window and either ^{nat}Ga or ^{232}Th in the lower-energy window.

It is useful to compare actual production yields from such targets, as predicted by the available nuclear data, for the relevant radionuclides. The IAEA recently published new evaluated cross sections and physical yields for the ^{nat}Rb(p,x)^{82}Sr and ^{nat}Ga(p,x)^{68}Ge reactions (Tárkányi *et al.* [TAR2019]) which have been adopted in this study. Two specific energy windows of $0 \rightarrow 26$ MeV and $38 \rightarrow 62$ MeV have been selected together with a 70 MeV incident proton beam. The significance of these two energy windows is that they represent the case where the thermal loads on the two targets are practically the same, i.e. balanced, taking also into account the energy loss in the target capsule walls of 0.5 mm thickness (which is quite similar whether the material is stainless steel, Inconel or niobium). The energy loss on both encapsulated targets will be close to 31 MeV in this case. It should be noted that one usually cannot exploit the full beam energy due to various dead layers in a real target system, e.g. from windows, capsule walls and cooling-water layers. Figure 3.14 shows the fitted or evaluated curves of the relevant excitation functions on the same plot. The appropriate energy window for each produced radionuclide is the one containing the maximum of the excitation function in all cases. For purposes of comparison, a 24-hour bombardment at a beam current of 250 μA was selected. The resulting physical yields and end-of-bombardment (EOB) production yields, the latter of which took decay during the bombardment period into account, are presented in Table 3.5.

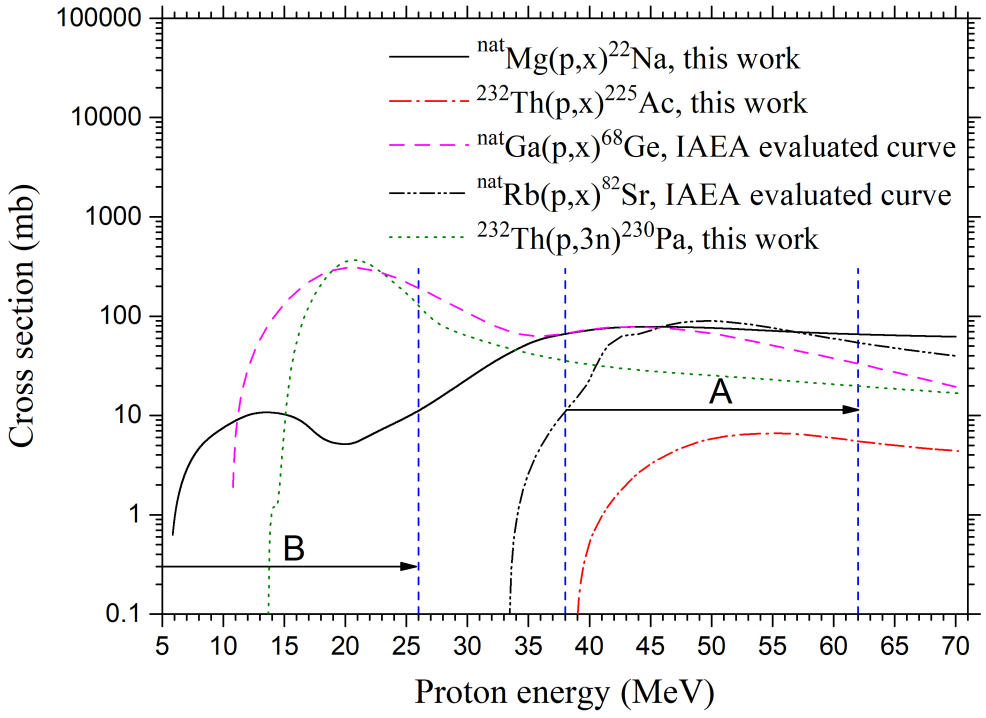


Figure 3.14: Fitted and/or evaluated excitation functions for the reactions ^{nat}Mg(p,x)^{22}Na, ^{232}Th(p,x)^{225}Ac, ^{nat}Ga(p,x)^{68}Ge, ^{nat}Rb(p,x)^{82}Sr, and ^{232}Th(p,3n)^{230}Pa. A and B denote the higher and lower energy windows (also called energy slots), respectively.

Interestingly, for three of the five radionuclides in Table 3.5 the physical yield is of the order of 1 MBq/μAh (^{22}Na, ^{68}Ge and ^{225}Ac) which, admittedly, is rather low. Yet the production

Table 3.5: Yields of radionuclides considered for tandem targetry at a 70 MeV cyclotron facility.

Nuclide	Target material	Energy window (MeV)	Target mass[a] (g)	Physical yield (MBq/μAh)	Production yield[b] (MBq ; mCi)
^{22}Na	^{nat}Mg	A (38 $\rightarrow$ 62)	51.1	0.826	4954.4 ; 133.9
^{68}Ge	^{nat}Ga	B (0 $\rightarrow$ 26)	24.7	1.14	6831.3 ; 184.6
^{82}Sr	^{nat}Rb	A (38 $\rightarrow$ 62)	67.3	10.69	63270.7 ; 1710.1
^{225}Ac	^{232}Th	A (38 $\rightarrow$ 62)	89.1	0.917	5314.2 ; 143.6
^{230}Pa	^{232}Th	B (0 $\rightarrow$ 26)	39.6	6.42	37739.3 ; 1020.0

[a]Assuming a target diameter of 52 mm (nominally 2 inches).
[b]For a 24-hour bombardment with a beam current of 250 μA.

yields at EOB after a 24-hour bombardment are significant, all well above 100 mCi. The produced activity is enough for two Krause-Rehberg type ^{22}Na positron sources or for two ^{225}Ac/^{213}Bi generators. The expected ^{225}Ac yield is even slightly higher than the ^{22}Na yield. One can conclude that a regular producer of ^{22}Na and ^{68}Ge should not find the inclusion of ^{225}Ac/^{213}Bi generators in their production programme a daunting task, at least not from a production-rate point of view. There are several caveats, however, e.g. a clean separation of the Ac from the Th target matrix as well as a plethora of co-produced radio-contaminants. The latter include several fission fragments with similar chemical properties to Ac (see e.g. Engle *et al.* [ENG2014a]). In his review article, Engle [ENG2018] also commented on factors referred to as "logistical hardships", e.g. the use of a controlled nuclear material, its availability, various radiological and logistical challenges, etc. Very relevant to some potential producers may be a transport issue, should target processing have to be performed at another location than where the targets are bombarded. It is also possible that the type of radiation waste produced has to be stored at a location significantly distant from that of the accelerator.

In Table 3.5 a 24-hour bombardment was considered for purposes of comparison but often, for the routine production of those relatively long-lived radionuclides, the bombardment will be over several days. Multi-day bombardments can produce Ci-quantities of all those radionuclides. For ^{22}Na and ^{68}Ge this has been done at iThemba LABS for many years.

The interest in ^{230}Pa is because of its role as a precursor for ^{230}U (see e.g. Friend *et al.* [FRI2020]). Unfortunately, its β^- branching ratio is only 7.8%. Assuming the Pa separation is performed just after EOB, the ^{230}U yield from ^{230}Pa decay will reach a maximum after 27.5 days from EOB, a point in time where the ^{230}U activity will only be 2.62% of the EOB ^{230}Pa yield. The 24-hour bombardment described above will, therefore, only produce 988.8 MBq (25.7 mCi) of ^{230}U. Morgenstern *et al.* [MOR2008] described a similar production in a 50-hour bombardment, 200 μA beam, with an energy window of 0 $\rightarrow$ 33.5 MeV resulting in a yield of 2.37 GBq (64 mCi) ^{230}U 28 days after EOB. An estimate for that case using the data of the present study corroborated that result to within 3%, i.e. within experimental uncertainties. This level of yield, while admittedly quite low, is nevertheless considered by Morgenstern and co-workers to be clinically relevant. The final ^{230}U product is also of very high radionuclidic quality, carrier-free for all practical purposes. Productions of several hundred mCi ^{230}Pa can be performed, taking into account that single bombardments with an accumulated charge in the region of 20 000 to

50 000 μAh, or even higher, are quite common at facilities that produce such relatively long-lived radionuclides on a large scale (such as iThemba LABS).

Table 3.5 also shows the corresponding target masses for thermally-balanced energy windows, assuming a target diameter of 52 mm. These are typical target sizes at facilities that produce those particular radionuclides in bulk. Indeed, such massive targets are routinely processed at several laboratories across the world. As thorium is quite abundant and not prohibitively expensive, irradiated target material does not have to be recycled and re-used.

To conclude this section, it may be mentioned that the balancing of the thermal loads on the two targets is not a hard requirement. Individual targets in a tandem configuration can be fine-tuned to have a different ratio, within limits. If the main aim is ^{230}Pa production, one might consider increasing the upper-energy value of the lower-energy window to increase its yield. A thermal balance, however, always remains a good approach.

3.5 COMMENTS ON ACTINIUM-227 CONTAMINATION

Returning to the matter of ^{227}Ac contamination of ^{225}Ac produced via Th+p reactions, it is fortunate that a thorough evaluation of the relevant ^{227}Ac cross sections has recently been published by Engle *et al.* [ENG2019] from threshold up to 200 MeV. The numerical data of these cross sections as well as the associated integral yields can be downloaded from the Medical Portal of the IAEA-NDS website (www-nds.iaea.org). This allowed us to evaluate the ^{227}Ac/^{225}Ac yield ratio for various energy windows, using the new ^{225}Ac data of this work up to 70 MeV in conjunction with the existing IAEA-NDS evaluated data between 70 and 200 MeV.

In Figure 3.15 the physical-yield ratio of ^{227}Ac to ^{225}Ac, expressed as a percentage, is plotted

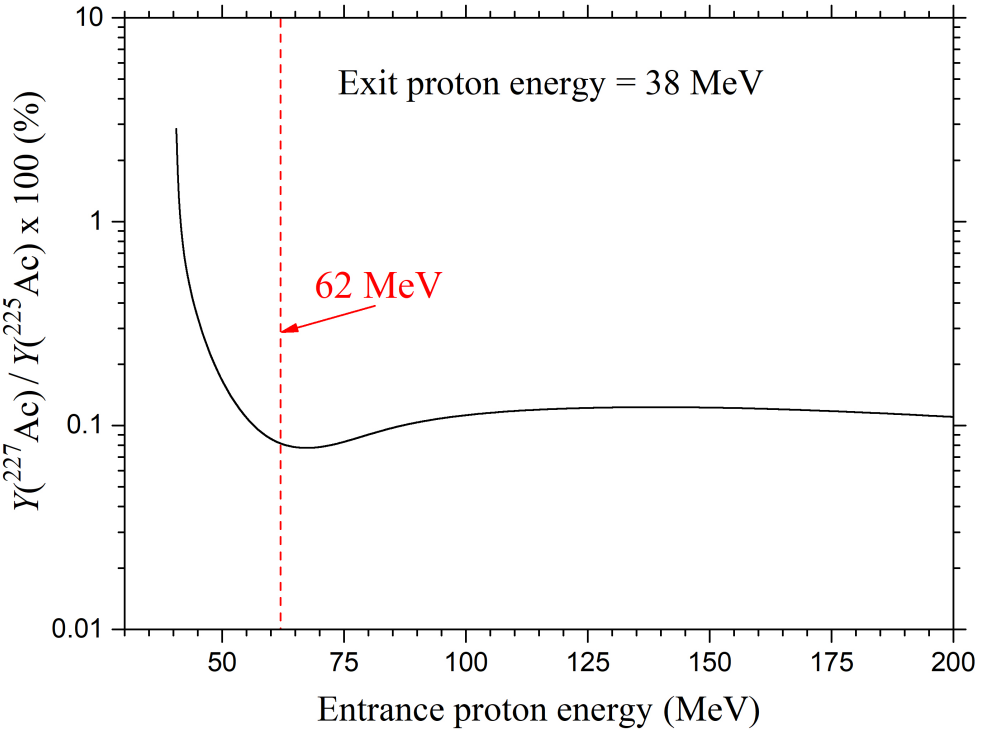


Figure 3.15: Physical-yield ratio of ^{227}Ac to ^{225}Ac, expressed as a percentage, as a function of entrance proton energy for the case of an exit proton energy of 38 MeV. Note that the suggested energy window for ^{225}Ac production on a Th target is 62 $\rightarrow$ 38 MeV in this study.

versus entrance proton energy for the case of an exit proton energy of 38 MeV (i.e. just below the effective ^{225}Ac formation threshold) on a thorium target. The resulting curve is rather flat and featureless over a large part of the energy region, from about 50 to 200 MeV, with a value of the order of 0.1%. Below 50 MeV the ^{227}Ac contamination level increases sharply.

Ermolaev *et al.* [ERM2012] made a statement that in addition to a low ^{225}Ac yield at energies below 70 MeV, the contamination level by co-produced, long-lived ^{227}Ac ($T_{1/2}$ = 21.772 a) will become unacceptably high. Below about 50 MeV their statement is true. However, the outlook seems much more positive with an entrance energy between 60 and 70 MeV. Table 3.6 presents the expected ^{227}Ac impurity level relative to the ^{225}Ac activity in a Th target at the end of a 24-hour bombardment, for selected energy windows up to 200 MeV. These energy windows have similar width but different entrance and exit energies, in order to compare the proposed energy window of $38 \rightarrow 62$ MeV with other possibilities over the full energy region up to 200 MeV. It is evident that the level of the ^{227}Ac contaminant is similar for all the energy windows and, for the $38 \rightarrow 62$ MeV energy window, even marginally better than at higher energies.

From the perspective of ^{225}Ac/^{213}Bi generators, it should be noted that there is no significant feeding of any Bi nuclides from ^{227}Ac decay, both because of its long half-life and very small cumulative α-decay branching ratio to relatively short-lived ^{215}Bi ($T_{1/2}$ = 7.6 m) of only 7.75×10^{-5}%. The presence of ^{227}Ac is not expected to affect the efficacy of an ^{225}Ac/^{213}Bi generator.

Table 3.6: ^{227}Ac impurity level in a Th target (as a percentage of the ^{225}Ac activity) at the end of a 24-hour bombardment, for selected energy windows.

Entrance energy (MeV)	Exit energy (MeV)	^{227}Ac impurity (%)
200	175	0.096
175	150	0.112
150	125	0.125
125	100	0.133
100	75	0.141
75	50	0.078
62	**38**	**0.083**
50	25	0.265

The values in bold font represent the energy window of most interest to a 70 MeV cyclotron facility.

3.6 CONCLUSIONS

Should the production of ^{225}Ac/^{213}Bi generators be deemed important enough, they can certainly be produced at a 70 MeV H^- cyclotron facility. While the production rate achievable with such a cyclotron can never compete with those of the larger, higher-energy linac facilities (e.g. BLIP at Brookhaven, IPF at Los Alamos, etc.), few of these larger accelerators exist in the world. Therefore, the new generation of commercial 70 MeV H^- cyclotrons can make a contribution. None of these accelerators will likely be able to produce ^{225}Ac on a truly commercial scale, in the way that a modern 70 MeV H^- cyclotron in recent years can supply a radionuclide like ^{82}Sr in bulk. Even the large linacs cannot produce ^{225}Ac without some level of ^{227}Ac contamination, an

issue which is still under investigation. Some authors have pointed out that the production of clean ^{225}Ac depends on future advances in technology [HAR2011, ENG2018]. It is noteworthy, however, that with a 70 MeV primary proton beam, utilizing a 38 $\rightarrow$ 62 MeV energy window on a thorium target, the radionuclidic purity of ^{225}Ac is, in fact, not worse (as previously reported) but rather slightly better than at other higher-energy windows in the region up to 200 MeV. Concerning production rate, typical yields for ^{225}Ac will be similar to that of ^{22}Na and ^{68}Ge, the latter two of which have already been produced for many years on a semi-commercial scale at a beam energy close to that of a modern 70 MeV H^- cyclotron.

Similar arguments can be made for the production of ^{230}U/^{226}Th generators. Since a lower production energy window is required, more facilities in the world can contribute to its provision even though the yield is low. Should it become an important generator, its production can be done with well-established infrastructure. In the context of a 70 MeV H^- cyclotron facility, high-performance Th targetry will introduce significant logistical challenges, however, should such an endeavour be deemed important enough, these issues can be solved.

The dual-beam capability of most commercial 70 MeV H^- cyclotrons provides additional flexibility as four targets can be bombarded simultaneously, utilizing two tandem-target systems. In principle, four different radionuclides can be produced simultaneously with the possibility to include both ^{22}Na and ^{225}Ac in the same production run, albeit on different beamlines.

To conclude, it may be mentioned that ^{225}Ac/^{213}Bi generators are already in use in South Africa by Sathekge and co-workers [SAT2017] at the University of Pretoria. Furthermore, the experimental results obtained from the stacked-foil experiments described in this chapter have already been published as a journal article [STE2021a] and the new associated numerical data have been incorporated into the EXFOR nuclear data library by the IAEA as entry no. D1013.

Chapter 4

Selected excitation functions of ^{232}Th+p reactions between 100 and 200 MeV

4.1 INTRODUCTION AND BACKGROUND

This part of the thesis project deviates somewhat from the original concept, which initially focused only on the new 70 MeV H^- cyclotron facility that is now becoming a reality at iThemba LABS. It should be realized that when this project commenced, the approval for the 70 MeV cyclotron facility was still a future event. Indeed, there was doubt at that time whether it would become a reality. In January 2018 the Programme Advisory Committee (PAC) of iThemba LABS favourably accepted a letter of intent (LOI) to investigate the production of some alpha emitters at the laboratory. In December 2018 the PAC approved a proposal to perform stacked-foil experiments that contain thorium foils. The original proposal asked for proton beams of 40 and 66 MeV only. The PAC, however, approved the project (PR312a) with a proviso, namely that it should be extended to higher proton energies of at least 140 MeV but ideally up to 200 MeV, in which case they would assign it the highest priority (i.e. priority 1).

Unfortunately the study at higher energies was seriously delayed. We planned to do the 40 and 66 MeV stack irradiations about 6 months apart in 2019, followed by a 200 MeV irradiation of a foil stack in early 2020. The two stacked-foil investigations at lower energies were performed as planned but then the Covid-19 pandemic arrived, causing a long delay for the availability of a 200 MeV proton beam until late in 2021. Due to various levels of lockdown, a significant percentage of laboratory staff worked off-site and/or from home. Student and external user access to iThemba LABS was also largely curbed during most of 2020 and 2021. All of these measures contributed to a situation where the earlier results have already been published (see [STE2021a]) while completion of the measurements and most of the analysis of the 200 MeV stack spilled over into 2022.

From the perspective of this project, the main interest in the 100–200 MeV energy region are the two products ^{227,225}Ac$^{!}$ and ^{225}Ac*, as defined by Robertson et al. [ROB2020] and already discussed in Chapter 3. Here, again, it should be kept in mind that at the time this project commenced, the notation ^{227,225}Ac$^{!}$ and ^{225}Ac* could not yet have been familiar to us as some of the seminal results from TRIUMF were then still unpublished. Events out of our control (such as the Covid-19 pandemic) and investigations elsewhere changed the landscape in which we

operated. Nevertheless, nuclear data relevant to ^{225}Ac* production still remain scarce, therefore some of our new data still appear to be relevant and needed.

From the perspective of iThemba LABS, the production of neither ^{227,225}Ac$^{!}$ nor ^{225}Ac* is currently pursued. Rather, the focus is on the feasibility to add them to a future production regimen, should they become important enough to do so in South Africa. The SSC can provide proton beams up to 200 MeV. Currently, however, there is no capability to provide 200 MeV proton beams with the required high intensity (e.g. beam current between, say, 100 and 300 μA) at iThemba LABS. In principle such a capability can be developed for the SSC, should it become a priority; there are ways to do this. Alternatively one can ponder what the properties should be of a dedicated accelerator to produce these ^{225}Ac products in bulk.

In this chapter we investigate some of these aspects purely from a nuclear data point of view, i.e. what is possible or not based on what one can glean from the nuclear data only. This is not to say that other aspects are not important, i.e. economics, supply chain, separation chemistry, radioactive waste handling, etc. Indeed they are, but are just not part of our current focus and outside the scope of this project.

4.2 EXPERIMENTAL ASPECTS AND CONSIDERATIONS

4.2.1 Irradiations

The foil stack was irradiated with a primary proton beam of 200 $\pm$ 1 MeV, delivered by the SSC facility of iThemba LABS. As explained in Section 2.5, the RERAME chamber was not used for this experiment but the irradiation chamber shown in Figure 2.12 was used instead. The beam was focused to a spot of about 3 mm in diameter on the front of the stack. The irradiation lasted 5 hours at a beam current of nominally 50 nA.

The stack contained nine thorium foils of 50 μm nominal thickness and 99.7% purity, supplied by Goodfellow, UK. Note that this is double the thickness used in the 40 and 66 MeV stacks. Similar to the previous stacks, these Th foils were sandwiched between Kapton foils of 25 μm thickness, which served as catchers for volatile reaction products, fission fragments, and recoil ions. Each sandwich was followed by an Al monitor foil of 125 μm thickness. Behind each Al foil was placed a relatively thick Cu degrader, accurately machined to the desired thickness to provide data points with close to 10 MeV spacing. Behind each Cu degrader was placed a Cu monitor foil of 50 μm nominal thickness. Initially the experiment was designed for only eight Th sandwiches spaced 10 MeV apart but it was decided during the assembly of the stack to add a ninth sandwich at the back of the stack. This last Th foil had a larger downstream energy spacing of about 25 MeV. The areal thicknesses of individual foils were accurately determined by weighing.

4.2.2 Radionuclide assays

The radionuclide assays were performed in exactly the same way as described in Section 3.2 for the 40 and 66 MeV stacks. As before, quantitative spectrometry of ^{225}Ac and ^{225}Ra was based on the 218.0 keV (11.44%) γ-line of the daughter radionuclide ^{221}Fr. Due to the fact that the Th foils had twice the thickness than before and the relevant cross sections were also significantly

larger at the higher proton energies, the observed 218.0 keV full-energy peaks of ^{221}Fr were much stronger in these measured spectra. This made it possible to collect data repeatedly over a longer period, thereby extending the decay-curve analysis to longer times post EOB. Further details are available in Section 3.2.

4.2.3 Data analysis

The stacked-foil experiment was simulated with the Monte Carlo radiation transport code MCNP6 [GOO2012] in a similar way as for the 40 and 66 MeV stacks (see Subsection 3.2.3 for details). This provided the associated proton energies and energy uncertainties. Cross sections were determined from the full-energy photopeak areas as described in Section 2.7, using the nuclear decay data of Table 3.2. The total uncertainties of the measured cross sections were obtained by summing all contributing uncertainties in quadrature. These values are expressed with a 1σ (68%) confidence level. The systematic uncertainties include an uncertainty in beam-current integration (4%), detector efficiency (5%), counting geometry (1%), decay corrections (2%), and foil thickness (2%).

The monitor reactions selected for this energy region are ^{27}Al(p,x)^{22}Na and ^{nat}Cu(p,x)^{58}Co, the results of which are shown in Figure 4.1. The relevant cross sections extracted from the Al and Cu monitor foils are compared with the most recent IAEA-recommended reference cross sections (Hermanne et al. [HER2018]) downloaded from the IAEA-NDS Medical Portal. The integrated charge was initially treated as a free parameter and adjusted until the measured monitor cross sections of this work simultaneously showed good overall agreement with both reference curves. The resulting charge agreed satisfactorily with the value measured directly

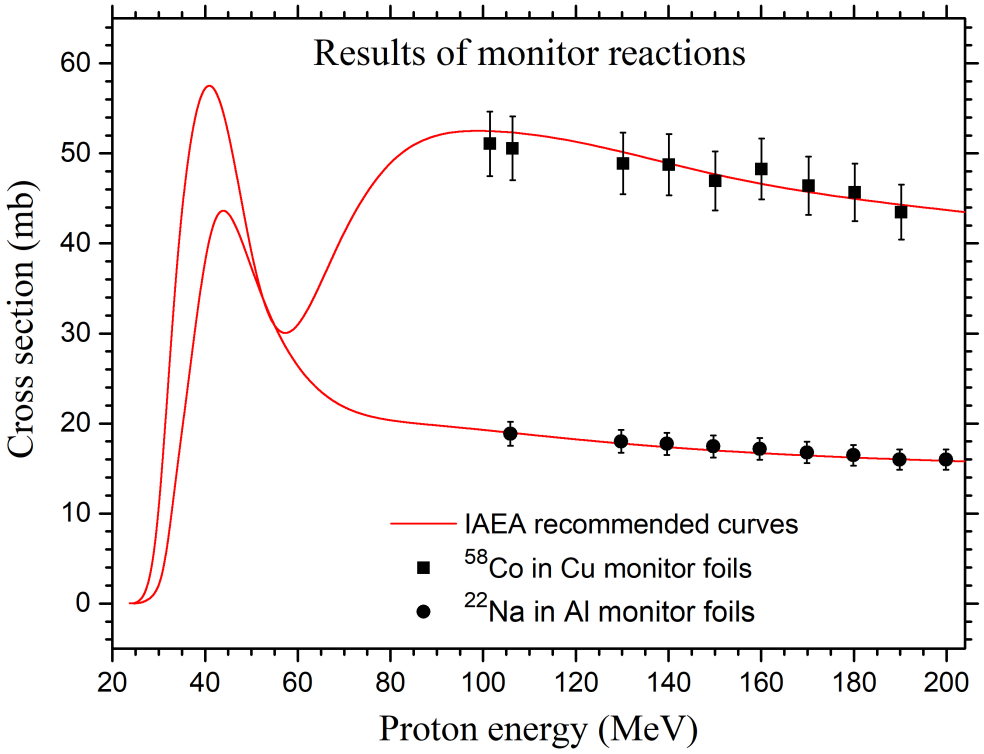


Figure 4.1: IAEA reference excitation functions for the ^{27}Al(p,x)^{22}Na and ^{nat}Cu(p,x)^{58}Co reactions (Hermanne et al. [HER2018]) and corresponding cross sections measured in this study for monitoring the 200 MeV stack.

with the current integrator, the difference being less than 3%, which is well within the experimental uncertainties. There is notably more scatter in the data extracted from the Cu foils than from the Al foils, which is almost negligible in the latter case.

The decay-curve analysis was performed in the same way as described in Subsection 3.2.3. The only difference was that a new set of decay-curve shape functions was introduced, extending to longer decay times of up to 90 days. A set of decay-curve shape functions having the form of Equation 3.1 was established for ^{225}Ra/^{225}Ac cross-section ratios ranging from 0 to 0.2 (i.e. the ^{225}Ra cross section having values that range from 0% to 20% relative to that of ^{225}Ac). This was done in steps of 0.005 (i.e. 0.5%), providing a set of 41 such shape functions. This set was introduced into the software system TableCurve [SYS2020] as a user-defined function library. As discussed before, with TableCurve one can fit the entire set of 41 shape functions on to a measured decay-curve data set, discovering which particular shape function reproduces the measurements the best. In this way one can quantify both the ^{225}Ac and ^{225}Ra cross sections and yields. More detail of the method can be found in Subsection 3.2.3.

The measured decay curve for foil Th-4 of the 200 MeV foil stack is shown in Figure 4.2. (Note that thorium foil Th-4 is the fourth one in the stack, where the numbering starts at the highest proton energy.) A selection of decay curves are also shown to illustrate the procedure. As mentioned before, these curves have a fixed shape and a single free parameter which is a normalization factor. For display purposes, a renormalization was performed so that all the curves join at a common point at the time of EOB. Normally, the normalization factors will be determined by the damped least-squares Levenberg-Marquardt algorithm of the TableCurve code in such a way as to minimize a goodness-of-fit criterion, which allows one to discover the decay curve that best fits the data. The results of such an analysis for foil Th-4 is shown in Figure 4.3. A further refinement can be made to the analysis by doing a B-spline fit to the

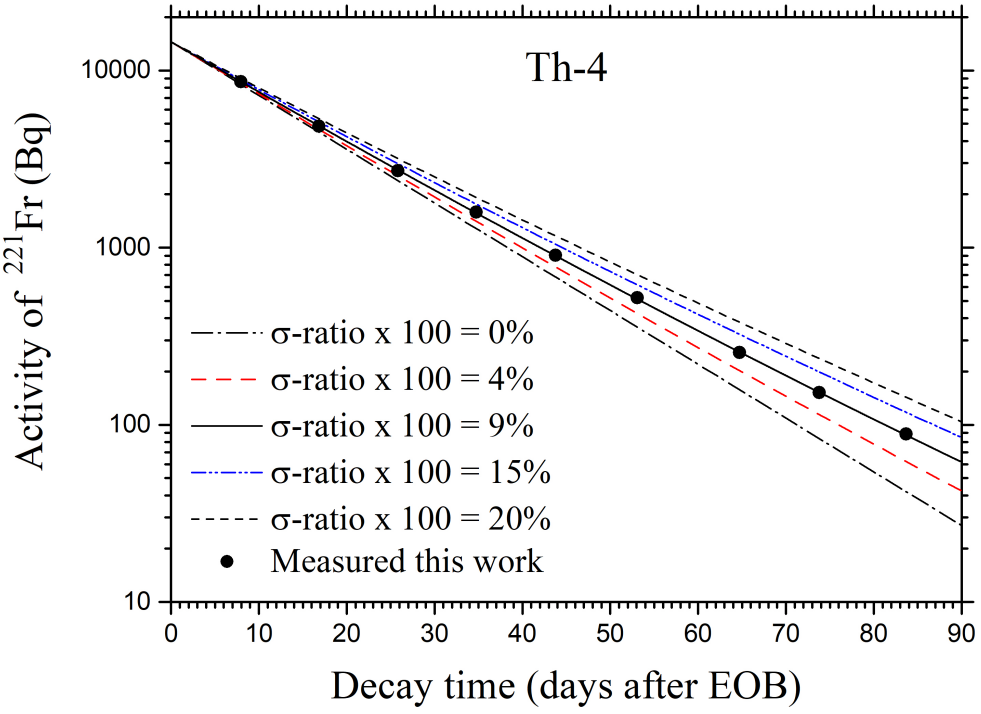


Figure 4.2: Activity of ^{211}Fr in foil Th-4 versus time since EOB. The decay curves were renormalized to join at a common point at the time of EOB (i.e. t = 0) for purposes of display.

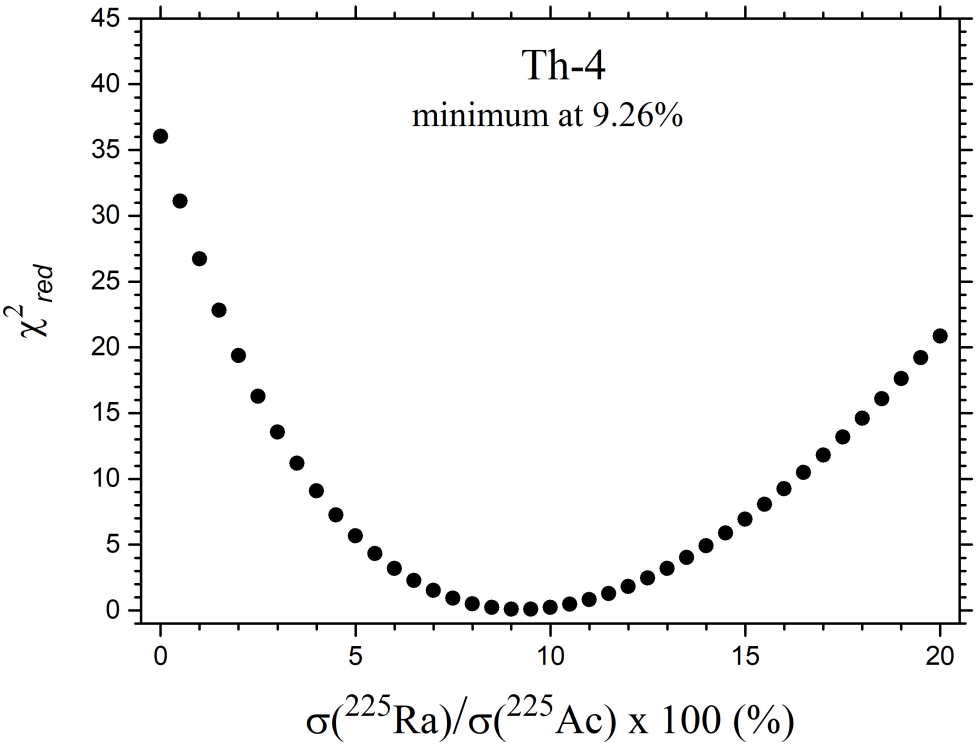


Figure 4.3: Reduced chi-squared statistic (χ^2_{red}) plotted versus the ^{225}Ra/^{225}Ac cross-section ratio for thorium foil Th-4 of the 200 MeV stack. Each point represents the value of the goodness-of-fit criterion pertaining to a least-squares fit of a calculated decay curve on a set of ^{221}Fr daughter activities, measured repeatedly over a period of more than 80 days (also see Figure 4.2).

data shown in Figure 4.3, from which an interpolated minimum can be found. This a standard operation in TableCurve. An interpolated minimum of the ^{225}Ra/^{225}Ac cross-section ratio was found to be at a ratio of 0.0926 (i.e. 9.26% ^{225}Ra).

To conclude this section, it is pertinent to make some comments on counting times. The measurements performed to arrive at a decay curve such as the one shown in Figure 4.2 take a relatively long time to complete. Our adopted philosophy was to rather measure fewer data points but to achieve excellent counting statistics for each point, i.e. an uncertainty due to counting statistics negligible in comparison to other systematic uncertainties. This required us to reduce the distance between source and detector and to increase counting intervals for the later counting sessions. Towards long times after EOB, the counting intervals became quite long but never exceeded a 24-hour real-time interval. In the case of a single radionuclide, without any feeding from precursor decay, Equation 2.17 of Subsection 2.7.3 gives the mean time within the counting interval where the instantaneous activity is equal to the average activity during the interval. In the case where precursor decay is significant, Equation 2.17 is no longer valid. Since ^{221}Fr is ultimately fed by both ^{225}Ac and ^{225}Ra decay, simulations of growth and decay were performed, from which the mean times within a counting interval could be derived. This gave results not much different than what one would obtain from Equation 2.17 for pure ^{225}Ac decay. In the worst case, a difference of only 1.3 min in a 24-hour real counting interval was obtained, which is negligible on a time scale extending to almost 3 months. The uncertainties in time of the measured data points of Figure 4.2 are therefore considered to be negligible.

4.3 RESULTS AND DISCUSSION

4.3.1 Excitation functions

The measured cross sections for ^{225}Ac and ^{225}Ra formation, as attained by the decay-curve analysis described in Subsection 4.2.3, are presented in Table 4.1. The ^{225}Ac cross sections are compared with selected literature data sets in Figure 4.4. Our new data are in good agree-

Table 4.1: Measured cross sections for formation of ^{225}Ac and ^{225}Ra in proton irradiation of ^{232}Th.

Proton energy (MeV)	Cross section (mb)	
	^{225}Ac	^{225}Ra
199.99 ± 0.75	$(1.97 \pm 0.15) \times 10^{+1}$	$(2.21 \pm 0.33) \times 10^{+0}$
190.06 ± 0.91	$(1.99 \pm 0.15) \times 10^{+1}$	$(2.16 \pm 0.32) \times 10^{+0}$
180.06 ± 1.07	$(1.98 \pm 0.15) \times 10^{+1}$	$(2.04 \pm 0.31) \times 10^{+0}$
170.04 ± 1.19	$(1.84 \pm 0.13) \times 10^{+1}$	$(1.77 \pm 0.27) \times 10^{+0}$
159.89 ± 1.34	$(1.71 \pm 0.12) \times 10^{+1}$	$(1.60 \pm 0.24) \times 10^{+0}$
149.87 ± 1.47	$(1.54 \pm 0.11) \times 10^{+1}$	$(1.43 \pm 0.21) \times 10^{+0}$
139.90 ± 1.64	$(1.45 \pm 0.11) \times 10^{+1}$	$(1.34 \pm 0.20) \times 10^{+0}$
129.98 ± 1.68	$(1.35 \pm 0.10) \times 10^{+1}$	$(1.19 \pm 0.18) \times 10^{+0}$
106.11 ± 2.09	$(1.06 \pm 0.08) \times 10^{+1}$	$(8.57 \pm 1.29) \times 10^{-1}$

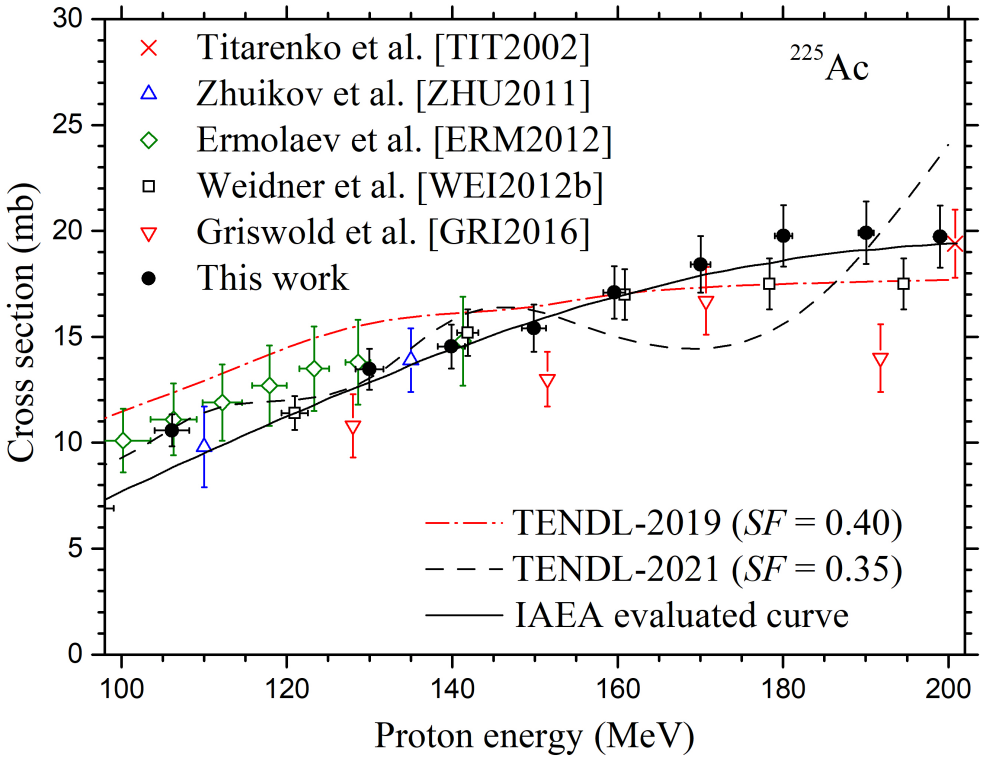


Figure 4.4: Cross sections for the formation of ^{225}Ac in the proton bombardment of ^{232}Th. Note that the TENDL-2019 and TENDL-2021 values have been renormalized using scale factors of *SF* = 0.40 and *SF* = 0.35, respectively. The TENDL cross sections contain the minority contribution from ^{225}Th beta decay. Literature values are from Titarenko et al. [TIT2002], Zhuikov et al. [ZHU2011], Ermolaev et al. [ERM2012], Weidner et al. [WEI2012b], and Griswold et al. [GRI2016].

ment with the values of Zhuikov et al. [ZHU2011], Ermolaev et al. [ERM2012], and Weidner et al. [WEI2012b], largely within the experimental uncertainties. The values of Griswold et al. [GRI2016] seem to be consistently lower. In this energy region there is only one data point of Titarenko et al. [TIT2002], which in fact overlaps with our data point at the highest energy. Note that in Figure 4.4 those two values were slightly displaced on the x-axis to show them next to each other as otherwise the data point of Titarenko would not be visible. The IAEA evaluated curve [ENG2019] passes through the majority of our data points within the experimental uncertainties. The IAEA evaluation was therefore adopted for subsequent estimates of production yields for different target configurations in the energy region 100–200 MeV. A comparison with recent TENDL data was also made. The values from the TENDL-2019 library clearly provide a better shape agreement than those of the latest version of the library, TENDL-2021. This is surprising. In both cases a renormalization was required for purposes of comparison with the experimental data as both TENDL data sets overpredict the overall trend of ^{232}Th(p,x)^{225}Ac excitation function in this energy region, by somewhat more than a factor of 2.

In the case of ^{225}Ra the only other data set in existence, to the best of our knowledge, is the one by Weidner et al. [WEI2012b] (see Figure 4.5). Our values are systematically higher than those of Weidner. The IAEA evaluated curve [ENG2019] in this case is based solely on the data of Weidner. When we renormalize this curve with a scale factor of SF = 1.35, the resulting curve passes through all our data points within their experimental uncertainties. For purposes of making yield estimates of targets, we used both the IAEA curve as is as well as renormalized to fit our data. In such cases we present two values and discuss the results

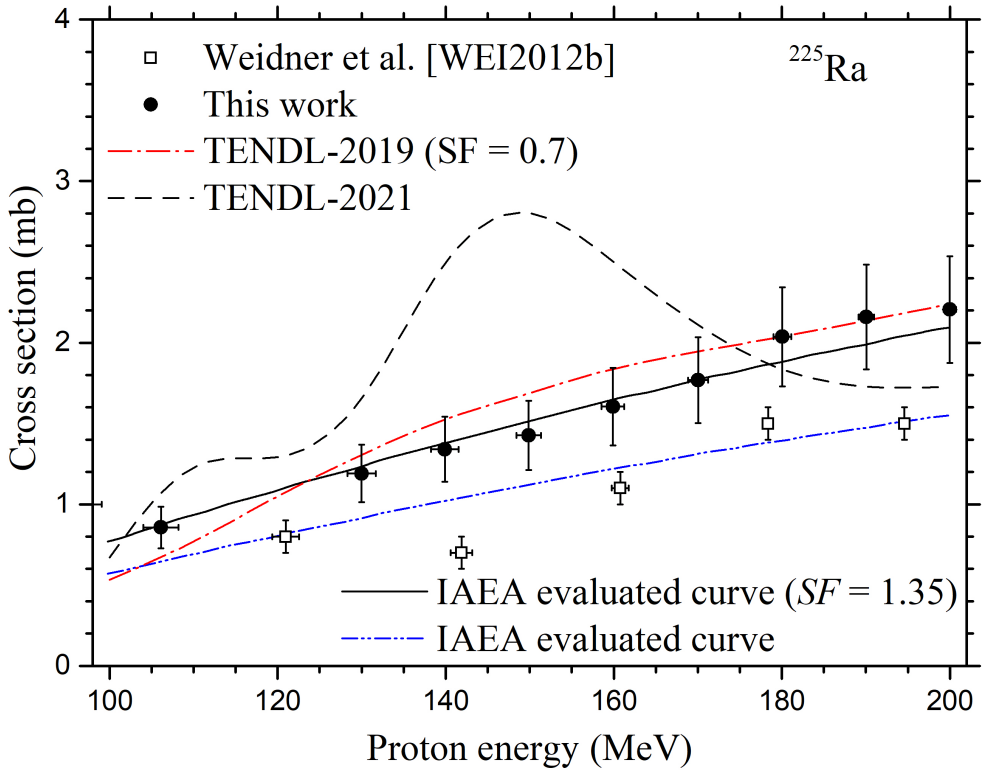


Figure 4.5: Cross sections for the formation of ^{225}Ra in the proton bombardment of ^{232}Th. Note that the TENDL-2019 values have been renormalized using a scale factor of SF = 0.7. The IAEA evaluated curve is shown both unscaled as well as renormalized using a scale factor of SF = 1.35. Literature values are from Weidner et al. [WEI2012b].

based on both values. A comparison with the TENDL data is also shown in Figure 4.5. Again it is found that the data from TENDL-2019 provide a much better shape agreement with the available experimental values than the latest data from TENDL-2021. For purposes of display, the TENDL-2019 values were renormalized with a scale factor of $SF = 0.7$ but the TENDL-2021 values were not renormalized as its shape is simply too different from the data.

Taken into consideration that the data of Weidner and the data of this study are in good agreement in the case of ^{225}Ac, it is somewhat surprising to find the larger disagreement in the case of ^{225}Ra. A lot of time was spent scrutinizing our method and looking for possible mistakes but none were found.

4.3.2 Integral yields

Since we adopted the evaluated cross sections from the IAEA Medical Portal (available from https://www-nds.iaea.org), the corresponding integral yields could be downloaded directly from the same website. In the case of ^{225}Ra, a scale factor of 1.35 was also introduced, as discussed above, as larger cross sections were obtained in this work than the data on which the IAEA evaluation was based. The relevant curves are shown in Figure 4.6.

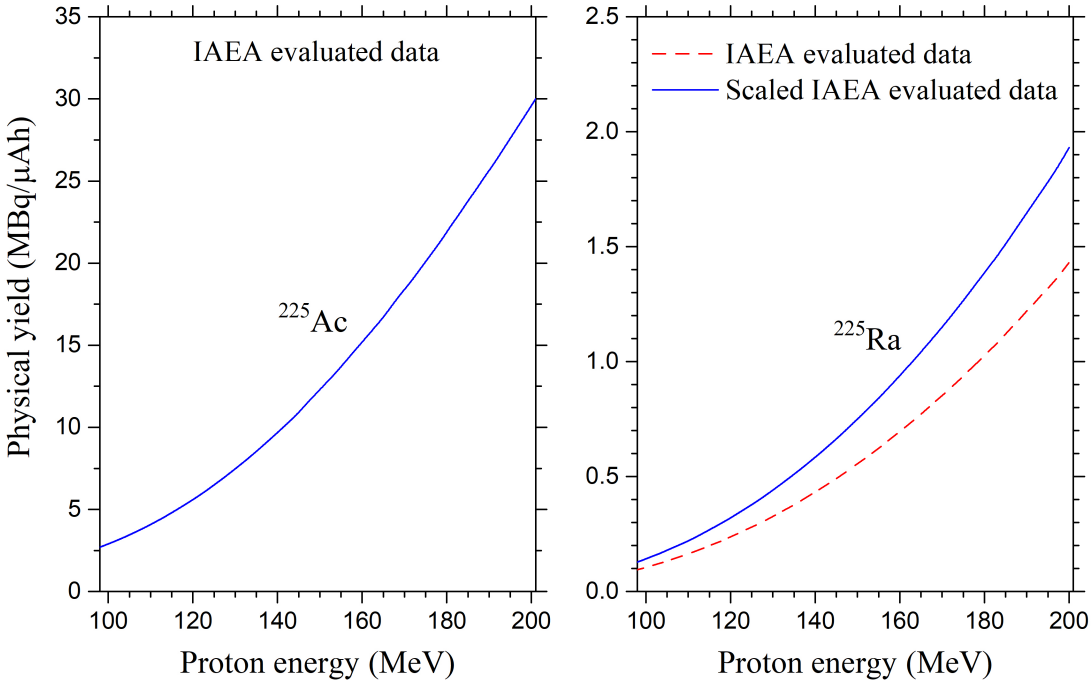


Figure 4.6: Integral physical yields for the production of ^{225}Ac (LEFT) and ^{225}Ra (RIGHT) in the proton bombardment of ^{232}Th. The data are from the IAEA-NDS Medical Portal. The scale factor introduced in the case of ^{225}Ra is 1.35.

4.4 TARGETRY

It is interesting to contemplate different target designs for producing ^{225}Ac with Th targets in the energy region 100–200 MeV. Here we consider the same design philosophy as currently used for 66 MeV targetry at iThemba LABS and which is also planned for the new 70 MeV targetry. A concept for a stacked-target within a single target holder is shown schematically

in Figure 4.7. Since a tandem-target geometry has been implemented very successfully at 66 MeV, it seems appropriate to scale up to a triple-target configuration for the energy region 100–200 MeV. In this way, the thermal load per individual target will be similar to that of the current targets. One significant difference is that the rest of the beam (i.e. below 100 MeV) has to be incident on further targets downstream and eventually stopped within the target holder. In Figure 4.7 these further target elements are simply denoted as a beamstop (BS) but they can be additional useful targets for production of radionuclides. Here we will focus only on the energy region down to about 100 MeV. The triple Th targets are denoted T1, T2, and T3 in the figure. They are assumed to be Inconel-encapsulated Th targets with similar thermal loads. In order to achieve this, their thicknesses need to decrease sequentially with decreasing beam energy (i.e. increasing beam penetration depth).

In order to make yield estimates for such a target system, a number of assumptions have to be made. It is assumed that the same helium-cooled Havar beam-window concept will be employed and that the Al target-holder entrance window will have the same thickness of 2 mm as currently employed on VBTS target holders. A wall thickness of 0.5 mm is adopted for the Inconel capsules and the cooling-water layers have a thickness of 1.8 mm, similar to the new 70 MeV targets. Under these assumptions, the Th targets will have the following thicknesses:

- T1: 10.6 mm,
- T2: 9.3 mm,
- T3: 7.8 mm,

where the choice is deliberate to constrain the specification to a tolerance not smaller than 0.1 mm. The corresponding energy windows are 195.61 → 166.03 MeV, 162.16 → 132.60 MeV,

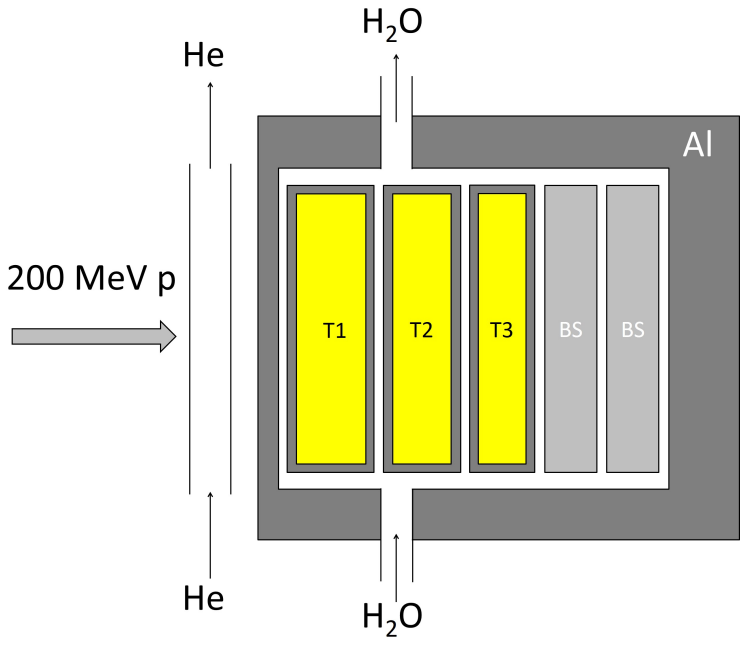


Figure 4.7: Schematic diagram illustrating the principle of a triple-stacked Th target with similar thermal load per target, achieved by reducing the target thickness with decreasing proton energy. The Inconel-encapsulated Th targets are denoted T1, T2, and T3, with BS the elements of a water-cooled beamstop.

and 128.08 → 98.51 MeV. The next step is to find the physical yields of ^{227,225}Ac$^{!}$ and ^{225}Ac* for these energy windows and subsequently to derive production yields from these values for different bombardment scenarios.

In order to derive yields for ^{225}Ac*, it is necessary to know the growth-and-decay characteristics of ^{225}Ac formed via ^{225}Ra decay. It is assumed that, shortly after EOB, the radiochemical separation of ^{225}Ra from the activated Th can be done quite rapidly (i.e. the separation time negligible in comparison with the ^{225}Ra half-life). After an optimum waiting time the clean ^{225}Ac product, formed via ^{225}Ra decay, is separated from the remaining ^{225}Ra in a second radiochemical procedure. It is also assumed that radiochemical losses are negligible. The growth-and-decay curve for this scenario is shown in Figure 4.8. The maximum ^{225}Ac yield is obtained after a waiting time of 17.5 days, at which time the ^{225}Ac activity is 44.47% of the ^{225}Ra activity at time t = 0.

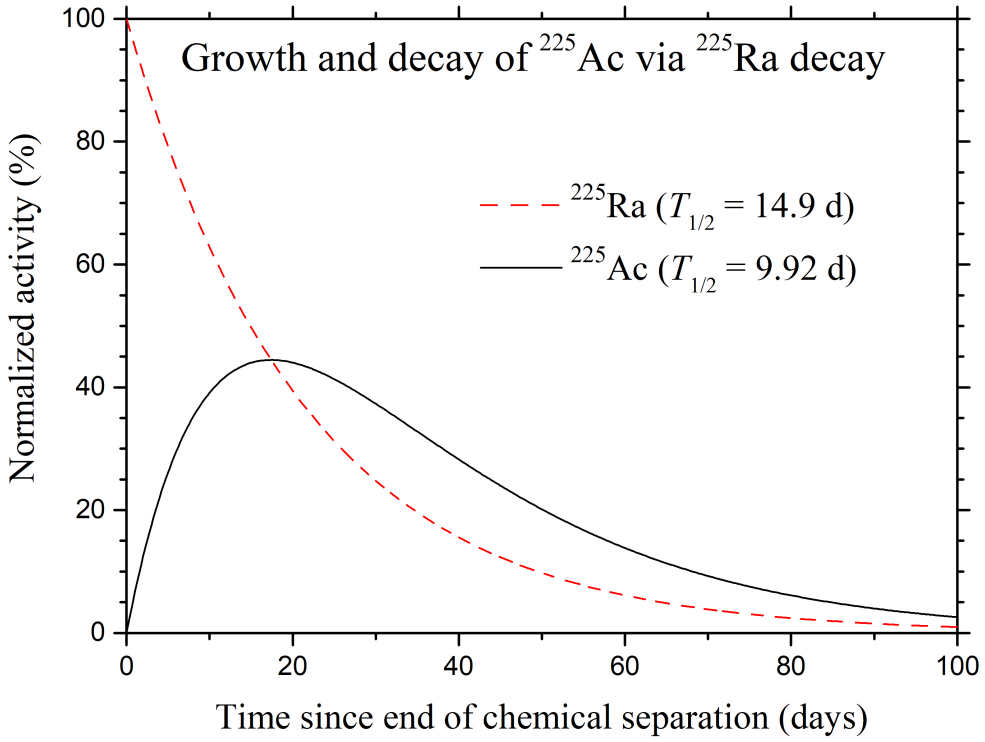


Figure 4.8: Decay curve of ^{225}Ra and growth-and-decay curve of ^{225}Ac formed via ^{225}Ra decay. Time t = 0 is the effective time of the end of the chemical separation of ^{225}Ra from the ^{232}Th target. All activities on the y-axis is relative to the activity of ^{225}Ra at time t = 0.

Table 4.2: Production yields of ^{227,225}Ac$^{!}$ and ^{225}Ac* for the triple-target system of Figure 4.7.

Target	Proton energy Window (MeV)	^{227,225}Ac$^{!}$ (MBq/μAh)	^{225}Ac* (MBq/μAh) IAEA	^{225}Ac* (MBq/μAh) This work
T1	195.61 → 166.03	10.76	0.546	0.737
T2	162.16 → 132.60	7.84	0.375	0.507
T3	128.08 → 98.51	4.31	0.211	0.284
Total		22.91	1.132	1.528

The ^{227,225}Ac$^{!}$ and ^{225}Ac* physical yields for the three Th targets are presented in Table 4.2. Note that for ^{225}Ac* two values are presented, namely based on the evaluated yields of the IAEA and scaled by a factor of 1.35 in this work. Total production yields for bombardments ranging from one day to 10 days are presented in Table 4.3, assuming a constant beam current of 250 μA. For ^{227,225}Ac$^{!}$ the yield at EOB is given and for ^{225}Ac* the yield at EOB + 17.5 days, when the maximum in-growth activity has been reached.

Table 4.3: Production yields of ^{227,225}Ac$^{!}$ and ^{225}Ac* for the triple-target system of Figure 4.7, assuming a beam current of 250 μA.

Bombardment time (days)	^{227,225}Ac$^{!}$ Y(EOB) (GBq ; [Ci])	^{225}Ac* Y(EOB + 17.5 days) (GBq ; [mCi]) IAEA	^{225}Ac* Y(EOB + 17.5 days) (GBq ; [mCi]) This work
1	132.8 ; [3.59]	3.0 ; [79.8]	3.98 ; [107.7]
2	256.8 ; [6.94]	5.8 ; [155.9]	7.79 ; [210.5]
3	372.4 ; [10.1]	8.5 ; [228.6]	11.42 ; [308.6]
4	480.3 ; [13.0]	11.0 ; [297.9]	14.88 ; [402.2]
5	580.9 ; [15.7]	13.5 ; [364.2]	18.19 ; [491.6]
6	674.7 ; [18.2]	15.8 ; [427.4]	21.35 ; [577.0]
7	762.3 ; [20.6]	18.1 ; [487.7]	24.36 ; [658.4]
8	844.0 ; [22.8]	20.2 ; [545.3]	27.24 ; [736.2]
9	920.2 ; [24.9]	22.2 ; [600.3]	29.98 ; [810.4]
10	991.3 ; [26.8]	24.2 ; [652.8]	32.61 ; [881.2]

From Table 4.3 it is evident that the large-scale production of multi-Ci quantities of ^{227,225}Ac$^{!}$ is feasible. It is also evident that even after a 10-day uninterrupted bombardment at a beam current of 250 μA, a 1 Ci quantity of ^{225}Ac* could still not be achieved. One can conclude that multi-Ci productions of ^{225}Ac* seem very much out of the question in the proton energy region 100–200 MeV on Th targets. If these massive Th targets can indeed be chemically processed with low radiochemical losses, production of several 100s of mCi only may be feasible.

To conclude this section, some comments on expected thermal behaviour of encapsulated Th targets can be made. It is perhaps relevant to mention that several thick Th targets had been bombarded with relatively high-intensity beams at iThemba LABS, a number of years ago. Ten Al-encapsulated Th targets were prepared for a nuclear physics experiment that measured cluster radioactive decay of the produced radionuclide ^{223}Ac [GUG2010]. Six of them were bombarded in the Elephant, for a duration of 2 hours each, with a 66 MeV proton beam of 80 μA. These Th disks were 4 mm thick and had diameters of only 15 mm, thus, they were quite small. Taken into consideration that most of the heat removal was done from the flat surfaces, the average surface power density was about 0.56 W/cm^2 to dissipate nominally 2 kW of heat. These targets behaved very well under those bombardment conditions. The targets proposed above for the energy region 100–200 MeV will have much larger surfaces to remove the heat from. Assuming Th disks with a diameter of 50 mm under bombardment with a beam current of 250 μA, i.e. subjected to a thermal load of about 7.5 kW, the average surface power density will be about 0.38 kW/cm^2, which is significantly lower than the corresponding

value for the smaller-format Th targets bombarded in the Elephant. Indeed, there seems to be enough headroom to increase the beam current above 250 μA. Full thermal modelling of such targets are being performed at iThemba LABS with both discrete ordinates and computational fluid dynamics (CFD) codes but this falls outside the scope of this thesis project. Here one can also mention that Inconel-encapsulated Th targets are routinely bombarded at the Los Alamos National Laboratory (LANL) but technical details on those targetry are scant in the literature. From a technical point of view, we can see no compelling reasons why a triple-target system, as described above, will not serve its intended purpose. Finally, while explicit uncertainties were not included in Table 4.3, it is expected that for ^{227,225}Ac$^{!}$ this will be of the order of 10% and for ^{225}Ac* unlikely to significantly exceed a level of 30%. Such uncertainties do not impact the comments and conclusions, or any inferences made.

4.5 CONCLUSIONS

Cross sections measured by means of the stacked-foil technique on Th foils, in the proton energy region 100–200 MeV, provided new data points for ^{225}Ac and ^{225}Ra. Good agreement was found with previous investigations in the case of ^{225}Ac but not so for ^{225}Ra, in which case the excitation function was found to be higher by about 35% than the sole data set used by the IAEA for evaluation purposes.

Multi-Curie productions of ^{227,225}Ac$^{!}$ appear to be feasible with high-intensity 200 MeV proton beams and encapsulated Th targets, utilizing the energy region of nominally 100–200 MeV. Since thorium has a similar abundance as lead on Earth, target material is certainly available, even though it is a controlled substance and procurement in bulk may not be straightforward. In contrast, the production of even 1 Ci of ^{225}Ac* in this production regimen will be a very tough assignment. In this chapter we looked at these productions purely from a nuclear data point of view, assuming similar targetry concepts than already in use at iThemba LABS for many years. Production-yield estimates were based on a beam current of 250 μA, which we think is realistic for the kind of targetry considered. Indeed, beam currents above 250 μA may be feasible.

Chapter 5

Radionuclides and neutron production from tandem targetry with 70 MeV protons

5.1 INTRODUCTION

In this chapter, some aspects relating to the radionuclide and neutron production from tandem targets will be discussed. Since the radionuclides of interest produced by a primary 70 MeV proton beam in Th targets have already been discussed in detail in Chapter 3, here the focus will be primarily on the remaining configurations, i.e. Rb/Ga, Mg/Ga, Zr/Y_2O_3, and Be/Ga. A comparison is presented of the predicted $^{82}Sr/^{68}Ge$ yields from the current VBTS Rb/Ga tandem targets (utilizing a 66 MeV proton beam) and the corresponding targets planned for the new 70 MeV cyclotron facility. A similar comparison is presented for the ^{22}Na yields from Mg/Ga tandem targets. The remaining two configurations, Zr/Y_2O_3 and Be/Ga, do not currently have any relevance with 66 MeV proton beams from the SSC. It is possible that the production of ^{88}Y may become important in future, in which case Zr/Y_2O_3 will become relevant. Note that large-scale productions of ^{88}Y have not hitherto been performed at iThemba LABS although some experimental work have been done to investigate various production possibilities for the new 70 MeV cyclotron facility. In contrast, the Be/Ga target is included in this study solely for its neutron production capability. It should be seen as a "toy target system" only as no such targetry is foreseen at iThemba LABS. Its purpose is to inform and provide insight into the target-nucleus mass dependence of secondary neutron emission. Here one may be reminded that light targets such as Li and Be are often employed in neutron generation (see e.g. Bayanov *et al.* [BAY2006] and references therein).

The current 66 MeV Rb/Ga target design for the VBTS is important from the perspective of this thesis project as secondary-neutron activations were performed behind these targets, the results of which will be presented in Chapter 6. The extension of this study to a selection of 70 MeV tandem targets will be presented in Chapter 7. Whereas Chapters 6 and 7 will focus on extensive Monte Carlo simulations of the VBTS and the new 70 MeV target stations, respectively, in this chapter the focus will be on the tandem targets in isolation, serving as source terms for neutron production in a separate series of simplified Monte Carlo simulations. This is done to get an idea of the in-beam neutron production only and to facilitate an intercomparison of the various tandem-target configurations in terms of their neutron production capabilities.

In other words, neutron production in out-of-beam materials via neutron-induced reactions by those neutrons emitted from in-beam materials, during bombardment, is eliminated by removing those materials from the respective Monte Carlo simulations.

A comparison is also made between the neutron production with 66 MeV protons versus 70 MeV protons, for a Rb/Ga tandem target. Finally, a comparison is presented for a Rb/Ga target in isolation versus one residing in a 70 MeV target station, allowing one to get an idea of the level of neutron production by other neutrons and the region of the energy spectrum to which such neutron-induced reactions predominantly contribute.

5.2 RADIONUCLIDE PRODUCTION – ADDITIONAL ASPECTS

5.2.1 Rb/Ga tandem targets for ^{82}Sr/^{68}Ga production

Table 5.1 presents a complete list of in-beam materials and their thicknesses in the current VBTS-type Rb/Ga targets as well as the corresponding values for the new 70 MeV targetry. These will serve as a template for the discussions on other tandem targets as well, since the concept is basically the same for all, except for some changes in certain of the material layers.

Table 5.1: Material layers of the Rb/Ga tandem-target systems, located on the beam axis, for the VBTS (66 MeV protons) and the new 70 MeV target stations.

Layer no.	Material	Thickness		Comments
		VBTS	70 MeV station	
1	Havar	50 μm	50 μm	50 mm diameter
2	Helium gas	15 mm	15 mm	High flow-rate coolant between Havar foils: 25 °C, 1.25 bar
3	Havar	50 μm	50 μm	50 mm diameter
4	Air	2 mm	6.9 mm	Target located in atmosphere
5	Aluminium	2 mm	2 mm	Target-holder entrance window
6	H_2O	1.2 mm	1.8 mm	Cooling-water layer no. 1
7	Stainless steel	0.5 mm	0.5 mm	S316 capsule wall
8	Rubidium metal	17 mm	19.4 mm	For production of ^{82}Sr
9	Stainless steel	0.5 mm	0.5 mm	S316 capsule wall
10	H_2O	1.2 mm	1.8 mm	Cooling-water layer no. 2
11	Niobium metal	0.5 mm	0.5 mm	Nb capsule wall
12	Gallium metal	3.75 mm	5.5 mm	For production of ^{68}Ge
13	Niobium metal	0.5 mm	0.5 mm	Nb capsule wall
14	H_2O	1.2 mm	1.8 mm	Cooling-water layer no. 3
15	Aluminium	23.65 mm	25.7 mm	Back end of target holder

The ^{82}Sr and ^{68}Ge physical yields for the 70 MeV target system have already been presented in Table 3.5, using rounded nominal energy windows of 38 $\rightarrow$ 62 MeV for the high-energy slot and 0 $\rightarrow$ 26 MeV for the low-energy slot. The 66 MeV target system is conceptually the same as the 70 MeV target system except the Rb and Ga layers are thinner, corresponding to rounded

Table 5.2: Yields of ^{22}Na, ^{82}Sr, and ^{68}Ge from Mg/Ga and Rb/Ga tandem targets relevant to the VBTS (66 MeV proton beams) and the new 70 MeV cyclotron facility.

		Physical yield		Production yield[a]	
Nuclide	Target material	VBTS (MBq/μAh)	70 MeV stations (MBq/μAh)	VBTS (MBq [mCi])	70 MeV stations (MBq [mCi])
^{22}Na	^{nat}Mg	0.691	0.826	4142.2 [112.0]	4954.4 [133.9]
^{82}Sr	^{nat}Rb	8.51	10.69	52725.6 [1425.0]	63270.7 [1710.1]
^{68}Ge	^{nat}Ga	0.950	1.14	5692.8 [153.9]	6831.3 [184.6]

[a]For a 24-hour bombardment with a beam current of 250 μA.

nominal energy windows of 36 $\rightarrow$ 57 MeV and 0 $\rightarrow$ 24 MeV, respectively. Note that the beam is always stopped inside the Ga layer. For purposes of comparison, the relevant physical yields as well as production yields for a 24-hour bombardment at a beam current of 250 μA are summarized in Table 5.2.

With the new 70 MeV targetry, the ^{82}Sr yield is expected to be about 25% higher than with current VBTS targetry and the ^{68}Ge yield will be about 20% higher, provided the beam intensity remains the same. It is hoped, however, that the new targetry will cope with a significant increase in beam intensity and that routine production yields will be further increased.

The radionuclides ^{82}Sr and ^{68}Ge are the two main export products currently produced by iThemba LABS. A large percentage of the available radionuclide production beamtime from the SSC is therefore allocated to Rb/Ga target bombardments, generating much needed income for the laboratory. The relatively long-lived ^{82}Sr ($T_{1/2}$ = 25.35 d) is the precursor of short-lived ^{82}Rb ($T_{1/2}$ = 1.2575 min) in ^{82}Sr/^{82}Rb generator systems. Rubidium-82 is an important marker for myocardial perfusion studies with PET (see e.g. the IAEA report by Filosofov *et al.* [FIL2010] which, even though somewhat old, is still an excellent read on medical generators important for PET). The long-lived ^{68}Ge ($T_{1/2}$ = 270.93 d) is the precursor of the relatively short-lived ^{68}Ga ($T_{1/2}$ = 67.71 min) in ^{68}Ge/^{68}Ga generator systems. Gallium-68 is likewise an important PET radionuclide, especially in ^{68}Ga-labelled tumour-specific peptides now in routine use for imaging of certain types of cancer. Its cyclotron-independent availability via the ^{68}Ge/^{68}Ga generator is also an advantage for PET centers that do not own their own PET cyclotron. There is currently enormous interest in ^{68}Ga-DOTATOC and similar ^{68}Ga-labelled radiopharmaceuticals for PET imaging of the so-called neuroendocrine tumours [FIL2010] as well as ^{68}Ga-labelled PSMA-617 or similar molecules for imaging prostate cancer [SAT2017].

5.2.2 Mg/Ga tandem targets for ^{22}Na/^{68}Ga production

The Mg/Ga tandem targets are currently the 2nd-most irradiated targets with 66 MeV protons at iThemba LABS. The encapsulated Ga target in the low-energy slot serves the same purpose as in the Rb/Ga configuration described in Subsection 5.2.1, namely ^{68}Ge production, therefore only target layers 7, 8 and 9 are different from the scheme of Table 5.1. These layers become Nb-Mg-Nb in the Mg/Ga configuration. The Nb capsules also have a nominal wall thickness of 0.5 mm. The Mg target thicknesses for 66 and 70 MeV proton beams are 11.5 and 13.2 mm, respectively. The expected ^{22}Na yields are summarized in Table 5.2. With a 70 MeV beam, an

increase of about 19.5% in yield can be expected compared to a 66 MeV beam, for the selected energy windows. In both cases, a 24-hour bombardment at a beam current of 250 μA will provide more than 100 mCi of ^{22}Na activity at EOB.

The long ^{22}Na half-life of more than 2.6 years has another advantage, namely that this radionuclide has a substantially long shelf-life. Any spare beamtime can therefore be profitably utilized for its production, with the likelihood of future sales quite certain.

According to Krause-Rehberg *et al.* [KRA2004], most positron-beam systems require strong radionuclide sources. The preferred positron emitter is ^{22}Na because of its long half-life and relatively modest price.

5.2.3 Zr/Y_2O_3 tandem targets for ^{88}Y production

A proof of concept study was performed at iThemba LABS on using Zr/Y_2O_3 tandem targets for the large-scale production of ^{88}Y as well as ^{88}Zr/^{88}Y generators [STE2021b]. In fracking operations, proppants are often spiked with a gamma-emitting radionuclide to verify flow pathways of deep underground cracks with a downhole detector. The use of ^{88}Y for this application has been suggested by Dale *et al.* [DAL2018]. For fracking and most other potential geophysical applications, a high radionuclidic or chemical purity is not a requirement, i.e. the presence of stable yttrium will not affect the radioactivity tracing procedure. This is why an yttrium-containing target can be used in the low-energy slot. For radiolabelling studies, very pure ^{88}Y can be provided by a ^{88}Zr/^{88}Y generator. In various studies, ^{88}Y has been employed as a substitute for the therapeutic radionuclide ^{90}Y to test radiochemical labelling procedures (see e.g. Griffiths *et al.* [GRI2003]). This was done to overcome a particular difficulty with ^{90}Y, namely that it does not have suitable emissions for its detection and tracing.

A Zr target with 6 mm thickness was proposed for the high-energy slot [STE2021b]. Since Zr does not have to be protected from contact with the cooling water, no encapsulation is required in this case. For this target system layers 7 and 9 are therefore eliminated in the scheme of Table 5.1. For the purposes of the Monte Carlo modelling, a 5 mm thick Y_2O_3 was adopted, encapsulated with Nb with 0.5 mm wall thickness. Consequently, layers 11 and 13 remained as in Table 5.1 but layer 12 was replaced with an Y_2O_3 disk.

5.2.4 Be/Ga tandem targets for fast neutron production

It is well-known for many decades that the proton bombardment of Be targets is useful for producing neutron spectra that are generally harder than obtainable from most other target materials. Beryllium targets have typically been employed, for example, in high-energy neutron therapy facilities. At iThemba LABS, a neutron therapy facility was operational from 1987 until 2018. This facility produced neutrons by means of the so-called p(66 MeV)/Be(40 MeV) reaction [JON1988]. This is a short-hand notation for a 66 MeV proton beam incident on a Be target with an energy window of 40 MeV, i.e. an exit energy of 26 MeV. This is achieved with a Be thickness of 19.6 mm. The abundance of 66 MeV proton beams from the SSC was primarily to service the neutron therapy programme (now defunct). This beam energy was also adopted for routine radionuclide productions to reduce the number of energy changes per week, saving SSC beam time as an energy change typically takes an 8-hour shift to complete.

As already mentioned, the inclusion of a Be/Ga target in this study was more out of curiosity than anything else. For the Monte Carlo modelling, the Rb target in the scheme of Table 5.1 was replaced with a Be target. Layer no. 8 was modelled as a 13.2 mm thick Be metal disk.

5.2.5 Tandem targets containing Th

When a Th target is located in the high-energy slot, layers 7, 8 and 9 of Table 5.1 are replaced with an Inconel-Th-Inconel configuration. When a Th target is located in the low-energy slot, layers 11, 12 and 13 are replaced with the same Inconel-Th-Inconel configuration. The capsule-wall thicknesses remained 0.5 mm and a Th thickness of 3.5 mm was adopted in both cases.

5.3 NEUTRON PRODUCTION

5.3.1 Spectra and flux ratios

The decision to perform Monte Carlo simulations of the tandem targets only, with most of the target-station material budget removed, was made only late into this study. It only occurred to us that such information would be useful after most of the target-station simulations had been completed. Therefore, the presentation of the Monte Carlo results is not in a chronological order but rather in a logical order. The starting point was an MCNP6 input file of a complete 70 MeV target station, which will only be discussed in Chapter 7. That model was then reduced by deleting most of the materials, retaining part of the beamline and the target system only. A schematic diagram of the model, as provided by the MCNP6 geometry plotting function, is presented in Figure 5.1. The cavity in the pusher assembly was retained for the sake of defining its flux tally, however, it was not constrained by any materials. A tally of neutrons moving away from the target was also defined on a sphere located 1 m away from the centre of the target. All particle tracking was stopped beyond this sphere. The beamline section and in-beam target-

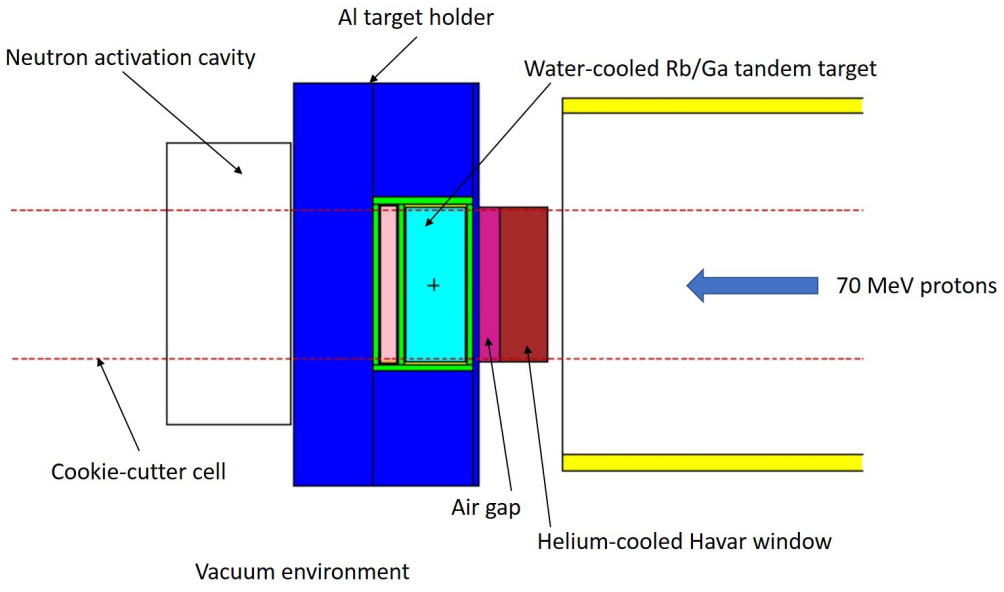


Figure 5.1: Simplified model of a 70 MeV Rb/Ga tandem target, as generated with the MCNP visual editor.

material layers are all located in vacuum. The entire irradiation vault was also removed but the Al target holder was retained.

Since not all the required cross-section data are available up to 70 MeV as tabulated values (referred to in MCNP parlance as "Table Physics"), it is necessary to specify a nuclear model to provide calculated cross sections where tabled values are lacking (referred to as "Model Physics" in the MCNP manuals). There are several models implemented in MCNP6, which will be described in more detail in the next chapter. One of the more recent and up-to-date models is the Cascade-Exciton Model (CEM), which is also the default model of the most recent versions of the code. As will be seen later, this is one of the better models from a predictive power point of view. The CEM model was therefore selected for the purposes of this intercomparison.

The proton beam was modelled as a superposition of Gaussian beams with an offset relative to the beam axis. In this way one can model a beam that is circularly swept (wobbled) on target. Figure 5.1 also shows the outlines of the so-called "cookie-cutter cell". This is a way to confine the beam protons to a region where one would normally expect them to be focused, by discarding protons when they are generated too far away from the beam axis. More details on source terms will be given in the next chapter.

For the purposes of the neutron-production intercomparison, it was convenient to specify fewer neutron energy groups (bins) with broader discrete energy ranges. This had an added advantage of achieving good statistics in all bins within reasonable running times (not exceeding 4 days per run on a modern Core-i9 top-end PC). An 18-bin energy-group structure was adopted. The lowest-energy bin tallied all neutrons with energies below 1 keV. The second bin covered the energy region between 1 and 10 keV, the third bin between 10 and 100 keV, and the fourth bin between 0.1 and 1 MeV. These first four bins are best presented on a logarithmic scale. Bin number five tallied neutrons in the energy region between 1 and 5 MeV. All subsequent bins have a constant width of 5 MeV, with bin no. 18 covering the energy region between 65 and 70 MeV. A so-called F4 flux tally was specified for the forward neutron activation cavity, which provided the average flux within the confines of the cavity. An F1 tally provided the total neutron count in all space (i.e. 4π steradian) around the target-holder centre.

Figure 5.2 shows the average neutron flux in the forward cavity on a linear energy scale, normalized for an accumulated proton charge of 1 μAh, for the Rb/Ga tandem target under bombardment with a 70 MeV proton beam. The total number of neutrons emitted in all space (4π steradian geometry around the target) with an integrated proton charge of 1 μAh, is shown in Figure 5.3.

It is not automatically evident what insights Figures 5.2 and 5.3 convey, however, some important observations can be made. The neutron flux in the forward cavity, as well as the total number of neutrons produced, increases with decreasing energy and peaks in the bin with energy range 1–5 MeV. Below 1 MeV one sees a significant drop-off.

Similar spectra were obtained for the other tandem targets, for particle histories of 2×10^8 incident protons in each case. Figures of these spectra look similar to Figures 5.2 and 5.3 and do not provide a convenient way for an intercomparison. It was necessary to compare each case to a "standard" of some kind. Since the Rb/Ga tandem-target configuration plays such a major role at iThemba LABS, it was decided to choose that as our standard case. Neutron flux

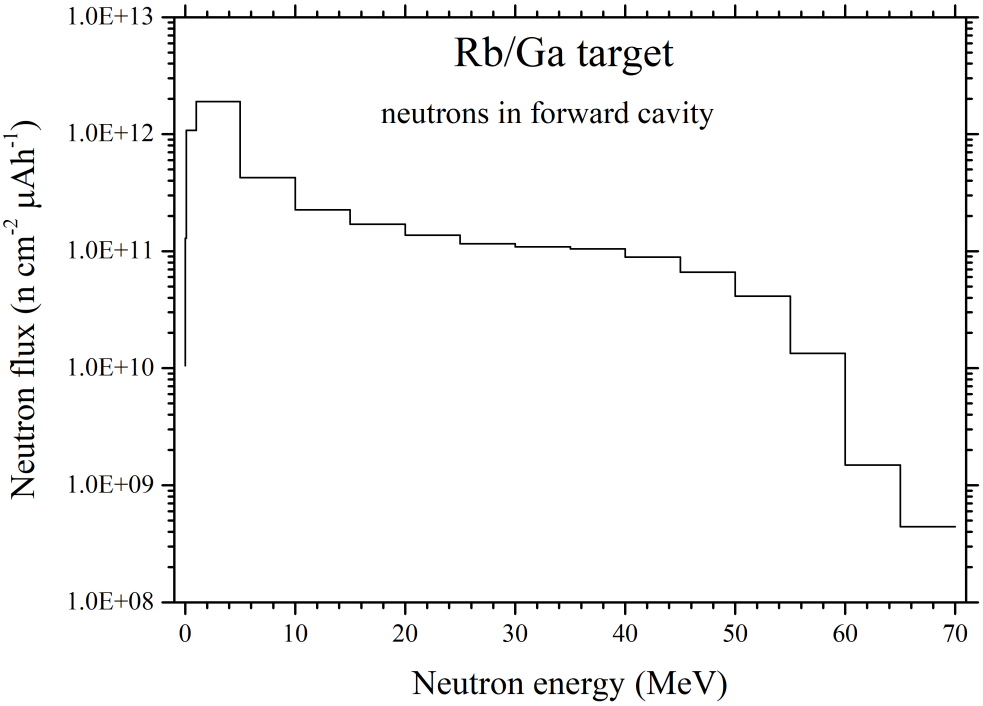


Figure 5.2: Neutron flux (i.e. neutrons/cm^2 produced with an integrated proton charge of 1 μAh) versus neutron energy in the forward cavity behind a Rb/Ga tandem target during irradiation with a 70 MeV proton beam.

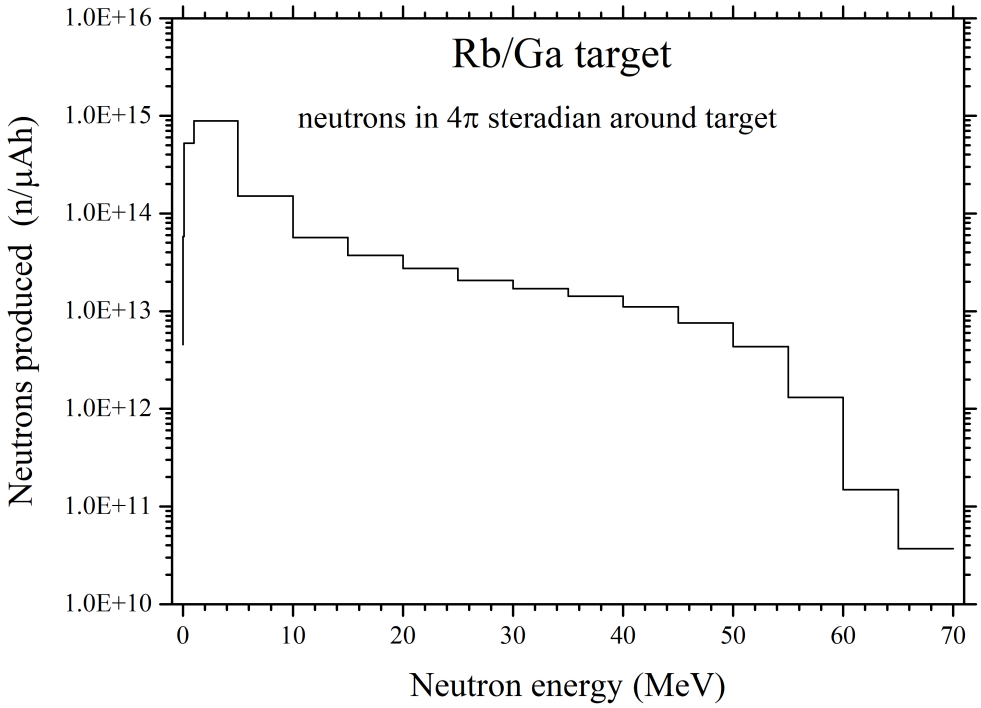


Figure 5.3: Total number of neutrons produced in all space (i.e. a 4π sr geometry around the target) with an integrated proton charge of 1 μAh, during irradiation of a Rb/Ga tandem target with a 70 MeV proton beam.

ratios were calculated for all the tandem targets relative to the Rb/Ga case. This is shown for the forward-cavity fluxes in Figure 5.4, for a selection of tandem-target configurations.

It is evident from Figure 5.4 that the Be/Ga target produces significantly higher neutron fluxes in the higher-energy bins, as compared to the Rb/Ga case. This excess is highest in the 55–60 MeV bin, by almost a factor of 6. Below 5 MeV, however, the Be/Ga target delivers

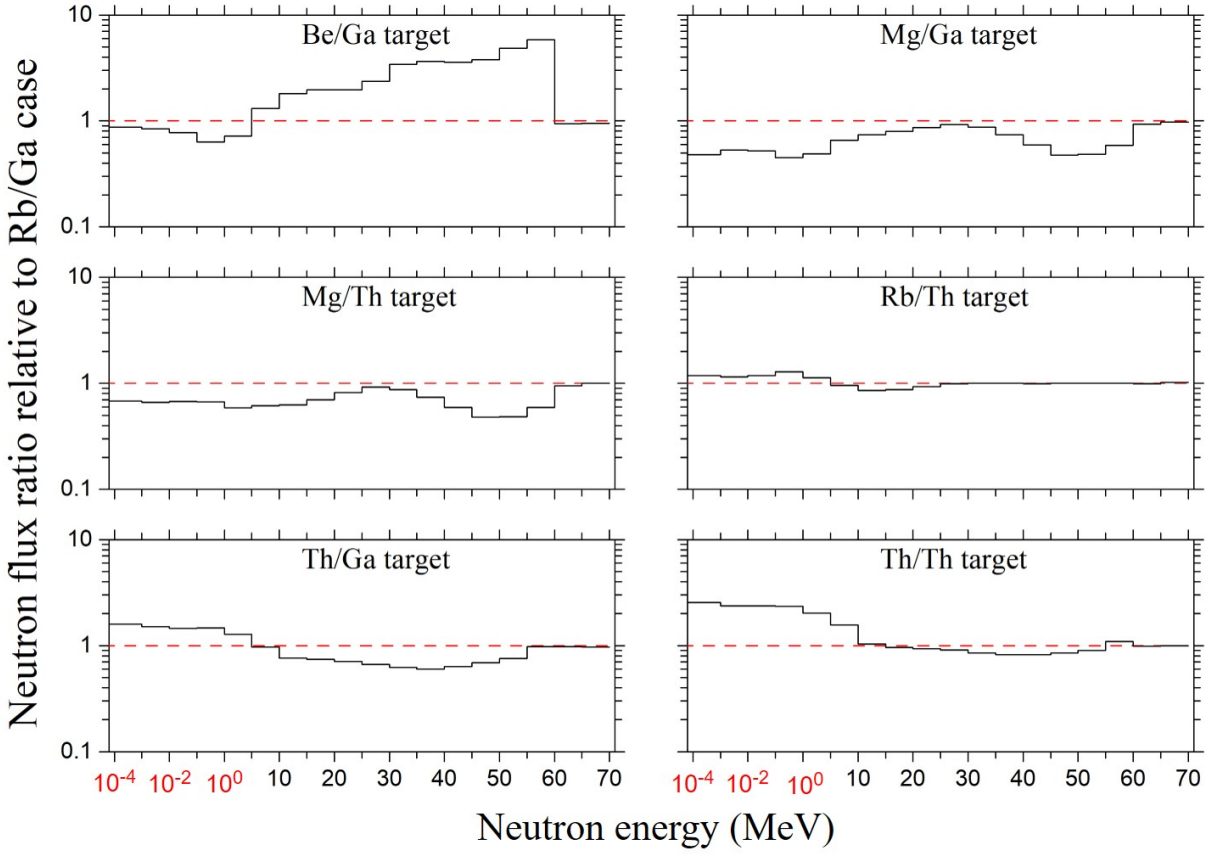


Figure 5.4: Comparison of neutron flux ratios for various tandem targets relative to the Rb/Ga target, as indicated, in the forward cavity downstream of the target (see text). Above 1 MeV the scale on the x-axis is linear (black text) but below 1 MeV it is logarithmic (red text). The red dashed lines represent the case for the Rb/Ga target itself, while the black histograms represent the indicated targets.

lower fluxes. The much harder neutron spectrum explains why Be targets were utilized for neutron therapy. In contrast, the Mg/Ga target shows a deficit in all energy bins. This is also the case for the Mg/Th target. In fact, the flux ratios from the Mg/Ga and Mg/Th targets are very similar except in the lowest energy bins. This is perhaps not surprising as the target in the high-energy slot (Mg in this case) should dominate at higher energies, while the target in the low-energy slot can only contribute to the lower-energy bins. The Rb/Th target shows marginal gains in the lower-energy bins only, otherwise looking very similar to the Rb/Ga case. Both the Th/Ga and Th/Th configurations show an increase in the lower-energy bins only, a notable decrease between 10 and 55 MeV, and a ratio of 1 above 55 MeV. These results indicate that for neutron-induced threshold reactions, the inclusion of Th in the target will not lead to an increased radionuclide production yield, as compared to what one can expect from the "standard" Rb/Ga target. When Mg replaces the Rb target in the high-energy slot, one should always expect a drop in production rate of any neutron-induced reaction.

A figure similar to Figure 5.4 was also made for the total neutrons emitted in 4π space. As the trends are very similar, it was decided not to show that figure in the body of the thesis but to include it in an appendix instead, as it does not contribute significantly to the discussion (see Appendix A). In spite of some differences, a comparison of Figures 5.4 and A.1 indeed shows a significant level of agreement. Figure 5.5 shows the corresponding results for the Zr/Y_2O_3 tandem-target system, both for the all-space (4π) case and the forward cavity. The similarity in

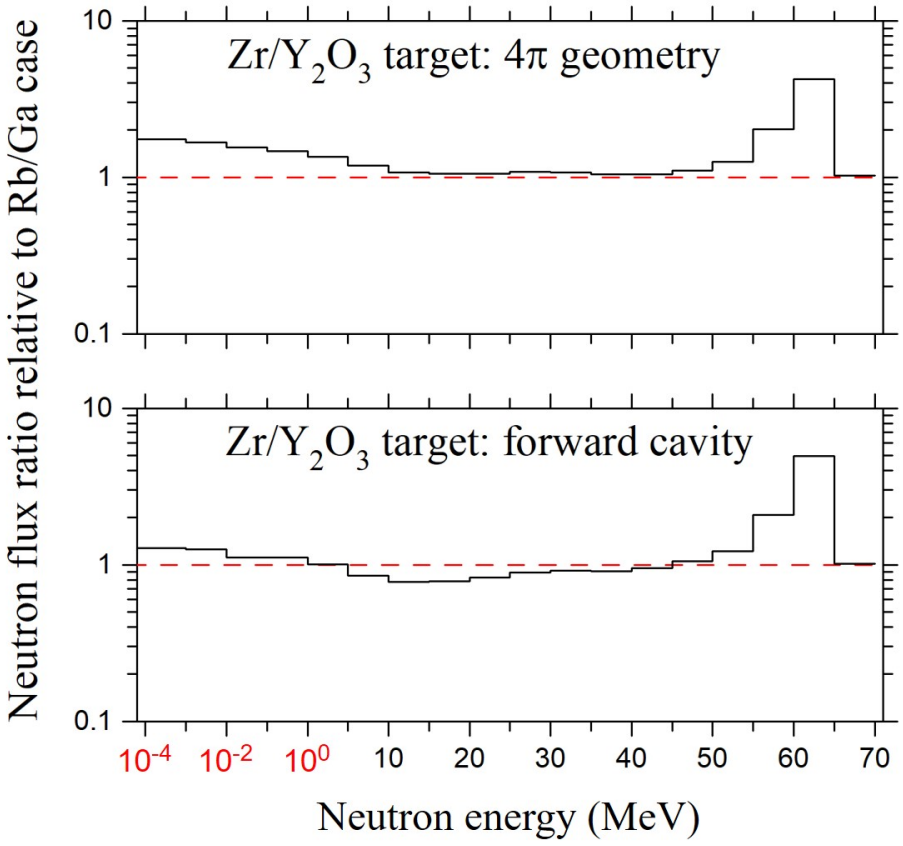


Figure 5.5: Comparison of neutron flux ratios for the Zr/Y_2O_3 tandem target relative to the Rb/Ga target, as indicated. Above 1 MeV the scale on the x-axis is linear (black text) but below 1 MeV it is logarithmic (red text). The red dashed lines represent the case for the Rb/Ga target itself, while the black histograms represent the indicated target.

trend is indeed evident. An interesting excess is evident above 50 MeV, reaching a maximum in the 60–65 MeV bin by more than a factor of 3. There is also some excess below 1 MeV. The total neutron productions, i.e. the sums of contributions from all bins, are compared for the various target configurations in Table 5.3. One can see that the Th/Th target indeed produces more neutrons than the other target configurations, however, we know that the overall spectrum is quite soft. This can be understood by realising that fission neutrons predominantly contribute to the lower-energy part of the spectrum.

Two more cases were investigated for the neutrons produced by protons on a Rb/Ga tandem target. Flux ratios in the forward cavity are shown in the top panel of Figure 5.6 for neutrons induced by a 66 MeV proton beam versus a 70 MeV proton beam. Between about 1 and 40 MeV the ratio is approximately constant at an average value near 0.85. Outside this energy region the flux ratio drops. The drop towards higher energies is expected but the drop below 1 MeV is not so easy to understand. The bottom panel of Figure 5.6 shows the neutron flux ratio from a Rb/Ga target bombarded in a 70 MeV target station versus an isolated target bombarded with a 70 MeV proton beam. This ratio is expected to be around unity at higher energies and this is indeed observed. Below about 5 MeV there is a rapid increase towards lower energies. This is the contribution from neutron-induced reactions with materials mainly outside of the beam axis, such as the inner iron shield, inducing additional neutrons of which a fraction is expected to scatter back into the cavity inside the pusher arm.

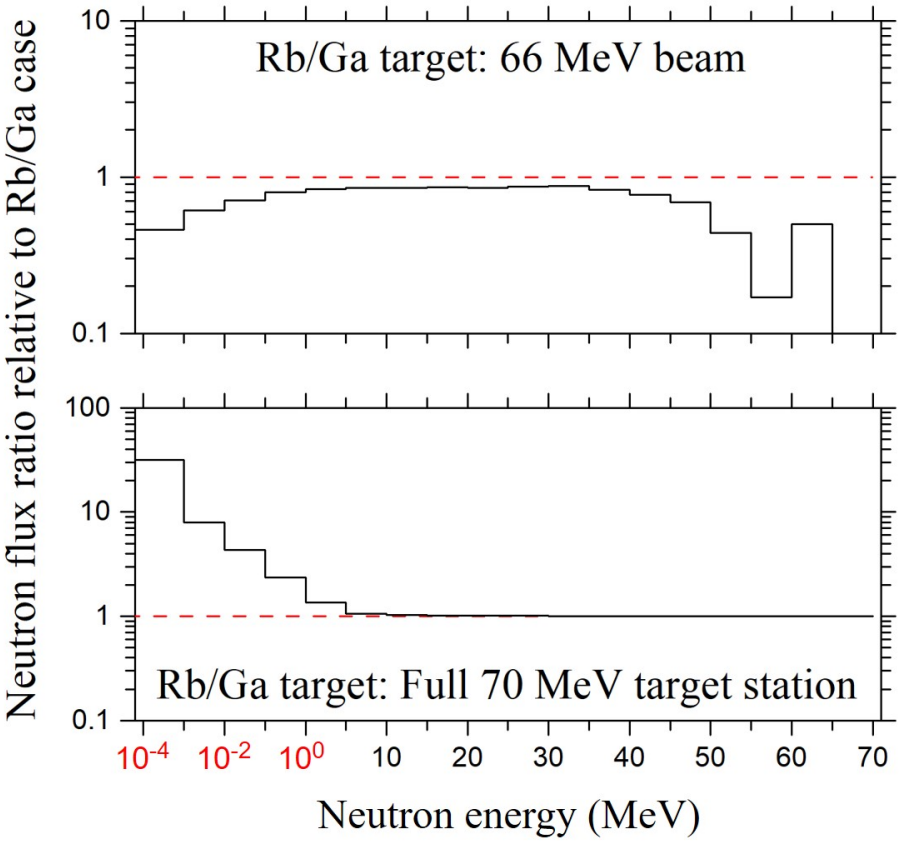


Figure 5.6: TOP: Comparison of neutron flux ratios for the 66 MeV Rb/Ga tandem target relative to the 70 MeV Rb/Ga target. BOTTOM: Comparison of neutron flux ratios for the 70 MeV Rb/Ga tandem target inside a new target station relative to the 70 MeV Rb/Ga target inside vacuum. Above 1 MeV the scale on the x-axis is linear (black text) but below 1 MeV it is logarithmic (red text). The red dashed lines represent the case for the 70 MeV Rb/Ga target in vacuum, while the black histograms represent the compared situation as indicated.

5.3.2 Total neutron production

Table 5.3 presents the total neutron production from the set of tandem targets during bombardment with a 70 MeV proton beam, normalized to an accumulated charge of 1 μAh. The table also contains the average neutron forward flux in the cavity of the pusher-arm for each target configuration. Our initial expectation was that the inclusion of fissionable material in a

Table 5.3: Total neutron production from tandem targets during bombardment with a 70 MeV proton beam as well as the average forward neutron flux in the cavity behind the target.

Tandem target	4π neutron yield (neutrons/μAh)	Forward neutron flux (neutrons cm^{-2} μAh^{-1})
Be/Ga	1.59×10^{15}	5.63×10^{12}
Mg/Ga	0.95×10^{15}	2.59×10^{12}
Mg/Th	1.16×10^{15}	2.97×10^{12}
Rb/Ga	1.83×10^{15}	4.64×10^{12}
Rb/Th	2.08×10^{15}	5.15×10^{12}
Th/Ga	3.31×10^{15}	5.42×10^{12}
Th/Th	3.63×10^{15}	5.84×10^{12}
Zr/Y_2O_3	2.48×10^{15}	4.63×10^{12}

tandem configuration would very significantly increase the neutron production. Even though the Th/Th target does produce the highest neutron flux and the largest total number of neutrons in this target set, this increase is rather modest. The differences in neutron production between the various target configurations are relatively small.

5.4 CONCLUSIONS

The neutron production from the different tandem targets do not differ by a large amount. The forward neutron flux values of between 10^{12} and 10^{13} n/cm$^{-2}\mu$Ah^{-1} may look large but this may be misleading. The precise significance of this level of neutron production cannot be judged from this information alone, especially from a radionuclide production point of view. Whether or not this is a useful resource should be judged by activation experiments. Three such experiments were performed, which will be discussed in the next chapter.

Chapter 6

Activation of samples in the secondary neutron flux behind a VBTS target

6.1 BACKGROUND AND OBJECTIVES

6.1.1 Expanding an existing investigation

An investigation into the feasibility to utilize the secondary neutron flux behind a radionuclide production target for producing additional radionuclides, exploiting neutron-induced reactions, already commenced during the MSc project of the author. That project was completed and the degree awarded, however, to date those results are still unpublished, mainly due to the following two reasons: Firstly, it was realized that the experimental data set produced by that project needed to be expanded. Secondly, predictions based on Monte Carlo simulations performed at that time, for a range of different physics selections, revealed an overall tendency to overpredict the corresponding experimental yields. This was not understood at that time. Additional work has since been done and a clearer picture emerged, shedding light on the reason for these unexpected overpredictions. In this chapter the full set of experimental results will be discussed in conjunction with new Monte Carlo simulations, utilizing newer versions of the relevant codes and related nuclear data libraries.

In addition to the experimental run of the MSc project (forthwith referred to as Run-1), two additional experimental runs were performed to expand the measured data set (referred to as Run-2 and Run-3). An in-depth explanation will be presented on the overpredictions obtained in the MSc study, which were mostly resolved in the subsequent Monte Carlo simulations. (At least a substantial overall improvement was achieved.) While all activations were performed behind a VBTS target under routine bombardment with a 66 MeV proton beam, the main focus was really on provisions for the new 70 MeV cyclotron facility. The supposition is that routine VBTS operations at 66 MeV are close enough to 70 MeV to shed light on many aspects and/or requirements for the new facility.

6.1.2 Previous studies from the literature

The idea to utilize the secondary neutron flux behind a radionuclide production target is not new. Recent studies at the Isotope Production Facility (IPF) of Los Alamos National Laboratory

(LANL), utilizing a proton beam energy of 100 MeV, have shown that such "commensalistic" productions have definite potential (see e.g. Engle *et al.* [ENG2012a, ENG2013, ENG2014b] and Mosby *et al.* [MOS2016]). Important earlier work with relevance to the present investigation was also performed at the Medium Energy Intense Neutron (MEIN) Beam Facility of Brookhaven National Laboratory (BNL), where secondary neutrons were produced by bombarding a water-cooled Cu-beamstop with a 200 MeV proton beam (see e.g. Katcoff *et al.* [KAT1975] and Mirzadeh *et al.* [MIR1983]). The proton beam was delivered by the same linear accelerator that provides beam to the Brookhaven Linear Isotope Producer (BLIP). Important aspects of the studies at LANL and BNL will be highlighted where relevant in this chapter.

Katcoff *et al.* [KAT1975] reported a considerable increase in the ratio of neutron-rich to neutron-deficient radionuclides with reactions induced by the secondary neutrons in comparison to the primary protons, but the resulting activity levels were low. These authors presented effective cross sections for various (n,xn), (n,pxn) and (n,αxn) reactions on a selection of targets covering a reasonably large mass region (^{24}Mg to ^{142}Ce); the neutron flux was reported to be "in excess of 1×10^{11} neutrons cm^{-2} s^{-1} in the energy region 25 to 200 MeV". One would not expect an overall different scenario with regards to low effective cross sections as the incident proton-beam energy is decreased. It is therefore not surprising that the LANL results [ENG2012a, ENG2013, ENG2014b] at 100 MeV show a similar trend to those of Katcoff *et al.* [KAT1975]. The broad energy spectra of secondary neutrons emitted by thick targets lack the selectivity of the "ideal energy windows" that can often be exploited in reactions by charged particles. Spectrum-averaged cross sections also usually have relatively low values.

The more important reactions are those where charged particles are emitted, leading to different atomic species than the target material. This is important if the product radionuclides have to be chemically separated from the target matrix, which is the case in the majority of applications of practical interest. Unfortunately, there is a general trend for the (n,pxn) and (n,αxn) reactions to have even lower cross sections than the (n,xn) reactions, except at very low masses [KAT1975]. This disadvantage of low effective cross sections can only be overcome by utilizing a sufficiently high neutron flux.

Engle *et al.* [ENG2014b] reported a total neutron flux of about 1×10^{12} neutrons cm^{-2} s^{-1} directly behind a routine production target at the IPF while under bombardment with a 100 MeV proton beam of 250 μA, with approximately 50% of the neutrons having energies above 1 MeV. The point was made that this neutron flux is beyond that of typical medical cyclotrons and distinctly different from that of reactors (i.e. considerably harder). Because of the significant increase in obtainable beam intensities evident in modern accelerators, there is a renewed interest in exploiting the secondary neutrons, particularly as aging research reactors are being closed down and usually not replaced. It has been reported that, in contradiction to their importance, experimental cross-section data for neutron-induced reactions are sparse above 14 MeV, i.e. the energy obtainable with ^{3}He(d,n)^{4}He neutron generators [QAI1974]. Certainly, one would prefer to have complete excitation functions for neutron-induced reactions to work with instead of only effective cross sections, the latter of which have limited value when predictions are required for a different energy region. As a result of this lack of experimental data, neutron spectra obtained from nuclear model calculations often have to suffice when making

yield predictions, leading to large uncertainties and errors up to an order of magnitude in exceptional cases [ENG2014b]. Experimental data are challenging to obtain as monoenergetic neutron sources do not exist except at quite low energies (typically 14 MeV and below). The so-called quasi-monoenergetic neutron (QMN) facilities are few in the world, with limited beam time due to sharing with other programmes. This situation is not expected to dramatically change anytime soon.

Despite their limitations, effective cross sections are useful as they do provide some constraints for model calculations. Until such time when better "monoenergetic" experimental cross-section data become available, effective cross sections for neutron-induced reactions will remain important.

6.1.3 Objectives

From the outset, it was clear that we would be confronted with relatively low effective production cross sections in the neutron flux behind a VBTS target. On the other hand, there are extensive routine productions throughout the year, mostly for the production of the relatively long-lived radionuclides ^{22}Na, ^{68}Ge and ^{82}Sr. The radionuclide production programme receives about 50% of the total beam time available on the SSC (in recent times even a little bit more than 50%). The total accumulated charge on target is approaching one million μAh per year, which translates into a large number of neutrons that are currently not utilized. With the new 70 MeV cyclotron facility becoming a reality, these numbers will be even significantly higher. It therefore seems prudent to investigate the possible use of these neutrons to produce useful radionuclides. Since the bombardments in the VBTS are typically quite long, with the nominal accumulated charge in a single run typically not less than 20 000 μAh, the focus with neutron-induced reactions should similarly be on relatively long-lived radionuclides. The idea is to perform neutron-induced reaction experiments in a commensalistic way with routine radionuclide production runs, e.g. in such a manner that the usual weekly beam schedule is not disturbed or affected in any way.

The advent of commercial 70 MeV cyclotrons with high-intensity, dual-beam capability is relatively recent. We are not aware of any dedicated studies to date that focused on utilizing the secondary neutrons on these machines. A number of experiments have therefore been planned, covering a wide mass region (7–209 AMU). The various tasks and objectives of this study are as follows:

- To design and build a small activation chamber that can be located in close proximity behind a standard VBTS target holder. To devise a method for placing this chamber into position and to retrieve it after an activation run without disrupting the routine production programme. Note that this objective has been met during the MSc project. A description of this facility is presented in Section 2.3.

- Collection of a relatively large number of samples to activate with secondary neutrons during routine radionuclide productions with 66 MeV protons in the VBTS. The selection should cover a wide mass region.

- After the activation, to assay all the samples for their induced radioactivity with an off-line gamma-ray spectrometer system.
- Analyze all the measured spectra and derive production yields for all reaction products that can be identified uniquely.
- Perform calculations and simulations in order to make predictions of all observed yields. Select a state-of-the-art Monte Carlo radiation transport code for this purpose to simulate the VBTS and to find in this way the expected neutron spectrum in the location of the activation chamber. Find the most recent evaluated cross-section data for the relevant neutron-induced reactions and use only those values for the calculated predictions.
- Find an appropriate way to compare the yield predictions with the corresponding measurements, where the number of radionuclides may be quite large.
- Estimate to what extent the predictions can be trusted for cases where no experimental data exist.
- Finally, to derive and list the effective cross sections for all the observed reaction products.

6.2 EXPERIMENTAL ASPECTS AND CONSIDERATIONS

6.2.1 Primary target composition

The 66 MeV proton beam traverses many layers of materials during the bombardment of a VBTS target. In this study, a tandem Rb/Ga target was bombarded in a usual ^{82}Sr/^{68}Ge routine production for each of the experimental runs. Table 5.1 in the previous chapter shows the material layers of the tandem target. The beam is expected to stop in layer no. 12, namely Ga metal, which will be in a molten state when there is beam on target.

6.2.2 Neutron-activated samples

A list of the samples activated in Run-1 is presented in Table 6.1. The majority were single elements but there were also some compounds. All samples had natural isotopic composition, chosen from available stock at iThemba LABS with the main purpose to cover a wide mass region. All samples were made up to fit into small plastic bags, 13 mm by 13 mm after being sealed. The plastic became brittle during the bombardment but survived. The samples had to be handled with extreme care after bombardment until adhesive tape could be applied on both sides, prior to mounting them on counting frames. Some of the larger samples were subdivided after activation for purposes of making good sources for counting.

In the case of Run-2, only seven different sample types were activated but with some multiplicities introduced. This was to test for possible asymmetry in the neutron flux with respect to the beam axis. Table 6.2 presents the complete list of samples. Three samples of enriched ^{66}Zn metal foil were included as well as two samples of ^{68}ZnCl salt, all sealed in 13 mm by 13 mm plastic bags as described above. The ^{68}ZnCl samples were included specifically because of our interest in ^{67}Cu production. Unfortunately these two salt targets were found to be destroyed after the bombardment. The hardened plastic coverings of these targets cracked either during

Table 6.1: Targets/samples activated by neutrons behind a VBTS target during Run-1.

Target material	Z	Mass (g)	Purity (%)	Supplier
^{9}Be	4	0.0104	99.5	Goodfellow, UK
^{23}Na (as NaI)	11	0.609	99.5	Sigma Aldrich, USA
^{nat}Ti	22	0.135	99.999	Goodfellow, UK
^{55}Mn	25	0.835	99.95	Goodfellow, UK
^{59}Co	27	0.983	99.9	Goodfellow, UK
^{nat}Ni	28	0.730	99.98	Goodfellow, UK
^{nat}Br (as CsBr)	35	0.694	99.5	Merck, Germany
^{nat}Rb (as RbCl)	37	0.473	99.8	Sigma Aldrich
^{89}Y	39	0.247	99.9	Goodfellow, UK
^{93}Nb	41	0.577	99.9	Goodfellow, UK
^{103}Rh	45	0.459	98.16	Reactor Experiments, USA
^{nat}Ag	47	0.362	99.95	Goodfellow, UK
^{115}In	49	0.635	99.99	Koch Chemicals
^{127}I (as NaI)	53	0.609	99.5	Sigma Aldrich, USA
^{133}Cs (as CsBr)	55	0.694	99.5	Merck, Germany
^{141}Pr	59	0.363	99.9	Goodfellow, UK
^{nat}Gd (as Gd_2O_3)	64	0.431	99.9	Sigma Aldrich, USA
^{169}Tm (as TmO)	69	0.696	99.9	Fluka, Switzerland
^{181}Ta	73	0.660	99.95	Goodfellow, UK
^{197}Au	79	0.436	99.99	Goodfellow, UK
^{nat}Tl (as TlCl)	81	0.531	>99.0	BDH Chemicals, UK
^{209}Bi	83	0.408	99.97	Goodfellow, UK

the bombardment or during their retrieval from the target station afterwards. The salt crystals dissolved in their own crystal water, which partially leaked out. While some sources could be made, no credible quantitative data could be obtained from these sources and they were subsequently discarded. Following this incident, enriched ^{68}Zn metal-foil samples were sourced and activated in Run-3. Because the analysis of the ^{68}ZnCl salt samples was abandoned, they are omitted from Table 6.2.

Concerning all the enriched Zn samples of this study, note that a distinction is made between the actual material and the main constituent isotope of the material. In the case of ^{66}Zn, for example, the sample material is denoted as s[^{66}Zn] to distinguish it from pure mono-isotopic ^{66}Zn. This is done because all the Zn samples are well characterized in terms of their isotopic composition. A summary of the constituent percentages for all the Zn materials employed is given in Table 6.3.

In Run-3 the focus was mainly on Zn samples relevant to ^{67}Cu formation. Only six samples were activated, a summary of which is presented in Table 6.4. Details of the ^{68}Zn sample preparation and composition are given in Ref. [SCH2001].

As already mentioned, in Run-2 an attempt was made to see if axial asymmetry of the

Table 6.2: Targets/samples activated by neutrons behind a VBTS target during Run-2.

Target material	Source name	Z	Mass (g)	Purity (%)	Supplier
^{nat}Mg	Mg-1	12	0.0130	99.9	Goodfellow, UK
	Mg-2		0.0120		
	Mg-3		0.0121		
^{27}Al	Al-1	13	0.0679	99.9	Goodfellow, UK
	Al-2		0.0654		
	Al-3		0.0757		
^{nat}Zn	^{nat}Zn-1	30	0.1326	99.8+	Goodfellow, UK
	^{nat}Zn-2		0.1119		
	^{nat}Zn-3		0.1215		
s[^{66}Zn]	s[^{66}Zn]-1	30	0.2222	99.0	Technabexport, Russia
	s[^{66}Zn]-2		0.1993		
	s[^{66}Zn]-3		0.2028		
^{103}Rh	Rh-1	45	0.1041	98.16	Reactor Experiments, USA
	Rh-2		0.1067		
	Rh-3		0.0982		
^{232}Th	Th-1	90	0.0538	99.7	Goodfellow, UK
	Th-2		0.0471		
	Th-3		0.0482		

Table 6.3: Zn sample/target materials employed and abundances* of their constituent stable isotopes.

Target material	^{64}Zn (%)	^{66}Zn (%)	^{67}Zn (%)	^{68}Zn (%)	^{70}Zn (%)
^{nat}Zn	49.17	27.73	4.04	18.45	0.61
s[^{66}Zn]	0.40	99.0	0.17	0.43	0.03
s[^{67}Zn]	1.44	2.2	91.5	4.78	0.08
s[^{68}Zn]	0.03	0.09	0.75	98.32	0.81

* For ^{nat}Zn according to the NuDat 3.0 library [SON2005].
For enriched Zn samples according to their suppliers.

Table 6.4: Targets/samples activated by neutrons behind a VBTS target during Run-3.

Target* material	Source name	Z	Mass (g)	Purity (%)	Supplier
^{27}Al		13	0.0535	99.9	Goodfellow, UK
^{nat}Zn		30	0.0835	99.8+	Goodfellow, UK
s[^{66}Zn]		30	0.1958	99.0% ^{66}Zn	Technabexport, Russia
s[^{67}Zn]		30	0.0481	91.5% ^{67}Zn	Technabexport, Russia
s[^{68}Zn]	s[^{68}Zn]-1	30	0.0438	98.32% ^{68}Zn	PSI, Switzerland
	s[^{68}Zn]-2	30	0.0416		

* See also Table 6.3.

neutron flux might be a problem. For this reason, three foil samples of the same material were activated in the case of the metal samples. These samples were spaced approximately 120° with respect to each other in a triangular fashion, shown schematically for the three Mg samples in Figure 6.1. In all the runs the samples were spaced approximately equidistant from each other in a circle, with partial overlap unavoidable in Run-1 and Run-2 but never more than two layers deep. The centre region of the sample chamber was blocked by attaching a circular piece of polystyrene (with a 30 mm diameter) in that position, ensuring that all samples were positioned in the remaining annular cavity. This was done in order for all samples to have the same orientation with respect to the beam axis, or as close to such a situation as one could reasonably achieve. The premise was that such a configuration would allow all samples to be subjected to the same neutron flux.

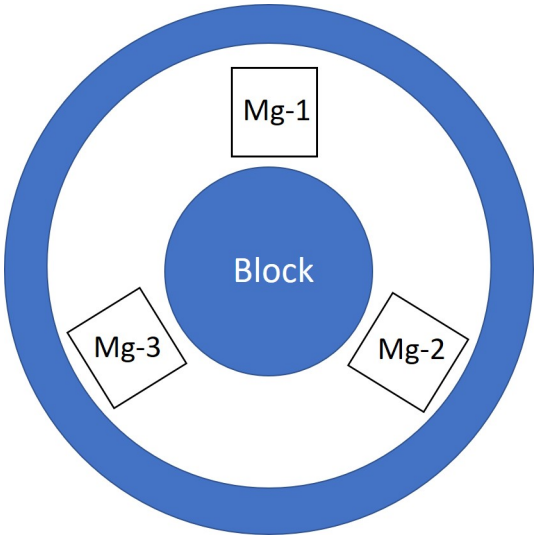


Figure 6.1: Schematic top view of the neutron irradiation chamber, showing the locations of the magnesium samples during Run-2.

6.2.3 Bombardments

In all three runs the samples were activated over several days. In Run-1 the accumulated charge was 20 000 μAh. Run-2 and Run-3 had shorter durations, the accumulated charges being 13 645 and 14 406 μAh, respectively. The beam current was logged in 1-second intervals. These beam histories were stored as numerical data and utilized in the analysis. The typical beam current, when beam was on target, varied between 180 and 220 μA.

6.2.4 Radionuclide assays

Gamma-ray spectra of all activated samples were measured off-line as described in Section 2.6. The source-detector distances varied between 10 cm and 2 m from the face of the HPGe detector, depending on the dead time, which was typically kept below 5%. A first counting session was started immediately after the samples could be removed from the VBTS, usually a few hours after a production run was stopped. These initial runs were quite short, with typical live times of the order of 1000 seconds. A second counting session was initiated about 24 hours

later, with live counting times typically between 30 minutes and 1 hour. A third counting session, starting about a week later, counted samples for typically between 8 and 12 hours. A fourth counting session was done about a month later but only for selected samples, in cases where radionuclides with very long half-lives had to be assayed. In these cases the live counting times could be up to a number of days. Meticulous records were kept of all spectra as the spectrometric counting progressed.

6.3 MONTE CARLO SIMULATIONS

Monte Carlo simulations were employed to obtain the neutron flux behind selected radionuclide production targets. There are several general Monte Carlo codes available that would have sufficed our needs, such as Geant4 and FLUKA, both of which are freely available from their custodian, CERN. The choice, however, was to employ the MCNP6 code, which is under the custodianship of Los Alamos National Laboratory (LANL) in the US. This decision was partly because of the main role of MCNP in recent studies of a similar nature elsewhere, particularly those performed at LANL [ENG2012a, ENG2013, ENG2014b]. An overview and history of the Monte Carlo method is presented first, followed by the specifics of the simulations performed in this study.

6.3.1 Overview and history

A 66 MeV proton beam incident into the VBTS will be completely stopped by a radionuclide production target. Only about 7% of these protons will induce nuclear reactions, most of which will lead to the emission of secondary neutrons. It is significant that the overwhelming majority of beam protons are slowed down and stopped as a result of a large number of interactions with atomic electrons only; from this perspective the nuclear interactions are not dominant. In spite of this, it is amazing how useful the relatively small percentage of nuclear interactions turns out to be, especially in the field of radionuclide production.

The spectrum of emitted neutrons comprises contributions from various nuclear processes. The so-called spallation neutrons are emitted at the highest energies. They are formed by direct (fast) interactions on a time scale of approximately the time required for a proton to traverse a nucleus (about 10^{-22} seconds.) They typically have a long range in matter and cause further neutron-induced reactions within the materials that they traverse. This is the main reason why the contents of an irradiation vault (including the walls, floor and roof) gradually become more radioactive. Highly excited nuclei are formed by nuclear reactions, mainly by the protons inside the target materials but also by long-range neutrons in all the other materials. These excited nuclei will eventually de-excite, in many cases leading to additional neutron emission but typically at much lower energies than the spallation neutrons. The so-called evaporation neutrons are emitted at the lowest-energy side of the spectrum (on a time scale of about 10^{-16} seconds), a process often likened to the emission of atoms or molecules from a hot liquid drop. Evaporation neutrons are emitted from excited nuclei that have reached statistical equilibrium, the available excitation energy having distributed statistically to all constituent nucleons. Indeed, the escape of an evaporation neutron from an equilibrated nucleus has

become a purely statistical process. Between these two extremes, i.e. spallation at the highest energies and evaporation at the lowest energies of an emission spectrum, a host of intermediate processes can be identified. These processes are collectively referred to as preequilibrium or precompound processes or reactions, leading to the emission of neutrons having intermediate energies. Intermediate-energy neutrons are emitted by excited nuclei that de-excite before reaching statistical equilibrium, earlier in the evolution of the nuclear reaction that initiated the equilibrating process but long after a direct nuclear reaction is likely to occur.

Monte Carlo radiation transport simulations can be performed in which all the various materials as well as the proton beam can be modelled with a significant degree of precision. The code MCNP6 version 6.1 was used for all the model development but final runs were performed with a later version of the code, version 6.2. MCNP is an acronym for Monte Carlo N-Particle [GOO2012, PEL2013]. This code, as well as the Monte Carlo technique in general, has a very long history, traceable to the years just after World War II. This history is too vast to summarize here but a few salient aspects are discussed below.

Harrison [HAR2010] describes Monte Carlo simulations as computer techniques used for random sampling and statistical modelling to estimate mathematical functions and/or mimic the operation of complex systems. The name is synonymous with a well-known casino in Monaco, since chance and random outcomes are central to gambling as much as they are to any statistical simulations. The idea was first introduced by a mathematician who participated on the Manhattan Project, Stanislaw Ulam. After the war, while recovering from surgery, Ulam spent most of his time playing the card game Solitaire. He started to plot the outcomes of completed games in order to observe their distribution, hoping to determine the probability of winning. Ulam later shared his ideas with John Von Neumann, a Hungarian-American mathematician and physicist who made massive contributions to the emerging field of computer science. These two started to collaborate and was later joined by a third colleague, Nicholas Metropolis, to develop what is now known as the Monte Carlo simulation technique [KWA2007]. It was Metropolis who gave the technique its name.

The Monte Carlo technique had an almost immediate impact on the nuclear sciences, already implemented on the first generation of electronic computers. Enrico Fermi, while at Los Alamos in 1947, traced the movements of neutrons through fissionable materials by means of some of the earliest Monte Carlo simulations in the field. Many different codes emerged during the 1950s and 1960s, some specialized for neutrons and others for photons. More general three-dimensional particle transport capability was developed and introduced into these codes. Various mergers took place to account for neutron-photon interactions. One such merger, in 1977, resulted in the first version of the MCNP code, which originally stood for Monte Carlo Neutron Photon [GOO2012]. The first version of the code released for public distribution was MCNP3 in 1983 (to the Radiation Safety Information Computational Center, RSICC). The change of the acronym MCNP to Monte Carlo N-Particle was introduced in 1990 when electron transport was added. There was a split in the development of MCNP during the MCNP4 era, when developers of the Accelerator Development of Tritium (ATP) team required the utility of many-particle transport (also called eXtended-particle or X-particle transport). This led to the separate development of MCNPX and MCNP4 by separate teams. During 2001 and 2002,

MCNP4 version C was completely rewritten in modern Fortran 90, including support for large-scale parallel processing on new generations of multi-core computer architectures. In July 2006, driven from the top by the management of LANL, the two development efforts merged again, taking MCNPX version 2.6B and MCNP5 to their last few individual releases. The first joint release was MCNP6 in 2013. The most recent version of the code is MCNP6.2. It is described by its developers as a general-purpose, many-particle, continuous-energy, generalized-geometry, time-dependent, Monte Carlo radiation transport code system [ARM2017].

MCNP6.2 was released bundled with processed nuclear data based on the ENDF/B-VII.1 library, which is an evaluated nuclear data file released in December 2011 [CON2013]. It was subsequently replaced with a new file based on the 2018 release of the ENDF/B-VIII.0 library [CON2018], which was implemented in the code version used for the final MCNP runs of this study. The Evaluated Nuclear Data File ENDF/B is maintained by the Cross Section Evaluation Working Group (CSEWG), which is an international collaboration coordinated by Brookhaven National Laboratory (BNL) in the US. In cases where evaluated nuclear data are not available – e.g. for many materials evaluated neutron-induced cross sections are unavailable above about 20 MeV – nuclear models are employed to provide predicted values.

6.3.2 Nuclear models and physics selections

The aim of the Monte Carlo simulations described here was solely to obtain the secondary neutron flux in the activation chamber located in the pusher assembly of the VBTS. The calculations required to make yield predictions, for radionuclides formed by neutron-induced reactions, were performed outside of the MCNP code. Since the so-called "table physics" was insufficient in terms of the required evaluated cross sections for most of the materials, physics models had to be selected to fill this gap. Six different combinations of models were employed in this part of the investigation. Three of them are so-called intranuclear cascade models, which have to be combined with an evaporation model for a complete "model physics" selection. The MCNP code provides two different evaporation models, both of which can be combined with any of the intra-nuclear cascade models. A fourth model contains both cascade and evaporation stages intrinsically. These models are briefly described below.

The basic assumption of the intranuclear cascade (INC) models is that the interactions of high-energy particles with a nucleus can be approximated by free particle-particle collisions (viz. nucleon-nucleon collisions) inside the nucleus. The justification for this approximation is an assumption that the wavelength of the incident particle is of the order of, or smaller than, the inter-nucleon distance. This physical process, described as free two-body collisions within the nucleus, is called the cascade. This approximation is really only valid at sufficiently high excitation energies. In the normal evolution of a nuclear reaction, the cascade is followed by other physical processes, such as preequilibrium particle emission (including cluster emission), evaporation, fission, or de-excitation by photon emission [FIL2009]. In principle the intra-nuclear cascade is a preequilibrium process but as the cascade is normally terminated while the nucleus is still decidedly in an unequilibrated state, another preequilibrium model is often required to describe the further evolution of the reaction towards equilibrium. The later stage of the reaction evolution is usually evaporation, except for fissionable materials where evaporation

is in competition with fission. When particle emission becomes improbable in the de-excitation stage of a nucleus, further de-excitation by gamma-ray emission will still occur.

Two of the earlier INC models implemented in MCNP, the Bertini and ISABEL models, date back to the early 1960s but have undergone numerous developments and additions over the years. They are both standard options in MCNP6. Filges and Goldenbaum [FIL2009], in their Handbook of Spallation Research, describe the Bertini model as the precursor of all modern INC models. This includes ISABEL, the Liège Intranuclear Cascade Model (INCL) and the Cascade-Exciton Model (CEM). The various INC models differ in their criteria to determine when a particle has left the cascade, i.e. when the first stage or cascade stage has ended. Spallation neutrons are produced by inelastic intranuclear collisions during this stage.

A later edition to the MCNP code is the Liège Intranuclear Cascade Model (INCL), developed by Joseph Cugnon and co-workers at the University of Liège, Belgium [KAI2011, LER2013]. The current version is INCL*4* (the latest stable edition is version 4.6). This model is frequently used in combination with ABLA, which is a fission and evaporation code [GAI1991]. The alternative to ABLA for modelling the evaporation stage is usually referred to as Dresner, the originator of an evaporation code with great longevity which is still widely used in various Monte Carlo codes [FIL2009, KON2011].

The Cascade-Exciton Model (CEM) is nowadays the default option in MCNP, since the release of version 6.1 [MAS2002]. (In prior versions the default was the Bertini/Dresner physics selection.) In CEM the reaction is treated in three distinct stages. The first stage is an intranuclear cascade, during which primary particles can be scattered and produce secondary particles. These secondary particles can be emitted or re-absorbed by the nucleus. By the time the cascade stage has terminated, an excited residual nucleus is left in a non-equilibrated state, having a particle-hole configuration that is the starting point of the second stage. The second stage is a preequilibrium stage, solved by means of the Modified Exciton Model (MEM), during which preequilibrium emission of individual nucleons or clusters may occur. The third stage is the evaporative final stage of a fully equilibrated nucleus, which may be in competition with fission in the case of fissionable nuclei. When the CEM model is selected, the parameter selecting an evaporation-fission model is ignored. The physics selections (models) chosen for this part of the thesis project are as follows:

1. Bertini/ABLA,
2. Bertini/Dresner,
3. CEM,
4. INCL/ABLA,
5. ISABEL/ABLA,
6. ISABEL/Dresner.

These six physics selections were investigated by Feghhi *et al.* [FEG2015] in a study of the emission spectra of neutrons from a spallation target, prompting us at the start of this study to also investigate them in a comparative study of their predictive power in our application.

6.3.3 Geometry specification

A three-dimensional model of the VBTS was developed by utilizing standard macrobodies and surfaces supplied within the MCNP code system [SHU2007, PEL2013]. About 95% of the model was retained since the MSc project [MOT2019] but some improvements and corrections were implemented. A visual inspection of the model was done as it was developed from stage to stage, utilizing the plot routine of MCNP6, which also provided diagnostics, errors and warnings of possible mistakes. While the total material budget is realistic, not every bolt and nut were modelled as this would have taken a very long time. Simplifications were introduced based on judgements that had to be made. We are convinced, however, that all major components have been incorporated with a sufficient degree of precision and that the model closely resembles the actual VBTS and its targetry.

The geometry of the model is shown in Figures 6.2 through 6.4, zooming in from figure to figure. A part of the vault and the complete VBTS are shown in Figure 6.2. The target region and pusher assembly are shown in more detail in Figures 6.3 and 6.4. The annular cavity that held the samples was modelled as a single cell, excluding the actual samples. The average neutron flux in this cell was obtained from a so-called F4 flux tally, the results given in units of neutrons/cm^2 per source proton.

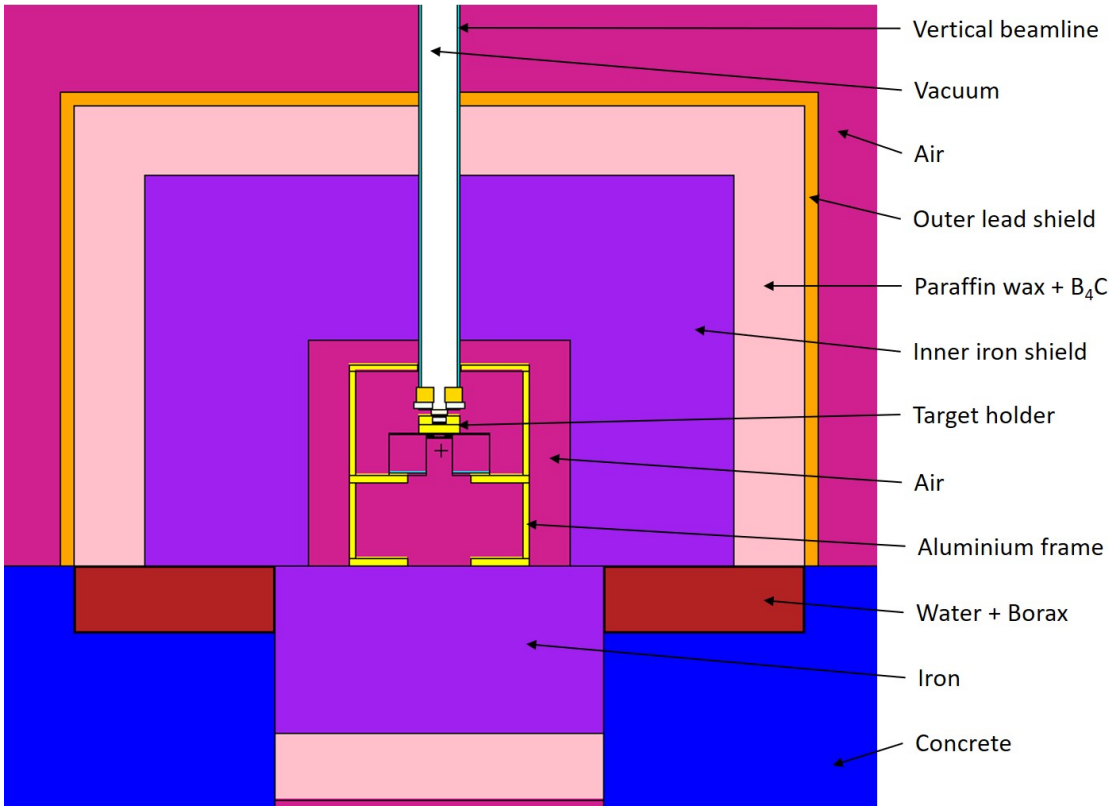


Figure 6.2: The geometry of the VBTS model and vertical beamline as generated with the MCNP6 code system. Note that subsequent figures zoom into the target region to show more detail. The image is coloured by materials selection.

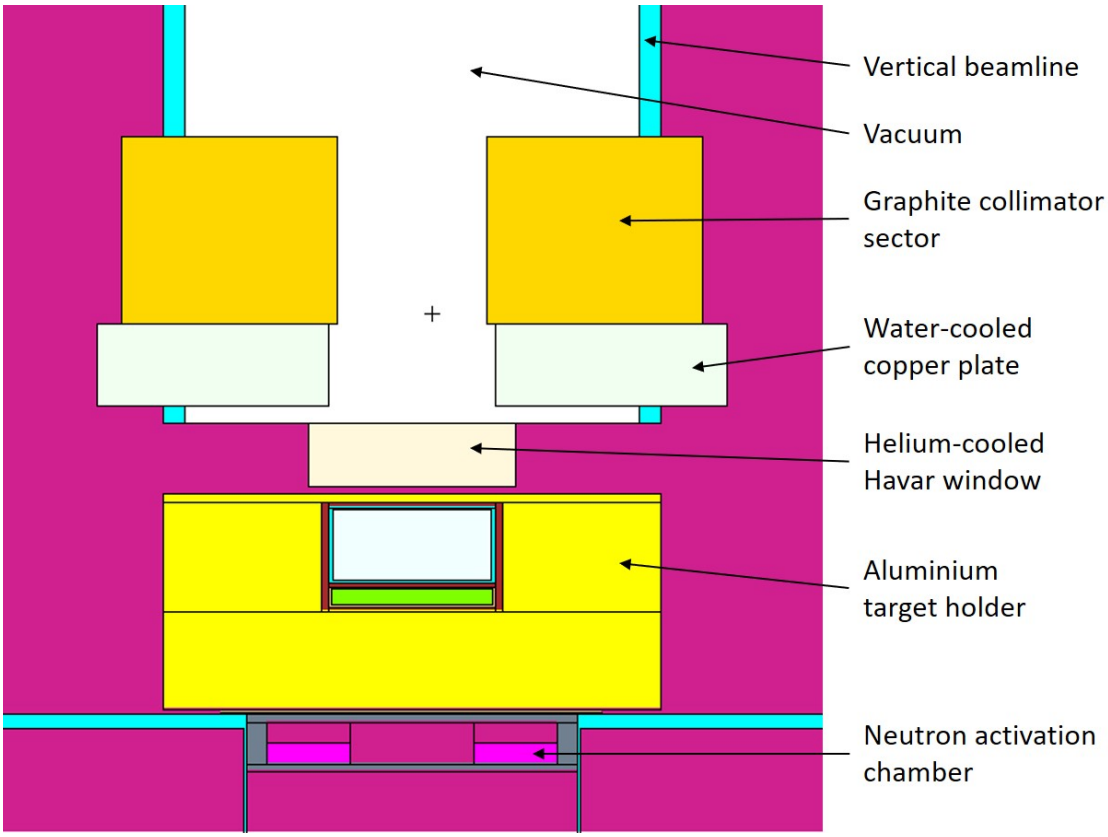


Figure 6.3: The target region of the VBTS model as generated with the MCNP6 code system. Note that Figure 6.4 zooms in further to show the region of the neutron activation chamber.

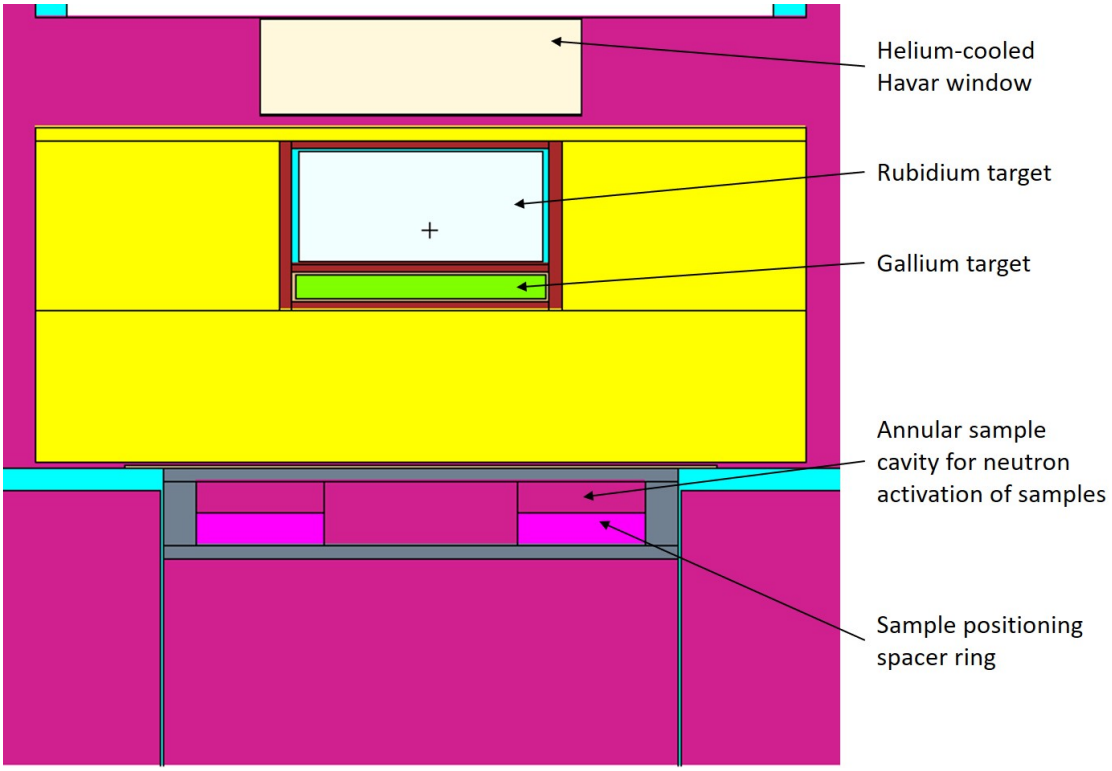


Figure 6.4: Zoomed-in view showing the target holder, tandem Rb/Ga targets, and the neutron activation chamber located in the target pusher assembly of the VBTS model, as generated with the MCNP6 code system. See also Figures 6.2 and 6.3.

6.3.4 The effect of the error in geometry on previous results

As already mentioned, a mistake was made in the geometry of the target set-up in the MCNP model, which affected the model predictions presented in reference [MOT2019]. This led to a consistent overprediction of the measured yields, irrespective of the choice of physics selections in the model. At that time, the issue was not understood and remained unresolved. Now it is understood that the thickness of the back-end of the target holder was incorrectly modelled. This has to do with two components inside the target holder that are generally referred to as the "inserts" in iThemba LABS jargon. A photograph of a target-holder back plate with a set of inserts is shown in Figure 6.5.

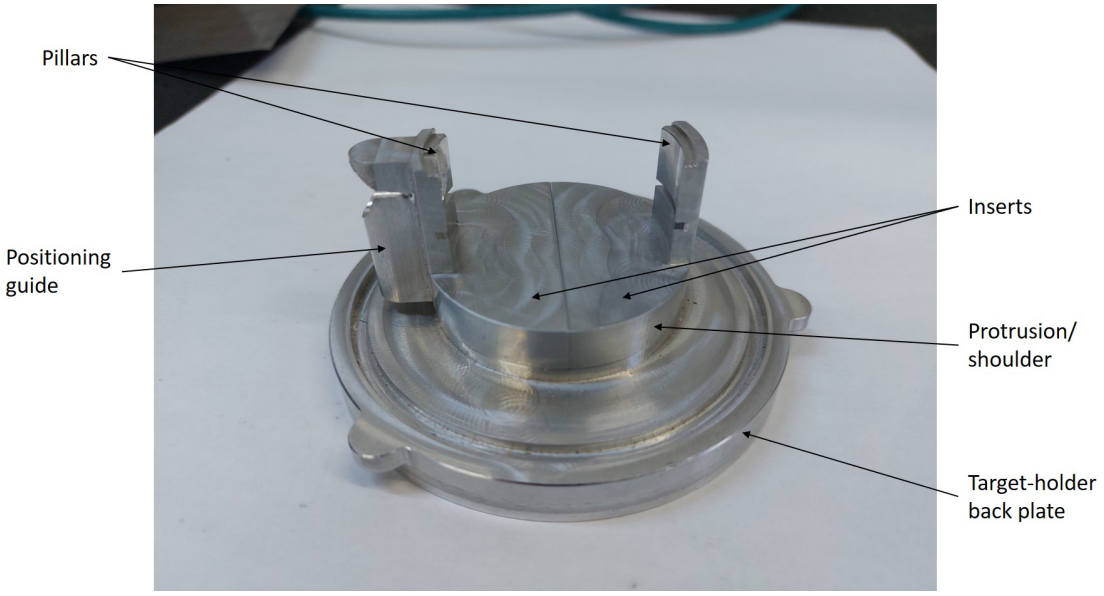


Figure 6.5: Photograph of the target-holder back plate and inserts, showing the protrusion/shoulder introduced onto the beam axis once an assembled target would be loaded into the irradiation position.

Essentially, the inserts provide two grooved pillars that assist in holding the actual targets in place inside the target holder. These two components fit together and locate as a unit into a recess machined into the target-holder back plate. During the initial discussions, when the MCNP modelling work commenced, it was decided that there was no need to include these two pillars in the model. At that time it seemed like a justifiable simplification to omit them. Unfortunately, this also led to an error of judgement as the two inserts, once assembled onto a back plate, introduces an additional layer of aluminium that adds to the total thickness of material at the back-end of the target holder. In other words, the inserts contain material that constitutes another aluminium layer on the beam axis. The omission of the inserts also led to the omission of this important material layer from the model. Furthermore, the way the input file was written did not check whether the sum of thicknesses of all on-axis target materials reproduces the thickness of the actual target holder. Once the mistake was discovered, a few lines of code implemented such a check. The omission of this essential material layer in the model resulted in the tandem targets being located closer to the neutron activation cavity than they would be in reality. The overprediction of the neutron flux was mainly due to two contributing factors: (1) less material between the targets and activation cavity than in reality;

(2) a larger solid-angle range subtended by the activation cavity to the neutron flux emitted from the targets. Both effects were thoroughly investigated in subsequent MCNP runs. It turned out that the latter contributor (i.e. the "solid-angle effect") was the main contributor by far to the overpredicted neutron flux in the sample cavity of the activation chamber. In the latest implementation of the model, the aluminium thickness of the back-end of the target holder is taken as the sum of the thicknesses of the actual back plate and the protrusion (shoulder) formed by the inserts. A sum check is also performed separately and compared to the actual target-holder thickness – the two values should be the same.

6.3.5 Proton-beam simulations and particle histories

The primary particles tracked in the simulation are the protons of the incident beam, referred to as "particle histories" in the parlance of MCNP. Simulations are typically developed and tested by running a relatively small number of particle histories (e.g. 100 000) followed by longer runs with a larger number of particle histories on a more mature problem (i.e. several millions). In the final runs of this work, problems were typically run with 2×10^8 particle histories.

The cyclotron beam from the SSC has a very typical Gaussian intensity profile. In order to spread the beam out and optimize the intensity profile on target, the beam is swept (or rastered) in a circular fashion with a sweep frequency of 3 kHz during VBTS operations. This also helps to prevent hot spots on a target. The MCNP code has several powerful implementations for beam sources. In the case of the MSc project, the source term was always specified as a single proton beam. After further investigations subsequently, a better way was discovered, utilizing the "transformation" (TR) statement in the source definition. The TR statement allows one to define multiple beams by duplicating a primary beam and placing its centre on new coordinates. In this study, all incident beams were defined to be parallel to each other but to be located with their centres on a circular trajectory with a radius similar to a typical beam sweep radius. The black circle in Figure 6.6 represents an unswept beam, i.e. when the sweeper magnets have been powered down. The red circles represent the swept beam for the case where the beam radius is the same as the sweep radius, which is close to the optimal case for circular sweeping at a constant radius [STE2013]. Eight discrete beams are shown in Figure 6.6, separated by azimuth angles of 45°. This is just for purposes of illustration. In the MCNP model the discrete set of beams totalled 72, separated by azimuth angles of 5°. In any Monte Carlo run, the protons are generated singly and tracked in a sequential manner. Each successive particle history had equal probability to be generated from any of the 72 beams.

Sensitivity runs were performed by varying the number of discrete beams. It was found that differences were only subtle between the case having 16 beams and cases specifying a larger number of beams, with no significant differences when choosing more than 72 beams. For the final runs the number of beams were kept at 72, which is considered to be a realistic approximation to a swept beam in the VBTS. A cookie-cutter cell with the same diameter as the collimator aperture was also specified, as in real bombardments more than 99% of beam protons will pass cleanly through the collimator. This is assured by the fact that strict current limits are enforced on collimator sectors to avoid them from becoming damaged, being interlocked to trip the accelerator RF should a sector current limit be exceeded.

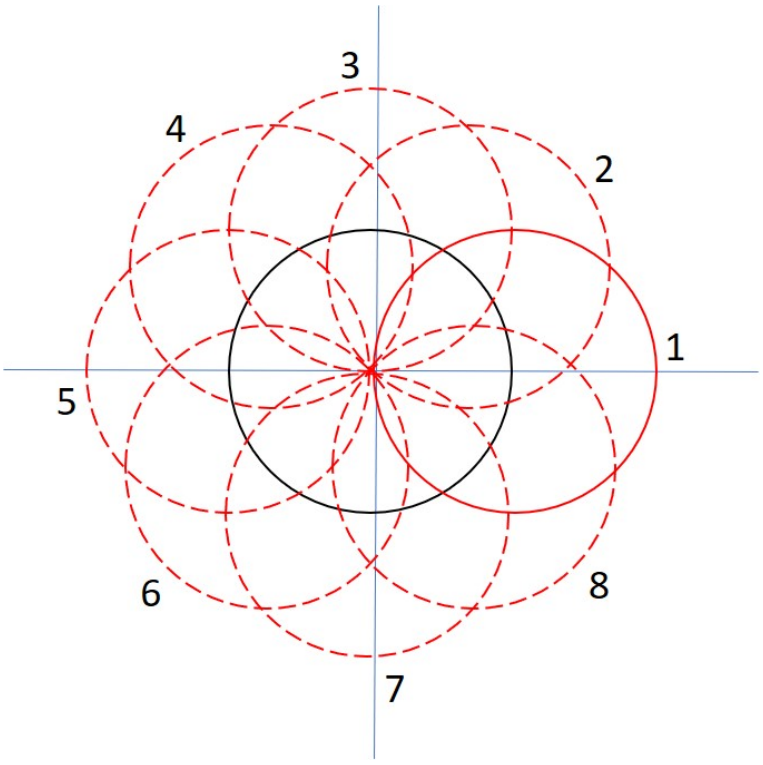


Figure 6.6: Schematic diagram illustrating the modelling of a circularly swept (rastered) beam (see text).

6.4 DATA ANALYSIS

6.4.1 Energy-group structure

The LaBauve energy-group structure is a 63-group structure ranging from 10^{-11} MeV to 25 MeV, defined by LaBauve for the CINDER'90 code [WIL1993]. This code was developed for activation and burn-up calculations in reactor problems. As the upper energy limit of 25 MeV would not be suitable for tallying neutrons with energies between 25 and 70 MeV, it was necessary to introduce a modified LaBauve energy-group structure. All the LaBauve groups below 1 MeV were adopted unchanged. The energy group that crossed 1 MeV was truncated at an upper value of 1 MeV. Energy groups above 1 MeV were defined to have a constant 1 MeV width, terminating at 67 MeV. This resulted in a total of 117 energy groups or bins, 51 of which tallied energies below 1 MeV. A table of the complete energy-group structure is presented in Appendix B. (Note that in Appendix B the energy-group structure has been extended to 120 groups as simulations were later extended to 70 MeV).

6.4.2 Pointwise and group-averaged cross sections

In this study, formation cross sections of radionuclide residues produced by neutron-induced reactions were taken from the TENDL-2019 and TENDL-2021 libraries [KON2019]. TENDL is an acronym for "TALYS-based evaluated nuclear data library", providing the output of nuclear model calculations with the TALYS code system for direct use in basic physics and applications. The latest edition, TENDL-2021, is the 11^{th} version of the library. Initially the yield predictions were performed with TENDL-2019, a task that nearly reached completion when TENDL-2021 was released. The process was then repeated with the new library.

The TENDL libraries provide cross sections for residue production as pointwise data. In contrast, the Monte Carlo simulations with the MCNP code provided neutron flux values in discrete energy intervals or bins, generally referred to as multigroup data. The use of both pointwise and multigroup data in calculations require some care. Fortunately, methods exist to derive one data type from the other and vice versa, provided certain conditions are met. The methods employed in this study are briefly discussed below, including the derivation of so-called group-averaged cross sections.

The tabular cross-section data provided by the TENDL libraries are sufficient to represent the shape of an excitation function quite well. To obtain cross sections at energies in-between the tabulated values requires the use of a suitable interpolation scheme. Cubic spline interpolation was utilized extensively. It was convenient to incorporate a natural cubic spline routine into our own Fortran codes, obtained from the well-known compilation "Numerical Recipes in Fortran 77" [PRE1997]. Most of the TENDL data could be fitted directly but in a few cases Runge's phenomenon was observed, namely noticable oscillations between sample points. This could be remedied satisfactorily by enlarging the specific TENDL pointwise data set by means of spline filters. The "curve fitting and equation discovery package" TableCurve 2D [SYS2020] was used for this purpose. The "Digital Spline Filter" option of that code provides on-screen visualization and an easy way to increase the number of discrete points in a pointwise data set. The user can select from a selection of NURBS splines with order ranging between 1 and 8. Alternatively a B-spline of order 2 can be selected. The term B-splines is short for "basis splines", representing a class of splines that are piecewise polynomial functions of degree $n-1$ in the independent variable for a spline function of order n [GOS1990]. The NURBS splines are a specific class of B-splines called the "non-uniform rational basis splines". The TableCurve software allows the user to rapidly cycle through the choices of filters and also to adjust points to improve the fit. The latter was mostly not required as the TENDL data are generally quite smooth. We found the workflow with TableCurve to be highly evolved, intuitive and fast. The most recent version is 5.01 but we used the somewhat older version 4.0. Typically a TENDL data set will contain 121 pointwise values between threshold and 200 MeV. After filtering, a new data set with 500 values between threshold and 100 MeV would be created, and visually checked for goodness of fit. The latter process was also very well assisted by TableCurve in that points that are not well fitted change colour to red.

According to Hodgson *et al.* [HOD2015], two basic approaches to using cross sections are utilized in computational physics, namely "continuous" and "multigroup". The latter comes into play in Monte Carlo simulations as the tallying of emitted particles (neutrons in our simulations) requires energy intervals or groups. Cross sections are therefore required in which the pointwise data have been averaged over the respective ranges of the energy groups, generally referred to as group-averaged cross sections or multigroup cross sections. Group-averaged cross sections can be expressed as follows:

$$\sigma_i = \frac{1}{\phi_i} \int_{E_i}^{E_{i+1}} \phi(E)\sigma(E)dE; \quad 1 \leq i \leq N_g, \tag{6.1}$$

where $\phi(E)$ is a weighting function, $\sigma(E)$ is the excitation function (cross-section function)

and N_g is the number of discrete energy groups. The integration limits are the boundaries of the group. The quantity ϕ_i is the weighting function integrated over the group:

$$\phi_i = \int_{E_i}^{E_{i+1}} \phi(E)dE. \tag{6.2}$$

The weighting function in this case should be the neutron flux causing the activation. The evaluation of Equation 6.1 requires point data for the neutron flux, which is somewhat problematic as the Monte Carlo simulations providing such data produce multigroup values, not pointwise values. Fortunately there are ways to address this problem. The cumulative neutron flux function, derived by a simple summing of the multigroup flux spectrum, provides point data at all the upper limits of the groups. This can be defined as follows:

$$\Phi(E_{i+1}) = \sum_{j=1}^{i+1} \phi_j; \quad 1 \leq i \leq N_g. \tag{6.3}$$

Next, these pointwise cumulative flux values can be fitted with simple polynomials in a piecewise manner, where again we found TableCurve very useful. The derivatives of simple polynomials are also simple polynomials of one unit lower order, which can easily be implemented in any Fortran code, the coefficients of which have been provided by TableCurve during the fitting process. These derivative functions can then be used to calculate pointwise flux values at any energies within the applicable range. The only group not covered by this method is the group at lowest energy (i.e. group 1 – see Appendix B). For this group a Newton-Cotes formalism was used, which is discussed next.

There are also other, simpler methods to average point data into multigroups, such as the closed-form Newton-Cotes formulae. The lower-order Newton-Cotes formulae are often employed in numerical integration algorithms. The Newton-Cotes formula of degree 1 is often referred to as the Trapezoid rule. Similarly, Newton-Cotes of degree 2 is Simpson's rule; degree 3 is Simpson's 3/8 rule; and degree 4 is Boole's rule. Let a and b denote the lower and higher group boundaries of an arbitrary chosen neutron group, as shown in Figure 6.7. Let E_j define a set of equispaced neutron energies within the region $a \rightarrow b$ as follows:

$$E_j = a + j(b-a)/n; \quad 0 \leq j \leq n, \tag{6.4}$$

where n is the "degree" of the scheme. For each neutron group i, the group cross section can be evaluated by applying the closed-form Newton-Cotes formulae as summarized in Table 6.5.

It was found that the different Newton-Cotes formulae gave very similar results to the group-averaged cross-section expression of Equation 6.1 in all groups above 1 MeV. Below 1 MeV the differences for some groups were sometimes relatively large between values obtained by means of Equation 6.1 and the Newton-Cotes expressions (up to 20% in some cases), probably because relatively few groups cover a range spanning many orders of magnitude. The decision was therefore made to adopt the Newton-Cotes expression of degree 4 for all groups above 1 MeV (to save some labour) but to evaluate Equation 6.1 rigorously for all groups below 1 MeV. Newton-Cotes of degree 4 was also used to evaluate group 1.

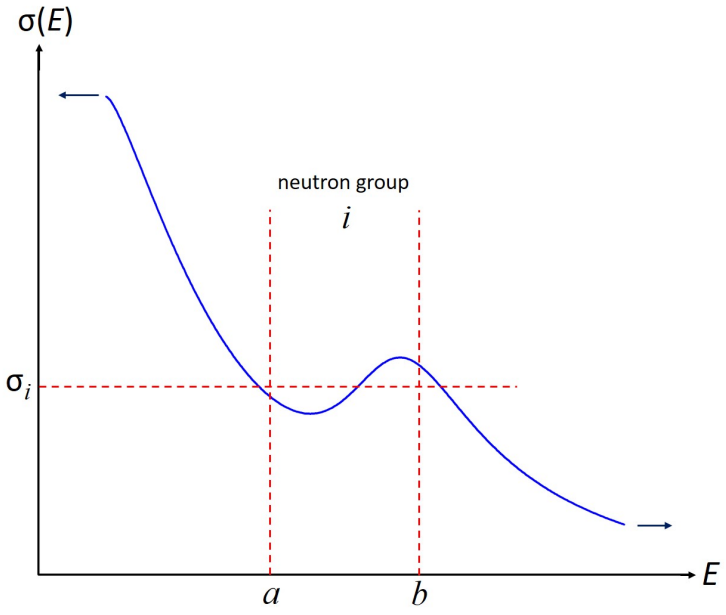


Figure 6.7: Illustration of a neutron energy group defined for an arbitrary excitation function (cross section $\sigma(E)$ versus neutron energy E) to discretize the cross section in that group (or bin). The nomenclature introduced in this figure are also used in the Newton-Cotes expressions listed in Table 6.5.

Table 6.5: The group cross section according to the closed-form Newton-Cotes formulae.

Degree	Formula used for σ_i	Common name
1	$\frac{b-a}{2}[\sigma(E_0)+\sigma(E_1)]$	Trapezoid rule
2	$\frac{b-a}{6}[\sigma(E_0)+4\sigma(E_1)+\sigma(E_2)]$	Simpson's rule
3	$\frac{b-a}{8}[\sigma(E_0)+3\sigma(E_1)+3\sigma(E_2)+\sigma(E_3)]$	Simpson's 3/8 rule
4	$\frac{b-a}{90}[7\sigma(E_0)+32\sigma(E_1)+12\sigma(E_2)+32\sigma(E_3)+7\sigma(E_4)]$	Boole's rule

6.4.3 The mean formation cross section

The mean formation cross section is a weighted average of all the group-averaged cross sections of all the individual groups. Let Φ_t denote the total neutron flux (neutrons/cm^2 per incident proton) in the annular cavity of the activation chamber, as given by the MCNP6 simulation. Let N_g denote the number of neutron groups of the adopted energy-group structure. The following identity then holds:

$$\frac{1}{\Phi_t}\sum_{i=1}^{N_g}\phi_i = 1, \tag{6.5}$$

where ϕ_i is the neutron flux in neutron group i; $1 \leq i \leq N_g$. One can interpret the ratio ϕ_i/Φ_t as the probability that a randomly observed neutron inside the activation cavity belongs to energy-group i. The mean cross section for the formation of a particular radionuclide by neutron activation can be defined as follows:

$$\overline{\sigma}_n = \frac{1}{\Phi_t}\sum_{i=1}^{N_g}\phi_i\sigma_i, \tag{6.6}$$

where σ_i is the group-averaged cross section pertaining to neutron group i.

6.4.4 Accumulated charge

Since the measured yields will usually be normalized to the unit of charge μAh, one would like to do the same for the predictions based on the MCNP6 neutron spectra in conjunction with excitation functions from the TENDL libraries. From a simulation one obtains the neutron flux per incident proton. Consequently, it is required to calculate the number of incident protons in an accumulated charge of 1 μAh. One proton has a charge of 1.602×10^{-19} C/s (Coulomb per second). Therefore 6.242×10^{18} protons have a combined charge of 1 C. We also have the following equivalence of units: 1 μAh $\equiv 3.6 \times 10^{-3}$ C. Thus 1 μAh contains 2.247×10^{16} protons, a number denoted by Q_p in the subsequent discussion on physical yields.

6.4.5 Predicted physical yields

The physical yield per unit mass of the sample, or more precisely per unit mass of the fraction of target nuclei of the same isotope in the sample, is given by

$$Y = \Phi_t Q_p \left(\frac{N_A}{A}\right) \lambda \overline{\sigma}_n (1 \times 10^{-27}) \qquad \text{Bq}\,(\mu\text{Ah})^{-1}\,\text{g}^{-1}, \tag{6.7}$$

where N_A is Avogadro's number, A is the atomic mass of the target nucleus in atomic mass units (AMU), λ is the decay constant of the produced radionuclide, and it is assumed that the mean formation cross section has units of millibarn. In cases where the target has a natural composition containing more than one isotope, Equation 6.7 can be successively applied to each target isotope, weighted with its natural abundance and summed.

6.4.6 Experimental physical yields

Most of the relevant equations related to experimental cross-section determinations and the related physical yields have been dealt with in Sections 2.7 and 2.8. They remain valid also for neutron-induced reactions. The physical yield per unit mass can be written as

$$Y = \frac{A_p \exp(\lambda[t_m - T])}{M\tau\epsilon_\gamma\epsilon_d \sum_{i=1}^{n} \Delta Q_i \exp(-\lambda[T - t_i])} \qquad \text{Bq}\,(\mu\text{Ah})^{-1}\,\text{g}^{-1}, \tag{6.8}$$

where M is the sample mass, A_p is the γ-ray full-energy peak area, τ is the counting live time, ϵ_γ is the γ-ray branching ratio, ϵ_d is the detector efficiency, t_m is the mean-value time within the real counting-time interval as given by Equation 2.17, T is the time of EOB where $t = 0$ is the time of the start of the bombardment, t_i is the incremental time when incremental charge Q_i of the beam was measured for all $1 \leq i \leq n$, where n is the number of incremental charge measurements made during the bombardment. Similar to Equation 6.7, in cases where the target has a natural composition containing more than one isotope, Equation 6.8 can likewise be successively applied to each target isotope, weighted with its natural abundance and summed.

6.4.7 Comparison between predicted and experimental yields

Physical yields for 121 reactions and/or nuclear processes could be uniquely determined from the measured γ-ray spectra, where the focus was on radionuclides with relatively long half-

lives. For all of these cases, corresponding predictions have been calculated using TENDL cross sections in conjunction with Monte Carlo simulations. These data cover a rather large mass range, from ^{7}Be to ^{207}Bi. During the MSc project, several approaches were considered to display such a large body of data in a way that provides a good visual insight into the overall level of agreement between predicted and measured values. In this work we followed a similar approach but with some changes, which will become apparent in the discussion below.

The first step was to establish a convenient numbering scheme by assigning a unique index or "reaction identification number" to each reaction or process. This numbering scheme starts at the light masses, with increasing index numbers in order of increasing Z as the first condition, followed by increasing A as the second condition. The idea is that this index can be displayed on the x-axis of a graph in order to show the trend of a quantity as a function of increasing atomic charge and mass. The quantity displayed on the y-axis should be something that facilitates a comparison between predicted and experimental yields. There are rather many ways in which this can be done. The initial effort was to simply use the ratios of the predicted and experimental yields.

Let i denote the reaction identification (ID) number, Y_{CALC} the calculated physical yield and Y_{EXP} the measured physical yield. As a first attempt, we plotted the ratio of the yields versus the reaction ID number, which can be expressed formally as follows:

$$H_0(Y_{CALC}(i), Y_{EXP}(i)) = \frac{Y_{CALC}(i)}{Y_{EXP}(i)}; \quad 1 \leq i \leq N_r, \tag{6.9}$$

where N_r is the total number of reactions for which physical yields could be extracted in the analysis (namely 121 from the extended data set). The reason for this particular notation will be explained in due course.

It turned out that plots made by means of Equation 6.9 were not very useful because of the asymmetric properties of ratios. A perfect agreement between a prediction and a measurement will give a value of 1. Ratios larger than 1 will indicate overpredictions and ratios smaller than 1 will indicate underpredictions. However, overpredictions and underpredictions do not display in a symmetric way. Underpredictions are always constrained between 0 and 1, while overpredictions are unconstrained. This makes it difficult to interpret plots of yield ratios versus ID numbers. Clearly, a way needed to be found to display overpredictions and underpredictions in a way that treats them the same. Such a way is provided by "indicators of relative difference", of which there are various types. If x and y are numerical values that need to be compared, an indicator of relative difference is any quantity $H(x, y)$ which possesses the symmetry property, namely $H(x, y) = -H(y, x)$. One class of indicators of relative difference is defined below:

$$H_1(x, y) = \frac{x - y}{M(x, y)}, \tag{6.10}$$

where $M(x, y)$ is a mean value of x and y. This can be the arithmetic mean, geometric mean, logarithmic mean, or any of many possible mean values that can be defined. Equation 6.10 will always result in a value of 0 if there is perfect agreement between a measurement and a prediction. Overpredictions will always result in positive values of H_1 and underpredictions will result in negative values. Overpredictions and underpredictions are now displayed in a symmetric way around 0 and both are unconstrained. In the MSc thesis, the logarithmic mean

was selected and results presented as the so-called "Log percentage difference" versus the reaction ID number. The Log percentage differences, or L% values, are sometimes employed in statistics because in addition to their "symmetry" properties they also have "homogeneity" properties, which allow them to be used in certain algebras [TOR1985].

While the above approach sufficed quite well to present our data (at least in our opinion), it was found that many people are unfamiliar with L% values. It turned out to be somewhat of a stumbling block when presenting our work, e.g. at conferences and seminars. A relatively simple concept seemed to always require a good deal of explanation.

In order to avoid confusion, we decided to abandon the use of indicators of relative difference in this thesis. Instead, we chose to use the logarithm of ratios, as follows:

$$H_2(Y_{CALC}(i), Y_{EXP}(i)) = \log_{10}\left(\frac{Y_{CALC}(i)}{Y_{EXP}(i)}\right); \quad 1 \leq i \leq N_r. \tag{6.11}$$

While ratios do not possess the symmetry property, one finds that the logarithm of ratios does: $H_2(x, y) = -H_2(y, x)$. Moreover, the logarithm to base 10 is widely familiar and results are easier to interpret and present.

6.4.8 Effective cross sections and uncertainties

As already mentioned in Section 6.4, two sets of predicted physical yields were established, one set based on cross sections from the TENDL-2019 library and the other set based on corresponding values from the more recent TENDL-2021 library. Each of these sets contains six subsets of results, one subset for each physics selection used in MCNP6 to calculate the neutron flux. It also seemed useful to calculate the predicted average yields to reduce the data. This was done separately for the TENDL-2019 and TENDL-2021 data sets. For each isotope, the arithmetic mean of the 6 predicted yields was calculated, assuming they constitute a discrete population of equal probability. The associated standard deviations were also calculated. These values have been designated the following notations: The predicted average (mean) physical yield and its standard deviation are denoted by $\langle Y \rangle_{CALC}$ and S_{CALC}, respectively. The associated measured value is denoted by Y_{EXP} and its statistical uncertainty by ΔY_{STAT}.

The mean cross section for the formation of a particular radionuclide by neutron activation, $\overline{\sigma}_n$, has already been introduced and is given by Equation 6.6. Within a TENDL data set, one can again average these values over the 6 physics selections, a quantity that we will denote by $\langle \overline{\sigma}_n \rangle$. This symbol represents the "average predicted formation cross section" for a particular radionuclide – averaged over all neutron energy groups (weighted by the neutron spectrum) and averaged over the 6 physics selections, all six considered to be equally probable.

It is also interesting to renormalize the above average predicted cross sections to the experimental values, assuming that the measurements better reflect reality than the predictions. For all 121 reactions studied in this study, these "average normalized formation cross sections" have been calculated as follows:

$$\langle \overline{\sigma} \rangle = \langle \overline{\sigma}_n \rangle \frac{Y_{EXP}}{\langle Y \rangle_{CALC}}. \tag{6.12}$$

The uncertainty $\langle\overline{\Delta\sigma}\rangle$ associated with Equation 6.12 was calculated by summing the individual uncertainties in quadrature. These include the experimental statistical uncertainty arising from the measured full-energy peak area (ΔY_{STAT}), the Monte Carlo statistical uncertainty associated with the neutron flux, estimated/assumed uncertainty in the beam current measurement (6%), detector efficiency (3%), decay corrections (2%), sample mass (1%), and finally the standard deviation arising from the 6 physics selections (S_{CALC}). We adopted S_{CALC} as an uncertainty since it does represent a spread in predicted values, of which we calculated the mean. In the case of the neutron flux, the statistical uncertainty introduced by the Monte Carlo process is sub-percent for the majority of reactions.

To conclude, it should be mentioned that averages and standard deviations of the "Base-10 logarithms of the ratios between predicted and measured physical yields" were also calculated for the 121 reactions observed. All the mathematical expressions presented in this chapter have been coded in Fortran. These codes needed the output from the Monte Carlo simulations as well as the raw data measured with the HPGe detector as input for further analysis. The final results are predicted and measured physical yields of the observed radionuclides induced by neutrons, as well as Base-10 logarithms of the ratios between predicted and measured physical yields to facilitate an overall comparison between the predictions and the measurements.

6.5 RESULTS AND DISCUSSION

The decay data used to identify the radioactive residues produced in the neutron-activated samples are first presented in Table 6.6, followed by the experimental results and predictions. The predictive powers of the different physics selections are also discussed.

6.5.1 Neutron-induced activation products

A total of 121 neutron-induced reactions or processes were uniquely identified from the measured spectra of gamma-rays emitted by their activation products. Concerning the corresponding predictions, processes with multiple channels to produce the final observed radionuclide were considered as a sum of all contributing reaction channels, e.g. where a target element with natural isotopic composition has more than one stable isotope. Care was also taken to properly include contributions from precursor decay. To have confidence in the results, any reaction with questionable identification was discarded, e.g. where a conflict was observed in results from the different counting sessions or where there was a lack of sufficiently strong photon emissions. Such cases, however, were relatively few. The observed reactions, their assigned identification numbers and the decay data used for their identification are presented in Table 6.6. The decay data were taken from NuDat 3.0 [SON2005].

Due to the relatively long bombardment times and fairly complex beam histories, there was some concern about radionuclides with half-lives shorter than one day. Nevertheless, those cases where at least two counting sessions produced a physical yield with reasonable statistics, free of conflicts, were retained. At the other end of the scale, it was surprising to see ^{207}Bi so clearly, as its half-life is longer than 31 years. In cases where the half-life is in order of years, an extra counting session was performed about four months after the bombardment.

Table 6.6: Target nuclides, neutron-induced reactions and the decay data of observed residues used for their identification and quantification.

Target	ID	Reaction	Half-life (d)	γ-ray (keV)	Intensity (%)
^{9}Be	1	^{9}Be(n,3n)^{7}Be	53.22	477.6035	10.44
^{23}Na	2	^{23}Na(n,2n)^{22}Na	950.287	1274.537	99.940
	3	^{23}Na(n,γ)^{24}Na	0.624875	1368.626	99.9936
^{nat}Mg	4	^{nat}Mg(n,x)^{22}Na	950.287	1274.537	99.940
	5	^{nat}Mg(n,x)^{24}Na	0.624875	1368.626	99.9936
^{27}Al	6	^{27}Al(n,x)^{22}Na	950.287	1274.537	99.940
	7	^{27}Al(n,x)^{24}Na	0.624875	1368.626	99.9936
^{nat}Ti	8	^{nat}Ti(n,x)^{47}Ca	4.536	1297.09	67.0
	9	^{nat}Ti(n,x)^{44m}Sc	2.44208	271.241	86.7
	10	^{nat}Ti(n,x)^{46}Sc	83.79	889.277	99.9840
	11	^{nat}Ti(n,x)^{47}Sc	3.3492	159.381	68.3
	12	^{nat}Ti(n,x)^{48}Sc	1.81958	983.526	100.0
^{55}Mn	13	^{55}Mn(n,x)^{48}V	15.9735	983.525	99.98
	14	^{55}Mn(n,x)^{51}Cr	27.704	320.0824	9.910
	15	^{55}Mn(n,4n)^{52}Mn	5.591	744.233	90.0
	16	^{55}Mn(n,2n)^{54}Mn	312.20	834.848	99.9760
^{59}Co	17	^{59}Co(n,x)^{52}Mn	5.591	1434.092	100.0
	18	^{59}Co(n,x)^{54}Mn	312.20	834.848	99.9760
	19	^{59}Co(n,p)^{59}Fe	44.495	1099.245	56.5
	20	^{59}Co(n,4n)^{56}Co	77.236	846.770	99.9399
	21	^{59}Co(n,3n)^{57}Co	271.74	122.06065	85.60
	22	^{59}Co(n,2n)^{58}Co	70.86	810.7593	99.450
	23	^{59}Co(n,γ)^{60}Co	1925.28	1332.492	99.9826
^{nat}Ni	24	^{nat}Ni(n,x)^{51}Cr	27.704	320.0824	9.910
	25	^{nat}Ni(n,x)^{52}Mn	5.591	1434.092	100.0
	26	^{nat}Ni(n,x)^{54}Mn	312.20	834.848	99.9760
	27	^{nat}Ni(n,x)^{59}Fe	44.495	1099.245	56.5
	28	^{nat}Ni(n,x)^{56}Co	77.236	846.770	99.9399
	29	^{nat}Ni(n,x)^{57}Co	271.74	122.06065	85.60
	30	^{nat}Ni(n,x)^{58}Co	70.86	810.7593	99.450
	31	^{nat}Ni(n,x)^{60}Co	1925.28	1332.492	99.9826
	32	^{nat}Ni(n,xn)^{56}Ni	6.075	158.38	98.8
	33	^{nat}Ni(n,xn)^{57}Ni	1.4833	1377.63	81.7
^{nat}Zn	34	^{nat}Zn(n,x)^{58}Co	70.86	810.7593	99.450
	35	^{nat}Zn(n,x)^{64}Cu	0.52919	1345.77	0.472
	36	^{nat}Zn(n,x)^{67}Cu	2.57625	184.577	48.7
	37	^{nat}Zn(n,x)^{65}Zn	243.93	1115.539	50.04
	38	^{nat}Zn(n,x)^{69m}Zn	0.57317	438.634	94.85
s[^{66}Zn]	39	s[^{66}Zn](n,x)^{64}Cu	0.52919	1345.77	0.472
	40	s[^{66}Zn](n,x)^{65}Zn	243.93	1115.539	50.04
s[^{67}Zn]	41	s[^{67}Zn](n,x)^{64}Cu	0.52919	1345.77	0.472

Table 6.6: Target nuclides, neutron-induced reactions and the decay data of observed residues used for their identification and quantification (continuing from previous page).

Target	ID	Reaction	Half-life (d)	γ-ray (keV)	Intensity (%)
s[^{67}Zn]	42	s[^{67}Zn](n,x)^{67}Cu	2.57625	184.577	48.7
	43	s[^{67}Zn](n,x)^{65}Zn	243.93	1115.539	50.04
	44	s[^{68}Zn](n,x)^{67}Cu	2.57625	184.577	48.7
	45	s[^{68}Zn](n,x)^{65}Zn	243.93	1115.539	50.04
	46	s[^{68}Zn](n,x)^{69m}Zn	0.57317	438.634	94.85
^{nat}Br	47	^{nat}Br(n,x)^{75}Se	119.78	264.6576	58.9
	48	^{nat}Br(n,x)^{74}As	17.77	595.83	59.0
	49	^{nat}Br(n,xn)^{77}Br	2.3765	238.98	23.1
	50	^{81}Br(n,γ)^{82}Br	1.47008	776.517	83.4
^{nat}Rb	51	^{nat}Rb(n,x)^{82}Br	1.47008	776.517	83.4
	52	^{nat}Rb(n,xn)^{83}Rb	86.2	520.3991	45.0
	53	^{nat}Rb(n,xn)^{84}Rb	32.82	881.6041	68.9
	54	^{nat}Rb(n,x)^{86}Rb	18.642	1077.0	8.64
^{89}Y	55	^{89}Y(n,x)^{83}Rb	86.2	520.3991	45.0
	56	^{89}Y(n,x)^{84}Rb	32.82	881.6041	68.9
	57	^{89}Y(n,x)^{86}Rb	18.642	1077.0	8.64
	58	^{89}Y(n,4n)^{86}Y	0.614167	1076.63	82.5
	59	^{89}Y(n,3n)^{87}Y	3.325	484.805	89.8
	60	^{89}Y(n,3n)^{87m}Y	0.55708	380.79	78.05
	61	^{89}Y(n,2n)^{88}Y	106.627	898.042	93.7
^{93}Nb	62	^{93}Nb(n,x)^{87}Y	3.325	484.805	89.8
	63	^{93}Nb(n,x)^{88}Y	106.627	898.042	93.7
	64	^{93}Nb(n,x)^{89}Zr	3.26708	909.15	99.04
	65	^{93}Nb(n,4n)^{90}Nb	0.60833	1129.224	92.7
	66	^{93}Nb(n,3n)^{91m}Nb	60.86	1204.67	2.0
	67	^{93}Nb(n,2n)^{92m}Nb	10.15	934.44	99.15
^{103}Rh	68	^{103}Rh(n,x)^{96}Tc	4.28	778.22	99.760
	69	^{103}Rh(n,p)^{103}Ru	39.247	497.085	91.0
	70	^{103}Rh(n,5n)^{99g}Rh	16.1	353.05	34.5
	71	^{103}Rh(n,4n)^{100}Rh	0.8667	539.512	80.6
	72	^{103}Rh(n,3n)^{101g}Rh	1205.3	127.226	68.0
	73	^{103}Rh(n,3n)^{101m}Rh	4.34	306.857	81.0
	74	^{103}Rh(n,2n)^{102g}Rh	207.3	468.58	2.90
	75	^{103}Rh(n,2n)^{102m}Rh	1366.77	631.29	56.0
^{nat}Ag	76	^{nat}Ag(n,x)^{105}Rh	1.4733	318.9	19.1
	77	^{nat}Ag(n,xn)^{105}Ag	41.29	344.52	41.4
	78	^{nat}Ag(n,xn)^{106m}Ag	8.28	1045.83	29.6
	79	^{109}Ag(n,γ)^{110m}Ag	249.83	657.7600	95.61
^{nat}In	80	^{nat}In(n,x)^{110m}Ag	249.83	657.7600	95.61
	81	^{115}In(n,p)^{115m}Cd	44.56	933.838	2.0

Table 6.6: Target nuclides, neutron-induced reactions and the decay data of observed residues used for their identification and quantification (continuing from previous page).

Target	ID	Reaction	Half-life (d)	γ-ray (keV)	Intensity (%)
^{nat}In	82	^{nat}In(n,xn)^{111}In	2.8047	245.35	94.1
	83	^{nat}In(n,x)^{114m}In	49.51	190.27	15.56
^{127}I	84	^{127}I(n,x)^{120m}Sb	5.76	1171.7	100.0
	85	^{127}I(n,x)^{122}Sb	2.7238	564.24	70.67
	86	^{127}I(n,x)^{124}Sb	60.20	602.7260	97.8
	87	^{127}I(n,x)^{123m}Te	119.2	159.00	84.0
	88	^{127}I(n,5n)^{123}I	0.550979	158.97	83.3
	89	^{127}I(n,4n)^{124}I	4.1760	602.73	62.9
	90	^{127}I(n,2n)^{126}I	12.93	388.633	35.6
^{133}Cs	91	^{133}Cs(n,5n)^{129}Cs	1.33583	371.918	30.6
	92	^{133}Cs(n,2n)^{132}Cs	6.480	667.714	97.59
	93	^{133}Cs(n,γ)^{134}Cs	754.314	604.721	97.62
^{141}Pr	94	^{141}Pr(n,x)^{139}Ce	137.641	165.8575	80.0
	95	^{141}Pr(n,p)^{141}Ce	32.511	145.4433	48.4
	96	^{141}Pr(n,γ)^{142}Pr	0.7967	1575.6	3.7
^{nat}Gd	97	^{nat}Gd(n,x)^{156}Eu	15.19	811.77	9.7
	98	^{nat}Gd(n,x)^{157}Eu	0.6325	410.723	17.8
	99	^{nat}Gd(n,xn)^{151}Gd	123.9	174.70	2.96
	100	^{nat}Gd(n,x)^{153}Gd	240.4	103.18012	21.1
	101	^{nat}Gd(n,x)^{159}Gd	0.76996	363.5430	11.78
	102	^{160}Gd(n,γ)^{161}Gd $\rightarrow^{161}$Tb	6.89	74.56669	10.2
^{169}Tm	103	^{169}Tm(n,5n)^{165}Tm	1.2525	242.917	35.5
	104	^{169}Tm(n,3n)^{167}Tm	9.25	531.54	1.61
	105	^{169}Tm(n,2n)^{168}Tm	93.1	815.989	50.95
^{181}Ta	106	^{181}Ta(n,p)^{181}Hf	42.39	482.18	80.5
	107	^{181}Ta(n,5n)^{177}Ta	2.3567	112.9	7.2
	108	^{181}Ta(n,γ)^{182}Ta	114.74	1121.290	35.24
^{197}Au	109	^{197}Au(n,x)^{192}Ir	73.829	316.50618	82.86
	110	^{197}Au(n,4n)^{194}Au	1.58417	328.464	60.4
	111	^{197}Au(n,3n)^{195}Au	186.01	98.857	11.21
	112	^{197}Au(n,2n)^{196}Au	6.1669	355.73	87.0
	113	^{197}Au(n,γ)^{198g}Au	2.6941	411.80205	95.62
^{nat}Tl	114	^{nat}Tl(n,x)^{203}Hg	46.594	279.1952	81.56
	115	^{nat}Tl(n,xn)^{200}Tl	1.0875	367.942	87.0
	116	^{nat}Tl(n,xn)^{201}Tl	3.0421	167.43	10.00
	117	^{nat}Tl(n,xn)^{202}Tl	12.31	439.510	91.5
^{209}Bi	118	^{209}Bi(n,6n)^{204}Bi	0.4675	899.15	99.0
	119	^{209}Bi(n,5n)^{205}Bi	15.31	703.45	31.1
	120	^{209}Bi(n,4n)^{206}Bi	6.243	803.10	99.0
	121	^{209}Bi(n,3n)^{207}Bi	11523.6	569.698	97.75

6.5.2 Sensitivity to multigroup structure

As described in Section 6.4, group-averaged cross sections were determined for all the neutron energy groups of the extended LaBauve multigroup structure employed in this work. For this purpose an interpolation scheme was required to convert the pointwise TENDL cross sections to group-averaged cross sections. Physical yield predictions were made using different interpolation schemes. Table 6.7 shows some results of this investigation for an arbitrary selected capture reaction and threshold reaction on the same target nucleus, namely ^{23}Na(n,γ)^{24}Na and ^{23}Na(n,2n)^{22}Na, respectively. Also shown are upper and lower yield limits based on the maximum and minimum cross-section values within each group, respectively, as provided by the cubic spline fits of the excitation functions of the selected reactions (see Subsection 6.4.2). These excitation functions, as represented by the cubic spline fits, are shown in Figure 6.8.

Table 6.7: Physical yields for a capture reaction and a threshold reaction, utilizing different interpolation strategies to determine group-averaged cross sections from the pointwise TENDL-2021 data. Upper and lower limits are also shown, determined from the minimum and maximum cross-section values in the individual groups.

Method[a]	Physical yield (Bq μAh^{-1} g^{-1})	
	^{23}Na(n,γ)^{24}Na	^{23}Na(n,2n)^{22}Na
Newton-Cotes of degree 1	2953.73	32.92
Newton-Cotes of degree 2	2791.54	32.91
Newton-Cotes of degree 3	2776.11	32.91
Newton-Cotes of degree 4	2758.86	32.91
Weighted average (Eq. 6.1)	2767.67	32.91
Lower limit based on group minimum values	2474.08	31.34
Upper limit based on group maximum values	3435.35	34.51

[a]Neutron spectrum according to CEM physics selection in MCNP6 version 6.2

In the case of the ^{23}Na(n,2n)^{22}Na reaction there was no sensitivity observed to the choice of interpolation method, which was found for all threshold reactions. An explanation for this insensitivity is because the 1 MeV width of the neutron groups above 1 MeV is sufficiently narrow to avoid any significant fluctuations (or slope variations) of the excitation function within individual groups. In contrast, some groups below 1 MeV are quite wide with respect to their respective scales, therefore one would expect capture reactions to show more sensitivity to both the choice of multigroup scheme as well as the interpolation method. Table 6.7 shows that this is indeed the case for the ^{23}Na(n,γ)^{24}Na reaction. Nevertheless, the results from the different interpolation methods are still quite similar. The adopted practice to use Newton-Cotes of degree 4 above 1 MeV and weighted averages below 1 MeV seems to be well justified.

It is also interesting to compare the upper and lower yield limits for the two above reactions. In the case of the ^{23}Na(n,2n)^{22}Na reaction the upper limit is only about 10% higher than the lower limit, with all the interpolation methods yielding values close to mid-way between them. In the case of the ^{23}Na(n,γ)^{24}Na reaction the upper limit is about 39% above the lower limit, with the interpolated values only slightly higher than the mid-way point between them. One can

conclude that the extended LaBauve multigroup structure seems to be appropriate for making predictions of physical yields for both capture and threshold neutron-induced reactions.

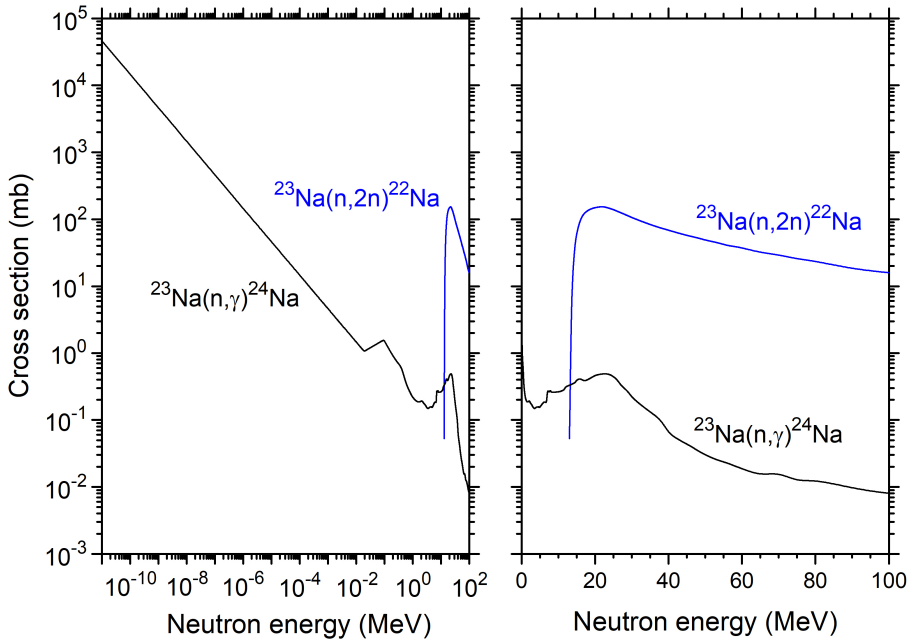


Figure 6.8: Excitation functions of the ^{23}Na(n,2n)^{22}Na and ^{23}Na(n,γ)^{24}Na reactions. The curves are cubic spline fits through the relevant pointwise data from the TENDL-2021 library. LEFT: Logarithmic scale on x-axis. RIGHT: Linear scale on x-axis.

Figure 6.8 provides some insight into the reasons why we were concerned about the energy region below 1 MeV in the multigroup scheme. A logarithmic scale on the x-axis reveals large cross sections towards lower energies in the case of the capture reaction, which is not evident on a linear scale. Relatively few LaBauve neutron groups cover many orders of magnitude in energy, in contrast to the region above 1 MeV which is well covered by groups of 1 MeV width. The $1/E$ relationship of the capture cross section is only revealed on the logarithmic scale.

6.5.3 Physical yields and yield ratios

The predicted physical yields of radionuclides produced via the selected 121 neutron-induced reactions, based on cross sections from the TENDL-2019 and TENDL-2021 libraries, for each of the six different physics selections in the MCNP6 code system employed to obtain the neutron flux, are considered too numerous to present in the body of the thesis. These values are therefore presented in Appendix C (based on TENDL-2019 data) and Appendix D (based on TENDL-2021 data). Their numerical averages and standard deviations, however, are presented in Table 6.8, together with the corresponding experimental data (see Subsection 6.4.8 for a description of symbols). Also included in Table 6.8 are the effective cross sections – evaluated using Equation 6.12 – as well as their uncertainties.

Values for the experimental yield of a specific radionuclide could normally be determined from γ-ray spectra acquired in more than one counting session. The value obtained from the counting session that yielded the best counting statistics in each case (i.e. the smallest statistical uncertainty) has been included in Table 6.8.

Table 6.8: Predicted average physical yields (TENDL-2019 + MCNP6) as well as corresponding measurements and associated cross sections.

		Physical yield (Bq μAh^{-1} g^{-1})				Cross section (mb)
ID	Reaction	$\langle Y \rangle_{\mathrm{CALC}}$	S_{CALC}	Y_{EXP}	ΔY_{STAT}	$\langle \overline{\sigma} \rangle \pm \langle \overline{\Delta\sigma} \rangle$
1	^{9}Be(n,3n)^{7}Be	42.55	6.24	22.53	0.22	0.215 ± 0.035
2	^{23}Na(n,2n)^{22}Na	41.19	9.79	23.81	0.31	10.33 ± 2.56
3	^{23}Na(n,γ)^{24}Na	2878.34	345.77	7177.74	259.56	2.05 ± 0.30
4	^{nat}Mg(n,x)^{22}Na	9.50	1.53	3.47	0.01	1.60 ± 0.28
5	^{nat}Mg(n,x)^{24}Na	70654.58	12892.54	42526.10	284.42	12.83 ± 2.51
6	^{27}Al(n,x)^{22}Na	1.03	0.14	1.22	0.00	0.626 ± 0.097
7	^{27}Al(n,x)^{24}Na	40653.98	7705.85	23142.84	88.46	7.75 ± 1.57
8	^{nat}Ti(n,x)^{47}Ca	29.88	6.59	22.86	1.61	0.0986 ± 0.0239
9	^{nat}Ti(n,x)^{44m}Sc	166.88	25.03	109.36	4.18	0.255 ± 0.043
10	^{nat}Ti(n,x)^{46}Sc	199.43	34.06	102.45	0.36	8.18 ± 1.51
11	^{nat}Ti(n,x)^{47}Sc	8018.87	1717.49	3851.23	9.86	12.27 ± 2.76
12	^{nat}Ti(n,x)^{48}Sc	3841.79	803.71	2325.18	22.65	4.02 ± 0.89
13	^{55}Mn(n,x)^{48}V	0.27	0.02	1.09	0.16	0.0192 ± 0.0034
14	^{55}Mn(n,x)^{51}Cr	12.07	0.63	5.09	0.41	0.155 ± 0.018
15	^{55}Mn(n,4n)^{52}Mn	213.58	24.12	90.72	0.54	0.556 ± 0.074
16	^{55}Mn(n,2n)^{54}Mn	300.56	71.95	191.73	0.15	65.29 ± 16.28
17	^{59}Co(n,x)^{52}Mn	0.55	0.04	0.80	0.13	0.0053 ± 0.0010
18	^{59}Co(n,x)^{54}Mn	7.61	1.34	7.60	0.08	2.79 ± 0.53
19	^{59}Co(n,p)^{59}Fe	166.45	29.27	136.03	0.27	7.09 ± 1.34
20	^{59}Co(n,4n)^{56}Co	14.96	1.74	7.75	0.09	0.704 ± 0.096
21	^{59}Co(n,3n)^{57}Co	81.43	17.65	51.94	0.07	16.54 ± 3.77
22	^{59}Co(n,2n)^{58}Co	1206.14	287.32	855.64	0.32	70.94 ± 17.61
23	^{59}Co(n,γ)^{60}Co	22.86	3.07	72.69	0.11	164.32 ± 24.91
24	^{nat}Ni(n,x)^{51}Cr	1.55	0.27	5.48	1.24	0.178 ± 0.052
25	^{nat}Ni(n,x)^{52}Mn	19.27	1.20	15.81	0.27	0.104 ± 0.010
26	^{nat}Ni(n,x)^{54}Mn	6.22	1.40	6.25	0.06	2.28 ± 0.54
27	^{nat}Ni(n,x)^{59}Fe	4.06	0.89	3.25	0.11	0.168 ± 0.039
28	^{nat}Ni(n,x)^{56}Co	104.31	20.19	70.70	0.12	6.38 ± 1.31
29	^{nat}Ni(n,x)^{57}Co	256.70	60.17	154.69	0.11	48.10 ± 11.99
30	^{nat}Ni(n,x)^{58}Co	1297.05	131.65	1123.45	0.43	93.03 ± 11.47
31	^{nat}Ni(n,x)^{60}Co	2.41	0.44	3.89	0.05	8.74 ± 1.72
32	^{nat}Ni(n,xn)^{56}Ni	21.91	3.75	14.07	0.61	0.100 ± 0.019
33	^{nat}Ni(n,xn)^{57}Ni	3762.52	874.90	2686.46	15.69	4.78 ± 1.16
34	^{nat}Zn(n,x)^{58}Co	1.96	0.14	3.13	0.17	0.284 ± 0.032
35	^{nat}Zn(n,x)^{64}Cu	48895.09	4858.55	38030.57	925.73	25.70 ± 3.19
36	^{nat}Zn(n,x)^{67}Cu	747.79	168.63	467.33	1.53	1.62 ± 0.38
37	^{nat}Zn(n,x)^{65}Zn	116.96	22.32	96.16	0.77	30.60 ± 6.22
38	^{nat}Zn(n,x)^{69m}Zn	1125.52	177.14	1067.09	7.28	0.84 ± 0.15
39	s[^{66}Zn](n,x)^{64}Cu	17626.05	3168.45	13128.09	409.72	9.11 ± 1.78
40	s[^{66}Zn](n,x)^{65}Zn	301.25	71.96	187.17	0.76	59.77 ± 14.88
41	s[^{67}Zn](n,x)^{64}Cu	7547.02	847.75	3584.75	605.00	2.51 ± 0.54

Table 6.8: Predicted average physical yields (TENDL-2019 + MCNP6) as well as corresponding measurements and associated cross sections (continuing from previous page).

		Physical yield (Bq μAh^{-1} g^{-1})				Cross section (mb)
ID	Reaction	$\langle Y \rangle_{\mathrm{CALC}}$	S_{CALC}	Y_{EXP}	ΔY_{STAT}	$\langle \overline{\sigma} \rangle \pm \langle \overline{\Delta\sigma} \rangle$
42	s[^{67}Zn](n,x)^{67}Cu	2231.91	452.67	1081.07	2.54	3.71 ± 0.80
43	s[^{67}Zn](n,x)^{65}Zn	115.66	26.16	70.21	0.76	22.76 ± 5.39
44	s[^{68}Zn](n,x)^{67}Cu	3498.48	803.21	2335.96	3.91	8.12 ± 1.95
45	s[^{68}Zn](n,x)^{65}Zn	24.76	3.45	17.63	0.37	5.82 ± 0.92
46	s[^{68}Zn](n,x)^{69m}Zn	2998.60	265.27	3094.32	15.62	2.42 ± 0.27
47	^{nat}Br(n,x)^{75}Se	1.88	0.11	0.86	0.29	0.164 ± 0.058
48	^{nat}Br(n,x)^{74}As	29.85	5.12	29.10	0.76	0.82 ± 0.15
49	^{nat}Br(n,xn)^{77}Br	5891.10	1277.88	3223.99	90.15	12.17 ± 2.79
50	^{81}Br(n,γ)^{82}Br	38911.60	6181.89	84363.84	319.85	197.34 ± 34.27
51	^{nat}Rb(n,x)^{82}Br	702.60	138.16	300.75	10.61	0.75 ± 0.16
52	^{nat}Rb(n,xn)^{83}Rb	220.90	48.88	203.30	0.46	29.77 ± 6.91
53	^{nat}Rb(n,xn)^{84}Rb	1710.76	402.35	1344.75	0.96	74.90 ± 18.38
54	^{nat}Rb(n,x)^{86}Rb	2756.03	448.38	3173.59	5.22	100.55 ± 17.81
55	^{89}Y(n,x)^{83}Rb	2.61	0.17	1.23	0.11	0.188 ± 0.025
56	^{89}Y(n,x)^{84}Rb	28.09	4.20	14.89	0.36	0.87 ± 0.14
57	^{89}Y(n,x)^{86}Rb	66.72	15.14	25.33	3.38	0.83 ± 0.23
58	^{89}Y(n,4n)^{86}Y	5648.57	630.82	4040.72	219.38	4.40 ± 0.63
59	^{89}Y(n,3n)^{87}Y	7772.82	1681.36	5956.05	12.05	35.00 ± 7.96
60	^{89}Y(n,3n)^{87m}Y	33056.08	7097.67	23104.23	429.87	22.75 ± 5.16
61	^{89}Y(n,2n)^{88}Y	676.39	164.73	457.41	0.52	86.08 ± 21.81
62	^{93}Nb(n,x)^{87}Y	46.67	3.92	96.12	2.35	0.59 ± 0.06
63	^{93}Nb(n,x)^{88}Y	6.48	1.11	9.14	0.09	1.80 ± 0.33
64	^{93}Nb(n,x)^{89}Zr	113.16	6.71	157.24	1.44	0.955 ± 0.088
65	^{93}Nb(n,4n)^{90}Nb	6760.63	922.35	7175.02	75.49	8.09 ± 1.24
66	^{93}Nb(n,3n)^{91m}Nb	87.93	19.75	63.71	1.86	7.16 ± 1.70
67	^{93}Nb(n,2n)^{92m}Nb	2466.72	553.50	1880.49	1.12	35.21 ± 8.28
68	^{103}Rh(n,x)^{96}Tc	108.37	5.93	27.27	0.29	0.241 ± 0.022
69	^{103}Rh(n,p)^{103}Ru	56.08	10.01	25.81	0.22	2.07 ± 0.40
70	^{103}Rh(n,5n)^{99g}Rh	19.48	1.64	10.34	0.31	0.342 ± 0.039
71	^{103}Rh(n,4n)^{100}Rh	3003.63	516.60	5854.79	12.27	10.40 ± 1.93
72	^{103}Rh(n,3n)^{101g}Rh	4.66	1.16	4.24	0.13	10.45 ± 2.72
73	^{103}Rh(n,3n)^{101m}Rh	4840.37	1190.35	3843.71	1.90	34.09 ± 8.72
74	^{103}Rh(n,2n)^{102g}Rh	143.29	32.52	138.80	0.98	58.79 ± 13.97
75	^{103}Rh(n,2n)^{102m}Rh	23.65	5.54	93.39	0.18	260.78 ± 63.73
76	^{nat}Ag(n,x)^{105}Rh	449.46	100.46	854.91	112.52	2.70 ± 0.73
77	^{nat}Ag(n,xn)^{105}Ag	425.27	97.29	288.04	0.52	25.49 ± 6.10
78	^{nat}Ag(n,xn)^{106m}Ag	2192.05	496.20	1593.24	3.21	28.26 ± 6.70
79	^{109}Ag(n,γ)^{110m}Ag	34.74	4.24	113.20	0.25	60.78 ± 8.53
80	^{nat}In(n,x)^{110m}Ag	1.47	0.26	0.73	0.03	0.418 ± 0.082
81	^{115}In(n,p)^{115m}Cd	24.03	5.51	9.58	0.84	0.97 ± 0.25

Table 6.8: Predicted average physical yields (TENDL-2019 + MCNP6) as well as corresponding measurements and associated cross sections (continuing from previous page).

		Physical yield (Bq μAh^{-1} g^{-1})				Cross section (mb)
ID	Reaction	$\langle Y \rangle_{\mathrm{CALC}}$	S_{CALC}	Y_{EXP}	ΔY_{STAT}	$\langle \overline{\sigma} \rangle \pm \langle \overline{\Delta\sigma} \rangle$
82	^{nat}In(n,xn)^{111}In	558.86	113.94	746.55	2.34	4.78 ± 1.03
83	^{nat}In(n,x)^{114m}In	1313.71	272.14	1100.08	0.70	124.21 ± 27.16
84	^{127}I(n,x)^{120m}Sb	2.94	0.16	1.98	0.05	0.0290 ± 0.0027
85	^{127}I(n,x)^{122}Sb	163.38	28.30	49.77	8.23	0.343 ± 0.085
86	^{127}I(n,x)^{124}Sb	10.65	2.17	1.70	0.02	0.259 ± 0.056
87	^{127}I(n,x)^{123m}Te	7.24	0.49	1.98	0.05	0.600 ± 0.060
88	^{127}I(n,5n)^{123}I	5644.75	499.02	2821.89	162.73	3.94 ± 0.50
89	^{127}I(n,4n)^{124}I	3017.31	525.12	2074.24	3.21	21.89 ± 4.11
90	^{127}I(n,2n)^{126}I	4897.82	1131.52	3524.25	1.74	114.82 ± 27.72
91	^{133}Cs(n,5n)^{129}Cs	1956.16	181.77	1427.20	193.97	5.06 ± 0.91
92	^{133}Cs(n,2n)^{132}Cs	10141.42	2324.31	6197.98	3.43	105.98 ± 25.40
93	^{133}Cs(n,γ)^{134}Cs	187.19	25.28	281.50	0.25	562.16 ± 85.52
94	^{141}Pr(n,x)^{139}Ce	242.51	56.86	168.37	0.13	64.87 ± 15.87
95	^{141}Pr(n,p)^{141}Ce	34.20	7.88	13.90	0.14	1.26 ± 0.30
96	^{141}Pr(n,γ)^{142}Pr	23782.82	3401.87	46179.77	913.85	103.31 ± 16.58
97	^{nat}Gd(n,x)^{156}Eu	57.82	10.99	53.46	1.20	2.54 ± 0.52
98	^{nat}Gd(n,x)^{157}Eu	1410.40	269.53	3164.81	251.38	6.26 ± 1.37
99	^{nat}Gd(n,xn)^{151}Gd	7.39	1.07	11.62	1.59	4.51 ± 0.95
100	^{nat}Gd(n,x)^{153}Gd	51.64	7.90	39.15	0.82	29.45 ± 4.99
101	^{nat}Gd(n,x)^{159}Gd	33388.38	4508.88	36248.00	94.08	87.29 ± 13.28
102	^{160}Gd(n,γ)^{161}Gd ^{161}Gd$\rightarrow^{161}$Tb	2228.07	321.09	1940.21	22.51	41.87 ± 6.73
103	^{169}Tm(n,5n)^{165}Tm	5409.16	700.06	2582.15	5.98	10.90 ± 1.60
104	^{169}Tm(n,3n)^{167}Tm	3920.42	962.56	2923.23	18.64	90.70 ± 23.16
105	^{169}Tm(n,2n)^{168}Tm	654.10	139.41	435.92	0.39	136.16 ± 30.55
106	^{181}Ta(n,p)^{181}Hf	10.98	2.51	4.51	0.31	0.69 ± 0.17
107	^{181}Ta(n,5n)^{177}Ta	4786.74	752.50	3281.67	47.79	27.88 ± 4.82
108	^{181}Ta(n,γ)^{182}Ta	2071.30	275.01	2351.63	9.05	972.48 ± 146.01
109	^{197}Au(n,x)^{192}Ir	1.91	0.32	0.64	0.12	0.184 ± 0.048
110	^{197}Au(n,4n)^{194}Au	10432.12	2263.86	7071.54	40.49	43.87 ± 10.01
111	^{197}Au(n,3n)^{195}Au	182.81	46.09	52.17	1.00	37.94 ± 9.95
112	^{197}Au(n,2n)^{196}Au	8124.29	1734.07	5867.86	2.52	141.54 ± 31.79
113	^{197}Au(n,γ)^{198g}Au	52732.34	6888.72	90171.43	36.47	953.45 ± 141.31
114	^{nat}Tl(n,x)^{203}Hg	21.95	4.15	9.13	0.10	1.73 ± 0.35
115	^{nat}Tl(n,xn)^{200}Tl	4090.04	599.77	2897.74	17.57	12.84 ± 2.09
116	^{nat}Tl(n,xn)^{201}Tl	4100.10	804.29	2537.86	20.40	31.39 ± 6.54
117	^{nat}Tl(n,xn)^{202}Tl	2409.37	518.75	1305.70	0.68	65.27 ± 14.78
118	^{209}Bi(n,6n)^{204}Bi	4166.88	237.26	1081.13	83.81	2.11 ± 0.25
119	^{209}Bi(n,5n)^{205}Bi	610.33	82.28	210.97	0.52	13.46 ± 2.05
120	^{209}Bi(n,4n)^{206}Bi	3109.73	671.48	1396.62	1.55	36.23 ± 8.22
121	^{209}Bi(n,3n)^{207}Bi	2.92	0.74	5.28	0.02	252.29 ± 66.22

Table 6.9: Predicted average physical yields (TENDL-2021 + MCNP6) as well as corresponding measurements and associated cross sections.

		Physical yield (Bq μAh^{-1} g^{-1})				Cross section (mb)
ID	Reaction	$\langle Y \rangle_{\mathrm{CALC}}$	S_{CALC}	Y_{EXP}	ΔY_{STAT}	$\langle \overline{\sigma} \rangle \pm \langle \overline{\Delta\sigma} \rangle$
1	^{9}Be(n,3n)^{7}Be	42.55	6.24	22.53	0.22	0.215 ± 0.035
2	^{23}Na(n,2n)^{22}Na	41.70	9.92	23.81	0.31	10.33 ± 2.56
3	^{23}Na(n,γ)^{24}Na	3131.00	362.13	7177.74	259.56	2.05 ± 0.29
4	^{nat}Mg(n,x)^{22}Na	9.14	1.45	3.47	0.01	1.60 ± 0.28
5	^{nat}Mg(n,x)^{24}Na	70644.94	12905.94	42526.10	284.42	12.83 ± 2.51
6	^{27}Al(n,x)^{22}Na	1.03	0.14	1.22	0.00	0.626 ± 0.097
7	^{27}Al(n,x)^{24}Na	40653.98	7705.85	23142.84	88.46	7.75 ± 1.57
8	^{nat}Ti(n,x)^{47}Ca	29.14	6.40	22.86	1.61	0.099 ± 0.024
9	^{nat}Ti(n,x)^{44m}Sc	144.13	23.52	109.36	4.18	0.255 ± 0.046
10	^{nat}Ti(n,x)^{46}Sc	188.89	31.74	102.45	0.36	8.18 ± 1.49
11	^{nat}Ti(n,x)^{47}Sc	8013.54	1705.55	3851.23	9.86	12.27 ± 2.75
12	^{nat}Ti(n,x)^{48}Sc	3977.85	839.02	2325.18	22.65	4.02 ± 0.89
13	^{55}Mn(n,x)^{48}V	0.15	0.01	1.09	0.16	0.0192 ± 0.0034
14	^{55}Mn(n,x)^{51}Cr	10.07	0.52	5.09	0.41	0.155 ± 0.018
15	^{55}Mn(n,4n)^{52}Mn	197.74	21.49	90.72	0.54	0.556 ± 0.072
16	^{55}Mn(n,2n)^{54}Mn	298.99	71.65	191.73	0.15	65.29 ± 16.30
17	^{59}Co(n,x)^{52}Mn	0.32	0.02	0.80	0.13	0.0053 ± 0.0010
18	^{59}Co(n,x)^{54}Mn	7.78	1.35	7.60	0.08	2.79 ± 0.52
19	^{59}Co(n,p)^{59}Fe	165.83	29.13	136.03	0.27	7.09 ± 1.34
20	^{59}Co(n,4n)^{56}Co	13.38	1.50	7.75	0.09	0.705 ± 0.094
21	^{59}Co(n,3n)^{57}Co	80.88	17.47	51.94	0.07	16.54 ± 3.76
22	^{59}Co(n,2n)^{58}Co	1202.36	286.80	855.64	0.32	70.94 ± 17.64
23	^{59}Co(n,γ)^{60}Co	22.60	3.06	72.69	0.11	164.32 ± 25.06
24	^{nat}Ni(n,x)^{51}Cr	1.44	0.25	5.48	1.24	0.178 ± 0.052
25	^{nat}Ni(n,x)^{52}Mn	14.18	0.83	15.81	0.27	0.1038 ± 0.0097
26	^{nat}Ni(n,x)^{54}Mn	5.93	1.33	6.25	0.06	2.28 ± 0.54
27	^{nat}Ni(n,x)^{59}Fe	3.50	0.75	3.25	0.11	0.169 ± 0.038
28	^{nat}Ni(n,x)^{56}Co	101.46	19.30	70.70	0.12	6.38 ± 1.29
29	^{nat}Ni(n,x)^{57}Co	259.10	60.67	154.69	0.11	49.00 ± 11.97
30	^{nat}Ni(n,x)^{58}Co	1288.87	130.77	1123.45	0.43	93.03 ± 11.47
31	^{nat}Ni(n,x)^{60}Co	2.35	0.43	3.89	0.05	8.74 ± 1.72
32	^{nat}Ni(n,xn)^{56}Ni	22.18	3.73	14.07	0.61	0.0999 ± 0.0187
33	^{nat}Ni(n,xn)^{57}Ni	3923.39	910.94	2686.46	15.69	4.78 ± 1.16
34	^{nat}Zn(n,x)^{58}Co	1.93	0.13	3.13	0.17	0.284 ± 0.032
35	^{nat}Zn(n,x)^{64}Cu	48311.06	4793.13	38030.57	925.73	25.70 ± 3.18
36	^{nat}Zn(n,x)^{67}Cu	772.94	173.56	467.33	1.53	1.62 ± 0.38
37	^{nat}Zn(n,x)^{65}Zn	112.82	21.94	96.16	0.77	30.61 ± 6.33
38	^{nat}Zn(n,x)^{69m}Zn	989.59	156.60	1067.09	7.28	0.84 ± 0.15
39	s[^{66}Zn](n,x)^{64}Cu	17241.48	3053.74	13128.09	409.72	9.11 ± 1.76
40	s[^{66}Zn](n,x)^{65}Zn	297.39	70.97	187.17	0.76	59.77 ± 14.87
41	s[^{67}Zn](n,x)^{64}Cu	7242.09	793.14	3584.75	605.00	2.51 ± 0.53

Table 6.9: Predicted average physical yields (TENDL-2021 + MCNP6) as well as corresponding measurements and associated cross sections (continuing from previous page).

		Physical yield (Bq μAh^{-1} g^{-1})				Cross section (mb)
ID	Reaction	$\langle Y \rangle_{\mathrm{CALC}}$	S_{CALC}	Y_{EXP}	ΔY_{STAT}	$\langle \overline{\sigma} \rangle \pm \langle \overline{\Delta\sigma} \rangle$
42	s[^{67}Zn](n,x)^{67}Cu	2479.00	505.50	1081.07	2.54	3.71 ± 0.80
43	s[^{67}Zn](n,x)^{65}Zn	110.54	24.75	70.21	0.76	22.76 ± 5.34
44	s[^{68}Zn](n,x)^{67}Cu	3577.18	817.75	2335.96	3.91	8.12 ± 1.94
45	s[^{68}Zn](n,x)^{65}Zn	22.03	2.98	17.63	0.37	5.82 ± 0.89
46	s[^{68}Zn](n,x)^{69m}Zn	2616.21	232.61	3094.32	15.62	2.42 ± 0.27
47	^{nat}Br(n,x)^{75}Se	1.35	0.07	0.86	0.29	0.164 ± 0.058
48	^{nat}Br(n,x)^{74}As	36.80	6.42	29.10	0.76	0.82 ± 0.16
49	^{nat}Br(n,xn)^{77}Br	5623.25	1208.28	3223.99	90.15	12.17 ± 2.77
50	^{81}Br(n,γ)^{82}Br	39271.20	6207.04	84363.84	319.85	197.35 ± 34.12
51	^{nat}Rb(n,x)^{82}Br	737.39	144.14	300.75	10.61	0.75 ± 0.16
52	^{nat}Rb(n,xn)^{83}Rb	215.66	47.16	203.30	0.46	29.77 ± 6.84
53	^{nat}Rb(n,xn)^{84}Rb	1707.07	402.32	1344.75	0.96	74.90 ± 18.41
54	^{nat}Rb(n,x)^{86}Rb	2758.08	449.46	3173.59	5.22	100.55 ± 17.83
55	^{89}Y(n,x)^{83}Rb	2.46	0.15	1.23	0.11	0.188 ± 0.025
56	^{89}Y(n,x)^{84}Rb	28.82	4.23	14.89	0.36	0.87 ± 0.14
57	^{89}Y(n,x)^{86}Rb	66.92	15.18	25.33	3.38	0.83 ± 0.23
58	^{89}Y(n,4n)^{86}Y	5049.98	532.47	4040.72	219.38	4.41 ± 0.61
59	^{89}Y(n,3n)^{87}Y	7693.65	1645.76	5956.05	12.05	35.01 ± 7.88
60	^{89}Y(n,3n)^{87m}Y	33932.66	7207.86	23104.23	429.87	22.75 ± 5.11
61	^{89}Y(n,2n)^{88}Y	676.46	165.03	457.41	0.52	86.08 ± 21.85
62	^{93}Nb(n,x)^{87}Y	48.16	3.91	96.12	2.35	0.593 ± 0.065
63	^{93}Nb(n,x)^{88}Y	6.90	1.18	9.14	0.09	1.80 ± 0.33
64	^{93}Nb(n,x)^{89}Zr	98.40	5.59	157.24	1.44	0.955 ± 0.087
65	^{93}Nb(n,4n)^{90}Nb	6235.39	821.78	7175.02	75.49	8.09 ± 1.21
66	^{93}Nb(n,3n)^{91m}Nb	112.04	24.75	63.71	1.86	7.16 ± 1.67
67	^{93}Nb(n,2n)^{92m}Nb	2833.30	642.12	1880.49	1.12	35.21 ± 8.35
68	^{103}Rh(n,x)^{96}Tc	70.41	4.05	27.27	0.29	0.241 ± 0.022
69	^{103}Rh(n,p)^{103}Ru	54.80	9.68	25.81	0.22	2.07 ± 0.39
70	^{103}Rh(n,5n)^{99g}Rh	12.26	0.87	10.34	0.31	0.342 ± 0.036
71	^{103}Rh(n,4n)^{100}Rh	6501.27	1607.64	5854.79	12.27	10.37 ± 2.66
72	^{103}Rh(n,3n)^{101g}Rh	4.67	1.16	4.24	0.13	10.45 ± 2.71
73	^{103}Rh(n,3n)^{101m}Rh	5461.39	1331.36	3843.71	1.90	34.09 ± 8.65
74	^{103}Rh(n,2n)^{102g}Rh	148.01	33.72	138.80	0.98	58.79 ± 14.02
75	^{103}Rh(n,2n)^{102m}Rh	23.18	5.44	93.39	0.18	260.77 ± 63.90
76	^{nat}Ag(n,x)^{105}Rh	1285.51	309.07	854.91	112.52	2.70 ± 0.76
77	^{nat}Ag(n,xn)^{105}Ag	430.84	101.91	288.04	0.52	25.48 ± 6.29
78	^{nat}Ag(n,xn)^{106m}Ag	2041.79	457.26	1593.24	3.21	28.27 ± 6.63
79	^{109}Ag(n,γ)^{110m}Ag	43.92	5.63	113.20	0.25	60.77 ± 8.87
80	^{nat}In(n,x)^{110m}Ag	1.96	0.34	0.73	0.03	0.418 ± 0.081
81	^{115}In(n,p)^{115m}Cd	17.69	4.11	9.58	0.84	0.97 ± 0.25

Table 6.9: Predicted average physical yields (TENDL-2021 + MCNP6) as well as corresponding measurements and associated cross sections (continuing from previous page).

		Physical yield (Bq μAh^{-1} g^{-1})				Cross section (mb)
ID	Reaction	$\langle Y \rangle_{\mathrm{CALC}}$	S_{CALC}	Y_{EXP}	ΔY_{STAT}	$\langle \overline{\sigma} \rangle \pm \langle \overline{\Delta\sigma} \rangle$
82	^{nat}In(n,xn)^{111}In	519.73	108.79	746.55	2.34	4.78 ± 1.06
83	^{nat}In(n,x)^{114m}In	1311.48	271.21	1100.08	0.70	124.21 ± 27.12
84	^{127}I(n,x)^{120m}Sb	2.03	0.12	1.98	0.05	0.0290 ± 0.0028
85	^{127}I(n,x)^{122}Sb	167.82	28.63	49.77	8.23	0.343 ± 0.085
86	^{127}I(n,x)^{124}Sb	10.47	2.14	1.70	0.02	0.259 ± 0.056
87	^{127}I(n,x)^{123m}Te	3.16	0.20	1.98	0.05	0.600 ± 0.059
88	^{127}I(n,5n)^{123}I	3742.92	266.65	2821.89	162.73	3.95 ± 0.46
89	^{127}I(n,4n)^{124}I	2850.54	464.24	2074.24	3.21	21.90 ± 3.88
90	^{127}I(n,2n)^{126}I	4978.98	1155.30	3524.25	1.74	114.82 ± 27.83
91	^{133}Cs(n,5n)^{129}Cs	1358.35	103.63	1427.20	193.97	5.07 ± 0.87
92	^{133}Cs(n,2n)^{132}Cs	10229.90	2354.11	6197.98	3.43	105.97 ± 25.49
93	^{133}Cs(n,γ)^{134}Cs	187.16	25.33	281.50	0.25	562.15 ± 85.66
94	^{141}Pr(n,x)^{139}Ce	246.58	57.39	168.37	0.13	64.87 ± 15.77
95	^{141}Pr(n,p)^{141}Ce	33.76	7.78	13.90	0.14	1.26 ± 0.30
96	^{141}Pr(n,γ)^{142}Pr	29010.63	4098.45	46179.77	913.85	103.31 ± 16.42
97	^{nat}Gd(n,x)^{156}Eu	61.40	11.69	53.46	1.20	2.54 ± 0.52
98	^{nat}Gd(n,x)^{157}Eu	1494.53	286.56	3164.81	251.38	6.26 ± 1.37
99	^{nat}Gd(n,xn)^{151}Gd	5.78	0.87	11.62	1.59	4.51 ± 0.97
100	^{nat}Gd(n,x)^{153}Gd	48.30	7.29	39.15	0.82	29.45 ± 4.94
101	^{nat}Gd(n,x)^{159}Gd	33853.76	4572.63	36248.00	94.08	87.29 ± 13.28
102	^{160}Gd(n,γ)^{161}Gd ^{161}Gd$\rightarrow$^{161}Tb	2806.86	396.07	1940.21	22.51	41.87 ± 6.61
103	^{169}Tm(n,5n)^{165}Tm	4236.04	458.50	2582.15	5.98	10.91 ± 1.41
104	^{169}Tm(n,3n)^{167}Tm	3983.61	972.97	2923.23	18.64	90.70 ± 23.05
105	^{169}Tm(n,2n)^{168}Tm	659.00	141.94	435.92	0.39	136.15 ± 30.83
106	^{181}Ta(n,p)^{181}Hf	10.90	2.50	4.51	0.31	0.69 ± 0.17
107	^{181}Ta(n,5n)^{177}Ta	4294.72	591.07	3281.67	47.79	27.91 ± 4.33
108	^{181}Ta(n,γ)^{182}Ta	2186.93	287.71	2351.63	9.05	972.50 ± 144.97
109	^{197}Au(n,x)^{192}Ir	2.10	0.35	0.64	0.12	0.184 ± 0.048
110	^{197}Au(n,4n)^{194}Au	10277.87	2124.35	7071.54	40.49	43.88 ± 9.58
111	^{197}Au(n,3n)^{195}Au	188.73	47.40	52.17	1.00	37.95 ± 9.92
112	^{197}Au(n,2n)^{196}Au	8402.03	1798.19	5867.86	2.52	141.54 ± 31.87
113	^{197}Au(n,γ)^{198g}Au	53773.16	6902.54	90171.43	36.47	953.47 ± 139.41
114	^{nat}Tl(n,x)^{203}Hg	22.39	4.23	9.13	0.10	1.73 ± 0.35
115	^{nat}Tl(n,xn)^{200}Tl	3518.40	521.16	2897.74	17.57	12.84 ± 2.10
116	^{nat}Tl(n,xn)^{201}Tl	3939.54	756.98	2537.86	20.40	31.39 ± 6.43
117	^{nat}Tl(n,xn)^{202}Tl	2456.11	523.94	1305.70	0.68	65.28 ± 14.66
118	^{209}Bi(n,6n)^{204}Bi	2293.78	131.27	1081.13	83.81	2.12 ± 0.25
119	^{209}Bi(n,5n)^{205}Bi	554.68	66.94	210.97	0.52	13.47 ± 1.88
120	^{209}Bi(n,4n)^{206}Bi	3163.04	662.30	1396.62	1.55	36.24 ± 8.00
121	^{209}Bi(n,3n)^{207}Bi	2.98	0.75	5.28	0.02	252.29 ± 66.13

A few discrepancies in Tables 6.8 and 6.9 should be pointed out, concerning ID numbers 1, 6 and 7. Both the TENDL-2019 and TENDL-2021 libraries lack data for the ^{9}Be(n,3n)^{7}Be reaction. Earlier versions of TENDL, however, do contain such data. The values used for this reaction were taken from TENDL-2015. TENDL-2021 do not contain data for neutron-induced reactions on ^{27}Al. The values adopted were taken from TENDL-2019 only. In a few cases natural targets containing multiple stable isotopes produced data to which only one constituent isotope contributed. The tabulated values with ID numbers 50, 79, 81, and 102 have been renormalized to reflect the entrance channel as mono-isotopic.

Figure 6.9 shows the Base-10 logarithms of the ratios between predicted and measured physical yields, plotted versus the reaction ID number, for all six MCNP6 physics selections

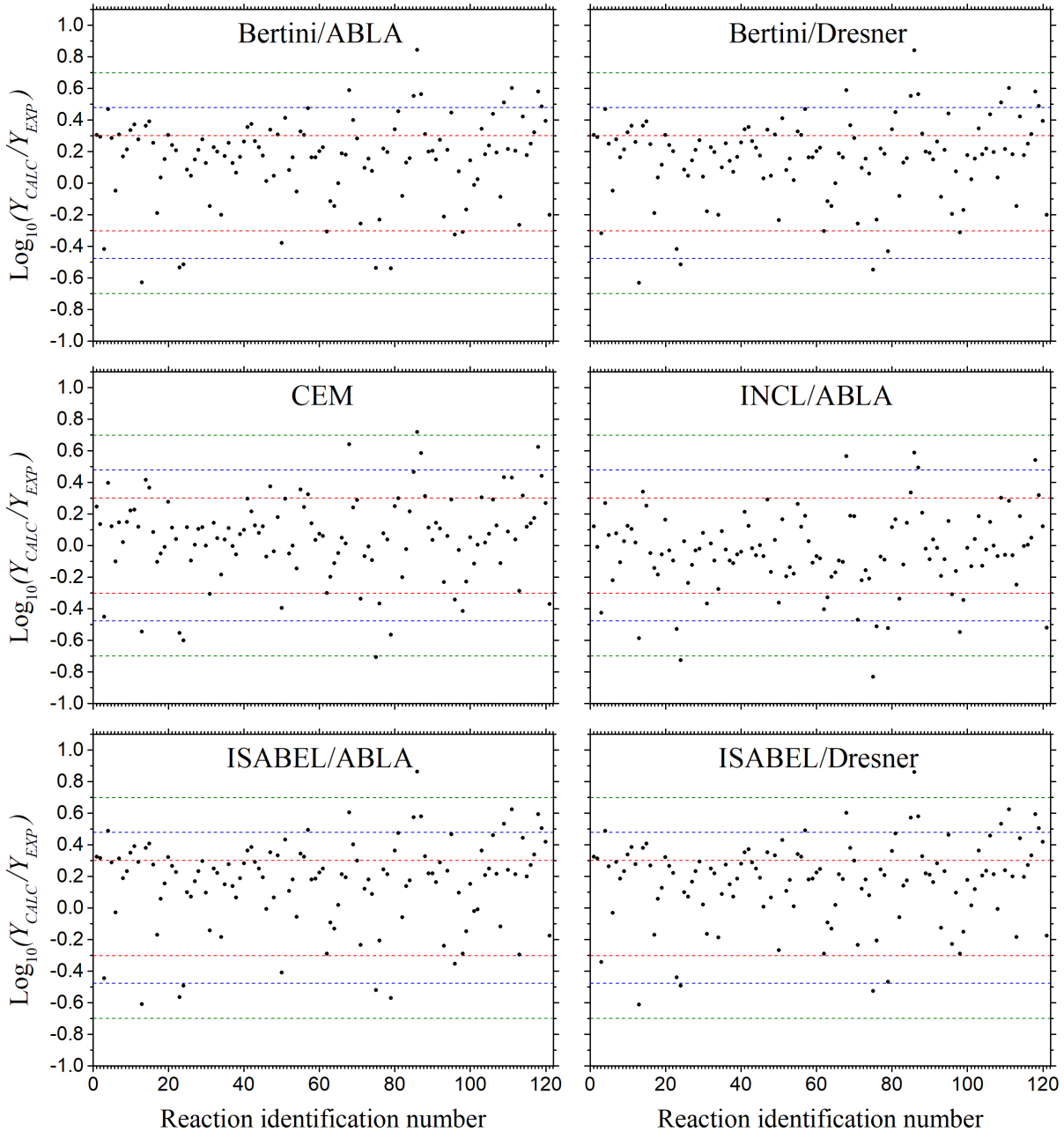


Figure 6.9: Base-10 logarithm of the ratio between predicted and measured physical yields, plotted versus the reaction ID number, for different MCNP6 physics selections used in calculating the the neutron flux. The cross sections used in the predictions were taken from the TENDL-2019 library.

in conjunction with TENDL-2019 cross sections. The corresponding plots based on TENDL-2021 cross sections are shown in Figure 6.10. In these figures the dashed red, blue and green lines indicate differences in ratios of a factor 2, 3, and 5, respectively. These scatter plots show that while the overall trends are similar, there clearly are differences between the various data sets, both with respect to the TENDL library used and also with respect to the physics selection. Overall overpredictions are immediately evident for the physics selections Bertini/ABLA, Bertini/Dresner, ISABEL/ABLA and ISABEL/Dresner, for both TENDL libraries. The CEM and INCL/ABLA physics selections provided values distributed more closely around zero, i.e. more symmetrical distributions in terms of underpredictions and overpredictions. Projections of these data should clearly illustrate this.

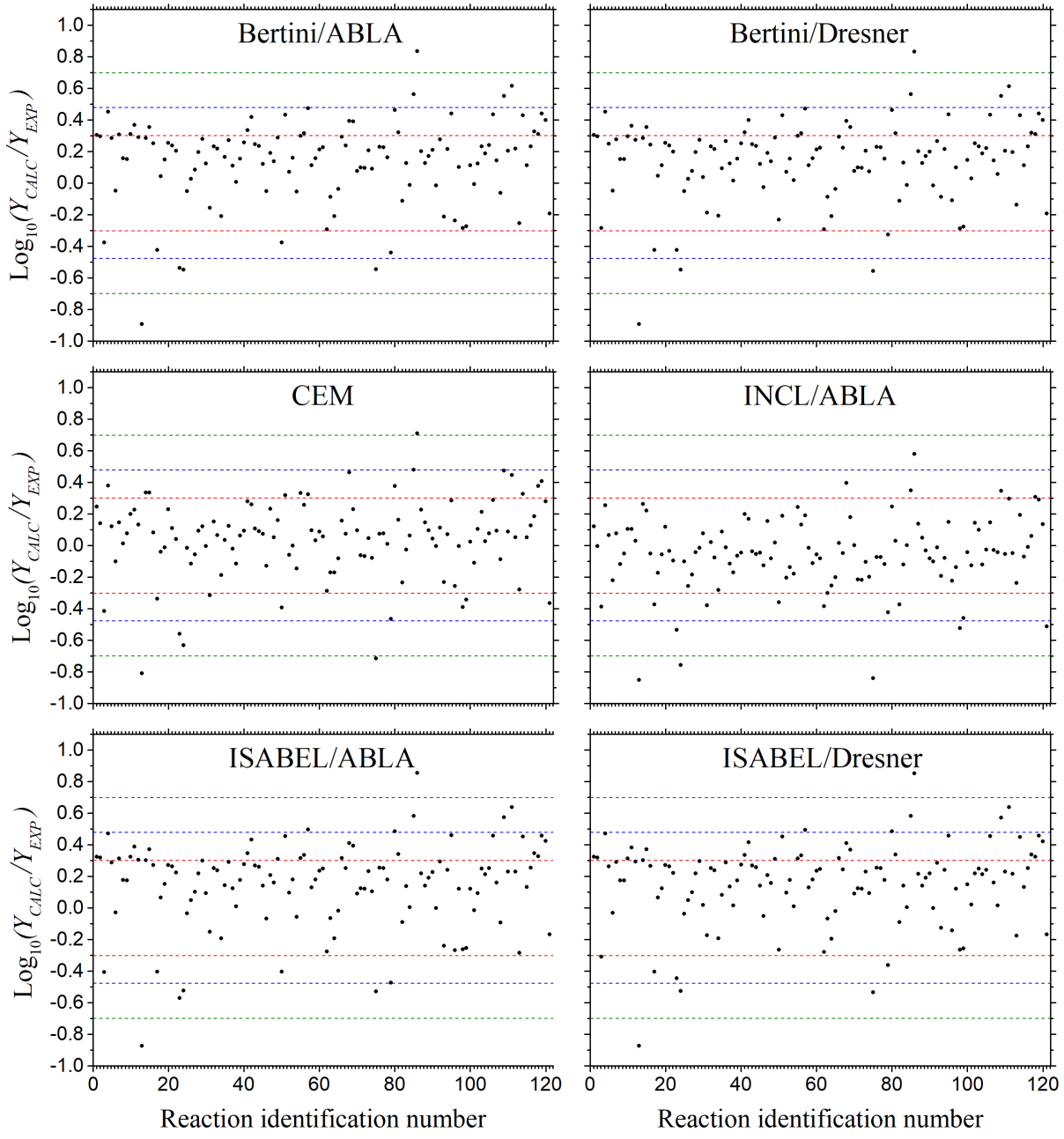


Figure 6.10: Base-10 logarithm of the ratio between predicted and measured physical yields, plotted versus the reaction ID number, for different MCNP6 physics selections used in calculating the the neutron flux. The cross sections used in the predictions were taken from the TENDL-2021 library.

Projections of the scatter plots of Figures 6.9 and 6.10 onto the y-axis, plotted as histograms, are shown in Figures 6.11 and 6.12, respectively. Indeed, the CEM and INCL/ABLA distributions are better distributed around zero than the others, with the CEM distributions in particular having quite symmetrical shapes.

Another way to investigate these distributions quantitatively is to calculate their means and standard deviations, which are presented in Table 6.10. The INCL/ABLA selection produced a relatively small overall underprediction with both libraries, while CEM produced a relatively small overprediction in both cases. The other physics selections all produced significantly larger overpredictions. With cross sections from the TENDL-2019 library, the INCL/ABLA

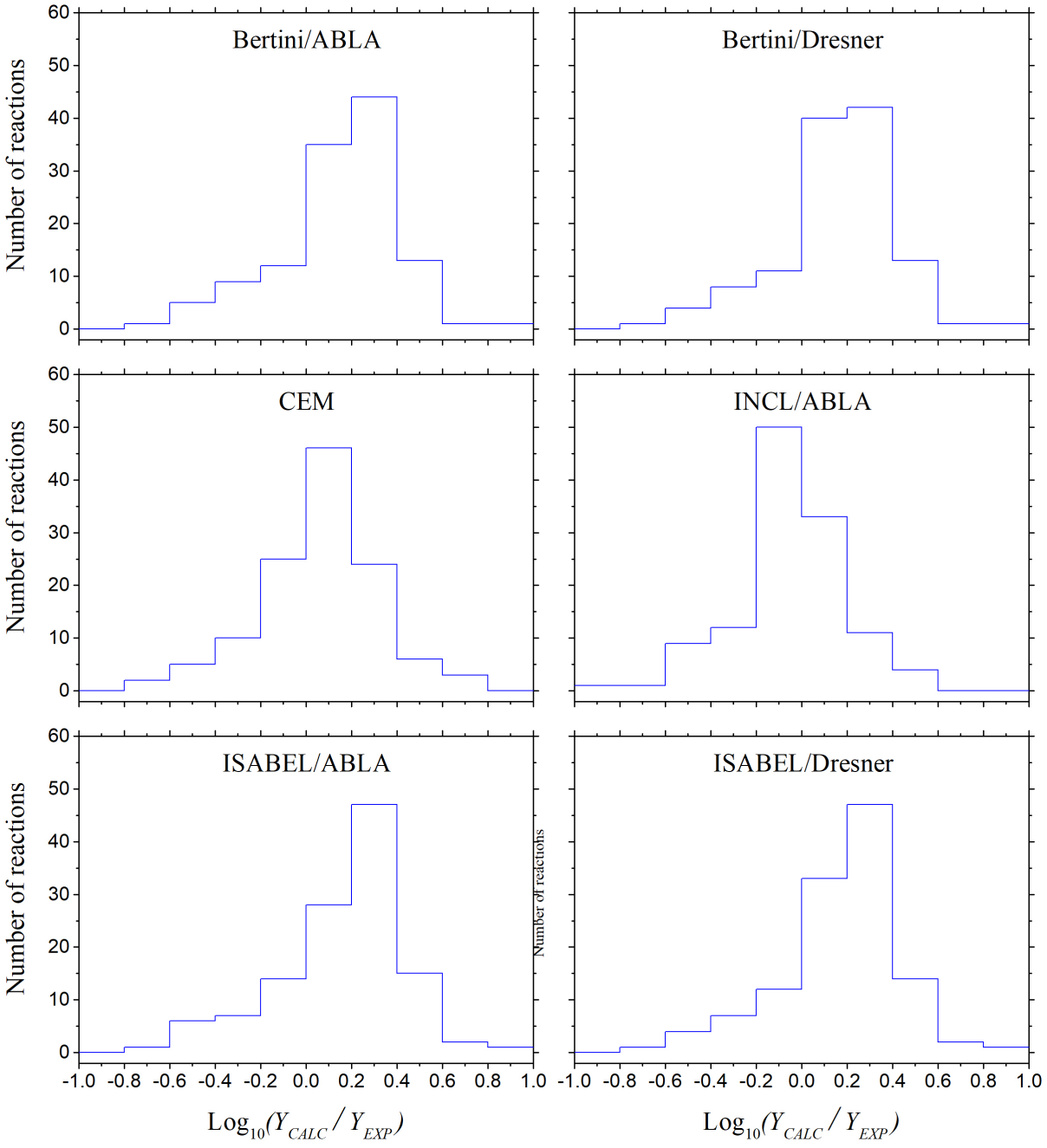


Figure 6.11: Number of reactions versus the base-10 logarithm of the ratio between predicted and measured physical yields, plotted as a histogram. The cross sections used in the predictions were taken from the TENDL-2019 library.

physics selection produced the average closest to zero for the $\mathrm{Log}_{10}(Y_{CALC}/Y_{EXP})$ values, corresponding to an underprediction of 9.72%. With cross sections from the TENDL-2021 library, the CEM physics selection produced the average closest to zero, corresponding to an overprediction of 10.23%. The best agreement between predictions and experimental data is clearly obtained with the INCL/ABLA and CEM physics selections but it is not easy to select a clear "winner" between these two. It is likewise difficult, from an overview perspective, to judge which of the libraries is better. There is perhaps a slight improvement with the newer TENDL-2021 library, considering that for five of the six physics selections marginally smaller averages of the $\mathrm{Log}_{10}(Y_{CALC}/Y_{EXP})$ values were obtained (i.e. closer to zero). The standard deviations are sim-

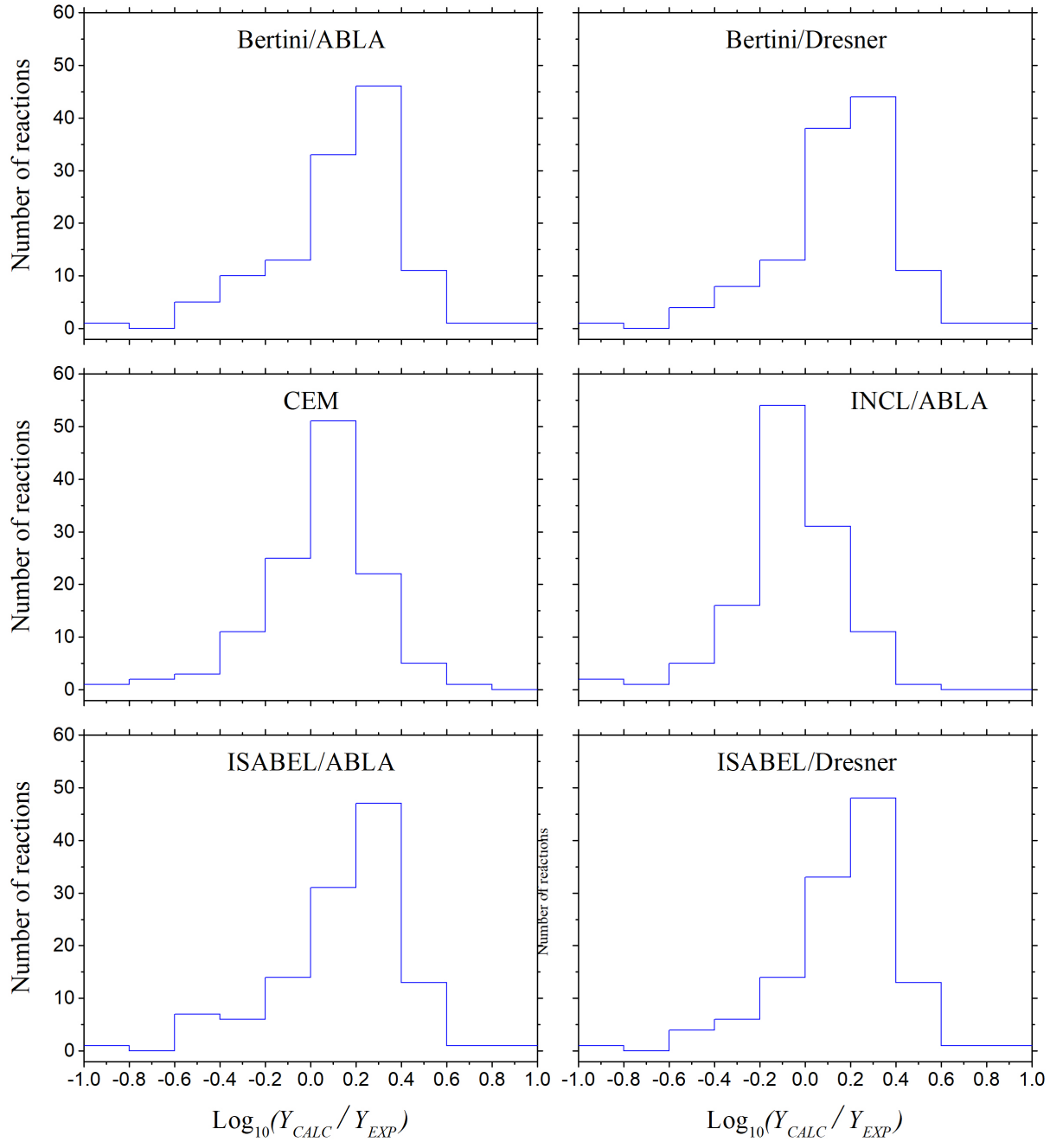


Figure 6.12: Number of reactions versus the base-10 logarithm of the ratio between predicted and measured physical yields, plotted as a histogram. The cross sections used in the predictions were taken from the TENDL-2021 library.

Table 6.10: Averages (of all 121 reactions) and associated standard deviations of Base-10 logarithms of the ratios between predicted and measured physical yields, for all MCNP6 physics selections, utilizing cross sections from the TENDL-2019 and TENDL-2021 libraries, respectively.

* TENDL-2019 *			
Physics selection	$\text{Log}_{10}(Y_{CALC}/Y_{EXP})$		Comments
	Average	Standard deviation	
Bertini/ABLA	0.1494	0.2673	41.06% overprediction factor 1.85 standard deviation
Bertini/Dresner	0.1550	0.2525	42.89% overprediction factor 1.79 standard deviation
CEM	0.0565	0.2609	13.89% overprediction factor 1.82 standard deviation
INCL/ABLA	-0.0444	0.2482	9.72% underprediction factor 1.77 standard deviation
ISABEL/ABLA	0.1627	0.2741	45.45% overprediction factor 1.88 standard deviation
ISABEL/Dresner	0.1687	0.2586	47.47% overprediction factor 1.81 standard deviation

* TENDL-2021 *			
Physics selection	$\text{Log}_{10}(Y_{CALC}/Y_{EXP})$		Comments
	Average	Standard deviation	
Bertini/ABLA	0.1338	0.2638	36.08% overprediction factor 1.84 standard deviation
Bertini/Dresner	0.1395	0.2505	37.88% overprediction factor 1.78 standard deviation
CEM	0.0423	0.2471	10.23% overprediction factor 1.77 standard deviation
INCL/ABLA	-0.0579	0.2330	12.48% underprediction factor 1.71 standard deviation
ISABEL/ABLA	0.1471	0.2703	40.31% overprediction factor 1.86 standard deviation
ISABEL/Dresner	0.1532	0.2563	42.30% overprediction factor 1.80 standard deviation

ilar in magnitude for all physics selections, with equivalent values significantly smaller than a factor of 2. One may therefore expect that for a significant percentage of the reactions the predictions and experimental values will differ by less than a factor of 2.

Table 6.11 presents the actual number of reactions in each case where calculated predictions are within a factor of either 2, 3, or 5 from the corresponding measured values. This is shown for each of the six physics selections in conjunction with either TENDL-2019 or TENDL-2021 cross sections. The case for an averaged neutron spectrum (i.e. averaged over the spectra

1

Table 6.11: Number of reactions where ratios between predicted and measured physical yields is smaller than the factor indicated, for each MCNP6 physics selection, utilizing cross sections from the TENDL-2019 and TENDL-2021 libraries, respectively. The case for an averaged neutron spectrum is also included.

Physics selection	TENDL-2019			TENDL-2021		
	< factor 2	< factor 3	< factor 5	< factor 2	< factor 3	< factor 5
Bertini/ABLA	77	108	120	86	110	118
Bertini/Dresner	80	110	120	91	114	119
CEM	90	112	119	94	115	118
INCL/ABLA	96	109	119	102	114	118
ISABEL/ABLA	78	106	120	81	111	119
ISABEL/Dresner	81	108	120	84	112	119
Averaged spectrum	85	109	120	90	113	119

obtained from the six physics selections with equal weight) has also been included. It will be assumed that the sample size of 121 reactions is large enough to make statements about the predictive power of the methods used. Based on these last-mentioned averages, one can deduce that roughly 70% of predictions are likely to be within a factor of 2 of the corresponding experimental values. More than 90% seems likely within a factor of 3 and about 98% within a factor of 5. Outliers beyond a factor of 5 are very rare. At least, these will be our expectations until a larger sample proves otherwise. It does seem from the overall trend of the results in Table 6.11 that the TENDL-2021 cross sections provide slightly better predictive power than the corresponding TENDL-2019 values. It can be argued that for similar predictions in future neutron-induced activation studies in this energy region, only the CEM and INCL/ABLA physics selections need to be included.

6.5.4 Averaged neutron spectrum and yield outliers

The amount of physical yield data generated in this study is quite extensive. It proved to be no simple task to get a complete overview of all 121 reactions at the same time, especially since there are 12 such data sets (due to the 6 physics selections and 2 cross-section data libraries). Also, one would like to look more closely at the outliers in order to see whether there are perhaps any patterns, e.g. whether the same type of reactions shows an over or underestimation, whether particular mass regions appear more problematic than others, etc. It has already been established that the CEM and INCL/ABLA physics selections provide a better overall agreement for neutron-induced reactions than the alternatives available in MCNP6. In other words, these two selections have fewer outliers. One can therefore argue that from an outlier point of view, one should rather study the worst case. Alternatively, one can study the average case. In fact, several such scenarios were investigated. We chose to present a closer look at the outliers obtained when using the average neutron spectrum (i.e. the average of the 6 neutron spectra obtained from all 6 physics selections) in the calculated predictions,

focusing initially only on those cases where the predictions and measured physical yields differ by more than a factor of 3. This was done separately for the TENDL-2019 and TENDL-2021 data sets of this work. It also seemed sensible to compare the TENDL-2019 and TENDL-2021 predictions directly with each other by calculating the $\mathrm{Log}_{10}(Y_{TENDL-2019}/Y_{TENDL-2021})$ values for all reactions, shown in Figure 6.13.

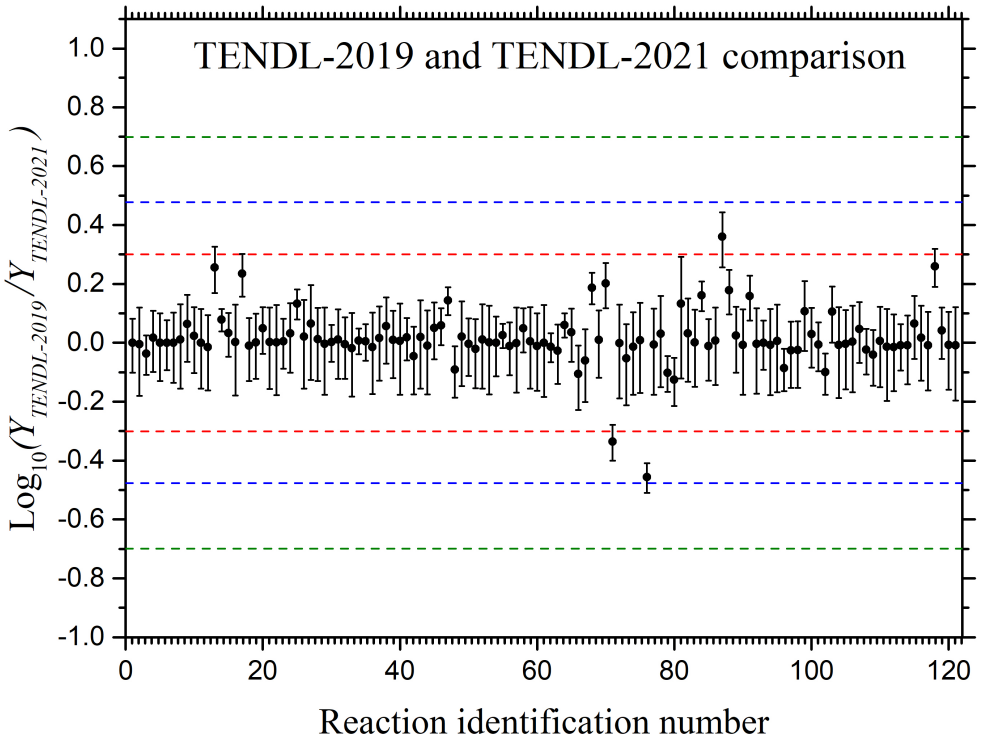


Figure 6.13: Base-10 logarithm of the ratio between predicted physical yields based on TENDL-2019 and TENDL-2021 cross sections, plotted versus the reaction ID number, for the case where an average neutron spectrum has been adopted for the neutron flux (see text for more detail).

While in the majority of cases these logarithms of yield ratios have values close to zero, which indicate good agreement between TENDL-2019 and TENDL-2021 excitation functions for those neutron-induced reactions, there are some outliers where this is not the case. We made a list of the reactions where no error bar crosses the zero line in Fig. 6.13, listed by their respective ID numbers as follows: 13, 14, 17, 25, 47, 48, 64, 66, 68, 70, 71, 76, 79, 80, 84, 87, 88, 91, 96, 102, 103, and 118. Here we need to mention that the error bars shown in the figure have been taken as the standard deviations associated with the averaged physical yields summed in quadrature. There are 22 such points, therefore we may make the statement that in the cases of 99 reactions (i.e. 81.8% of cases) the TENDL-2019 and TENDL-2021 data are in excellent agreement within the uncertainties, as pertaining to their predictive power concerning physical yields. The list of outlier ID numbers span almost the entire mass range, precluding any statements about mass regions that are notably better or notably worse than others. However, in some of the 22 cases the error bars happen to be quite small, therefore some of them should not really be labelled as outliers (e.g. ID numbers 14, 48, 64, and 96). The exercise was therefore repeated by changing the test from the zero line to lines that are 25% above and below the zero line (i.e. $\mathrm{Log}_{10}(Y_{TENDL-2019}/Y_{TENDL-2021}) = \pm\ 0.09691$). This test leaves only 9 outliers: ID numbers 13,17, 68, 70, 71, 76, 84, 87, and 118. None

of these reactions are capture reactions. When the level of the test is raised to 50% (i.e. $\mathrm{Log}_{10}(Y_{TENDL-2019}/Y_{TENDL-2021})$ = ± 0.17609) then only 4 outliers remain: ID numbers 71, 76, 87, and 118. Our verdict is that the overall level of agreement between the TENDL-2019 and TENDL-2021 libraries is substantial, which is to be expected. They are, after all, already the 10^{th} and 11^{th} versions of the library, respectively. There are, however, exceptional cases where the tabulated data for the same reaction differ substantially in the two libraries.

Figures 6.14 and 6.15 show the Base-10 logarithms of the physical yield ratios between the averaged predictions and measurements, based on TENDL-2019 and TENDL-2021 cross sections, plotted versus the reaction ID number. Focussing on those cases exceeding a factor of 3 between predicted and measured yields, 12 outliers are revealed using TENDL-2019 data: ID numbers 13, 23, 24, 68, 75, 79, 85, 86, 87, 109, 111, and 118. This number is reduced to 8 outliers when TENDL-2021 data are used: ID numbers 13, 23, 24, 75, 86, 109, and 111. All of these latter outliers are present also in the corresponding TENDL-2019 set. Only one of them is an (n,γ) capture reaction. The others constitute one (n,2n) reaction, one (n,3n) reaction, and five reactions labelled as (n,x). Not much of a pattern emerged. We can confidently state that a similar level of agreement was found amongst the capture reactions than amongst the threshold reactions. In fact, there are 18 (n,γ) reactions in this study or cases where an (n,γ) reaction notably contributes to the yield. Looking only at the TENDL-2021 data set, in only 4 of these 18 cases did we obtain yield ratios above a factor of 2. This is a comparable statistic to that of the threshold reactions.

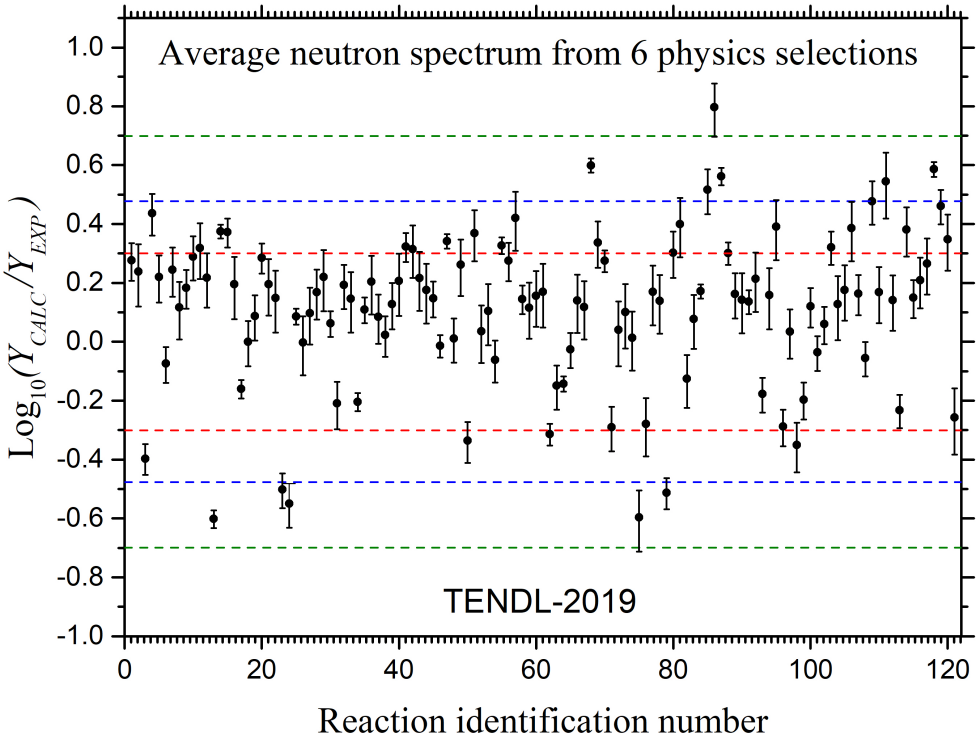


Figure 6.14: Base-10 logarithm of the ratio between predicted and measured physical yields, plotted versus the reaction ID number. The arithmetic average neutron flux spectrum from all six MCNP6 physics selections was used in the predictions and the error bars are based on the associated standard deviations. The cross sections used in the predictions were taken from the TENDL-2019 library.

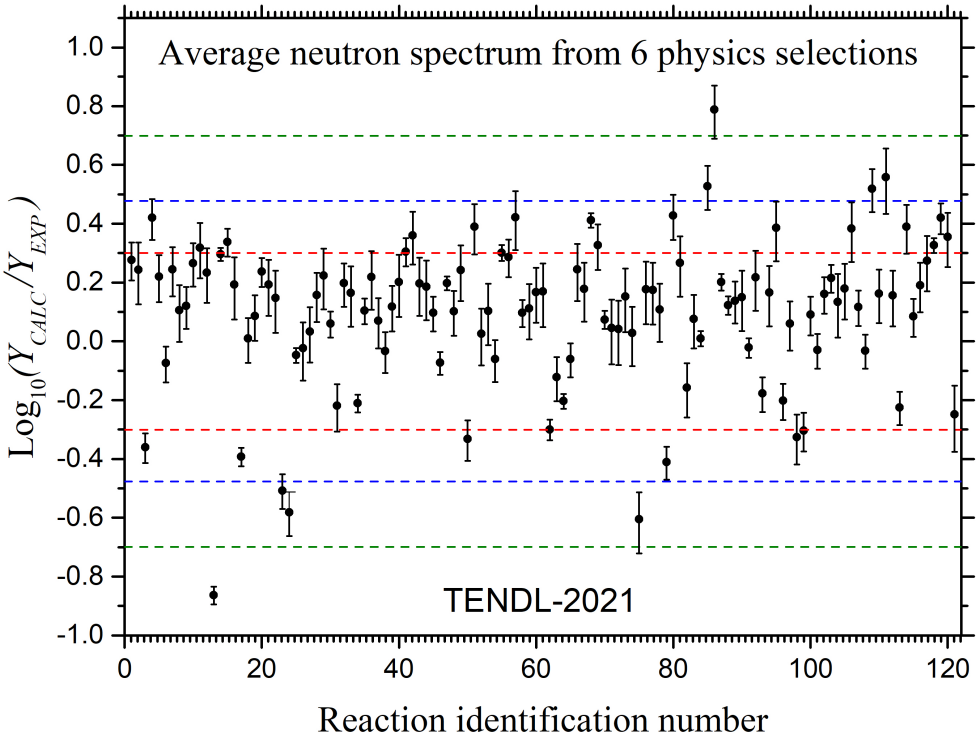


Figure 6.15: Base-10 logarithm of the ratio between predicted and measured physical yields, plotted versus the reaction ID number. The arithmetic average neutron flux spectrum from all six MCNP6 physics selections was used in the predictions and the error bars are based on the associated standard deviations. The cross sections used in the predictions were taken from the TENDL-2021 library.

6.5.5 Testing for asymmetry in the neutron flux

It was mentioned in Subsection 6.2.2 that Run-2 contained three samples of certain target materials, placed in different positions inside the annular sample space of the activation chamber, as a way to look for a possible asymmetry of the neutron flux with respect to the beam axis. An asymmetry may, for example, be introduced if the beam is not perfectly aligned with the beam axis, the beam spot is off-centre, or the sweep trajectory is not exactly circular. Table 6.12 contains the results from the three Mg and the three Al samples, as well as their averages. These average values have been incorporated in Tables 6.8 and 6.9 in the columns for the experimental yields of those reactions. No significant asymmetry issue is evident.

Table 6.12: Experimental physical yields of ^{22,24}Na obtained from neutron activation experiment Run-2.

Sample	Reaction	Physical yield[a] (Bq μAh^{-1} g^{-1})	Reaction	Physical yield (Bq μAh^{-1} g^{-1})
Mg-1	^{nat}Mg(n,x)^{22}Na	3.595 ± 0.010	^{nat}Mg(n,x)^{24}Na	43229.87 ± 291.21
Mg-2		3.416 ± 0.011		41902.45 ± 286.04
Mg-3		3.412 ± 0.010		42445.97 ± 276.01
Mean		3.474 ± 0.010		42526.10 ± 284.42
Al-1	^{27}Al(n,x)^{22}Na	1.198 ± 0.002	^{27}Al(n,x)^{24}Na	22996.96 ± 88.88
Al-2		1.238 ± 0.003		23552.05 ± 91.60
Al-3		1.227 ± 0.003		22879.50 ± 84.91
Mean		1.221 ± 0.003		23142.84 ± 88.46

[a]The tabulated uncertainties are statistical uncertainties only.

6.5.6 Comments in conclusion

It is clear that the neutron flux behind a VBTS target, and therefore also behind one of the new 70 MeV targets, will generally be too low for purposes of radionuclide production on a commercial scale. It will be possible, however, to produce some valuable radionuclides close to the line of stability for experimental-scale applications, e.g. chemical radiolabelling studies, *in vitro* radiobiology investigations, etc. Since secondary neutrons will always be copiously produced throughout the year, it will be a bonus if they can be exploited in a more meaningful way than simply being absorbed in shielding materials.

Since production targets in the VBTS and also the new 70 MeV target stations will typically remain in place for several days, the most appropriate candidates for production with the secondary neutron flux should ideally have half-lives on a similar scale, i.e. several days to perhaps several 10s of days (but not months or years). We identified ^{67}Cu ($T_{1/2}$ = 2.58 d) as a possible candidate and selected it for further investigation; the topic of Chapter 7.

One aspect of this work that may be criticized is the use of the intranuclear cascade model (INC, e.g. by activating the physics selection INCL/ABLA) in the Monte Carlo simulations with the code MCNP. According to Cugnon *et al.* [CUG2003] the INC is generally considered to be valid when the incident particle has a sufficiently small de Broglie wavelength to interact with individual nucleons. For nucleon-induced reactions a lower limit is often quoted as about 200 MeV. Cugnon *et al.* questioned this limit, in a pragmatic approach, by comparing a large body of data with model predictions in the energy region 10–250 MeV. It was found that the INC, as implemented by the Liége group, gives surprisingly good results at energies well below the limit mentioned above. It was concluded by these authors, who are also the developers of the Liége version of the model, that the INC shows promising potential for nucleon-induced reactions in the energy region 40–200 MeV, including good predictions of neutron emission spectra originating from (p,xn) reactions.

Chapter 7

Production of ^{67}Cu

This chapter reviews existing methods to produce the therapeutic radionuclide ^{67}Cu. Aspects related to ^{67}Cu supply and its importance in medicine are also discussed. Against this background, the feasibility to produce ^{67}Cu with secondary neutrons emitted from radionuclide production targets, during bombardment with 70 MeV protons, is subsequently investigated.

7.1 BACKGROUND AND OBJECTIVES

7.1.1 The supply and demand mismatch

A 2012 review article by Smith *et al.* [SMI2012] estimated the potential market in the US for the therapeutic radioisotope ^{67}Cu at ∼12 000 Ci (444 TBq) per year. A decade later, this has not materialized and the entire world production is a mere fraction of this estimate, by some orders of magnitude. In fact, a 2018 review article on clinical results of copper radionuclides in humans [FOL2018] lists only one phase I/II clinical trial that was performed with a ^{67}Cu-labelled antibody, involving 12 patients. Why this enormous mismatch between past predictions and current reality? Unfortunately, not unlike the case of the radioisotope ^{225}Ac discussed in Chapters 3 and 4, there are enormous difficulties associated with the production and reliable supply of ^{67}Cu, to the extent that this renders the prospects for any large-scale clinical trials near impossible. The more that one studies the literature on ^{67}Cu, the more the similarities between the ^{225}Ac and ^{67}Cu supply imbalances become clear. Smith *et al.* pointed out that the level of production required would need multiple producers running constantly and that the technology available (at that time) would not be capable to meet the demand.

Many articles have commented on problems associated with the lack of a reliable supply (see e.g. the very recent review by Mou *et al.* [MOU2022]). Currently most of the ^{67}Cu productions are located at facilities associated with universities and national laboratories. These are mostly multi-purpose experimental facilities, hardly in a position to sustain any large-scale ^{67}Cu production on a routine basis. In spite of this, the importance of radiocopper in the radiomedical field, and ^{67}Cu in particular, has grown enormously, based on continued progress in that field (e.g. radiolabelling and small-animal studies). Production technology also exhibited further development, which will be discussed in some detail in Section 7.1. It does not appear, however, that the large-scale industrialization and/or commercialization of ^{67}Cu production should be expected in the near future. The time for that to happen, however, will surely come.

In this study the possibility to exploit secondary neutrons for ^{67}Cu production at a 70 MeV cyclotron facility has been investigated. From the outset, however, it must be clearly stated that the aim was not to try and address the above-mentioned supply problem, an endeavour that would be very naïve. Rather, the aim should be to make a contribution on a much smaller scale, mainly to support a research effort. The rationale should be the same as presented by Engle [ENG2018] concerning ^{225}Ac production, namely that current progress in the field depends strongly on the combined contributions of many suppliers, using an array of different methodologies tailored to their respective infrastructure capabilities. Until such time that ^{67}Cu production becomes fully industrialized, this seems to be the only way to proceed.

7.1.2 Copper radioisotopes in medicine

Five copper radioisotopes have become important in nuclear medicine, i.e. ^{60}Cu ($T_{1/2}$ = 23.7 m), ^{61}Cu ($T_{1/2}$ = 3.339 h), ^{62}Cu ($T_{1/2}$ = 9.673 m), ^{64}Cu ($T_{1/2}$ = 12.701 h), and ^{67}Cu ($T_{1/2}$ = 2.576 d). The first four are positron emitters suitable for PET imaging, while ^{64}Cu and ^{67}Cu both have potential in targeted radiotherapy as so-called "theranostics" [BOS2018]. Copper-64 is a theranostic isotope because its β^+-decay is suitable for PET, while its 190 keV average β^--decay provides radiotherapy capabilities [JOH2015, BOS2018]. Copper-67 is a theranostic isotope due to its suitable β^--emissions for radiotherapy combined with its 184.577 keV (48.7%) γ-ray, which is in the ideal energy range for imaging with a SPECT camera.

There are several key reasons why copper radionuclides are generating so much interest. Neither copper nor their zinc decay products are chemically toxic to humans at the levels required for diagnostic and therapeutic procedures. According to Boschi *et al.* [BOS2018] the total body copper content is about 100 mg and the daily dietary intake is between 1 and 2 mg per day, orders of magnitude higher than the trace amounts added by the radiomedical procedures. Johnsen *et al.* [JOH2015] stated that copper and zinc are the second and third most prevalent trace elements in the human body, respectively, and that various kinds of tumours have a high copper content. In addition, copper is not involved in inflammatory processes, unlike the most-utilized PET radiotracer in the world, 2-deoxy-2-[^{18}F-fluoro-D-glucose] (^{18}F-FDG). Imaging by means of PET or SPECT of a copper radiotracer will therefore provide information on cancer only due to its insensitivity to inflammation. In order words, radioactive copper probes can serve as highly specific tumour markers. Various biological molecules (e.g. peptides and antibodies) can be labelled by copper radionuclides, similarly to many other radiometals (see e.g. [BOS2018] and references therein). Equally important, however, is a different category of application, exploiting simple radioactive monoatomic ions for their well-recognized natural role in a multitude of biological processes [BOS2018].

Serving as both the imaging probe and the bioactive substrate after being administered as simple metallic ions, Cu radiometals can be used to image (or trace) their own journey through a living organism. Since copper ions play a key role in cell replication and growth, it is not surprising that they are deeply involved in cancer development and progression [BOS2018]. This means that, in addition to their potential in radiolabelled pharmaceuticals, ^{64}Cu and ^{67}Cu can also be harnessed as true theranostic agents in their simple ionic form. Furthermore, their physiological uptake largely excludes the skeleton as copper does not seek out or accumulate

in bone tissue (see e.g. [JOH2015]), thereby enhancing its specificity in other organs for certain cancers. The longer half-life of ^{67}Cu make it attractive in cases where the half-life of ^{64}Cu is deemed to be too short.

7.1.3 Production of ^{67}Cu with medium-energy protons

The energy region of a 70 MeV proton cyclotron is usually considered to be medium energy. There are only two feasible routes to produce ^{67}Cu with a reasonable yield and quality with medium-energy protons. The relevant reactions are ^{68}Zn(p,2p)^{67}Cu and ^{70}Zn(p,x)^{67}Cu. Unfortunately both production routes have pros and cons. Natural Zn is not an option as too much other Cu contaminants are co-produced, in particular copious amounts of ^{64}Cu. Relatively massive targets of enriched ^{68}Zn or ^{70}Zn are required, both of which are not widely available and extremely costly, requiring quantitative recycling. Even with highly enriched targets, some ^{64}Cu will usually be unavoidable. We are tempted to adopt something similar to Robertson's notation [ROB2020] for ^{225}Ac (i.e. ^{227,225}Ac† and ^{225}Ac* – see Section 3.1) also for ^{67}Cu. One can refer to a product with notable ^{64}Cu contaminant as ^{64,67}Cu† and a radionuclidically pure product as ^{67}Cu*. Since the above two reactions may become important to iThemba LABS at some future time period in the context of the new 70 MeV cyclotron facility, they are discussed in some detail below. The expected yields from these proton-induced reactions also provide a framework for comparison with the neutron-induced reactions that will follow afterwards.

Cross sections and corresponding physical yields for the ^{68}Zn(p,x)^{64}Cu and ^{68}Zn(p,2p)^{67}Cu reactions have been evaluated by the IAEA [ENG2019], shown in Figures 7.1 and 7.2, respectively. These evaluations extend up to 100 MeV. In the case of the ^{70}Zn(p,x)^{67}Cu reac-

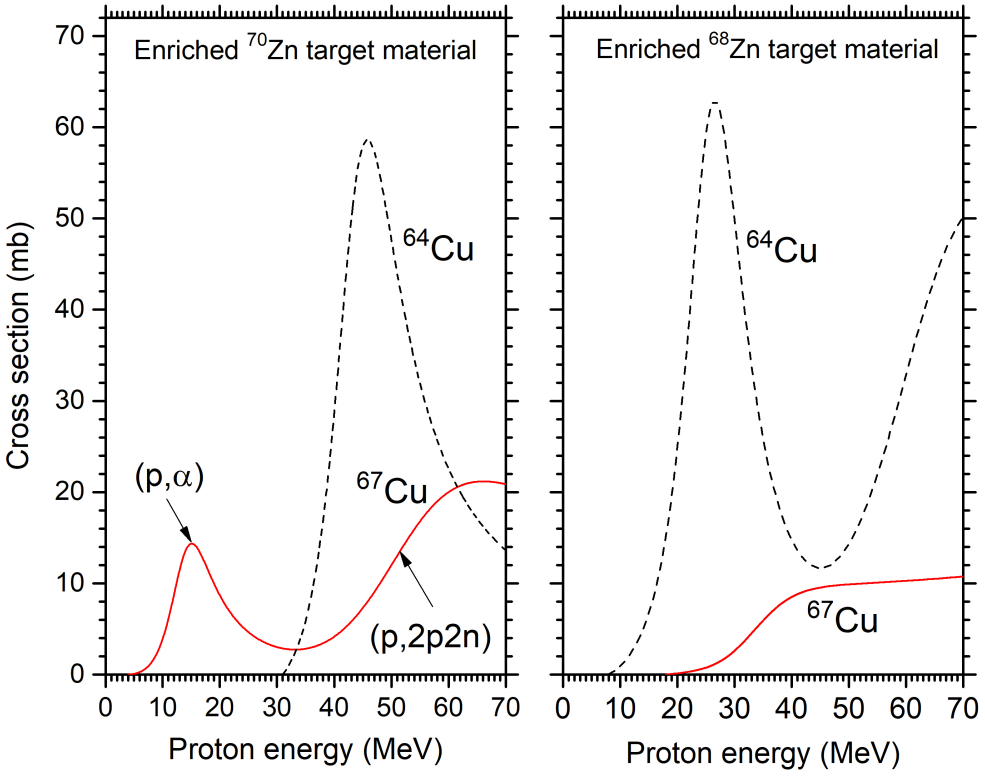


Figure 7.1: Evaluated excitation functions for the formation of ^{64}Cu (broken curves) and ^{67}Cu (solid red curves) in the proton bombardment of enriched ^{70}Zn and ^{68}Zn, respectively.

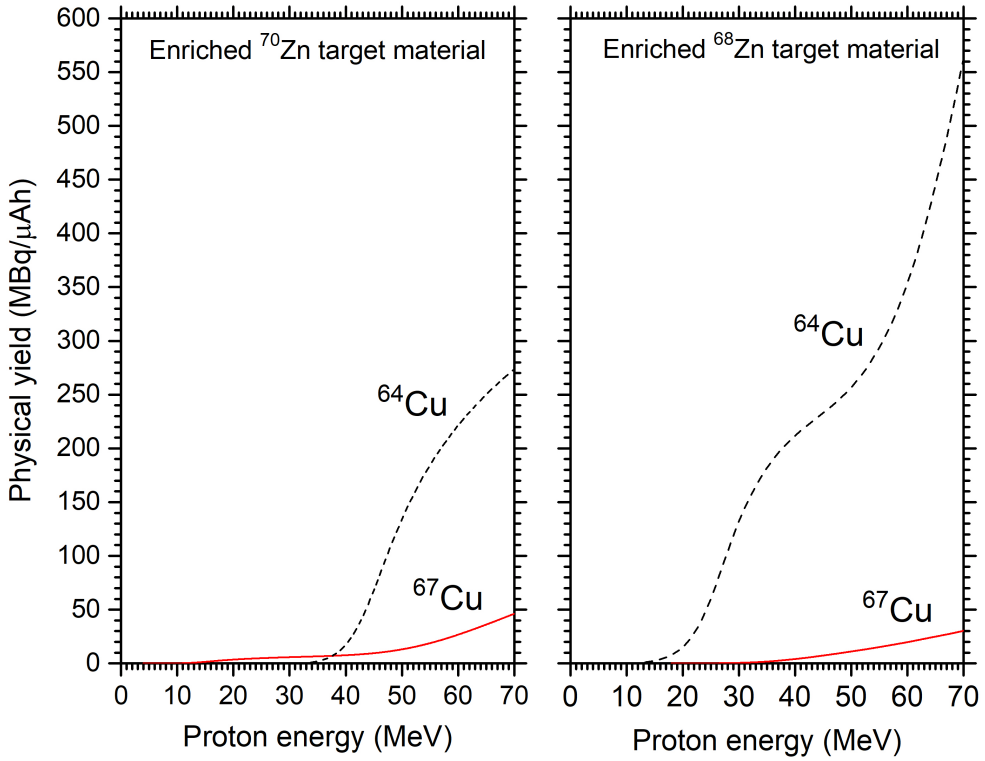


Figure 7.2: Integral physical yields for the production of ^{64}Cu (broken curves) and ^{67}Cu (solid red curves) in the proton bombardment of enriched ^{70}Zn and ^{68}Zn, respectively.

tion, however, the IAEA evaluation only extends up to 40 MeV, which is the region where the ^{70}Zn(p,α)^{67}Cu reaction dominates. This latter reaction was investigated by a group in Jülich (Kastleiner *et al.* [KAS1999], Hilgers *et al.* [HIL2003]) and reported for the small-scale production of ^{67}Cu on a small medical cyclotron; the potential for batch size up to 500 MBq was reported. In order to extend the evaluation up to 70 MeV, we added the data recently reported by Pupillo *et al.* [PUP2020], measured between 45 and 70 MeV, and performed our own re-evaluation, the results of which are also included in Figures 7.1 and 7.2. The rise above 40 MeV is dominated by the ^{70}Zn(p,2p2n)^{67}Cu reaction, i.e. emitted unbound nucleons, in contrast to the lower-energy peak where these nucleons are bound in an α-particle cluster.

The only experimental data found in the literature for the ^{70}Zn(p,x)^{64}Cu reaction were also measured by Pupillo *et al.* [PUP2020] between 45 and 70 MeV. Therefore, for this production route, we adopted the TENDL-2021 cross sections but renormalized these values (by a factor of about 1.5) to correctly reproduce the maximum of the measured excitation function of Pupillo. The resulting renormalized data are also shown in Figures 7.1 and 7.2.

From Figures 7.1 and 7.2 it is clear that ^{64}Cu contamination will always be present except when the ^{70}Zn(p,x)^{67}Cu reaction can be exploited below about 30 MeV on 100% enriched ^{70}Zn targets. In practice, even highly enriched ^{70}Zn is expected to contain some stable Zn contaminants, which will feed some ^{64}Cu formation. Fortunately, the much lower half-life of ^{64}Cu ($T_{1/2}$ = 12.701 h) compared to ^{67}Cu ($T_{1/2}$ = 2.576 d) means that by introducing a cooling time before administration, the ^{64}Cu contamination level can be reduced to an acceptable level. Unfortunately this will always come at a cost of some loss of the valuable ^{67}Cu product.

The physical yields shown in Figure 7.2 were used to make predictions of ^{67}Cu production yields and ^{64}Cu contamination levels. The bombardment time, beam intensity, and cooling time

after EOB were treated as free parameters that could be chosen with any values that we wanted to investigate. Our approach to perform these calculations (see Section 2.8) was tested against results published by Pupillo *et al.* [PUP2020] and could reproduce their values. Those authors conceived a stacked-target configuration that endeavoured to optimize ^{67}Cu production while minimizing ^{64}Cu contamination, an innovation which they subsequently patented [ESP2019]. The patented concept target has four layers: ^{70}Zn with energy window 70 → 56 MeV, followed by ^{68}Zn with energy window 56 → 35 MeV, followed by ^{27}Al with energy window 35 → 25 MeV, followed by a second ^{70}Zn layer with an energy window of 25 → 10 MeV. This concept certainly has merit but one may question some practical aspects of its implementation in high-performance targetry, e.g. the presence of cooling-water layers, encapsulation materials, etc., which incorporate dead layers. It seems to us that an extended optimization study is required that includes these unavoidable dead layers. From the perspective of this thesis project, after consideration of the alternatives, we chose to retain a tandem-target concept. The energy windows introduced in Chapter 5 were again adopted, namely 62 → 38 MeV and 26 → 0 MeV. As discussed before, the encapsulation materials and cooling-water layers will consume some of the available energy range. The higher-energy window can accommodate either ^{68}Zn or ^{70}Zn but it only makes sense to consider ^{70}Zn for the lower-energy window due to the relatively high threshold of the ^{68}Zn(p,2p)^{67}Cu reaction (see Figure 7.1). Comparisons of production yields have been made using a bombardment time of 5 days (i.e. about 2 half-lives of ^{67}Cu), a 70 MeV proton beam with a beam current of 250 μA, and a cooling time that will give an arbitrary selected ^{64}Cu impurity of 5%, which should be acceptable in most cases. All the results will be discussed in Section 7.4, “Results and Discussion”.

7.1.4 Production of ^{67}Cu with composite light projectiles

A number of studies will be highlighted without attempting to give an exhaustive account of previous work. Several groups investigated the reaction ^{64}Ni(α,p)^{67}Cu. Skakun *et al.* [SKA2004] investigated this production route on enriched ^{64}Ni and concluded that the integral yield is about 4.3 times lower than can be obtained with the alternative ^{70}Zn(p,α)^{67}Cu route. Ohya *et al.* [OHY2018] utilized this reaction with a 36 MeV α-particle beam to produce small-scale but high quality ^{67}Cu on >99% enriched ^{64}Ni for pre-clinical studies. The lower yield is a disadvantage but an approximately 30-times lower ^{64}Cu contamination level is a significant advantage. They also noted that the radiochemistry of Ni may be somewhat simpler than the radiochemistry of Zn, which is possibly another advantage.

Kozempel *et al.* [KOZ2012] investigated the ^{70}Zn(d,αn)^{67}Cu reaction up to 20 MeV, reporting an estimated yield of 4.2 MBq/μAh (110 μCi/μAh). While this production rate is quite low, a much reduced level of ^{64}Cu contamination compared to alternative production routes is cited as a significant advantage. Nigron *et al.* [NIG2021] recently pointed out that with very highly enriched ^{70}Zn and deuterons with energy below 26 MeV, a ^{67}Cu product can be made that is essentially free of ^{64}Cu contamination. The authors concluded that this production route may be of interest for the future as linear accelerators are under development that will provide milli-ampere (mA) deuteron beams, provided adequate targetry can be developed that can accommodate such high-intensity beams under prolonged bombardments.

7.1.5 Production of ^{67}Cu with heavy ions

Mastren *et al.* [MAS2014, MAS2015], as part of a larger study on harvesting isotopes at a projectile fragmentation facility [ABE2019], reported on the collection of ^{67}Cu from a secondary beam cocktail at the National Superconducting Cyclotron Facility (NSCF) at Michigan State University in the US. They made the point that therapeutic doses can be on the order of hundreds of millicurie per patient, well out of the reach of small medical cyclotrons. In proof-of-principle studies, ^{67}Cu was successfully harvested from an aqueous beam dump downstream of the primary target facility that produced secondary beams (RIBs) for on-line experiments. It was reported that a saturated ^{67}Cu activity of up to 2 Ci was achievable, depending on the primary beam. We will defer our own comments about this approach to the Comments in Conclusion section later in this chapter.

7.1.6 Production of ^{67}Cu with photonuclear reactions

Explorative studies have been performed on the production of ^{67}Cu using the ^{68}Zn(γ,p)^{67}Cu reaction [EHS2012, STO2016, ALI2019]. These studies exploited bremsstrahlung photons produced with existing electron linacs, the photons being secondary particles emitted from high-Z targets (e.g. tungsten or tantalum) being bombarded with the primary electron beam. Stoner *et al.* [STO2016] describes a production size of 30 mCi during a 2-hour bombardment on a 40 g enriched ^{68}Zn target, while Ehst *et al.* [EHS2012], by extrapolating their results on a natural Zn target to an enriched ^{68}Zn target, reports the feasibility of a 2 Ci production with a 48-hour linac run. It is not possible to directly compare these various efforts as electron energies, average beam currents and target geometries differ. To the best of our knowledge, no large-scale production of ^{67}Cu has yet been demonstrated via photonuclear production but we are aware of development work at Argonne National Laboratory in the US, utilizing the 50 MeV/25 kW electron linac of the Low-Energy Accelerator Facility (LEAF).

Photonuclear reactions, however, will most likely play a major role in future large-scale production strategies for a number of radionuclides, including ^{67}Cu. To explain this adequately, one needs to elaborate on recent developments concerning electron accelerators, and high-energy Rhodotrons in particular. Recently Northstar Medical Isotopes in the US purchased the first two (of eight planned) Rhodotron electron accelerators for ^{99}Mo/^{99m}Tc generator production, utilizing the ^{100}Mo(γ,n)^{99}Mo reaction on highly enriched ^{100}Mo targets [FIS2019, HAR2018]. Rhodotrons are electron accelerators based on the principle of re-circulating a beam through successive diameters of a single coaxial RF cavity. Their design makes them much more compact than electron linacs. These particular Rhodotrons purchased by Northstar are 40 MeV, 125 kW units, specially developed for this purpose by IBA [HAR2018]. Traditionally ^{99}Mo production resided almost exclusively in the domain of nuclear reactors but the closure of many reactors in recent years prompted the development of alternative production strategies. This makes the Rhodotron procurement by Northstar Medical Isotopes particularly significant. An interesting peculiarity of this development is that a single ^{100}Mo stacked-target is bombarded from both ends simultaneously by two electron beams, utilizing a pair of Rhodotrons for a single target system. This is the first commercial, large-scale production facility of ^{99}Mo not based on nuclear-reactor technology in the world.

The Rhodotron story, however, becomes even more interesting. Late in 2021 Northstar Medical Isotopes announced the purchase of a third 40 MeV, 125 kW Rhodotron from IBA for ^{225}Ac production, utilizing the ^{226}Ra(γ,n)^{225}Ra$\rightarrow^{225}$Ac process [FIS2021, HAR2018]. In this case the target material is radioactive ^{226}Ra ($T_{1/2}$ = 1600 y). This announcement specifically mentions that Northstar also plans to pursue ^{67}Cu production in future with similar technology, utilizing the ^{68}Zn(γ,p)^{67}Cu reaction. Prior comments on the feasibility of the Rhodotron TT300 HE accelerator for ^{67}Cu and ^{47}Sc production have also been made by IBA [BER2019].

To summarize this section, one can reflect on these developments by asking whether smaller producers, in smaller countries, can emulate them. The accelerator technology is relatively simple and would be affordable to many potential producers. The targetry, however, is a completely different story. The targets themselves are massive, considering they constitute enriched and/or radioactive material. A recent article by Tkac *et al.* [TKA2021], for example, reports on the radiochemical processing of ^{100}Mo target batches of up to 600 g per batch. The procurement, handling and recovery of such material will likely be beyond the capabilities of most countries in the world. The same applies to ^{68}Zn and radioactive ^{226}Ra. In order to be commercially viable, large infrastructures are required to process, recover and recycle these large quantities of target materials; these are endeavours where the actual accelerators only constitute a minor cost in comparison. Cost is not the only criterion but the ability to procure and secure these materials will pose a virtually insurmountable obstacle for producers in most countries, at least in the foreseeable future. This technology is therefore likely to reside only in countries with large-scale enrichment capabilities and massive nuclear technology infrastructure, in the context of strong private/public partnerships. It is highly likely that such countries will keep the technology safely within their borders, judging by current policies on enrichment and various other nuclear technologies. Small players will struggle to join this club.

7.1.7 Production of ^{67}Cu with neutron-induced reactions

Traditionally, neutron-induced reactions for the production of radionuclides have long been the domain of nuclear reactors. This has started to change since about the start of the new Millennium, at least in terms of investigations on production possibilities with accelerator-produced neutrons (i.e. secondary neutrons). Spahn *et al.* [SPA2004] published one of the earliest investigations on ^{67}Cu production with secondary neutrons, to the best of our knowledge. These authors compared new measurements of spectrum-averaged cross sections of the ^{67}Zn(n,p)^{67}Cu reaction, using a 14 MeV d(Be) neutron source, with corresponding values obtained with a fission neutron spectrum. These results are summarized in Table 7.1. Also shown

Table 7.1: Experimentally determined average ^{67}Cu formation cross sections of neutron-induced reactions on highly enriched ^{67}Zn.

Neutron source	Average cross section $\langle\sigma\rangle$ (mb)	Reference
14 MeV d(Be) neutron spectrum	5.13 $\pm$ 0.87	Spahn [SPA2004]
Fission neutron spectrum	1.07 $\pm$ 0.04	Spahn [SPA2004]
66 MeV p(Rb/Ga) neutron spectrum	3.71 $\pm$ 0.80	This work[a]

[a] See tables 6.8 and 6.9, reaction ID = 42.

in Table 7.1 is the corresponding value obtained from secondary neutron activation behind a VBTS target of this work. The spectrum averaged cross section with a 14 MeV d(Be) neutron spectrum is about a factor 5 larger than the value obtained with a fission neutron spectrum, with the 66 MeV p(Rb/Ga) neutron spectrum producing a value somewhere in-between. This is mainly an indication of spectrum hardness. Spahn *et al.* [SPA2004] estimated the average neutron energy of the 14 MeV d(Be) neutron spectrum to be 4.95 MeV and that of spallation neutrons to be 3.98 MeV. In contrast, the fission spectrum is considerably softer, with a reported average neutron energy of 2.06 $\pm$ 0.05 MeV [ISL1973] from the fission of ^{235}U induced by 0.4 MeV neutrons. Certainly, further neutron interactions with materials surrounding a source and the overall geometry may significantly alter the neutron spectrum at the position where samples are activated. Nevertheless, it was not surprising to find a value in-between the two published values of Spahn *et al.*, as summarized in Table 7.1.

Some authors commented on the development of intense neutron sources using deuteron break-up, and suggested that such infrastructure may also be useful for ^{67}Cu production, amongst several other useful radionuclides. Kin *et al.* [KIN2013] and also Gopalakrishna *et al.* [GOP2018] based some of their discussion on the SPIRAL 2 development at GANIL, France, utilizing the ^{nat}C(d,n) reaction to produce a neutron spectrum with an average neutron energy of approximately 18 MeV using a 40 MeV, 5 mA deuteron beam. The cross section of the ^{67}Zn(n,p)^{67}Cu reaction is about a factor 10 larger at these energies than the corresponding value from a 14 MeV d(Be) neutron spectrum. The International Fusion Materials Irradiation Facility (IFMIF) will generate a neutron flux with a broad peak at 14 MeV, based on the Li(d,xn) reaction utilizing 40 MeV deuterons and two parallel 125 mA beams [KNA2017]. These developments may be useful for investigating production possibilities of certain radionuclides, including ^{67}Cu.

The activation studies on the VBTS, discussed in the previous chapter, also shed light on the predictive power of MCNP simulations in conjunction with the TENDL cross sections. This study, exploiting a 66 MeV proton beam, is important from the point of view of a future 70 MeV facility, especially as the beam energies are so close to each other. Good predictive power with a 66 MeV proton beam should provide significant reassurance that similar simulations may be trusted with a 70 MeV proton beam. The yield results exploiting the ^{67}Zn(n,p)^{67}Cu and ^{68}Zn(n,x)^{67}Cu reactions, on highly-enriched target materials, are summarized in Table 7.2. Both the CEM and INCL/ABLA physics selections led to very satisfactory agreement with the measurements. For this reason, both the CEM and INCL/ABLA physics selections were adopted for simulations with 70 MeV proton beams in the new target stations.

It is evident from Table 7.2 that the ^{68}Zn(n,x)^{67}Cu reaction will provide significantly higher

Table 7.2: Experimentally determined physical yields compared to predictions based on MCNP + TENDL for ^{67}Cu produced by secondary neutron activation in the bombardment of a Rb/Ga tandem target with 66 MeV protons in the VBTS.

Target material	Physical yield (Bq μAh^{-1} g^{-1})				
	Experimental	TENDL-2019		TENDL-2021	
		CEM	INCL/ABLA	CEM	INCL/ABLA
s[^{67}Zn]	1081.1	1779.6	1442.5	1971.4	1599.4
s[^{68}Zn]	2336.0	2812.2	2021.1	2881.2	2071.4

yields than will be obtainable from the ^{67}Zn(n,p)^{67}Cu reaction. Also, ^{68}Zn has a significantly higher natural abundance than ^{67}Zn (18.45% and 4.04%, respectively). It is therefore less expensive to enrich ^{68}Zn than ^{67}Zn to the same level. For these reasons, the ^{68}Zn(n,x)^{67}Cu reaction was selected as the reaction of choice.

The remainder of this chapter is dedicated to the production of ^{67}Cu in the secondary neutron flux behind a primary tandem target under bombardment with a 70 MeV proton beam. The process is shown schematically in Figure 7.3. Two additional tandem-target configurations were included in the study. A Zr/Y_2O_3 target for the production of ^{88}Y was selected as this radionuclide has some potential in a number of geophysical applications in addition to a sufficiently long half-life for export purposes. A Be/Ga configuration was selected solely because the beryllium produces a harder neutron spectrum than the other targets. The idea stems from the fact that, for many years, the neutrons used in radiotherapy at iThemba LABS were generated by 66 MeV proton beams on a Be target with an energy window of 40–66 MeV.

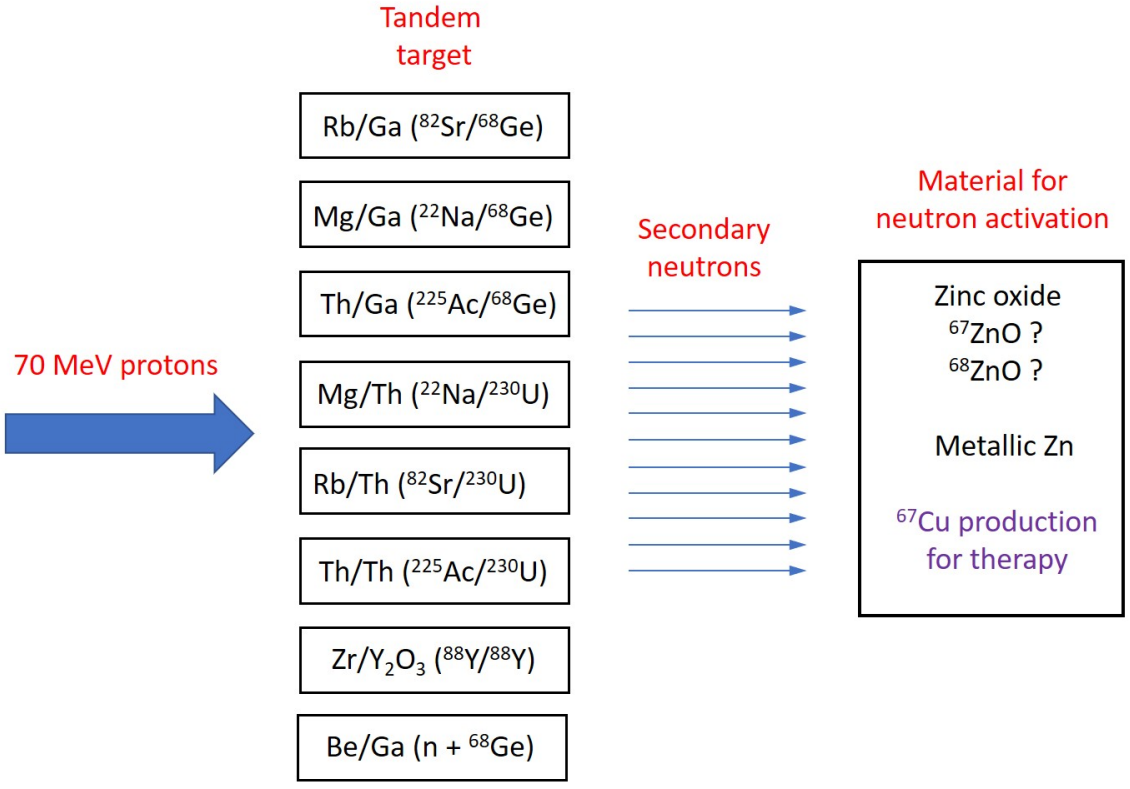


Figure 7.3: Schematic diagram of the tandem targets considered for bombardment with a 70 MeV primary proton beam, followed by another target for activation with secondary neutrons. The relevant target materials and radioisotopes of main interest are as indicated.

7.2 MONTE CARLO SIMULATIONS

The new 70 MeV target station was simulated in a similar way as the VBTS (see Section 6.3), utilizing the Monte Carlo radiation transport code MCNP6. The existing VBTS model input file was used as the starting point for the development of a model for the new stations. This was convenient as certain parts of the file stayed nearly the same or needed only minor editing, such as the material specifications, the source term of the proton beam, the model selection

statements, etc. The main task was to develop station and target geometries that are realistic, yet simplified in less important areas. Small structures, such as nuts and bolts, were not modelled. Similar to the VBTS model, the focus was on achieving a suitable model in terms of the overall material budget as well as accurate dimensions where the beam/target configuration is concerned. Most of the details described in Section 6.3 also apply here and will therefore not be further elaborated on.

The geometry of the model is shown in Figures 7.4 through 7.6. Figure 7.4 shows the entire station while Figures 7.5 and 7.6 show the target regions of two different target-holder concepts. The *standard target holder* is similar to the VBTS target holder except that it has been extended in the in-beam direction to accommodate somewhat thicker target configurations. Prototypes of these target holders have been manufactured and are currently (i.e. at the time of writing) being tested and evaluated at iThemba LABS. The cylindrical inner cavity, which houses the actual targets, has a larger diameter than the VBTS target holder, as the diameters of the new targets have been increased (outer diameters of nominally 40 mm for VBTS target disks and 52 mm for the new 70 MeV targetry). This is to provide more surface area from which heat can be removed during bombardments. The neutron activation cavity behind the target holder, located in the head of the pusher arm, will allow about 250 cm^3 of material to be simultaneously neutron activated with a primary target bombardment.

The *modified target holder* in Figure 7.6 was introduced as an additional simulation study in an attempt to increase the neutron flux in the neutron activation cavity. No such target holders have yet been produced but the idea is worthy of investigation, which will be evident

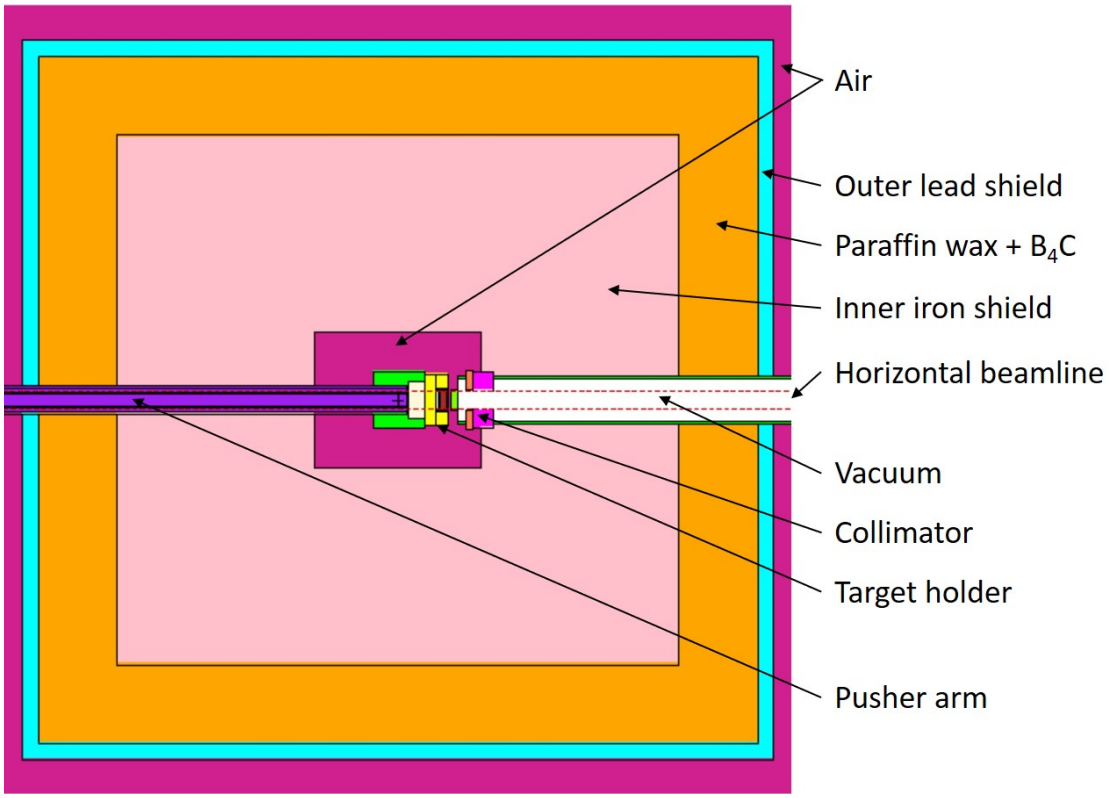


Figure 7.4: The model geometry of the new 70 MeV target station with its horizontal beamline as generated with the MCNP6 code system. Note that subsequent figures zoom into the target region to show more detail. The image is coloured by materials selection.

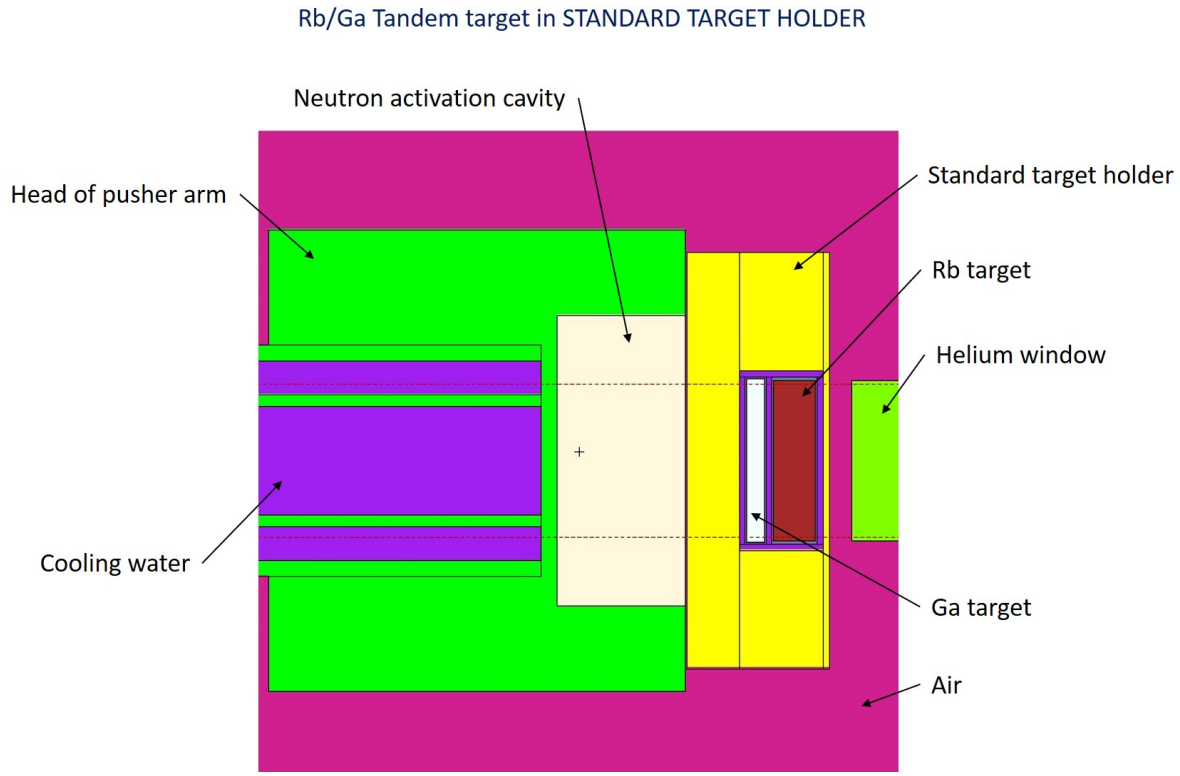


Figure 7.5: Zoomed-in view showing the standard target holder, tandem Rb/Ga targets, and the neutron activation chamber located in the head of the pusher arm, as generated with the MCNP6 code system. See also Figure 7.4.

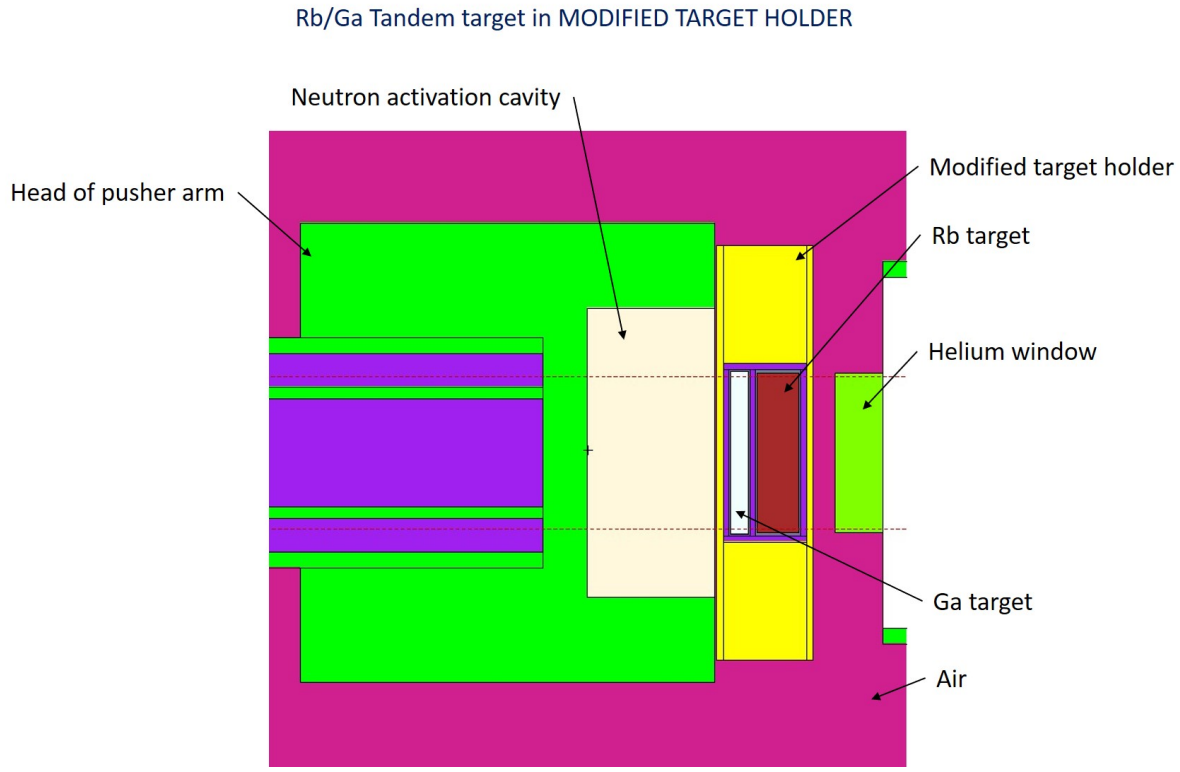


Figure 7.6: Zoomed-in view showing the modified target holder, tandem Rb/Ga targets, and the neutron activation chamber located in the head of the pusher arm, as generated with the MCNP6 code system. See also Figures 7.4 and 7.5.

from the results that will be presented shortly. The modified target holder has been provided with a backing plate with the same thickness as its beam entrance window (of nominally 2 mm). This results in a reduction of the mean distance between the neutron activation cavity and the primary targets. A few words of caution on this approach are in order. In the case of a target failure where significant target material is lost from a target capsule, a thick backing (such as in Figure 7.5) provides for the ability to degrade and stop the beam before it can punch through the target holder. In the case of a thin backing (such as in Figure 7.6) such a failure may lead to beam traversing through the target holder, entering the neutron activation cavity. This would not be a healthy situation as the material in the neutron activation cavity will become heated by the beam, as no external cooling in that space is foreseen and provided for. In practice, should such target holders be considered in future, it would be prudent to measure the temperature of the material to be neutron activated (e.g. with a K-type thermocouple) and to provide an interlock to remove the beam should a sudden temperature rise be observed. Provision has therefore been made in the actual design for thin electrical wires to be fed out of the neutron activation cavity, through a radial port with a 10 mm diameter, which has not been incorporated in the Monte Carlo model.

To conclude this section, it should be mentioned why the modified target holder was investigated in the first place. This part of the investigation was prompted by the geometry error discussed in Subsection 6.3.4. Once we realized the sensitivity of the neutron flux to small changes in the geometry of the activation cavity relative to the targets, it made sense to expand the investigation to a scenario where the cavity is placed as close as possible to the actual targets. This can only be achieved by reducing the thickness of the backing.

7.3 ACTIVATION CAVITY AND SECONDARY TARGETS

In order to perform realistic Monte Carlo simulations, it is necessary to formulate a sensible design approach not only of the primary tandem targets but also of the secondary targets to be activated by neutrons behind the target holder containing the primary targets. The activation cavity provided in the head of the pusher arm is cylindrical in shape with a diameter of 90.7 mm and a depth of 40 mm. The idea was that this cavity should accommodate an exchangeable cylindrical container with an outer diameter of 90 mm and 40 mm outer length. Such containers are anticipated to have thin walls, machined out of a suitable metal. Assuming a 1 mm wall thickness, an inner cavity of 88 mm diameter and 38 mm in depth would be available. This gives an inside volume is 231 cm^3 that can be filled with material to be neutron activated. Such containers can be loaded and unloaded into a bombardment station using the same pole-with-suction-cup system described in Section 2.3.

The above idea was first suggested by a visiting scientists and user at iThemba LABS, Dr Ferenc Szelecsényi of ATOMKI, Debrecen, Hungary. Dr Szelecsényi suggested filling the cavity with a salt of an enriched target isotope, such as a ^{68}Zn-salt. After bombardment, the salt would be dissolved and the solution passed through an ion-exchange resin to remove the desired radionuclide(s), whereafter the target material would be quantitatively recovered for re-use.

It transpires that many of the salts of Zn are hygroscopic and some (like several of the chlorides, of which nine crystalline forms are known) are deliquescent [ULL1985]. In contrast, ZnO

is insoluble in water and non-toxic, making it a useful dental amalgam material [QOS2018]. Zinc oxide is highly soluble in many acids, including hydrochloric acid. It is frequently used as a target material (see e.g. Jamriska *et al.* [JAM1997], Katabuchi *et al.* [KAT2008], Johnsen *et al.* [JOH2015]) as an alternative to the metallic form. Methods for the quantitative recovery of Zn, both in its metallic and oxide forms, have been developed (see e.g. [KAT2008]). In this work we only considered metallic Zn and ZnO as potential target materials.

7.3.1 A candidate ZnO secondary target

The theoretical density of ZnO is 5.681 g/cm^3 [RAD2018] but ceramic materials of ZnO may have relative densities significantly lower than this value, depending on the method of manufacture. Most of the methods combine powder compaction with a sintering scheme (i.e. the application of pressure and heat). At iThemba LABS, a large 300 ton hydraulic press facility was established years ago for the manufacture of targets by powder compaction [STE2018b]. Various punch-and-die sets of different sizes are available and new sizes can be added when required. This facility has been the backbone of target manufacture since the nineties and it is still extensively utilized for this purpose. This facility should be ideal for manufacturing cylindrical ZnO pellets, to be stacked in the neutron-activation container as shown schematically in the left panel of Figure 7.7. This pattern of stacking will allow 55 cylindrical pellets of 10.6 mm diameter and 38 mm long to be packed fairly loosely into the container.

There are methods to promote densification of ceramics during powder compression, e.g. by means of spark plasma sintering [RAD2018]. However, for the purposes of this study we only considered cold powder compaction with the large 300 ton press of iThemba LABS. From green densities published in the literature and taking into account the significant capability of the 300 ton press, it seems very feasible to achieve a green density of 3.49 g/cm^3 (i.e. 61.4% of the

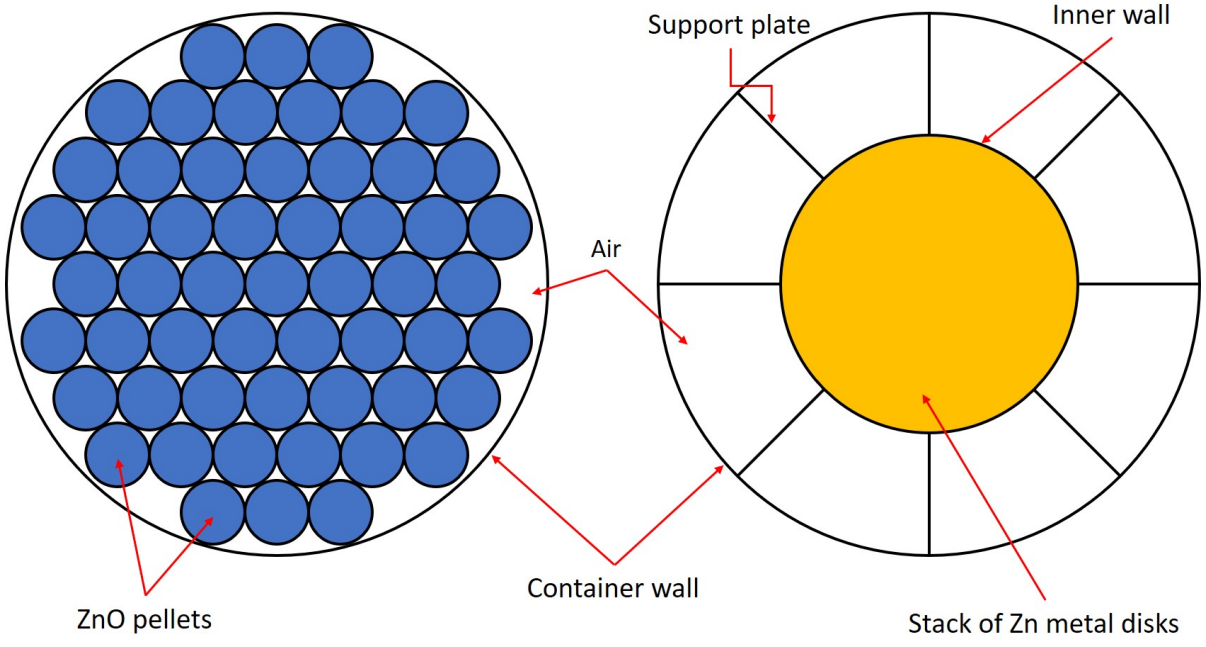


Figure 7.7: LEFT: Schematic top view of the ZnO secondary target concept. RIGHT: Schematic top view of the metallic Zn secondary target concept.

theoretical density – see e.g. [PUS2013]). The total mass of ZnO that can be accommodated in the container in this way will be about 643 g, which has a Zn content of about 521 g. For purposes of the simulation and subsequent yield estimates, we adopted a rounded quantity of 500 g ^{68}Zn. There are also a few quite large spaces between the wall of the container and the ZnO pellets where more material can be added, if required (e.g. by filling those cavities with smaller ZnO fragments). We are therefore confident that 500 g ^{68}Zn can be fitted comfortably into such a container. The matter of availability and procurement of such a relatively large amount of enriched ^{68}Zn needs to be considered. At the present time such a procurement will not be trivial, however, there are indications that this may change in future. This aspect will be discussed in more detail later.

7.3.2 A candidate metallic Zn secondary target

Another scenario was considered for the secondary target, namely where the same amount of 500 g ^{68}Zn is stacked as metallic disks in the centre of the neutron-activation container. This is shown schematically in the right panel of Figure 7.7. Since Zn in metallic form has a higher density than ZnO (7.133 g/cm^3 and 5.681 g/cm^3, respectively), the Zn disks will occupy significantly less volume. A smaller inner cavity inside the container is therefore envisaged. iThemba LABS has for many years prepared natural Zn target disks by means of the 300 ton hydraulic press (for the production of ^{67}Ga) and densities near the theoretical value have consistently been achieved.

7.4 RESULTS AND DISCUSSION

7.4.1 Proton-induced reactions on ^{68}Zn and ^{70}Zn

Following on from Subsection 7.1.3, the results of our predictions of ^{67}Cu yields from ^{68}Zn+p and ^{70}Zn+p reactions are presented. Table 7.3 shows the physical yield and corresponding radionuclidic purity of ^{67}Cu produced by both the ^{68}Zn(p,2p)^{67}Cu and ^{70}Zn(p,x)^{67}Cu reactions in an energy window of 62 $\rightarrow$ 38 MeV, as well as for the ^{70}Zn(p,x)^{67}Cu reaction in the energy window 26 $\rightarrow$ 0 MeV. In principle, a tandem ^{68}Zn/^{70}Zn tandem target is possible, with the ^{70}Zn target located in the lower-energy window. In the higher-energy window, the ^{70}Zn+p route gives a somewhat higher yield than the ^{68}Zn+p route, by about 23%. Since ^{70}Zn is much less abundant in nature (natural abundances of 18.45% and 0.61% for ^{68}Zn and ^{70}Zn, respectively) the ^{68}Zn+p production route would still normally be the preferred one. Both

Table 7.3: Predicted ^{67}Cu physical yields in the proton bombardment of enriched ^{68}Zn and ^{70}Zn targets.

Energy window (MeV)	^{68}Zn target		^{70}Zn target	
	Physical yield[a] (MBq/μAh)	Purity[b] (%)	Physical yield[a] (MBq/μAh)	Purity[b] (%)
62 $\rightarrow$ 38	18.84	9.3	23.21	9.3
26 $\rightarrow$ 0	–	–	5.11	100

[a]For mono-isotopic targets.

[b]Radionuclidic purity of ^{67}Cu relative to longer-lived Cu total activity (i.e. ^{61}Cu + ^{64}Cu + ^{67}Cu).

The incident beam is 70 MeV protons.

production routes have significant co-produced Cu contaminants, rather surprisingly leading to virtually the same instantaneous radionuclidic purity of 9.3% (in practice at the end of a very short bombardment where no significant radioactive decay could have taken place). In contrast, the ^{70}Zn(p,x)^{67}Cu reaction will give a radionuclidically pure product if produced exclusively in the lower-energy window, once the Cu has been separated from the Zn target matrix.

In productions utilizing the higher-energy window, a long cooling time is required for the shorter lived Cu contaminants to decay to a level below 5% of the total radioactive Cu content. This is shown in Table 7.4 for a bombardment time of 5-days with a beam current of 250 μA, where a 91 hour cooling time is required to reach a ^{67}Cu radionuclidic purity of 95%. Even so, both production routes will provide in excess of 3 Ci of ^{67}Cu, which would be enough for several therapeutic doses. With a tandem target system, the production yield can almost be doubled. These are very significant yields, suitable to support clinical trials. Once again we would like to point out that these results were obtained from available nuclear data, not taking into consideration any procurement issues of the enriched target material, neither the cost of such material or the effort required to recover spent target material.

Table 7.4: Production yields of ^{67}Cu in the proton bombardment of enriched ^{68}Zn and ^{70}Zn targets.

Energy window	^{68}Zn target			^{70}Zn target		
(MeV)	Cooling time[a]	Yield[b]		Cooling time[a]	Yield[b]	
	(hours)	(GBq)	(mCi)	(hours)	(GBq)	(mCi)
62 → 38	91.0	112.03	3027.8	91.0	138.02	3730.4
26 → 0	–	–	–	0	84.23	2477.3

[a] Cooling time after EOB to reach 95% radionuclidic purity of ^{67}Cu or better.
[b] For a 5-day bombardment with 70 MeV protons at a beam current of 250 μA.

7.4.2 Neutron-induced reactions on ^{68}Zn

Tables 7.5 and 7.6 present the predicted ^{67}Cu physical yields from secondary-neutron activation of 100% enriched ^{68}Zn (as an oxide) in a new 70 MeV target station, using TENDL-2019 and TENDL-2021 cross sections, respectively. The CEM physics selection mostly leads to somewhat higher yields than the INCL/ABLA physics selection; the differences vary between about 1% and 44% but on average by about 25%. The differences in yield associated with the different primary tandem targets are relatively small – in fact, they are remarkably similar. The exception is the Be/Ga target, leading to yields between a factor of 2 and 3 higher than any of the other tandem targets. This is not surprising, considering that it provides a significantly harder neutron spectrum (see Section 5.3). Corresponding results obtained with cross sections from the TENDL-2019 and TENDL-2021 libraries are generally in good agreement. In most cases the ^{67}Cu radionuclidic purity (relative to the sum of all longer-lived Cu radioactivity) is above 50%, which will require a cooling time post EOB for any production regimen to produce a ^{67}Cu product with 95% radionuclidic purity or better.

Tables 7.7 and 7.8 present the predicted ^{67}Cu production yields for a bombardment period of 5-days at a beam current of 250 μA, using TENDL-2019 and TENDL-2021 cross sections, respectively. These yield values are for a ^{67}Cu product with a radionuclidic purity of 95%,

Table 7.5: Predicted ^{67}Cu physical yields from secondary-neutron activation of 100% enriched ^{68}Zn in a new 70 MeV target station, using TENDL-2019 cross sections.

Target holder	Tandem target	CEM		INCL/ABLA	
		Physical yield (kBq μAh^{-1} g^{-1})	Purity[a] (%)	Physical yield (kBq μAh^{-1} g^{-1})	Purity[a] (%)
Standard	Rb/Ga	1.536	59.4	1.136	56.5
	Mg/Ga	1.213	68.6	1.050	53.6
	Th/Ga	1.038	55.9	0.924	53.3
	Mg/Th	1.183	67.9	1.045	53.4
	Rb/Th	1.496	58.8	1.129	56.3
	Th/Th	1.004	55.0	0.921	53.2
	Zr/Y_2O_3	1.422	48.7	0.987	50.2
	Be/Ga	4.458	48.2	4.414	48.1
Modified	Rb/Ga	2.724	64.0	2.110	60.0
	Mg/Ga	2.352	70.8	2.273	58.5
	Th/Ga	2.941	63.3	2.669	59.1
	Mg/Th	2.409	70.5	2.410	58.8
	Rb/Th	2.800	63.8	2.235	60.3
	Th/Th	3.026	63.2	2.825	59.4
	Zr/Y_2O_3	3.685	57.7	2.735	56.1
	Be/Ga	8.342	55.8	8.261	55.6

[a]Radionuclidic purity of ^{67}Cu relative to longer-lived Cu total activity (i.e. ^{61}Cu + ^{64}Cu + ^{67}Cu). The incident beam is 70 MeV protons.

Table 7.6: Predicted ^{67}Cu physical yields from secondary-neutron activation of 100% enriched ^{68}Zn in a new 70 MeV target station, using TENDL-2021 cross sections.

Target holder	Tandem target	CEM		INCL/ABLA	
		Physical yield (kBq μAh^{-1} g^{-1})	Purity[a] (%)	Physical yield (kBq μAh^{-1} g^{-1})	Purity[a] (%)
Standard	Rb/Ga	1.576	64.4	1.165	61.4
	Mg/Ga	1.241	72.7	1.078	58.6
	Th/Ga	1.063	60.8	0.949	58.2
	Mg/Th	1.212	72.1	1.073	58.4
	Rb/Th	1.536	63.8	1.159	61.3
	Th/Th	1.029	59.9	0.946	58.2
	Zr/Y_2O_3	1.461	53.4	1.014	55.0
	Be/Ga	4.605	53.6	4.560	53.5
Modified	Rb/Ga	2.788	68.7	2.162	64.9
	Mg/Ga	2.401	74.7	2.329	63.4
	Th/Ga	3.005	67.9	2.734	63.8
	Mg/Th	2.460	74.4	2.469	63.7
	Rb/Th	2.868	68.6	2.290	65.2
	Th/Th	3.093	67.8	2.893	64.2
	Zr/Y_2O_3	3.773	62.2	2.804	60.8
	Be/Ga	8.595	61.0	8.513	60.9

[a]Radionuclidic purity of ^{67}Cu relative to longer-lived Cu total activity (i.e. ^{61}Cu + ^{64}Cu + ^{67}Cu). The incident beam is 70 MeV protons.

Table 7.7: Predicted ^{67}Cu production yields from secondary-neutron activation of 100% enriched ^{68}Zn in a new 70 MeV target station, using TENDL-2019 cross sections.

Target	Tandem	Cooling time[a]	CEM yield[b]		Cooling time[a]	INCL/ABLA yield[b]	
holder	target	(hours)	(MBq)	(mCi)	(hours)	(MBq)	(mCi)
Standard	Rb/Ga	29.4	9108.5	246.2	32.3	6518.8	176.2
	Mg/Ga	20.3	7969.0	215.4	35.0	5850.1	158.1
	Th/Ga	32.8	5926.5	160.2	35.2	5136.1	138.8
	Mg/Th	21.0	7710.6	208.4	35.2	5809.0	157.0
	Rb/Th	30.1	8799.8	237.8	32.6	6463.0	174.7
	Th/Th	33.8	5668.3	153.2	30.7	4969.2	134.3
	Zr/Y_2O_3	39.6	7524.8	203.4	38.1	5309.7	143.5
	Be/Ga	40.0	23466.3	634.2	40.0	23234.1	627.9
Modified	Rb/Ga	27.7	16457.5	444.8	28.9	12579.4	340.0
	Mg/Ga	17.8	15877.9	429.1	30.4	13334.2	360.4
	Th/Ga	25.8	18160.0	490.8	29.9	15742.0	425.5
	Mg/Th	18.3	16173.6	437.1	30.2	14171.8	383.0
	Rb/Th	25.3	17383.4	469.8	28.7	13357.6	361.0
	Th/Th	25.8	18681.9	504.9	29.4	16748.6	452.7
	Zr/Y_2O_3	31.1	21437.9	579.4	32.6	15656.4	423.1
	Be/Ga	33.0	47496.0	1283.7	35.7	45657.1	1234.0

[a]Cooling time after EOB to reach 95% radionuclidic purity of ^{67}Cu.

[b]For a 5-day bombardment with 70 MeV protons at a beam current of 250 μA.

Table 7.8: Predicted ^{67}Cu production yields from secondary-neutron activation of 100% enriched ^{68}Zn in a new 70 MeV target station, using TENDL-2021 cross sections.

Target	Tandem	Cooling time[a]	CEM yield[b]		Cooling time[a]	INCL/ABLA yield[b]	
holder	target	(hours)	(MBq)	(mCi)	(hours)	(MBq)	(mCi)
Standard	Rb/Ga	24.6	9862.4	266.6	27.5	7059.8	190.8
	Mg/Ga	15.7	8586.0	232.1	30.4	6322.1	170.9
	Th/Ga	28.2	6389.1	172.7	30.6	5549.9	149.9
	Mg/Th	16.4	8314.3	224.7	30.4	6295.7	170.2
	Rb/Th	25.3	9537.1	257.8	27.7	7000.9	189.2
	Th/Th	28.9	6134.0	165.8	30.6	5532.8	149.5
	Zr/Y_2O_3	35.2	8116.6	219.4	33.8	5728.7	154.8
	Be/Ga	35.0	25654.6	693.4	35.2	25338.5	684.8
Modified	Rb/Ga	20.3	18317.7	495.1	24.1	13603.2	367.7
	Mg/Ga	13.3	17061.9	461.1	25.8	14380.4	388.7
	Th/Ga	21.0	19582.5	529.3	25.3	16972.9	458.7
	Mg/Th	13.7	17388.4	470.0	25.3	15324.8	414.2
	Rb/Th	20.3	18842.6	509.3	23.9	14446.0	390.4
	Th/Th	21.2	20103.4	543.3	24.8	18059.7	488.1
	Zr/Y_2O_3	26.8	23046.9	622.9	28.2	16854.0	455.5
	Be/Ga	28.0	51792.3	1400.0	28.2	51163.5	1382.8

[a]Cooling time after EOB to reach 95% radionuclidic purity of ^{67}Cu.

[b]For a 5-day bombardment with 70 MeV protons at a beam current of 250 μA.

i.e. after a sufficiently long cooling time post EOB, as listed in the tables. The typical cooling time is between 1 and 2 days. Except for the Be/Ga target, which was included merely for

academic purposes, with all the other tandem targets a production yield of only a couple of 100 mCi seems possible with the standard target holder. With the modified target holder a production yield between 400 and 500 mCi seems feasible. We know that the Rb/Ga target will receive a significant fraction of the available beam from the new 70 MeV cyclotron, hence we will concentrate the discussion mostly on this case. Our estimates indicate a production yield below 0.5 Ci even with the modified target holder. This value of 0.5 Ci was an objective that we hoped to reach. In order to make a significant improvement to the yield, it will be necessary to relax the requirement for a 95% radionuclidic yield. The use of metallic Zn as the secondary target material may also improve the yield. These possibilities are discussed next.

Table 7.9 presents a comparison between ^{67}Cu production yields predicted for the ^{68}Zn oxide and metallic ^{68}Zn secondary targets (shown schematically in Figure 7.7), using cross sections from the TENDL-2019 library. In both cases the equivalent ^{68}Zn content was 500 g, the bombardment period 5-days, and the beam current 250 μA. Yields are shown for different cooling times, namely directly after EOB (i.e. no additional cooling beyond the decay that took place during the bombardment period) as well as at those times when the ^{67}Cu radionuclidic purity would reach values of 90% and 95%. It is evident that the radionuclidic purity is already above 80% at EOB and that cooling times to reach radionuclidic purity levels of 90% and 95% are relatively short. Nevertheless, by relaxing the requirement for a 95% pure product some gains in yield can be obtained. Taking into account that some processing time post EOB will be required, this gain is unlikely to exceed about 30%. There is also a gain when opting for a metallic target rather than an oxide target, however, this gain is only between 21% and 25%, depending on the waiting time. These gains are not enough to secure a production yield above 0.5 Ci with a standard target holder. In contrast, with a modified target holder such productions do indeed seem feasible.

During the course of this investigation, a Fortran code was developed to compute ^{67}Cu yields and radionuclidic purities for Zn targets of any composition of stable Zn constituents (i.e. any combination of ^{64}Zn, ^{66}Zn, ^{67}Zn, ^{68}Zn, and ^{70}Zn, which are the constituents of natural Zn). In the input file one can supply the percentage of each stable Zn, the bombardment time, cooling time, beam current, and target size. Either TENDL-2019 or TENDL-2021 cross sections can be selected. Any neutron spectrum can be provided, as long as it has the modified LaBauve

Table 7.9: Predicted ^{67}Cu production yields from secondary-neutron activation of 100% enriched ^{68}Zn in a new 70 MeV target station, using TENDL-2019 cross sections. Comparison of ^{68}ZnO and metallic ^{68}Zn secondary targets (see Fig. 7.7).

Target	Cooling[a]	Purity	Yield (^{68}Zn oxide)[b]		Cooling[a]	Purity	Yield (^{68}Zn metal)[b]	
holder	time (h)	(%)	(MBq)	(mCi)	time (h)	(%)	(MBq)	(mCi)
Standard	0.0	84.1	12668.4	342.4	0.0	82.4	15823.8	427.7
	12.3	90.0	11036.4	298.3	15.2	90.0	13345.5	360.7
	29.4	95.0	9108.5	246.2	32.3	95.0	11014.5	297.7
Modified	0.0	86.5	22460.1	607.0	0.0	85.1	36096.7	975.6
	8.0	90.0	20542.8	555.2	10.6	90.0	32047.6	866.2
	27.7	95.0	16457.5	444.8	28.0	95.0	26378.0	712.9

[a] Cooling time (in hours) after EOB to reach the ^{67}Cu radionuclidic purity indicated in the subsequent column.
[b] For a 5-day bombardment with 70 MeV protons at a beam current of 250 μA.

energy-group structure given in Appendix B. This allowed yield and purity comparisons from different Zn target materials to be made. Of most interest was a comparison between ^{nat}Zn, 100% enriched ^{68}Zn, and the s[^{68}Zn] material defined in Table 6.3, the latter of which was used in the activation experiments of this work. Table 7.10 presents this comparison for the different Zn compositions as oxide targets, again assuming a 5-day bombardment at a beam current of 250 μA. The primary target was Rb/Ga, which is envisaged to be the most exploited configuration at the new 70 MeV cyclotron facility. TENDL-2019 cross sections were used and the neutron spectrum used was obtained from an MCNP6 simulation with the CEM physics selection.

It is evident from Table 7.10 that with a secondary ZnO target having natural Zn composition, the yield is both low and of poor radionuclidic purity. This is mainly due to the copious amounts of co-produced ^{64}Cu. Such a product will not have any applicability in patient treatments but may be of value in developing or testing the separation chemistry. To obtain a product with good radionuclidic purity clearly requires the use of highly enrichment ^{68}Zn. In practice, a 100% level of enrichment will be unlikely to be obtained. This, however, may not be necessary. The results in Table 7.10 for the s[^{68}Zn] and monoisotopic ^{68}Zn secondary targets are very similar. This is fortunate. There was some concern that reactions such as

Table 7.10: Predicted ^{67}Cu production yields from secondary-neutron activation of ZnO targets, having different Zn isotopic compositions, in a new 70 MeV target station. Cross sections were taken from the TENDL-2019 library.

Case 1: Rb/Ga primary target in standard target holder						
Cooling time (hours)	Secondary target					
	^{nat}Zn oxide		^{68}Zn oxide		s[^{68}Zn] oxide	
	(Yield[a]) (mCi)	(Purity (%)	(Yield[a]) (mCi)	(Purity (%)	(Yield[a]) (mCi)	(Purity (%)
0	72.3	4.6	342.4	84.1	339.1	83.5
12	63.2	7.7	299.3	89.9	296.5	89.5
24	55.3	12.4	261.6	93.7	259.1	93.5
36	48.3	19.3	228.7	96.2	226.5	96.0
48	42.2	28.6	199.9	97.7	198.0	97.6

Case 2: Rb/Ga primary target in modified target holder						
Cooling time (hours)	Secondary target					
	^{nat}Zn oxide		^{68}Zn oxide		s[^{68}Zn] oxide	
	(Yield[a]) (mCi)	(Purity (%)	(Yield[a]) (mCi)	(Purity (%)	(Yield[a]) (mCi)	(Purity (%)
0	129.2	4.2	607.0	86.5	601.3	85.9
12	113.0	7.0	530.6	91.5	525.6	91.1
24	98.8	11.3	463.8	94.8	459.4	94.5
36	86.3	17.7	405.5	96.8	401.6	96.7
48	75.5	26.5	354.4	98.1	351.1	98.0

[a]For a 5-day bombardment with 70 MeV protons at a beam current of 250 μA.
Conversion to alternative units: 1 mCi = 3.7 $\times$ 10^7 Bq.

^{64}Zn(n,p)^{64}Cu might have a detrimental effect on ^{67}Cu radionuclidic purity, even with low levels of ^{64}Zn present in the target material. It transpired, however, that s[^{68}Zn] is of suitable quality.

7.5 COMMENTS IN CONCLUSION

Facilities allowing harvesting of projectile fragments, e.g. FRIB [MAS2014, MAS2015, ABE2019], provide fantastic opportunities for scientific discovery. This is their chief role. That kind of technology is unlikely to be suitable for ^{67}Cu production on an industrial scale. We think the same applies to intense neutron sources (e.g. the European Spallation Source (ESS) in Sweden), although their ability for large-scale production is not doubted. The primary roles of the above facilities are different, serving the needs of exotic physics experiments, with the supply of radionuclides somewhat secondary. They are large, expensive and complex facilities. It is entirely possible that the future will select the photonuclear production route as the most suitable for industrialization, which seems to have already started to happen for the radionuclide ^{99}Mo, utilizing the reaction ^{100}Mo(γ,n)^{99}Mo [BER2010, TKA2021].

Photonuclear production also has huge challenges, most notably the supply and recovery of highly enriched target material in bulk quantities. A recent article by Tkac *et al.* [TKA2021], for example, reports on processing of ^{100}Mo target batches of up to 600 g per batch, which is a large undertaking. A big advantage of photonuclear production is the significant simplification in the required infrastructure, especially from the accelerator side. The electron accelerators required for producing the bremsstrahlung photons are relatively simple machines. Ultimately, the future success of large-scale photonuclear production of radionuclides, and perhaps also production via neutron-induced reactions, depends on the availability of enriched target materials in bulk quantities.

7.5.1 Comments on enrichment – economies of scale

Sufficient production of ^{67}Cu to perform large-scale clinical trials has hitherto been hampered by the lack of availability and high cost of highly enriched ^{68}Zn, which is required for targetry. In a 2012 publication by Engle *et al.* [ENG2012b], a price of US$3/mg was reported. Pricing at that level will constitute a road block to many producers or potential producers. In fact, many potential production routes are effectively closed due to similar issues for a whole range of radionuclides. While ^{68}Zn is abundant on Earth, its availability as an enriched stable isotope has remained a major obstacle. It is possible, however, that this situation may change in the foreseeable future as a result of economies of scale.

We found it difficult to obtain reliable market information on the current supply and pricing of enriched ^{68}Zn. Reports on relevant market research can be found online but access beyond the Table of Contents pages are typically barred; such reports can sometimes be purchased but at an extremely high cost. Two other examples in the nuclear field are therefore highlighted here to shed light on the power of economies of scale.

The PET radionuclide ^{18}F is predominantly produced via the proton bombardment of ^{18}O-water, with the ^{18}O enrichment at a level of typically 98 atom% or higher. As ^{18}O has a very low natural abundance of only 0.205%, many successive cycles of enrichment are required

to achieve this high level. A report that is available on the International Nuclear Information System (INIS) of the IAEA [INIS1999] provides data on the total world supply of ^{18}O-water in the years 1997 to 1999, with estimates for the years 2000 and 2001:

- 1997: 35 kg
- 1998: 20 kg
- 1999: 65 kg
- 2000: 85 kg
- 2001: 100 kg

The report mentions that there were only four producers of ^{18}O-water in the world in 1999. Older staff members at iThemba LABS remember a time where users had to meticulously collect spent ^{18}O-water and send it back to the manufacturers for reprocessing. As production volumes went up and prices came down, the cost of reprocessing became comparable to fresh production and this practice was stopped. Today there are many more commercial producers. While most producers do not often divulge their production capacities, there is at least one exception. A visit to the websites of eight major producers provided an exception, namely a producer in Japan, who mentions an annual production of 600 kg since 2015. Thus, one can deduce that current world demand is met by the commercial producers and amounts to several metric ton of ^{18}O-water per year. At iThemba LABS it is treated as just another consumable.

A joint report in 2020 by the Nuclear Energy Agency (NEA) and the IAEA [NEA2020] contains a vast amount of information on the resources, production and demand for uranium required by the nuclear reactor sector, mainly for power generation. At the time of writing, about 450 nuclear reactors were connected to electricity grids and about 55 were under construction. Global uranium requirements were about 59 200 tU (metric tons of natural uranium) per year, equivalent to between 10 000 and 11 000 ton of Low Enriched Uranium (LEU) fuel per year. Commercial ^{235}U enrichment is nowadays mainly performed using the gas centrifuge process, which is about 50 times more efficient than a prior process based on gaseous diffusion used at legacy enrichment plants. The Uranium Enrichment Consortium (URENCO) is progressively adding the enrichment of other stable nuclides to their list benefitting from this technology, including the stable isotopes of Zn. This may, perhaps, be the beginning of another revolution that will change the radionuclide production landscape in the years to come.

Chapter 8

Summary and Conclusion

This chapter reviews the main aspects addressed in the study and highlights some of the more salient conclusions. Some possibilities for further investigations are also pointed out.

The new 70 MeV H^- cyclotron facility at iThemba LABS, still under construction but about 90% complete at the end of August 2022, is expected to deliver first beam in the early months of 2023. The commissioning of the new target stations and their ancillary facilities (such as cooling systems, the target transport and handling systems, etc.), as well as the transfer of routine radionuclide production activities from the SSC to the new facility, will happen in stages, which may take a couple of years to reach full maturity. Some of the first radionuclides that will be migrated to the new facility will be the main long-lived export products, namely ^{22}Na, ^{68}Ge and ^{82}Sr, which have been produced with 66 MeV proton beams from the SSC for several decades. The 70 MeV cyclotron will be the ideal machine for their production. The laboratory will be looking for new products to be added to this list, in order to fully utilize the expanded production capacity. One candidate may be ^{88}Y, amongst numerous other possibilities.

While a 70 MeV H^- cyclotron is an excellent choice for the production of many radionuclides, there are some high-value radionuclides in great demand that cannot be bulk produced with such a machine. This is the case for the therapeutic radionuclides ^{67}Cu and ^{225}Ac. Even though a 70 MeV cyclotron is not the accelerator of choice for their bulk production, some production is possible on a smaller scale. This may be very useful for pre-clinical trials and/or the support of experimental investigations that require these scarce radionuclides.

The inclusion of natural Th targets in tandem-target configurations was investigated, based on an expanded nuclear database for Th + p cross sections after measuring new data by means of the stacked-foil technique. In particular, this study greatly improved the database at energies in the threshold region and in the region 40 to 70 MeV. It was clearly shown that 70 MeV H^- cyclotrons can contribute to the supply of ^{230}U/^{226}Th generators and ^{225}Ac, both having potential in targeted alpha-particle therapy (TAT). This will be a difficult endeavour, however, not only because thorium, as a fissionable material, is a controlled substance with significant procurement issues. These obstacles can hopefully be overcome, taking into account that thorium is not scarce on Earth, about as abundant as lead. One possibility may be to perform the bombardment of Th targets at iThemba LABS and ship the targets in depleted uranium (DU) shipping containers to Necsa (at Pelindaba near Pretoria) for processing. Necsa has much larger hot-cell processing facilities than iThemba LABS and years of experience in the processing and

handling of fissionable materials. Such an arrangement will also simplify various licensing requirements. Indeed, such collaborations are not unusual; Irradiated Th targets are routinely shipped from the Los Alamos National Laboratory (LANL) to the Oak Ridge National Laboratory (ORNL) for processing.

A separate investigation was made on Th+p reactions in the energy region 100–200 MeV, with the main aim to provide more data relevant to the concept of a ^{225}Ra/^{225}Ac generator. Such generators would provide ^{225}Ac with negligible radionuclidic contamination from other actinium radionuclides, notably ^{227}Ac. iThemba LABS will have to develop a high-intensity capability for 200 MeV proton beams on the SSC to make this a viable prospect. This is something that is technically possible. Based on our new cross-section results, a more reliable and complete database is available now to estimate the production conditions of the ^{225}Ra/^{225}Ac generator in this energy region.

A part of this project focused on exploiting the secondary neutron flux behind a tandem target under bombardment with a proton beam with an energy of either 66 or 70 MeV. These neutrons are always present when beam is on target and may be a useful resource. It was shown that ^{67}Cu can be produced with neutron-induced reactions to a very high radionuclidic purity, on condition that the secondary target material is highly enriched ^{68}Zn. The procurement of such enriched material, in sufficient quantities, may be problematic at the present time but there are strong indications that economies of scale at enrichment facilities may solve this problem in the future. A higher ^{67}Cu yield can be obtained by exploiting proton-induced reactions on ^{68}Zn targets directly but the radionuclidic purity will always be lower at EOB, requiring a longer cooling time before such a product can be used on patients. Nevertheless, this may also be something for iThemba LABS to consider. The cost of the target material can be reduced by recovering the enriched Zn for re-use, which is a standard practice in this field. Accelerator-produced neutrons may become important in radionuclide production. While the secondary neutron flux at a 70 MeV H^- cyclotron facility may be too low to satisfy certain production needs, intense neutron fluxes from deuteron breakup on Be targets may perhaps become an attractive technology for this purpose in future.

Monte Carlo simulations played a major role in this thesis project. A possible future project may focus on more experimental work to compare with the simulations. It may be interesting to actually construct the secondary ZnO and metallic Zn targets proposed in Chapter 7, using natural Zn instead of enriched Zn to keep costs realistic, and to neutron activate them in one of the new target stations when 70 MeV proton beams become available. Such an investigation will require extensive radiochemical processing, which should form part of the project. The chemical recovery of the Zn target material can also be included in the investigation. Monte Carlo simulations for natural Zn targets will provide a useful comparison with experimental yield measurements, which will assist to refine the Monte Carlo models and improve predictions for enriched secondary targets. The study can also be expanded to include natural Zn in the primary tandem target, both from the point of view of neutron production as well as ^{67}Cu production by proton-induced reactions.

When we started the neutron activations of small samples behind a VBTS target and word of this activity started to spread, we were approached by other scientists to also neutron activate

samples for them. These were mainly for nuclear structure studies of beta emitters close to the line of stability. This made us aware of such other experimental possibilities, which may be pursued once regular beams become available from the 70 MeV cyclotron.

Appendix A

Neutron source terms in coarse energy intervals – additional information

This appendix contains additional information relevant to Chapter 5. Neutron fluxes and yields are according to Monte Carlo simulations with the code MCNP6. The Cascade-Exciton Model (CEM) was enabled to calculate cross sections missing from the default tables of the code.

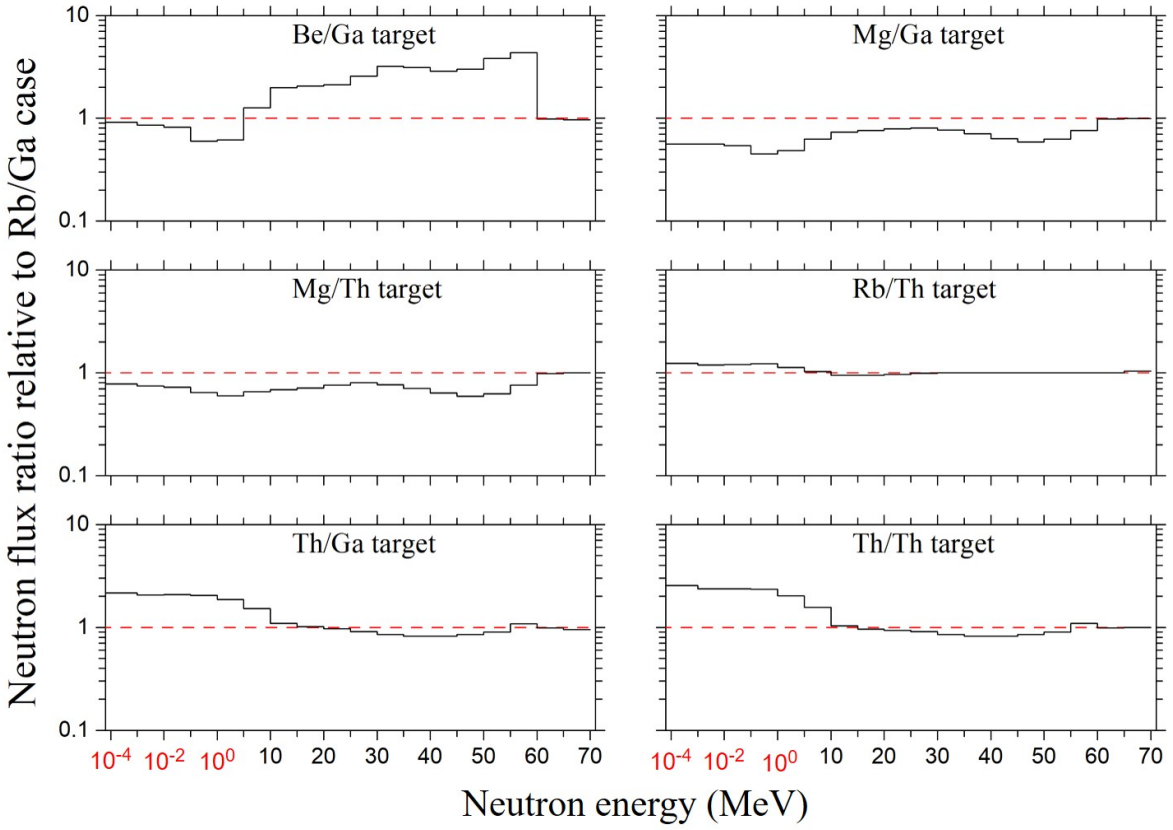


Figure A.1: Comparison of neutron flux ratios for various tandem targets relative to the Rb/Ga target, as indicated, for the case of total neutrons emitted in 4π space. Above 1 MeV the scale on the x-axis is linear (black text) but below 1 MeV it is logarithmic (red text). The red dashed line represents the case for the Rb/Ga target itself, while the black histogram represents the indicated target.

Table A.1: Total neutron yield and forward neutron flux in coarse energy bins for a Rb/Ga tandem target under bombardment with a 70 MeV proton beam.

Energy range (MeV)	4π neutron yield (neutrons/μAh)	Forward neutron flux (neutrons/cm^2-μAh)
thermal $\rightarrow$ 0.001	4.553×10^{12}	1.053×10^{10}
0.001 $\rightarrow$ 0.01	1.253×10^{13}	2.888×10^{10}
0.01 $\rightarrow$ 0.1	5.796×10^{13}	1.289×10^{11}
0.1 $\rightarrow$ 1.0	5.220×10^{14}	1.079×10^{12}
1.0 $\rightarrow$ 5.0	8.885×10^{14}	1.891×10^{12}
5.0 $\rightarrow$ 10.0	1.510×10^{14}	4.241×10^{11}
10.0 $\rightarrow$ 15.0	5.673×10^{13}	2.250×10^{11}
15.0 $\rightarrow$ 20.0	3.718×10^{13}	1.702×10^{11}
20.0 $\rightarrow$ 25.0	2.732×10^{13}	1.368×10^{11}
25.0 $\rightarrow$ 30.0	2.069×10^{13}	1.153×10^{11}
30.0 $\rightarrow$ 35.0	1.700×10^{13}	1.090×10^{11}
35.0 $\rightarrow$ 40.0	1.422×10^{13}	1.048×10^{11}
40.0 $\rightarrow$ 45.0	1.102×10^{13}	8.905×10^{10}
45.0 $\rightarrow$ 50.0	7.543×10^{12}	6.607×10^{10}
50.0 $\rightarrow$ 55.0	4.331×10^{12}	4.125×10^{10}
55.0 $\rightarrow$ 60.0	1.310×10^{12}	1.339×10^{10}
60.0 $\rightarrow$ 65.0	1.487×10^{11}	1.493×10^{09}
65.0 $\rightarrow$ 70.0	3.708×10^{10}	4.418×10^{08}

Table A.2: Total neutron and forward neutron flux ratios for selected tandem targets relative to the Rb/Ga target under bombardment with a 70 MeV proton beam.

Energy range	Ratio of total 4π neutron yield (neutrons/μAh) relative to Rb/Ga case							
(MeV)	Be/Ga	Mg/Ga	Mg/Th	Rb/Ga	Rb/Th	Th/Ga	Th/Th	Zr/Y_2O_3
thermal $\rightarrow$ 0.001	0.92	0.56	0.78	1.00	1.24	2.17	2.56	1.75
0.001 $\rightarrow$ 0.01	0.86	0.56	0.74	1.00	1.19	2.07	2.37	1.67
0.01 $\rightarrow$ 0.1	0.82	0.54	0.72	1.00	1.20	2.08	2.36	1.56
0.1 $\rightarrow$ 1.0	0.60	0.45	0.64	1.00	1.23	2.04	2.35	1.47
1.0 $\rightarrow$ 5.0	0.62	0.49	0.60	1.00	1.13	1.87	2.03	1.35
5.0 $\rightarrow$ 10.0	1.27	0.63	0.66	1.00	1.03	1.52	1.56	1.19
10.0 $\rightarrow$ 15.0	1.98	0.73	0.69	1.00	0.95	1.09	1.04	1.07
15.0 $\rightarrow$ 20.0	2.06	0.76	0.72	1.00	0.95	1.02	0.96	1.05
20.0 $\rightarrow$ 25.0	2.11	0.79	0.76	1.00	0.97	0.97	0.93	1.06
25.0 $\rightarrow$ 30.0	2.56	0.80	0.80	1.00	1.00	0.91	0.91	1.08
30.0 $\rightarrow$ 35.0	3.22	0.77	0.77	1.00	1.00	0.85	0.86	1.07
35.0 $\rightarrow$ 40.0	3.12	0.71	0.71	1.00	1.00	0.82	0.82	1.05
40.0 $\rightarrow$ 45.0	2.87	0.64	0.64	1.00	1.00	0.82	0.82	1.04
45.0 $\rightarrow$ 50.0	3.02	0.59	0.59	1.00	1.00	0.86	0.86	1.11
50.0 $\rightarrow$ 55.0	3.82	0.62	0.63	1.00	1.00	0.90	0.90	1.25
55.0 $\rightarrow$ 60.0	4.36	0.76	0.76	1.00	1.00	1.09	1.09	2.03
60.0 $\rightarrow$ 65.0	0.99	0.98	0.98	1.00	1.00	0.99	0.99	4.23
65.0 $\rightarrow$ 70.0	0.96	0.99	1.00	1.00	1.04	0.95	1.00	1.03
Total	0.87	0.52	0.63	1.00	1.14	1.80	1.98	1.35
Energy range	Ratio of forward neutron flux (neutrons/cm^2-μAh) relative to Rb/Ga case							
(MeV)	Be/Ga	Mg/Ga	Mg/Th	Rb/Ga	Rb/Th	Th/Ga	Th/Th	Zr/Y_2O_3
thermal $\rightarrow$ 0.001	0.87	0.48	0.68	1.00	1.19	1.60	1.83	1.28
0.001 $\rightarrow$ 0.01	0.84	0.53	0.66	1.00	1.16	1.51	1.72	1.25
0.01 $\rightarrow$ 0.1	0.78	0.52	0.68	1.00	1.18	1.46	1.64	1.12
0.1 $\rightarrow$ 1.0	0.63	0.45	0.67	1.00	1.29	1.47	1.70	1.11
1.0 $\rightarrow$ 5.0	0.72	0.49	0.59	1.00	1.13	1.28	1.39	1.01
5.0 $\rightarrow$ 10.0	1.31	0.65	0.61	1.00	0.96	0.97	0.94	0.85
10.0 $\rightarrow$ 15.0	1.80	0.74	0.63	1.00	0.86	0.76	0.67	0.78
15.0 $\rightarrow$ 20.0	1.97	0.80	0.70	1.00	0.87	0.74	0.65	0.79
20.0 $\rightarrow$ 25.0	1.97	0.86	0.82	1.00	0.93	0.71	0.65	0.83
25.0 $\rightarrow$ 30.0	2.37	0.92	0.92	1.00	1.00	0.67	0.66	0.89
30.0 $\rightarrow$ 35.0	3.44	0.88	0.87	1.00	1.00	0.62	0.62	0.92
35.0 $\rightarrow$ 40.0	3.67	0.74	0.74	1.00	1.00	0.60	0.60	0.91
40.0 $\rightarrow$ 45.0	3.60	0.60	0.59	1.00	1.00	0.63	0.63	0.95
45.0 $\rightarrow$ 50.0	3.81	0.48	0.48	1.00	1.00	0.69	0.69	1.05
50.0 $\rightarrow$ 55.0	4.84	0.49	0.49	1.00	1.00	0.75	0.76	1.23
55.0 $\rightarrow$ 60.0	5.87	0.59	0.59	1.00	1.00	0.98	0.98	2.09
60.0 $\rightarrow$ 65.0	0.94	0.93	0.95	1.00	0.99	0.98	0.99	4.95
65.0 $\rightarrow$ 70.0	0.95	0.97	1.00	1.00	1.03	0.97	0.99	1.02
Total	1.22	0.56	0.64	1.00	1.11	1.17	1.26	1.00

Appendix B

Modified LaBauve energy-group structure

Table B.1: Group boundaries (bins) of the Modified LaBauve neutron multigroup structure.

Gr no	Lower limit (MeV)	Upper limit (MeV)	Gr no	Lower limit (MeV)	Upper limit (MeV)	Gr no	Lower limit (MeV)	Upper limit (MeV)
1	1.000E-11	5.000E-09	41	1.997E-02	2.526E-02	81	3.000E+01	3.100E+01
2	5.000E-09	1.000E-08	42	2.526E-02	4.087E-02	82	3.100E+01	3.200E+01
3	1.000E-08	1.500E-08	43	4.087E-02	6.738E-02	83	3.200E+01	3.300E+01
4	1.500E-08	2.000E-08	44	6.738E-02	1.111E-01	84	3.300E+01	3.400E+01
5	2.000E-08	2.500E-08	45	1.111E-01	1.832E-01	85	3.400E+01	3.500E+01
6	2.500E-08	3.000E-08	46	1.832E-01	3.020E-01	86	3.500E+01	3.600E+01
7	3.000E-08	3.500E-08	47	3.020E-01	3.887E-01	87	3.600E+01	3.700E+01
8	3.500E-08	4.200E-08	48	3.887E-01	4.979E-01	88	3.700E+01	3.800E+01
9	4.200E-08	5.000E-08	49	4.979E-01	6.393E-01	89	3.800E+01	3.900E+01
10	5.000E-08	5.800E-08	50	6.393E-01	8.209E-01	90	3.900E+01	4.000E+01
11	5.800E-08	6.700E-08	51	8.209E-01	1.000E+00	91	4.000E+01	4.100E+01
12	6.700E-08	8.000E-08	52	1.000E+00	2.000E+00	92	4.100E+01	4.200E+01
13	8.000E-08	1.000E-07	53	2.000E+00	3.000E+00	93	4.200E+01	4.300E+01
14	1.000E-07	1.520E-07	54	3.000E+00	4.000E+00	94	4.300E+01	4.400E+01
15	1.520E-07	2.510E-07	55	4.000E+00	5.000E+00	95	4.400E+01	4.500E+01
16	2.510E-07	4.140E-07	56	5.000E+00	6.000E+00	96	4.500E+01	4.600E+01
17	4.140E-07	6.830E-07	57	6.000E+00	7.000E+00	97	4.600E+01	4.700E+01
18	6.830E-07	1.125E-06	58	7.000E+00	8.000E+00	98	4.700E+01	4.800E+01
19	1.125E-06	1.855E-06	59	8.000E+00	9.000E+00	99	4.800E+01	4.900E+01
20	1.855E-06	3.059E-06	60	9.000E+00	1.000E+01	100	4.900E+01	5.000E+01
21	3.059E-06	5.043E-06	61	1.000E+01	1.100E+01	101	5.000E+01	5.100E+01
22	5.043E-06	8.315E-06	62	1.100E+01	1.200E+01	102	5.100E+01	5.200E+01
23	8.315E-06	1.371E-05	63	1.200E+01	1.300E+01	103	5.200E+01	5.300E+01
24	1.371E-05	2.260E-05	64	1.300E+01	1.400E+01	104	5.300E+01	5.400E+01
25	2.260E-05	3.727E-05	65	1.400E+01	1.500E+01	105	5.400E+01	5.500E+01
26	3.727E-05	6.144E-05	66	1.500E+01	1.600E+01	106	5.500E+01	5.600E+01
27	6.144E-05	1.013E-04	67	1.600E+01	1.700E+01	107	5.600E+01	5.700E+01
28	1.013E-04	1.670E-04	68	1.700E+01	1.800E+01	108	5.700E+01	5.800E+01
29	1.670E-04	2.754E-04	69	1.800E+01	1.900E+01	109	5.800E+01	5.900E+01
30	2.754E-04	4.540E-04	70	1.900E+01	2.000E+01	110	5.900E+01	6.000E+01
31	4.540E-04	7.485E-04	71	2.000E+01	2.100E+01	111	6.000E+01	6.100E+01
32	7.485E-04	1.234E-03	72	2.100E+01	2.200E+01	112	6.100E+01	6.200E+01
33	1.234E-03	2.035E-03	73	2.200E+01	2.300E+01	113	6.200E+01	6.300E+01
34	2.035E-03	2.404E-03	74	2.300E+01	2.400E+01	114	6.300E+01	6.400E+01
35	2.404E-03	2.840E-03	75	2.400E+01	2.500E+01	115	6.400E+01	6.500E+01
36	2.840E-03	3.338E-03	76	2.500E+01	2.600E+01	116	6.500E+01	6.600E+01
37	3.338E-03	5.603E-03	77	2.600E+01	2.700E+01	117	6.600E+01	6.700E+01
38	5.603E-03	9.403E-03	78	2.700E+01	2.800E+01	118	6.700E+01	6.800E+01
39	9.403E-03	1.505E-02	79	2.800E+01	2.900E+01	119	6.800E+01	6.900E+01
40	1.505E-02	1.997E-02	80	2.900E+01	3.000E+01	120	6.900E+01	7.000E+01

Appendix C

Calculated physical yields: TENDL-2019

Table C.1: Physical yields determined from TENDL-2019 cross sections and neutron spectra generated with MCNP 6.2.

ID	Reaction	Physical yield (Bq μAh^{-1} g^{-1})					
		Bertini ABLA	Bertini Dresner	CEM	INCL ABLA	ISABEL ABLA	ISABEL Dresner
1	^{9}Be(n,3n)^{7}Be	45.4	45.4	39.6	29.9	47.5	47.5
2	^{23}Na(n,2n)^{22}Na	46.7	46.5	32.5	23.4	49.1	49.0
3	^{23}Na(n,γ)^{24}Na	2752.8	3447.9	2547.0	2700.2	2569.4	3252.7
4	^{nat}Mg(n,x)^{22}Na	10.2	10.2	8.64	6.45	10.7	10.7
5	^{nat}Mg(n,x)^{24}Na	82008.9	75683.1	56376.8	49509.2	82503.8	77845.8
6	^{27}Al(n,x)^{22}Na	1.09	1.10	0.97	0.74	1.14	1.14
7	^{27}Al(n,x)^{24}Na	47028.4	43888.7	32455.7	27674.9	47579.0	45297.3
8	^{nat}Ti(n,x)^{47}Ca	33.8	33.3	24.1	17.8	35.3	35.0
9	^{nat}Ti(n,x)^{44m}Sc	178.4	178.4	154.4	116.4	187.0	186.7
10	^{nat}Ti(n,x)^{46}Sc	222.0	214.7	170.5	136.8	229.2	223.4
11	^{nat}Ti(n,x)^{47}Sc	9033.0	8904.5	6493.4	4893.5	9450.3	9338.6
12	^{nat}Ti(n,x)^{48}Sc	4401.0	4227.6	3058.4	2425.6	4531.7	4406.4
13	^{55}Mn(n,x)^{48}V	0.26	0.26	0.31	0.28	0.27	0.27
14	^{55}Mn(n,x)^{51}Cr	11.8	11.8	13.2	11.2	12.2	12.2
15	^{55}Mn(n,4n)^{52}Mn	222.8	223.2	210.5	162.0	231.6	231.4
16	^{55}Mn(n,2n)^{54}Mn	344.2	338.7	233.7	171.3	359.5	355.9
17	^{59}Co(n,x)^{52}Mn	0.52	0.52	0.63	0.58	0.54	0.54
18	^{59}Co(n,x)^{54}Mn	8.26	8.26	6.77	4.99	8.69	8.68
19	^{59}Co(n,p)^{59}Fe	192.7	177.6	132.9	119.5	193.8	182.3
20	^{59}Co(n,4n)^{56}Co	15.6	15.7	14.6	11.3	16.3	16.3
21	^{59}Co(n,3n)^{57}Co	90.7	90.6	67.4	48.4	95.8	95.7
22	^{59}Co(n,2n)^{58}Co	1378.8	1358.4	941.6	688.7	1441.2	1428.2
23	^{59}Co(n,γ)^{60}Co	21.3	27.8	20.3	21.6	19.8	26.4
24	^{nat}Ni(n,x)^{51}Cr	1.67	1.67	1.37	1.03	1.76	1.76
25	^{nat}Ni(n,x)^{52}Mn	19.2	19.2	20.6	16.8	19.9	19.9
26	^{nat}Ni(n,x)^{54}Mn	6.97	6.96	5.03	3.63	7.36	7.35
27	^{nat}Ni(n,x)^{59}Fe	4.59	4.52	3.29	2.44	4.80	4.75
28	^{nat}Ni(n,x)^{56}Co	114.5	114.5	90.0	65.6	120.7	120.5
29	^{nat}Ni(n,x)^{57}Co	292.5	288.5	202.0	147.9	306.0	303.3
30	^{nat}Ni(n,x)^{58}Co	1501.6	1237.4	1118.1	1346.4	1399.0	1179.8
31	^{nat}Ni(n,x)^{60}Co	2.78	2.59	1.93	1.67	2.81	2.67

Table C.1: Physical yields determined from TENDL-2019 cross sections and neutron spectra generated with MCNP 6.2 (continuing from previous page).

ID	Reaction	Physical yield (Bq μAh^{-1} g^{-1})					
		Bertini ABLA	Bertini Dresner	CEM	INCL ABLA	ISABEL ABLA	ISABEL Dresner
32	^{nat}Ni(n,xn)^{56}Ni	23.7	23.7	19.6	14.5	24.9	24.9
33	^{nat}Ni(n,xn)^{57}Ni	4256.3	4230.3	2994.7	2164.4	4473.7	4455.8
34	^{nat}Zn(n,x)^{58}Co	1.97	1.97	2.05	1.66	2.05	2.04
35	^{nat}Zn(n,x)^{64}Cu	56426.2	47897.8	41651.9	47040.7	53693.5	46660.4
36	^{nat}Zn(n,x)^{67}Cu	842.9	836.7	601.1	439.1	886.2	880.9
37	^{nat}Zn(n,x)^{65}Zn	128.8	132.7	95.3	77.4	132.0	135.4
38	^{nat}Zn(n,x)^{69m}Zn	1240.0	1255.0	935.6	823.1	1244.8	1254.6
39	s[^{66}Zn](n,x)^{64}Cu	19254.5	19184.8	15470.3	11500.2	20215.7	20130.7
40	s[^{66}Zn](n,x)^{65}Zn	343.5	339.7	235.7	171.2	359.9	357.5
41	s[^{67}Zn](n,x)^{64}Cu	8098.5	7856.2	7087.6	5858.7	8297.2	8083.8
42	s[^{67}Zn](n,x)^{67}Cu	2556.2	2445.8	1779.6	1442.5	2625.3	2542.0
43	s[^{67}Zn](n,x)^{65}Zn	129.6	129.6	93.8	67.3	136.9	136.8
44	s[^{68}Zn](n,x)^{67}Cu	3935.4	3927.5	2812.2	2021.1	4152.0	4142.8
45	s[^{68}Zn](n,x)^{65}Zn	26.3	26.3	23.4	17.7	27.5	27.4
46	s[^{68}Zn](n,x)^{69m}Zn	3179.9	3322.1	2631.6	2648.0	3058.3	3151.8
47	^{nat}Br(n,x)^{75}Se	1.86	1.86	2.03	1.67	1.93	1.92
48	^{nat}Br(n,x)^{74}As	32.3	32.3	26.7	19.8	34.0	33.9
49	^{nat}Br(n,xn)^{77}Br	6561.5	6558.2	4870.6	3500.9	6933.0	6922.3
50	^{81}Br(n,γ)^{82}Br	35269.3	49189.0	33886.8	36566.8	32978.5	45579.0
51	^{nat}Rb(n,x)^{82}Br	778.9	773.2	595.4	442.1	815.1	810.8
52	^{nat}Rb(n,xn)^{83}Rb	246.7	246.5	181.2	129.8	260.8	260.3
53	^{nat}Rb(n,xn)^{84}Rb	1952.8	1923.6	1342.8	984.5	2039.7	2021.2
54	^{nat}Rb(n,x)^{86}Rb	2806.2	3309.1	2277.9	2106.1	2784.9	3252.1
55	^{89}Y(n,x)^{83}Rb	2.61	2.61	2.77	2.24	2.70	2.70
56	^{89}Y(n,x)^{84}Rb	30.0	30.0	26.1	19.6	31.4	31.4
57	^{89}Y(n,x)^{86}Rb	75.5	74.8	53.3	39.1	79.1	78.6
58	^{89}Y(n,4n)^{86}Y	5888.1	5898.5	5580.0	4296.1	6116.9	6111.7
59	^{89}Y(n,3n)^{87}Y	8651.3	8645.7	6446.4	4619.2	9144.2	9130.2
60	^{89}Y(n,3n)^{87m}Y	36756.7	36733.9	27495.4	19721.8	38844.0	38784.7
61	^{89}Y(n,2n)^{88}Y	773.9	764.8	524.0	380.2	810.6	804.9
62	^{93}Nb(n,x)^{87}Y	47.6	47.7	48.0	38.0	49.4	49.3
63	^{93}Nb(n,x)^{88}Y	7.02	7.02	5.80	4.29	7.37	7.36
64	^{93}Nb(n,x)^{89}Zr	112.4	112.5	121.6	99.8	116.5	116.3
65	^{93}Nb(n,4n)^{90}Nb	7163.9	7172.6	6409.8	4859.0	7483.2	7475.2
66	^{93}Nb(n,3n)^{91m}Nb	98.4	98.4	71.6	51.3	104.0	103.9
67	^{93}Nb(n,2n)^{92m}Nb	2839.5	2743.6	1936.0	1484.0	2930.8	2866.4
68	^{103}Rh(n,x)^{96}Tc	105.8	105.8	119.6	100.1	109.6	109.3
69	^{103}Rh(n,p)^{103}Ru	64.8	60.0	44.9	39.7	65.3	61.7
70	^{103}Rh(n,5n)^{99g}Rh	19.9	19.9	20.1	15.9	20.6	20.5
71	^{103}Rh(n,4n)^{100}Rh	3253.7	3255.4	2693.1	1985.4	3419.3	3415.0
72	^{103}Rh(n,3n)^{101g}Rh	5.29	5.29	3.62	2.56	5.61	5.60
73	^{103}Rh(n,3n)^{101m}Rh	5487.6	5483.4	3784.4	2674.9	5810.9	5801.0
74	^{103}Rh(n,2n)^{102g}Rh	165.3	159.6	111.9	85.7	170.5	166.8
75	^{103}Rh(n,2n)^{102m}Rh	27.2	26.5	18.4	13.8	28.2	27.8
76	^{nat}Ag(n,x)^{105}Rh	503.0	502.6	366.5	263.1	531.3	530.4
77	^{nat}Ag(n,xn)^{105}Ag	477.4	477.2	343.0	245.8	504.5	503.7

Table C.1: Physical yields determined from TENDL-2019 cross sections and neutron spectra generated with MCNP 6.2 (continuing from previous page).

ID	Reaction	Physical yield (Bq μAh^{-1} g^{-1})					
		Bertini ABLA	Bertini Dresner	CEM	INCL ABLA	ISABEL ABLA	ISABEL Dresner
78	^{nat}Ag(n,xn)^{106m}Ag	2500.9	2448.5	1738.6	1296.2	2601.3	2566.8
79	^{109}Ag(n,γ)^{110m}Ag	33.6	42.2	30.9	33.8	30.3	38.6
80	^{nat}In(n,x)^{110m}Ag	1.60	1.60	1.30	0.96	1.68	1.68
81	^{115}In(n,p)^{115m}Cd	27.3	27.0	19.1	14.0	28.5	28.3
82	^{nat}In(n,xn)^{111}In	618.1	617.9	471.3	343.8	651.5	650.5
83	^{nat}In(n,x)^{114m}In	1480.0	1482.7	1041.6	836.1	1516.4	1525.4
84	^{127}I(n,x)^{120m}Sb	2.85	2.86	3.27	2.77	2.96	2.95
85	^{127}I(n,x)^{122}Sb	177.1	177.2	145.9	107.8	186.3	186.0
86	^{127}I(n,x)^{124}Sb	11.9	11.8	8.91	6.59	12.4	12.4
87	^{127}I(n,x)^{123m}Te	7.26	7.27	7.63	6.19	7.53	7.52
88	^{127}I(n,5n)^{123}I	5780.0	5789.0	5788.4	4546.4	5985.9	5978.7
89	^{127}I(n,4n)^{124}I	3272.5	3274.0	2695.7	1985.1	3440.5	3436.1
90	^{127}I(n,2n)^{126}I	5631.3	5478.7	3824.6	2880.0	5836.0	5736.3
91	^{133}Cs(n,5n)^{129}Cs	2010.5	2013.7	1989.6	1557.7	2084.0	2081.6
92	^{133}Cs(n,2n)^{132}Cs	11637.5	11332.8	7954.1	5985.7	12070.1	11868.4
93	^{133}Cs(n,γ)^{134}Cs	173.4	230.7	165.2	180.5	161.9	211.3
94	^{141}Pr(n,x)^{139}Ce	273.0	272.8	194.0	137.9	288.9	288.4
95	^{141}Pr(n,p)^{141}Ce	38.7	38.4	27.2	19.8	40.7	40.4
96	^{141}Pr(n,γ)^{142}Pr	21878.8	29487.8	20966.6	22630.7	20403.0	27330.0
97	^{nat}Gd(n,x)^{156}Eu	63.5	63.4	49.9	36.8	66.7	66.6
98	^{nat}Gd(n,x)^{157}Eu	1548.8	1547.3	1216.5	894.6	1629.1	1626.1
99	^{nat}Gd(n,xn)^{151}Gd	7.90	7.87	6.84	5.24	8.25	8.22
100	^{nat}Gd(n,x)^{153}Gd	54.6	58.7	44.3	37.8	55.5	59.0
101	^{nat}Gd(n,x)^{159}Gd	35268.8	38351.1	27854.4	26716.3	34604.8	37535.0
102	^{160}Gd(n,γ)^{161}Gd $\rightarrow^{161}$Tb	2185.0	2769.5	1961.3	2129.7	1904.4	2555.8
103	^{169}Tm(n,5n)^{165}Tm	5707.7	5717.1	5195.4	3946.7	5946.6	5941.5
104	^{169}Tm(n,3n)^{167}Tm	4451.3	4444.2	3055.1	2175.6	4702.8	4693.6
105	^{169}Tm(n,2n)^{168}Tm	755.2	720.3	515.9	410.1	773.6	749.4
106	^{181}Ta(n,p)^{181}Hf	12.4	12.3	8.81	6.37	13.0	13.0
107	^{181}Ta(n,5n)^{177}Ta	5140.3	5146.6	4397.8	3274.6	5383.1	5378.0
108	^{181}Ta(n,γ)^{182}Ta	1925.3	2551.7	1819.7	2019.1	1796.0	2316.0
109	^{197}Au(n,x)^{192}Ir	2.06	2.06	1.72	1.28	2.17	2.16
110	^{197}Au(n,4n)^{194}Au	11607.7	11596.6	8663.0	6177.8	12284.2	12263.4
111	^{197}Au(n,3n)^{195}Au	208.4	208.1	140.6	99.8	220.3	219.8
112	^{197}Au(n,2n)^{196}Au	9398.9	8944.6	6393.2	5098.5	9611.8	9298.8
113	^{197}Au(n,γ)^{198g}Au	49075.4	64643.3	46654.4	51060.2	45786.4	59174.3
114	^{nat}Tl(n,x)^{203}Hg	24.1	24.1	19.0	14.0	25.3	25.3
115	^{nat}Tl(n,xn)^{200}Tl	4360.8	4361.2	3800.5	2878.6	4573.1	4566.1
116	^{nat}Tl(n,xn)^{201}Tl	4516.6	4517.0	3507.5	2567.6	4749.2	4742.6
117	^{nat}Tl(n,xn)^{202}Tl	2729.5	2669.6	1949.9	1464.5	2842.8	2799.9
118	^{209}Bi(n,6n)^{204}Bi	4099.6	4102.4	4561.8	3763.0	4241.3	4233.3
119	^{209}Bi(n,5n)^{205}Bi	646.4	647.6	582.0	439.4	673.5	673.0
120	^{209}Bi(n,4n)^{206}Bi	3458.2	3455.1	2586.8	1846.8	3658.8	3652.7
121	^{209}Bi(n,3n)^{207}Bi	3.33	3.33	2.24	1.59	3.53	3.52

Appendix D

Calculated physical yields: TENDL-2021

Table D.1: Physical yields determined from TENDL-2021 cross sections and neutron spectra generated with MCNP 6.2.

ID	Reaction	Physical yield (Bq μAh^{-1} g^{-1})					
		Bertini ABLA	Bertini Dresner	CEM	INCL ABLA	ISABEL ABLA	ISABEL Dresner
1	^{9}Be(n,3n)^{7}Be	45.4	45.4	39.6	29.9	47.5	47.5
2	^{23}Na(n,2n)^{22}Na	47.3	47.0	32.9	23.6	49.8	49.6
3	^{23}Na(n,γ)^{24}Na	3014.9	3731.2	2767.7	2940.6	2815.5	3514.2
4	^{nat}Mg(n,x)^{22}Na	9.83	9.83	8.36	6.24	10.3	10.3
5	^{nat}Mg(n,x)^{24}Na	81981.0	75693.4	56372.6	49455.6	82499.9	77867.0
6	^{27}Al(n,x)^{22}Na	1.09	1.10	0.97	0.74	1.14	1.14
7	^{27}Al(n,x)^{24}Na	47028.4	43888.7	32455.7	27674.9	47579.0	45297.3
8	^{nat}Ti(n,x)^{47}Ca	32.9	32.5	23.5	17.4	34.4	34.1
9	^{nat}Ti(n,x)^{44m}Sc	155.3	155.4	130.7	97.5	163.1	162.9
10	^{nat}Ti(n,x)^{46}Sc	209.9	203.0	162.2	130.4	216.7	211.1
11	^{nat}Ti(n,x)^{47}Sc	9019.3	8891.8	6506.0	4905.4	9435.0	9323.8
12	^{nat}Ti(n,x)^{48}Sc	4555.9	4383.5	3162.9	2497.1	4696.1	4571.5
13	^{55}Mn(n,x)^{48}V	0.14	0.14	0.17	0.15	0.15	0.15
14	^{55}Mn(n,x)^{51}Cr	9.82	9.83	11.0	9.34	10.2	10.2
15	^{55}Mn(n,4n)^{52}Mn	205.7	206.0	196.2	151.5	213.6	213.4
16	^{55}Mn(n,2n)^{54}Mn	342.4	337.0	232.5	170.3	357.6	354.2
17	^{59}Co(n,x)^{52}Mn	0.30	0.30	0.37	0.34	0.32	0.32
18	^{59}Co(n,x)^{54}Mn	8.44	8.44	6.94	5.12	8.87	8.86
19	^{59}Co(n,p)^{59}Fe	192.0	176.9	132.4	119.2	193.0	181.5
20	^{59}Co(n,4n)^{56}Co	13.9	14.0	13.2	10.2	14.5	14.5
21	^{59}Co(n,3n)^{57}Co	90.0	90.0	67.0	48.1	95.1	95.0
22	^{59}Co(n,2n)^{58}Co	1374.4	1354.5	938.4	685.7	1436.9	1424.2
23	^{59}Co(n,γ)^{60}Co	21.1	27.5	20.1	21.3	19.6	26.1
24	^{nat}Ni(n,x)^{51}Cr	1.56	1.56	1.28	0.96	1.64	1.64
25	^{nat}Ni(n,x)^{52}Mn	14.1	14.1	15.3	12.6	14.6	14.6
26	^{nat}Ni(n,x)^{54}Mn	6.64	6.63	4.81	3.47	7.01	7.00
27	^{nat}Ni(n,x)^{59}Fe	3.94	3.88	2.85	2.13	4.12	4.07
28	^{nat}Ni(n,x)^{56}Co	111.2	111.2	88.0	64.3	117.1	117.0
29	^{nat}Ni(n,x)^{57}Co	295.1	291.2	204.1	149.3	308.8	306.2
30	^{nat}Ni(n,x)^{58}Co	1491.8	1229.3	1111.5	1339.1	1389.7	1171.8
31	^{nat}Ni(n,x)^{60}Co	2.72	2.53	1.88	1.63	2.75	2.61

Table D.1: Physical yields determined from TENDL-2021 cross sections and neutron spectra generated with MCNP 6.2 (continuing from previous page).

ID	Reaction	Physical yield (Bq μAh^{-1} g^{-1})					
		Bertini ABLA	Bertini Dresner	CEM	INCL ABLA	ISABEL ABLA	ISABEL Dresner
32	^{nat}Ni(n,xn)^{56}Ni	24.0	24.0	19.9	14.8	25.2	25.2
33	^{nat}Ni(n,xn)^{57}Ni	4436.1	4410.3	3126.0	2258.2	4663.8	4645.9
34	^{nat}Zn(n,x)^{58}Co	1.94	1.94	2.03	1.64	2.01	2.01
35	^{nat}Zn(n,x)^{64}Cu	55735.2	47342.9	41161.1	46459.7	53048.0	46119.6
36	^{nat}Zn(n,x)^{67}Cu	871.0	864.2	622.1	455.1	915.5	909.7
37	^{nat}Zn(n,x)^{65}Zn	124.3	128.2	91.7	73.8	127.7	131.1
38	^{nat}Zn(n,x)^{69m}Zn	1088.4	1107.3	821.3	722.7	1092.2	1105.7
39	s[^{66}Zn](n,x)^{64}Cu	18804.8	18737.4	15198.8	11319.9	19735.6	19652.4
40	s[^{66}Zn](n,x)^{65}Zn	338.9	335.3	232.9	169.0	355.2	352.9
41	s[^{67}Zn](n,x)^{64}Cu	7763.0	7524.2	6820.6	5660.0	7947.4	7737.3
42	s[^{67}Zn](n,x)^{67}Cu	2842.7	2717.2	1971.4	1599.4	2918.8	2824.5
43	s[^{67}Zn](n,x)^{65}Zn	123.7	123.7	90.1	64.7	130.6	130.5
44	s[^{68}Zn](n,x)^{67}Cu	4021.3	4013.4	2881.2	2071.4	4242.6	4233.1
45	s[^{68}Zn](n,x)^{65}Zn	23.3	23.4	20.9	15.9	24.3	24.3
46	s[^{68}Zn](n,x)^{69m}Zn	2759.2	2916.7	2297.1	2315.3	2649.9	2759.0
47	^{nat}Br(n,x)^{75}Se	1.33	1.33	1.46	1.22	1.38	1.38
48	^{nat}Br(n,x)^{74}As	39.9	39.9	32.8	24.2	42.0	41.9
49	^{nat}Br(n,xn)^{77}Br	6255.1	6252.1	4667.8	3358.0	6608.3	6598.2
50	^{81}Br(n,γ)^{82}Br	35627.1	49586.5	34194.9	36950.3	33307.2	45961.1
51	^{nat}Rb(n,x)^{82}Br	816.9	811.0	626.2	465.3	854.8	850.3
52	^{nat}Rb(n,xn)^{83}Rb	240.4	240.3	177.8	127.6	254.1	253.7
53	^{nat}Rb(n,xn)^{84}Rb	1948.4	1920.2	1339.2	980.8	2035.8	2018.0
54	^{nat}Rb(n,x)^{86}Rb	2808.9	3311.5	2278.8	2105.9	2788.1	3255.3
55	^{89}Y(n,x)^{83}Rb	2.45	2.45	2.63	2.15	2.53	2.53
56	^{89}Y(n,x)^{84}Rb	30.7	30.8	26.9	20.2	32.2	32.1
57	^{89}Y(n,x)^{86}Rb	75.7	75.0	53.5	39.2	79.3	78.8
58	^{89}Y(n,4n)^{86}Y	5240.4	5249.6	5038.2	3898.5	5439.0	5434.1
59	^{89}Y(n,3n)^{87}Y	8551.0	8545.7	6408.8	4599.2	9035.4	9021.7
60	^{89}Y(n,3n)^{87m}Y	37680.2	37658.1	28342.2	20360.1	39807.7	39747.6
61	^{89}Y(n,2n)^{88}Y	773.9	765.1	523.9	379.6	810.8	805.4
62	^{93}Nb(n,x)^{87}Y	49.0	49.1	49.8	39.6	50.8	50.7
63	^{93}Nb(n,x)^{88}Y	7.47	7.48	6.18	4.58	7.86	7.85
64	^{93}Nb(n,x)^{89}Zr	97.3	97.3	106.4	87.9	100.8	100.6
65	^{93}Nb(n,4n)^{90}Nb	6587.7	6596.4	5955.0	4529.8	6875.3	6868.1
66	^{93}Nb(n,3n)^{91m}Nb	125.1	125.1	91.9	66.0	132.2	132.0
67	^{93}Nb(n,2n)^{92m}Nb	3253.3	3159.0	2225.9	1687.5	3368.7	3305.4
68	^{103}Rh(n,x)^{96}Tc	67.5	67.5	79.1	68.1	70.2	70.0
69	^{103}Rh(n,p)^{103}Ru	63.3	58.5	43.9	39.1	63.8	60.2
70	^{103}Rh(n,5n)^{99g}Rh	12.3	12.4	12.9	10.4	12.8	12.8
71	^{103}Rh(n,4n)^{100}Rh	7376.8	7371.8	5066.8	3581.7	7812.0	7798.5
72	^{103}Rh(n,3n)^{101g}Rh	5.30	5.30	3.64	2.58	5.62	5.61
73	^{103}Rh(n,3n)^{101m}Rh	6182.8	6178.3	4289.8	3033.7	6547.4	6536.3
74	^{103}Rh(n,2n)^{102g}Rh	170.7	165.0	115.6	88.2	176.2	172.4
75	^{103}Rh(n,2n)^{102m}Rh	26.7	26.0	18.0	13.5	27.7	27.2
76	^{nat}Ag(n,x)^{105}Rh	1455.3	1452.4	1012.5	722.3	1536.9	1533.6
77	^{nat}Ag(n,xn)^{105}Ag	485.7	485.4	342.9	244.0	514.0	513.1

Table D.1: Physical yields determined from TENDL-2021 cross sections and neutron spectra generated with MCNP 6.2 (continuing from previous page).

ID	Reaction	Physical yield (Bq μAh^{-1} g^{-1})					
		Bertini ABLA	Bertini Dresner	CEM	INCL ABLA	ISABEL ABLA	ISABEL Dresner
78	^{nat}Ag(n,xn)^{106m}Ag	2324.0	2278.3	1628.9	1213.1	2418.3	2388.2
79	^{109}Ag(n,γ)^{110m}Ag	41.0	53.6	38.9	42.6	38.1	49.1
80	^{nat}In(n,x)^{110m}Ag	2.13	2.13	1.75	1.29	2.24	2.23
81	^{115}In(n,p)^{115m}Cd	20.1	19.8	14.0	10.3	21.1	20.9
82	^{nat}In(n,xn)^{111}In	576.6	576.3	434.2	315.5	608.4	607.4
83	^{nat}In(n,x)^{114m}In	1476.2	1481.7	1039.8	835.7	1512.1	1523.3
84	^{127}I(n,x)^{120m}Sb	1.93	1.93	2.29	1.99	2.01	2.01
85	^{127}I(n,x)^{122}Sb	181.7	181.7	150.5	111.5	190.9	190.7
86	^{127}I(n,x)^{124}Sb	11.7	11.6	8.75	6.47	12.2	12.2
87	^{127}I(n,x)^{123m}Te	3.16	3.16	3.35	2.73	3.28	3.27
88	^{127}I(n,5n)^{123}I	3771.5	3776.1	3946.0	3164.7	3902.6	3896.7
89	^{127}I(n,4n)^{124}I	3071.0	3073.4	2593.8	1925.3	3221.8	3218.0
90	^{127}I(n,2n)^{126}I	5722.2	5574.4	3885.6	2917.1	5935.5	5839.0
91	^{133}Cs(n,5n)^{129}Cs	1375.9	1377.8	1418.4	1131.1	1424.5	1422.5
92	^{133}Cs(n,2n)^{132}Cs	11734.6	11441.1	8019.3	6017.6	12180.4	11986.4
93	^{133}Cs(n,γ)^{134}Cs	173.3	230.8	165.1	180.5	161.8	211.4
94	^{141}Pr(n,x)^{139}Ce	277.3	277.1	197.9	140.9	293.4	292.9
95	^{141}Pr(n,p)^{141}Ce	38.3	37.9	26.8	19.6	40.1	39.8
96	^{141}Pr(n,γ)^{142}Pr	26729.0	35900.2	25582.7	27700.3	24914.3	33237.3
97	^{nat}Gd(n,x)^{156}Eu	67.4	67.3	53.0	39.0	70.9	70.7
98	^{nat}Gd(n,x)^{157}Eu	1641.9	1640.2	1287.5	946.6	1727.1	1723.8
99	^{nat}Gd(n,xn)^{151}Gd	6.21	6.17	5.30	4.05	6.49	6.45
100	^{nat}Gd(n,x)^{153}Gd	51.0	54.9	41.5	35.5	51.8	55.1
101	^{nat}Gd(n,x)^{159}Gd	35750.6	38885.9	28264.6	27067.0	35094.0	38060.5
102	^{160}Gd(n,γ)^{161}Gd $\rightarrow^{161}$Tb	2586.7	3476.4	2475.2	2693.0	2404.0	3205.8
103	^{169}Tm(n,5n)^{165}Tm	4404.6	4412.1	4205.8	3248.8	4574.6	4570.4
104	^{169}Tm(n,3n)^{167}Tm	4517.6	4511.7	3115.0	2216.4	4774.9	4766.0
105	^{169}Tm(n,2n)^{168}Tm	760.5	727.2	519.1	409.9	780.2	757.2
106	^{181}Ta(n,p)^{181}Hf	12.3	12.2	8.74	6.31	12.9	12.9
107	^{181}Ta(n,5n)^{177}Ta	4556.4	4563.8	4073.9	3073.5	4752.3	4748.4
108	^{181}Ta(n,γ)^{182}Ta	2035.6	2689.9	1923.5	2133.8	1897.5	2441.4
109	^{197}Au(n,x)^{192}Ir	2.27	2.27	1.90	1.41	2.38	2.38
110	^{197}Au(n,4n)^{194}Au	11365.4	11358.3	8690.7	6246.3	12013.1	11993.5
111	^{197}Au(n,3n)^{195}Au	214.9	214.6	145.5	103.2	227.3	226.8
112	^{197}Au(n,2n)^{196}Au	9719.1	9255.2	6607.1	5263.8	9943.5	9623.6
113	^{197}Au(n,γ)^{198g}Au	50158.8	65721.0	47621.7	52230.1	46759.3	60148.0
114	^{nat}Tl(n,x)^{203}Hg	24.6	24.5	19.3	14.3	25.8	25.8
115	^{nat}Tl(n,xn)^{200}Tl	3753.7	3754.2	3257.5	2470.0	3940.5	3934.6
116	^{nat}Tl(n,xn)^{201}Tl	4329.3	4329.7	3392.9	2491.4	4550.2	4543.8
117	^{nat}Tl(n,xn)^{202}Tl	2777.4	2718.9	1996.9	1498.8	2893.3	2851.4
118	^{209}Bi(n,6n)^{204}Bi	2206.2	2206.5	2575.1	2199.7	2290.2	2285.0
119	^{209}Bi(n,5n)^{205}Bi	582.0	583.0	541.0	412.7	604.9	604.4
120	^{209}Bi(n,4n)^{206}Bi	3503.7	3501.4	2661.7	1909.6	3703.9	3698.0
121	^{209}Bi(n,3n)^{207}Bi	3.39	3.39	2.29	1.62	3.59	3.58

Bibliography

[ABE2019] E. P. Abel, M. Avilov, V. Ayres, E. Birnbaum, G. Bollen, G. Bonito, T. Bredeweg, H. Clause, A. Couture, J. DeVore, M. Dietrich, P. Ellison, J. Engle, R. Ferrieri, J. Fitzsimmons, M. Friedman, D. Georgobiani, S. Graves, J. Greene, S. Lapi, S. C. Loveless, T. Mastren, C. Martinez-Gomez, S. McGuinness, W. Mittig, D. Morrissey, G. Peasley, F. Pellemoine, J. D. Robertson, N. Scielzo, M. Scott, G. Severin, D. Shaughnessy, J. Shusterman, J. Singh, M. Stoyer, L. Sutherlin, A. Visser, J. Wilkinson, Isotope harvesting at FRIB: additional opportunities for scientific discovery. J. Phys. G 46 (2019) 100501-1 – 100501-33.

[ALI2019] R. A. Aliev, S. S. Belyshev, A. A. Kuznetsov, L. Z. Dzhilavyan, V. V. Khankin, G. Yu. Aleshin, A. G. Kazakov, A. B. Priselkova, S. N. Kalmykov, B. S. Ishkhanov, Photonuclear production and radiochemical separation of medically relevant radionulides: ^{67}Cu. J. Radioanal. Nucl. Chem. 321 (2019) 125–132.

[AND1977] H. H. Andersen, J. F. Ziegler, Hydrogen stopping powers and ranges in all elements. In: *The stopping and Ranges of Ions in Matter*, Vol. 3 (ed. J. F. Ziegler), Pergamon, New York, 1977, p. 1.

[ARM2017] J. Armstrong, S. Mashnik, G. W. McKinney, F. B. Brown, M. E. Rising, G. E. McMath, J. S. Bull, C. J. Solomon, J. S. Hendricks, L. Casswell, A. Sood, D. B. Pelowitz, L. J. Cox, J. E. Sweezy, R. E. Prael, D. Dixon, C. J. Werner, T. E. Booth, R. A. Forster, A. Zukaitis, M. R. James, J. T. Goorley, C. Anderson, M. L. Fensin, H. G. Hughes, J. S. Elson, T. A. Wilcox, J. Favorite, J. W. Durkee, B. C. Kiedrowski, R. Martz, R. C. Johns, MCNP User's Manual: Code Version 6.2. RSICC Code Package CCC-850, Oak Ridge, US, 2017.

[AZA2020] F. Azaiez, R. Nemutudi, R. Nchodu, M. Wiedeking, iThemba LABS Laboratory Portrait, Nucl. Phys. News 30, 4 (2020) 5–10.

[BAY2006] B. Bayanov, V. Belov, S. Taskaev, Neutron producing target for accelerator based neutron capture therapy. J. Phys. Conf. Ser. 41 (2006) 460–465.

[BER2019] S. Bertrand, J.-M. Geets, C. Gameiro, B. Nactergal, J. Brison, A new compact high power e-beam accelerator for radioisotopes production: a first evaluation. In: Proc. Int. Symposium on Trends in Radiopharmaceuticals (ISTR-2019), Vienna, 28 October – 11 November 2019, Extended abstract no. 199. Available from: <https://www.iba-radiopharmasolutions.com/sites/default/files/2020-08/poster_istr_rhodo_0.pdf>.

[BER2010] K. Bertsche, Accelerator production options for ^{99}Mo. In: Proc. 1^{st} Int. Particle Accelerator Conference (IPAC'10), Kyoto, Japan, May 23–28, 2010, paper MOPEA025. Available from: <http://www.jacow.org>.

[BON2003] M. L. Bonardi, F. Groppi, C. Birattari, L. Gini, C. Mainardi, A. Ghioni, E. Menapace, K. Abbas, U. Holzwarth, M. F. Stroosnijder, Thin-target excitation functions and optimization of simultaneous production of NCA copper-64 and gallium-66,67 by deuteron induced nuclear reactions on a natural zinc target. J. Radioanal. Nucl. Chem. 257 (2003) 229–241.

[BOS2018] A. Boschi, P. Martini, E. Janevik-Ivanovska, A. Duatti, The emerging role of copper-64 radiopharmaceuticals as cancer theranostics. Drug Discov. 23 (2018) 1453–1570.

[CON2005] J. L. Conradie, P. J. Celliers, J. P. A. Crafford, J. L. G. Delsink, J. G. de Villiers, H. du Plessis, R. E. F. Fenemore, D. T. Fourie, Z. Kormány, Y. E. Manjoo, G. S. Muller, G. S. Price, P. F. Rohwer, J. F. Sharpey-Schafer, G. F. Steyn, J. T. van der Walt, T. N. van der Walt, M. J. van Niekerk, J. Dietrich, I. Mohos, Cyclotrons at iThemba LABS. In: Proc. 17^{th} Int. Conf. on Cyclotrons and their Applications, Tokyo, Japan, October 18–22, 2004, Particle Accelerator Society of Japan, 2005, 105. Available from: <http://www.jacow.org>.

[CON2013] J. L. Conlin, D. K. Parsons, S. J. Gardiner, A. C. Kahler, M. B. Lee, M. C. White, M. G. Gray, Continuous Energy Neutron Cross Section Data Based upon ENDF/B-VII.1. Los Alamos National Laboratory Report LA-UR-13-20137, US, 2013.

[CON2018] J. L. Conlin, W. Haeck, D. Neudecker, D. K. Parsons, M. C. White, Release of ENDF/B-VIII.0-Based ACE Data Files. Los Alamos National Laboratory Report LA-UR-18-24034, US, 2018.

[CUG2003] J. Cugnon, P. Henrotte, The low-energy limit of validity of the intranuclear cascade model. Eur. Phys. J. A 16 (2003) 393–407.

[DAL2018] D. S. Dale, V. N. Starovoitova, T. A. Forest, E. Oliphant, Photonuclear production of yttrium-88 – A high energy gamma emitter for hydrocarbon extraction applications. Appl. Radiat. Isot. 139 (2018) 137–140.

[DUA2013] A. Duatti, R. Nuñez, G. Poli, U. Bhonsle, M. Haji-Saeid, M. Dondi, A. Meghzifene, O. Pozzi, S. Guatelli, B. Allen, J. Barbet, M. Chérel, M. Bardies, F. Bruchertseifer, C. Seidl, E. Bombardieri, A. Bilewics, J. Choiński, J. O'Sullivan, G. Sgouros, S. Wilbur, J. Carrasquillo, D. Scheinberg, M. Zalutsky, Technical Meeting on Alpha Emitting Radionuclides and Radiopharmaceuticals for Therapy, IAEA Report TM-44815, Vienna, 2013.

[DUC2015] C. Duchemin, A. Guertin, F. Haddad, N. Michel, V. Métivier, Production of medical isotopes from a thorium target irradiated by light charged particles up to 70 MeV. Phys. Med. Biol. 60 (2015) 931–946.

[EHS2012] D. A. Ehst, N. A. Smith, D. L. Bowers, V. Makarashvili, Copper-67 production on electron linacs – Photonuclear technology development. In: Proc. 14^{th} Int. Workshop on Targetry and Target Chemistry, AIP Conf. Proc. 1509 (2012) 157–161.

[ENG2012a] J. W. Engle, C. T. Kelsey, H. Bach, B. D. Ballard, M. E. Fassbender, K. D. John, E. R. Birnbaum, F. M. Nortier, Preliminary investigation of parasitic radioisotope production using the LANL IPF secondary neutron flux. In: Proc. 14^{th} Int. Workshop on Targetry and Target Chemistry, AIP Conf. Proc. 1509 (2012) 171–175.

[ENG2012b] J. W. Engle, V. Lopez-Rodriguez, R. E. Gaspar-Carcamo, H. F. Valdovinos, M. Valle-Gonzalez, F. Trejo-Ballado, G. W. Severin, T. E. Barnhart, R. J. Nickles, M. A. Avila-Rodriguez, Very high specific activity $^{66/68}$Ga from zinc targets for PET. Appl. Radiat. Isot. 70 (2012) 1792–1796.

[ENG2013] J. W. Engle, E. R. Birnbaum, M. E. Fassbender, K. D. John, F. M. Nortier, Parasitic isotopic production with cyclotron beam generated neutrons. In: Proc. 20^{th} Int. Conf. on Cyclotrons and their Applications, Vancouver, Canada, September 16–20, 2013, pp. 451–453. Available from: <http://www.jacow.org>.

[ENG2014a] J. W. Engle, J. W. Weidner, B. D. Ballard, M. E. Fassbender, L. A. Hudston, K. R. Jackman, D. E. Dry, L. E. Wolfsberg, L. J. Bitteker, J. L. Ullman, M. S. Gulley, C. Pillay, G. Goff, E. R. Birnbaum, K. D. John, S. G. Mashnik, F. M. Nortier, Ac, La, and Ce radioimpurities in ^{225}Ac produced in 40–200 MeV proton irradiations of thorium. Radiochim. Acta 102 (2014) 569–581.

[ENG2014b] J. W. Engle, M. R. James, S. G. Mashnik, C. T. Kelsey IV, L. W. Wolfsberg, D. A. Reass, M. A. Connors, H. T. Bach, M. E. Fassbender, K. D. John, E. R. Birnbaum, F. M. Nortier, MCNPX characterization of the secondary neutron flux at the Los Alamos Isotope Production Facility. Nucl. Instrum. Methods A 754 (2014) 71–82.

[ENG2018] J. W. Engle, The production of Ac-225. Curr. Radiopharm. 11 (2018) 173–179.

[ENG2019] J. W. Engle, A. V. Ignatyuk, R. Capote, B. V. Carlson, A. Hermanne, M. A. Kellett, T. Kibédi, G. Kim, F. G. Kondev, M. Hussain, O. Lebeda, A. Luca, Y. Nagai, H. Naik, A. L. Nichols, F. M. Nortier, S. V. Suryanarayana, S. Takács, F. T. Tárkányi, M. Verpelli, Recommended nuclear data for the production of selected therapeutic radionuclides. Nucl. Data Sheets 155 (2019) 56-74. Available from: <https://www-nds.iaea.org>, Medical Portal.

[ERM2012] S. V. Ermolaev, B. L. Zhuikov, V. M. Kokhanyuk, V. L. Matushko, S. N. Kalmykov, R. A. Aliev, I. G. Tananaev, B. F. Myasoedov, Production of actinium, thorium and radium isotopes from natural thorium irradiated with protons up to 141 MeV. Radiochim. Acta 100 (2012) 223–229.

[ESP2019] J. Esposito, D. Bettoni, A. Boschi, M. Calderolla, S. Cisternino, G. Fiorentini, G. Keppel, P. Martini, M. Maggiore, L. Mou, M. Pasquali, L. Pranovi, G. Pupillo, C. Rossi Alvarez, L. Sarchiapone, G. Sciacca, H. Skliarova, P. Favaron, A. Lombardi, P. Antonini, A. Duatti, LARAMED: A laboratory for radioisotopes of medical interest. Molecules 24 (2019) 20-1 – 20-14. Patent P2974IT00 discussed on p. 8.

[EYC2021] R. Eychenne, M. Chérel, F. Hadda, F. Guérard, J.-F. Gestin, Overview of the most promising radionuclides for targeted alpha therapy: The “Hopeful Eight”. Pharmaceuticals 13 (2021) 906:1–50.

[FEG2015] A. A. H. Feghhi, Z. Gholamzadeh, C. Tenreiro, Z. Alipoor, Comparison of different INC physical modles of MCNPX to compute spallation neutronics of LBE target. J. Phys. Conf. Ser. 590 (2015) 012043.

[FIL2009] D. Filges, F. Goldenbaum, Handbook of Spallation Research: Theory, Experiments and Applications. Wiley-VCH Verlag GmbH, ISBN: 978-3-527-40714-9, 2009.

[FIL2010] D. V. Filosofov, M. Garland, H. D. John, F. F. Knapp, R. Kuznetsov, L. Mausner, S. Mirzadeh, M. R. A. Pillai, B. Ponsard, F. Roesch, T. J. Ruth, D. K. Samanta, Production of Long Lived Parent Radionuclides for Generators: ^{68}Ge, ^{82}Sr, ^{90}Sr and ^{188}W. IAEA Radioisotopes and Radiopharmaceuticals Series No. 2, Report STI/PUB/1436, ISBN 978-92-0-101110-7, IAEA Vienna, Austria, 2010.

[FIS2019] J. R. Fischer, Northstar buys IBA electron accelerators for Mo-99 production. Healthcare Business News, DOTmed.com, April 01, 2019. Available from: <https://dotmed.com/news/story/46768/>.

[FIS2021] J. R. Fischer, Northstar Medical Isotopes and IBA sign contract for Rhodotron electron beam accelerator. Healthcare Business News, DOTmed.com, November 18, 2021. Available from: <https://dotmed.com/news/story/56450/>.

[FOL2018] G. A. Follacchio, M. S. De Feo, G. de Vincentis, F. Monteleone, M. Liberatore, Radiopharmaceuticals labelled with copper radionuclides: Clinical results in human beings. Curr. Radiopharm. 11 (2018) 22–33.

[FRE1994] R. Fresca Fantoni, E. Gadioli, P. Guazzoni, P. Vergani, L. Zetta, P.L. Dellera, F. Tomasi, V. Campagna, G. Ciavola, C. Marchetta, RERAME: A facility for investigating heavy ion reactions with activation techniques. Appl. Radiat. Isot. 45 (1994) 325–334.

[FRI2020] M. T. Friend, T. Mastren, T. G. Parker, C. Vermeulen, M. Brugh, E. R. Birnbaum, F. M. Nortier, M. E. Fassbender, Production of ^{230}Pa by proton irradiation of ^{230}Th at the LANL isotope production facility: Precursor of ^{230}U for targeted alpha therapy. Appl. Radiat. Isot. 156 (2020) 108973.

[GAI1991] J. J. Gaimard, K. H. Schmidt, A reexamination of the abrasion-ablation model for the description of the nuclear fragmentation reaction. Nucl. Phys. A 531 (1991) 709–745.

[GAU1963] H. Gauvin, Réactions (p,2pxn) sur le thorium 232 de 30 a 120 MeV. J. de Physique 24 (1963) 836–838.

[GOO2012] T. Goorley, M. James, T. Booth, F. Brown, J. Bull, L. J. Cox, J. Durkee, J. Elson, M. Fensin, R. A. Forster, J. Hendricks, H. J. Hughes, R. Johns, B. Kiedrowski, R. Martz, S. Mashnik, G. McKinney, D. Pelowitz, R. Prael, J. Sweezy, L. Waters, T. Wilcox, T. Zukaitis, Initial MCNP6 Release Overview. J. Nucl. Technol. 180 (2012) 298–315.

[GOP2018] A. Gopalakrishna, S. V. Suryanarayana, H. Naik, T. S. Dixit, B. K. Nayak, A. Kumar, P. Maletha, K. Thakur, A. Deshpande, R. Krishnan, K. S. Banerjee, A. Saxena, Production, separation and supply prospects of ^{67}Cu with the development of fast neutron sources and photonuclear technology. Radiochim. Acta 106 (2018) 549–557.

[GOS1990] A. Goshtasby, F. Cheng,, B. A. Barsky, B-spline curves and surfaces viewed as digital filters. Comput. Gr. Image Process. 52 (1990) 264–275.

[GRI2003] G. L. Griffiths, S. V. Govindan, R. M. Sharkey, D. R. Fisher, D. M. Goldenberg, ^{90}Y-DOTA-hLL2: An agent for radioimmunotherapy of non-Hodgkin's lymphoma J. Nucl. Med. 44 (2003) 77–84.

[GRI2016] J. R. Griswold, D. G. Medvedev, J. W. Engle, R. Copping, J. M. Fitzsimmons, V. Radchenko, J. C. Cooley, M. E. Fassbender, D. L. Denton, K. E. Murphy, A. C. Owens, E. R. Birnbaum, K. D. John, F. M. Nortier, D. W. Stracener, L. H. Heilbronn, L. F. Mausner, S. Mirzadeh, Large scale accelerator production of ^{225}Ac: Effective cross sections for 78–192 MeV protons incident on ^{232}Th targets. Appl. Radiat. Isot. 118 (2016) 366–374.

[GUG2010] A. Guglielmetti, D. Faccio, G. F. Steyn, R Bonetti, S. P. Tretyakova, S. V. Shishkin, A. A. Ogloblin, G. A. Pik-Pichak, C. Vermeulen, N. P. van der Meulen, T. N. van der Walt, D. McGee, Cluster emission in the radioactive decay of ^{223}Ac. In: Proc. 12^{th} Int. Conf. on Nuclear Reaction Mechanisms, Varenna, Italy, June 15–19, 2009, eds. F. Cerutti, A. Ferrari, CERN-Proceedings-2010-1, ISBN 978-92-9083-339-0, 2010, pp. 307–315.

[HAR2010] R. L. Harrison, Introduction to Monte Carlo simulation. AIP Conf. Proc. 1204 (2010) 17–21.

[HAR2011] J. T. Harvey, J. Nolen, G. Vandegrift, I. Gomes, T. Kroc, P. Horwitz, D. McAlister, D. Bowers, V. Sullivan, J. Greene, Production of Actinium-225 via High Energy Proton Induced Spallation of Thorium-232, DOE Report DE-SC0003602-1, United States, 2011.

[HAR2018] J. T. Harvey, Northstar perspectives for Actinium-225 production at commercial scale. Curr. Radiopharm. 11 (2018) 180–191.

[HAR2018] J. T. Harvey, Northstar: The new producer and distributor of Mo-99. Talk presented at 2019 Mo-99 Stakeholers Meeting, Chicago, Illinois, Sept. 12, 2019. Presentation available from: <https://mo99.ne.anl.gov/meetings>.

[HER2018] A. Hermanne, A. V. Ignatyuk, R. Capote, B. V. Carlson, J. W. Engle, M. A. Kellett, T. Kibédi, G. Kim, F. G. Kondev, M. Hussain, O. Lebeda, A. Luca, Y. Nagai, H. Naik, A. L. Nichols, F. M. Nortier, S. V. Suryanarayana, S. Takács, F. T. Tárkányi, M. Verpelli, Reference cross sections for charged-particle monitor reactions. Nucl. Data Sheets 148 (2018) 338–382. Available from: <https://www-nds.iaea.org>, Medical Portal.

[HIL2003] K. Hilgers, T. Stoll, Y. Skakun, H. H. Coenen, S. M. Qaim, Cross-section measurements of the nuclear reactions ^{nat}Zn(d,x)^{64}Cu, ^{66}Zn(d,α)^{64}Cu and ^{68}Zn(p,αn)^{64}Cu for production of ^{64}Cu and technical developments for small-scale production of ^{67}Cu via the ^{70}Zn(p,α)^{67}Cu process. Appl. Radiat. Isot. 59 (2003) 343–351.

[HOD2015] A. P. J. Hodgson, R. W. Grimes, M. J. D. Rushton, O. J. Marsden, The impact of neutron cross section group structures on the accuracy of radiological source models. Nucl. Sci. Eng. 181 (2015) 1–8.

[IAEA2019] IAEA, 2019. World Thorium Occurrences, Deposits and Resources. IAEA-TECDOC-1877, ISBN 978-92-0-103719-0, International Atomic Energy Agency, Vienna. Available from: <https://www.iaea.org/publications>.

[INIS1999] INIS, 1999. Report on the supply and demand of ^{18}O enriched water. INIS Report XA0054850, 1999.

[ISL1973] M. M. Islam, H. -H. Knitter, The energy spectrum of prompt neutrons from the fission of Uranium-235 by 0.4 MeV neutrons. Nucl. Sci. Eng. 50 (1973) 108–114.

[JAM1997] D. J. Jamriska, E. J. Peterson, J. Carty, Spallation production of neutron deficient radioisotopes in North America. In: Proc. Second Int. Conference on Isotopes (2ICI), Sydney, 12–16 October 1995, ed. C. J. Hardy, Australian Nuclear Association Inc. pp. 220–224.

[JAN1982] J. F. Janni, Proton range-energy tables: Part 1. At. Data Nucl. Data Tables 27 (1982) 142–339. Proton range-energy tables: Part 2. At. Data Nucl. Data Tables 27 (1982) 341–529.

[JEN2019] R. Jennings, F. de la Cueva, LabVIEW Graphical Programming – Fifth edition. McGraw Hill, 2019.

[JON1988] D. T. L. Jones, M. Yudelev, W. L. J. Hendrikse, Physical characteristics of the South African high energy neutron therapy facility. Radiat. Prot. Dosimetry 23 (1988) 365–368.

[JOH2015] A. M. Johnsen, B. J. Heidrich, C. B. Durrant, A. J. Bascom, K. Ünlü, Reactor production of ^{64}Cu and ^{67}Cu using enriched target material. J. Radioanal. Nucl. Chem. 305 (2015) 61–71.

[JOS2013] C. U. Jost, J. R. Griswold, S. H. Bruffey, S. Mirzadeh, D. W. Stracener, C. L. Williams, Measurement of cross sections for the ^{232}Th(p,4n)^{229}Pa reaction at low proton energies. AIP Conf. Proc. 1525 (2013) 520–524.

[KAI2011] P. Kaitaniemi, A. Boudard, S. Leray, J. Cugnon, D. Mancusi, INCL intra-nuclear cascade and ABLA de-excitation models in Geant4. Prog. Nucl. Sci. Technol. 2 (2011) 788–793.

[KAS1999] S. Kastleiner, H. H. Coenen, S. M. Qaim, Possibility of production of ^{67}Cu at a small-sized cyclotron via the (p,α)-reaction on enriched ^{70}Zn. Radiochim. Acta 84 (1999) 107–110.

[KAT1975] S. Katcoff, J. B. Cumming, J. Godel, V. J. Buchanan, H. Susskind, C. J. Hsu, A medium energy intense neutron facility at the Brookhaven 200 MeV linac. Nucl. Instrum. Methods 129 (1975) 473–485.

[KAT2008] T. Katabuchi, S. Watanabe, N. S. Ishioka, Y. Iida, H. Hanaoka, K. Endo, S. Matsuhashi, Production of ^{67}Cu via the ^{68}Zn(p,2p)^{67}Cu reaction and recovery of ^{68}Zn target. J. Radioanal. Nucl. Chem. 277 (2008) 467–470.

[KIN2013] T. Kin, Y. Nagai, N. Iwamoto, F. Minato, O. Iwamoto, Y. Hatsukawa, M. Segawa, H. Harada, C. Konno, K. Ochiai, K. Takakura, New production routes for medical isotopes ^{64}Cu and ^{67}Cu using accelerator neutrons. J. Phys. Soc. Japan 82 (2013) 034201-1 – 134201-8.

[KNA2017] J. Knaster, P. Garin, H. Matsumoto, Y. Okumura, M. Sugimoto, F. Arbeiter, P. Cara, S. Chel, A. Facco, P. Favuzza, T. Furukawa, R. Heidinger, A. Ibarra, T. Kanemura, A. Kasugai, H. Kondo, V. Massaut, J. Molla, G. Micciche, S. O'hira, K. Sakamoto, T. Yokomine, E. Wakai, and the IFMIF/EVEDA Integrated Project Team, Overview of the IFMIF/EVEDA project. Nucl. Fusion 57 (2017) 102016-1 – 102016-25.

[KON2011] A. Yu. Konobeyev, U. Fischer, A. J. Koning, H. Leeb, S. Leray, Y. Yariv, What can we expect from the use of nuclear models implemented in MCNPX at projectile energies below 150 MeV? Detailed comparison with experimental data. J. Korean Phys. Soc. 59 (2011) 927–930.

[KON2019] A. J. Koning, D. Rochman, J.-Ch. Sublet, N. Dzysiuk, M. Fleming, S. van der Marck, TENDL: Complete Nuclear Data Library for Innovative Nuclear Science and Technology. Nucl. Data Sheets 155 (2019) 1–55.

[KOZ2012] J. Kozempel, K. Abbas, F. Simonelli, A. Bulgheroni, U. Holzwarth, N. Gibson, Preparation of ^{67}Cu via deuteron irradiation of ^{70}Zn. Radiochim. Acta 100 (2012) 419–423.

[KRA2004] R. Krause-Rehberg, T. N. van der Walt, L. Büttner, F. Börner, A ^{22}Na positron source for use in UHV. Nucl. Instrum. Methods B 221 (2004) 165–167.

[KUD1982] H. Kudo, H. Muramatsu, H. Nakahara, K. Miyano, I. Kohno, Fission fragment yields in the fission of ^{232}Th by protons of energies 8 to 22 MeV. Phys. Rev. C 25 (1982) 3011–3023.

[KWA2007] Y. H Kwak, and L. Ingall, Exploring Monte Carlo simulation applications for project management. Risk Management 9 (2007) 44–57.

[LAG1990] M. C. Lagunas-Solar, O. F. Carvacho, 1990. Cyclotron production of PET radionuclides: ^{18}F (109.77 min; β^+ 96.9%; EC 3.1%) from high-energy protons on natural magnesium targets. Appl. Radiat. Isot. 41 (1990) 349–357.

[LER2013] S. Leray, D. Mancusi, P. Kaitaniemi, J. C. David, A. Boudard, B. Braunn, C. Cugnon, Extension of the Liège Intra Nuclear Cascade model to light-ion collisions for medical and space applications. J. Phys. Conf. Ser. 420 (2013) 012065.

[MAS2002] S. G. Mashnik, A. J. Sierk, Recent developments of the Cascade-Exciton Model of nuclear reactions. J. Nucl. Sci. and Technol. Suppl. 2 (2002) 720–725.

[MAS2014] T. Mastren, A. Pen, G. F. Peaslee, N. Wozniak, S. Loveless, S. Essenmacher, L. G. Sobotka, D. J. Morrissey, S. E. Lapi, Feasibility of isotope harveting at a projectile fragmentation facility: ^{67}Cu. Sci. Rep. 4 (2014) 6706-1 – 6706-6.

[MAS2015] T. Mastren, A. Pen, S. Loveless, B. V. Marquez, E. Bollinger, B. Marois, N. Hubley, K. Brown, D. J. Morrissey, G. F. Peaslee, S. E. Lapi, Harvesting ^{67}Cu from the collection of a secondary beam cocktail at the National Superconducting Cyclotron Laboratory. Anal. Chem. 87 (2015) 10323–10329.

[MED2012] D. G. Medvedev, L. F. Mausner, G. E. Meinken, S. O. Kurczak, H. Schnakenberg, C. J. Dodge, E. M. Korach, S. C. Srivastava, Development of a large scale production of ^{67}Cu from ^{68}Zn at the high energy proton accelerator: Closing the ^{68}Zn cycle. Appl. Radiat. Isot. 70 (2012) 423–429.

[MIC1997] R. Michel, R. Bodemann, H. Busemann, R. Daunke, M. Gloris, H.-J. Lange, B. Klug, A. Krins, I. Leya, M. Lüpke, S. Neumann, H. Reinhardt, M. Schnatz-Büttgen, U. Herpers, Th. Schiekel, F. Sudbrock, B. Holmqvist, H. Condé, P. Malmborg, M. Suter, B. Dittrich-Hannen, P.-W. Kubik, H.-A. Synal, D. Filges, Cross sections for the production of residual nuclides by low- and medium-energy protons from the target elements C, N, O, Mg, Al, Si, Ca, Ti, V, Mn, Fe Co, Ni, Cu, Sr, Y, Zr, Nb, Ba and Au. Nucl. Instrum. Methods B 129 (1997) 153-193. Numerical data in IAEA Report INDC(GER)-0052.

[MIL1989] S. J. Mills, F. M. Nortier, W. L. Rautenbach, H. A. Smit, G. F. Steyn, A multi-purpose target station for radioisotope production at medium energies. In: Proc. 12^{th} Int. Conf. on Cyclotrons and their Applications (1989, Berlin, Germany, eds. B. Martin, K. Ziegler), World Scientific, 1989, pp. 527–530.

[MIR1983] S. Mirzadeh, P. P. Parekh, S. Katcoff, Y. Y. Chu, Cross-section systematics for nuclide production at a medium energy spallation neutron facility. Nucl. Instrum. Methods 216 (1983) 149–154.

[MOR2008] A. Morgenstern, C. Apostolides, F. Bruchertseifer, R. Capote, T. Gouder, F. Simonelli, M. Sin, K. Abbas, Cross-sections of the reaction ^{232}Th(p,3n)^{230}Pa for production of ^{230}U for targeted alpha therapy. Appl. Radiat. Isot. 66 (2008) 1275–1280.

[MOS2016] M. A. Mosby, J. W. Engle, K. R. Jackman, F. M. Nortier, E. R. Birnbaum, Determination of spallation neutron flux through spectral adjustment techniques. Nucl. Intrum. Methods B 381 (2016) 29–33.

[MOT2019] M. A. Motetshwane, Activation of samples in the secondary neutron flux generated with a 66 MeV proton beam on a radionuclide production target. MSc dissertation, Botswana International University of Science & Technology (BIUST), 2019, unpublished.

[MOU2022] L. Mou, P. Martini, G. Pupillo, I. Cieszykowska, C. S. Cutler, R. Mikolajczak, ^{67}Cu Production capabilities: A mini review. Molecules 27 (2022) 1501-1 – 1501-18.

[NEA2020] NEA, 2020. Uranium 2020: Resources, Production and Demand. Joint Report by the Nuclear Energy Agency and the International Atomic Energy Agency, Report NEA 7551, Organisation for Economic Cooperation and Development, 2020.

[NEL2021] B. J. B. Nelson, J. D. Andersson, F. Wuest, Targeted alpha therapy: Progress in radionuclide production, radiochemistry, & applications. Pharmaceuticals 13 (2021) 49-1 – 49-27.

[NIG2021] E. Nigron, A. Guertin, F. Haddad, T. Sounalet, Is ^{70}Zn(d,x)^{67}Cu the best way to produce ^{67}Cu for medical applications? Front. Med. 8 (2021) 674617-1 – 674617-7.

[NOR1990] F. M. Nortier, Considerations concerning targetry for the radioisotope production at the NAC and the production of gallium-67, indium-111 and cadmium-109. Thesis, Stellenbosch University, 1990, unpublished.

[OHY2018] T. Ohya, K. Nagatsu, H. Suzuki, M. Fukada, K. Minegishi, M. Hanyu, M.-R. Zhang, Small-scale production of ^{67}Cu for preclinical study via the ^{64}Ni(α,p)^{67}Cu channel. Nucl. Med. Biol. 59 (2018) 56–60.

[OSS2018] J. A. Osso, V. Starovoitova, A. Jalillian, A. Korde, A. Morgenstern, F. Bruchertseifer, A. Kellerbauer, Report on Joint IAEA-JRC Workshop "Supply of Actinium-225". IAEA, Vienna, October, 2018. Available from: <http://www-naweb.iaea.org/napc/iachem/working_materials.html>.

[PEL2013] D. B. Pelowitz, J. T. Goorley, M. R. James, T. E. Booth, F. B. Brown, J. S. Bull, L. J. Cox, J. W. Durkee, J. S. Elson, M. L. Fensin, R. A. Forster, J. S. Hendricks et al., MCNP 6 User's Manual. Los Alamos National Laboratory Report LA-CP-13-00634, 2013.

[POU2021] J.-P. Pouget, J. Constanzo, Revisiting the radiobiology of targeted alpha therapy. Frontiers in Medicine 8 (2021) 692436: 1–11.

[PRE1997] W. H. Press, S. A. Teukolsky, W. T. Vetterling, B. P. Flannery, Numerical Recipes in Fortran 77: The Art of Scientific Computing–Second Edition. Software version 2.08, Cambridge University Press, 1997.

[PRI2016] B. Pritychenko, A. Sonzogni, Q-value Calculator (QCalc). Atomic Mass Data Center, NNDC, Brookhaven National Laboratory, 2016. Available from: <https://www.nndc.bnl.gov/qcalc/>.

[PUP2020] G. Pupillo, L. Mou, P. Martini, M. Pasquali, A. Boschi, G. Cicoria, A. Duatti, F. Haddad, J. Esposito, Production of ^{67}Cu by enriched ^{70}Zn targets: first measurements of cross sections of ^{67}Cu, ^{64}Cu, ^{67}Ga, ^{66}Ga, ^{69m}Zn and ^{65}Zn in interactions of ^{70}Zn with protons above 45 MeV. Radiochim. Acta 108 (2020) 593–602.

[PUS2013] P. Puspitasari, Analysis of the physical properties of zinc oxide (ZnO) nanoparticles as an alternative innovation of the dental amalgam material. Int. J. Nanomechanics Sci. Technol. 4 (2013) 221–225.

[QAI1974] S. M. Qaim, R. Wölfle, G. Stöcklin, Radiochemical investigations of fast neutron-induced low-yield nuclear reactions. J. Radioanal. Nucl. Chem. 21 (1974) 395–405.

[QOS2018] N. Qosim, P. Murdanto, P. Puspitasari, Physical properties and compressive strength of zinc oxide nanopowder as a potential dental amalgam material. Int. J. Advances Appl. Sci. 7 (2018) 97–101.

[RAD2016] V. Radchenko, J. W. Engle, J. J. Wilson, J. R. Maassen, F. M. Nortier, E. R. Birnbaum, K. D. John, M. E. Fassbender, Formation cross-sections and chromatographic separation of protactinium isotopes formed in proton-irradiated thorium metal. Radiochim. Acta 104 (2016) 291–304.

[RAD2021] V. Radchenko, A. Morgenstern, A. R. jalilian, C. F. Ramogida, C. Cutler, C. Duchemin, C. Hoehr, F. Haddad, F. Bruchertseifer, H. Gausemel, H. Yang, J. A. Osso, K. Washiyama, K. Czerwinski, K. Leufgen, M. Pruszyński, O. Valzdolf, P. Causey, P. Schaffer, R. Perron, S. Maxim, D. S. Wilbur, T. Stora, Y. Li, Production and supply of α-particle-emitting radionuclides for targeted α-therapy. J. Nucl. Med. 62 (2021) 1495–1503.

[RAD2018] P. M. Radingoana, S. Guillemet-Fritsch, P. A. Olubambi, G. Chevallier, C. Estournès, Influence of processing parameters on the densification and the microstructure of pure zinc oxide ceramics by spark plasma sintering. Ceram. Int. 45 (2019) 10035–10043.

[ROB2018] A. K. H. Robertson, C. F. Ramogida, P. Schaffer, V. Radchenko, Development of ^{225}Ac radiopharmaceuticals: TRIUMF perspectives and experiences. Curr. Radiopharm. 11 (2018) 156–172.

[ROB2020] A. K. H. Robertson, B. L. McNeil, H. Yang, D. Gendron, R. Perron, V. Radchenko, S. Zeisler. P. Causey, P. Schaffer, ^{232}Th-spallation-produced ^{225}Ac with reduced ^{227}Ac content. Inorg. Chem. 59 (2020) 12156–12165.

[ROS1997] A. Roshchin, S. Yavshits, V. Jakovlev, E. Karttunen, J. Aaltonen, S. Heselius, Cross sections of nonfission reactions induced in Th-232 by low-energy protons. Yad. Fiz. 60, 2121; Phys. At. Nucl. 60 (1997) 1941.

[SAT2017] M. Sathekge, O. Knoesen, M. Meckel, M. Modiselle, M. Vorster, S. Marx, ^{213}Bi-PSMA-617 targeted alpha-radionuclide therapy in metastatic castration-resistant prostate cancer. Eur. J. Nucl. Med. Mol. Imaging 44 (2017) 1099–1100.

[SCH1995] R. Schwarzbach, K. Zimmermann, P. Bl auenstein, A. Smith, P. A. Schubiger, Development of a simple and selective separation of ^{67}Cu from irradiated zinc for use in antibody labelling: A comparison of methods. Appl. Radiat. Isot. 46 (1995) 329–336.

[SCH2001] R. Schwarzbach, K. Zimmermann, I. Novak-Hofer, P. A. Schubiger, A comparison of ^{67}Cu production by proton (67 to 12 MeV) induced reactions on ^{nat}Zn and enriched ^{68,70}Zn. J. Labelled Cpd. Radiopharm. 44, Suppl. 1 (2001) S809–S811.

[SHU2007] J. K. Shultis, R. E. Faw, An MCNP Primer. Kansas State University, Manhattan, Revised edition Sept. 2007.

[SIS1997] J. M. Sisterson, K. Kim, A. Beverding, P. A. J. Englert, M. W. Caffee, J. Vincent, C. Castaneda, R. C. Reedy, Measuring excitation functions needed to interpret cosmogenic nuclide production in lunar rocks. AIP Conf. Proc. 392 (1997) 811–814.

[SIS2008] J. M. Sisterson, Measurement of recoil nuclei losses for proton-induced reactions in Al, Si, Mg and Fe at 200 and 500 MeV. Nucl. Instrum. Methods B 266 (2008) 3913–3918.

[SKA2004] Ye. Skakun, S. M. Qaim, Excitation function of the ^{64}Ni(α,p)^{67}Cu reaction for production of ^{67}Cu. Appl. Radiat. Isot. 60 (2004) 33–39.

[SMI2012] N. A. Smith, D. L. Bowers, D. A. Ehst, The production, separation and use of ^{67}Cu for radioimmunotherapy: A review. Appl. Radiat. Isot. 70 (2012) 2377–2383.

[SON2005] A. A. Sonzogni, NuDat 2.0: Nuclear Structure and Decay Data on the Internet. AIP Conf. Proc. 769 (2005) 574–577. Latest version – NuDat 3.0 – available from: <http://www.nndc.bnl.gov/nudat2/>.

[SPA2004] I. Spahn, H. H. Coenen, S. M. Qaim, Enhanced production possibility of the therapeutic radionuclides ^{64}Cu, ^{67}Cu and ^{89}Sr via (n,p) reactions induced by fast spectral neutrons. Radiochim. Acta 92 (2004) 183–186.

[STE1992] G. F. Steyn, T. J. van Rooyen, P. J. Binns, J. H. Hough, F. M. Nortier, S. J. Mills, Design calculations for a local radiation shield of a radioisotope production target bombardment station. Nucl. Instrum. Methods A 316 (1992) 128–113.

[STE2013] G. F. Steyn, C. Vermeulen, A. H. Botha, J. L. Conradie, J. P. A. Crafford, J. L. G. Delsink, J. Dietrich, H. du Plessis, D. T. Fourie, Z. Kormány, M. J. van Niekerk, P. F. Rohwer, N. P. Stodart, J. G. de Villiers, A vertical-beam target station and high-power targetry for the cyclotron production of radionuclides with medium energy protons. Nucl. Instrum. Methods A 727 (2013) 131–144.

[STE2018a] G. F. Steyn, L. S. Anthony, F. Azaiez, S. Baard, R. A. Baard, A. H. Barnard, P. Beukes, J. I. Broodryk, J. L. Conradie, J. C. Cornell, J. G. de Villiers, S. G. Dolley, H. du Plessis, W. D. Duckitt, D. T. Fourie, M. E. Hogan, I. H. Kohler, J. J. Lawrie, C. Lussi, J. P. Mira, K. V. Mjali, H. W. Mostert, C. Naidoo, F. Nemulodi, D. Saal, N. P. Stodart, R. W. Thomae, J. van Niekerk, P. A. van Schalkwyk, Development of new target stations for the South African Isotope Facility. Instruments 2 (2018) 29-1 – 29-7.

[STE2018b] G.F. Steyn, C. Vermeulen, E. Isaacs, Encapsulation methods for solid radionuclide production targets at a medium-energy cyclotron facility. In: Proc. 28th World Conference of the International Target Development Society (INTDS2016), AIP Conf. Proc. 1962 (2018) 030016-1 – 030016-8.

[STE2021a] G. F. Steyn, M. A. Motetshwane, F. Szelecsényi, J. W. Brümmer, Pairing of thorium with selected primary target materials in tandem configurations: Co-production of ^{225}Ac/^{213}Bi and ^{230}U/^{226}Th generators with a 70 MeV H^- cyclotron. Appl. Radiat. Isot. 168 (2021) 109514:1–12.

[STE2021b] G. F. Steyn, T. N. van der Walt, F. Szelecsényi, C. Perrang, J. W. Brümmer, C. Vermeulen, N. P. van der Meulen, M. A. Motetshwane, M. R. van Heerden, Large-scale production of ^{88}Y and ^{88}Zr/^{88}Y generators: A proof of concept study for a 70 MeV H^- cyclotron. Appl. Radiat. Isot. 168 (2021) 109469:1–11.

[STO2016] J. Stoner, T. Gardner, A comparison of DOTA and DiamSar chelates of high specific activity eLINAC produced ^{67}Cu. J. Nucl. Med. 57 Suppl. 2 (2016) 1107.

[SYS2020] Systat Software, 2020. TableCurve 2D Automated Curve Fitting and Equation Discovery. Systat Software, https://systatsoftware.com.

[SZE2005] F. Szelecsényi, G. F. Steyn, Z. Kovács, C. Vermeulen, N. P. van der Meulen, S. G. Dolley, T. N. van der Walt, K. Suzuki, K. Mukai, Investigation of the ^{66}Zn(p,2pn)^{64}Cu and ^{68}Zn(p,x)^{64}Cu nuclear processes up to 100 MeV: Production of ^{64}Cu. Nucl. Instrum. Methods B 240 (2005) 625–637.

[SZE2017] F. Szelecsényi, G. F. Steyn, F. M. Nortier, Z. Kovács, New cross sections for the ^{27}Al(p,x)^{7}Be nuclear process: Monitoring proton beam energy via the ^{22}Na/^{7}Be cross-section radio between 45 and 200 MeV. EPJ Web Conf. 146 (2017) 08011: 1–4.

[TAR2019] F. T. Tárkányi, A. V. Ignatyuk, A. Hermanne, R. Capote, B. V. Carlson, J. W. Engle, M. A. Kellett, T. Kibédi, G. N. Kim, F. G. Kondev, M. Hussain, O. Lebeda, A. Luca, Y. Nagai, H. Naik, A. L. Nichols, F. M. Nortier, S. V. Suryanarayana, S. Takács, M. Verpelli, Recommended nuclear data for radioisotope production: Diagnostic positron emitters. J. Radioanal. Nucl. Chem. 319 (2019) 533–666.

[TKA2021] P. Tkac, D. A. Rotsch, S. D. Chemerisov, J. P. Byrnes, J. L. Bailey, S. G. Wiedmeyer, Large-scale dissolution of sintered Mo disks. J. Radioanal. Nucl. Chem. 327 (2021) 617–626.

[TIT2002] Yu. E. Titarenko, V. F. Batyaev, E. I. Karpikhin, R. D. Mulambetov, A. B. Koldobsky, V. M. Zhivun, S. V. Mulambetova, K. A. Lipatov, Yu. A. Nekrasov, A. V. Belkin, N. N. Alexeev, V. A. Schegolev, Yu. M. Goryachev, V. E. Luk'yashin, E. N. Firsov, Experimental and theoretical study of the yields of residual product nuclei produced in thin targets irradiated by 100–2600 MeV protons, Section 3.7: Experimental yields for ^{232}Th irradiated with 0.1, 0.2, 0.8, 1.2, 1.6 GeV protons. IAEA Report INDC(CCP)-434, 72–78, IAEA, Vienna, Austria, 2002. Available from: <www-nds.iaea.org/publications/>.

[TOR1985] L. Törnqvist, P. Vartia, Y. O. Vartia, How should relative changes be measured. Am. Stat. 39 (1985) 43–46.

[ULL1985] F. Ullman, Ullman's Encylopedia of Industrial Chemistry (eds. B. Elvers, C. Ley), ISBN: 978-3-527-30673-2, Wiley, 1985.

[VER2014] C. Vermeulen, Production of Radionuclides with Medium Energy Protons with the Emphasis on Targetry. PhD thesis, Stellenbosch University, 2014, unpublished.

[WEI2012a] J. W. Weidner, S. G. Mashnik, K. D. John, B. Ballard, E. R. Birnbaum, L. J. Bitteker, A. Couture, M. E. Fassbender, G. S. Goff, R. Gritzo, F. M. Hemez, W. Runde, J. L. Ullmann, L. E. Wolfsberg, F. M. Nortier, ^{225}Ac and ^{223}Ra production via 800 MeV proton irradiation of natural thorium targets. Appl. Radiat. Isot. 70 (2012) 2590–2595.

[WEI2012b] J. W. Weidner, S. G. Mashnik, K. D. John, B. Ballard, H. Bach, E. R. Birnbaum, L. J. Bitteker, A. Couture, D. Dry, M. E. Fassbender, M. S. Gulley, K. R. Jackman, J. L. Ullmann, L. E. Wolfsberg, F. M. Nortier, Proton-induced cross sections relevant to production

of ^{225}Ac and ^{223}Ra in natural thorium targets below 200 MeV. Appl. Radiat. Isot. 70 (2012) 2602–2607.

[WIL1976] R. L. Wilson, D. J. Frantsvog, A. R. Kunselman, C. Détraz, C. S. Zaidins, Excitation functions of reactions induced by ^{1}H and ^{2}H ions on natural Mg, Al, and Si. Phys. Rev. C 13 (1976) 976–983.

[WIL1993] W. B. Wilson, T. R. England, E. D. Arthur, C. A. Beard, C. D. Bowman, L. N. Engel, A. Gavron, D. C. George, L. L. Daemen, G. G. Hughes III, W. W. Kinnison, R. J. LaBauve, D. M. Lee, H. Lichtenstein, P. W. Lisowski, D. W. Muir, A. P. Palounek, R. T. Perry, E. J. Pitcher, R. E. Prael, G. J. Russell, G. Sanders, L. S. Waters, P. G. Young, H.-J. Ziock, Accelerator Transmutation Studies at Los Alamos with LAHET, MCNP, and CINDER'90. Los Alamos National Laboratory Report LA-UR-93-3080, 1993.

[ZHU2011] B. L. Zhuikov, S. N. Kalmykov, S. V. Ermolaev, R. A. Aliev, V. M. Kokhanyuk, V. L. Matushko, I. G. Tananaev, B. F. Myasoedov, Production of ^{225}Ac and ^{223}Ra by irradiation of Th with accelerated protons. Radiochemistry 53 (2011) 73–80.

[ZIE1980] J. F. Ziegler, Stopping cross-sections for energetic ions in all elements. In: The Stopping and Ranges of Ions in Matter, Vol. 5, Pergamon, New York, 1980.